

MAGNETIC COUPLINGS AND SUPERPARAMAGNETIC PROPERTIES OF
SPINEL FERRITE NANOPARTICLES

A Dissertation
Presented to
The Academic Faculty


By
Christy Riann Vestal

In Partial Fulfillment
Of the Requirements for the Degree
Doctor of Philosophy in Chemistry

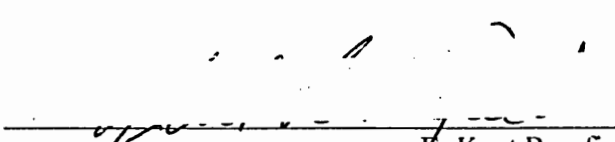
Georgia Institute of Technology

March 2004

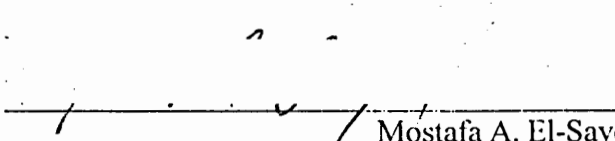
MAGNETIC COUPLINGS AND SUPERPARAMAGNETIC PROPERTIES OF
SPINEL FERRITE NANOPARTICLES



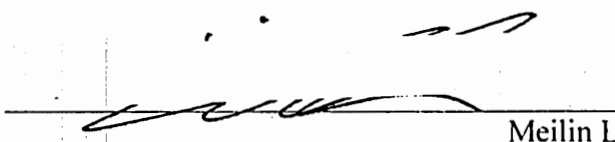
Z. John Zhang



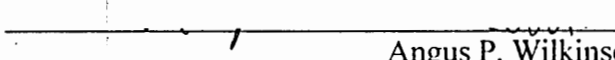
E. Kent Barefield



Mostafa A. El-Sayed



Meilin Liu



Angus P. Wilkinson

Date Approved

ACKNOWLEDGEMENTS

I would like to thank the following people who have made this work possible: First and foremost, Dr. Z. John Zhang, my advisor, who has provided support and allowed me the flexibility to pursue the topics that interested me. I would also like to thank my committee members for their comments and feedback over the years; I especially appreciate your interest and the time you took to stop me in the hallway or drop by my lab to see how things were going. A special thanks goes to Dr. Angus Wilkinson, for all of his assistance answering my numerous questions about neutron and x-ray diffraction, taking the time to work with me on GSAS refinements, and allowing me access to chemicals and equipment in his laboratory.

I would also like to thank Dr. Chris Jones for allowing me access to his TGA/DSC equipment and Dr. Jiri Janata for allowing me use of the FTIR-PAS. TEM studies were performed at the Georgia Institute of Technology Microscopy Center and the assistance and training by Ms. Yolande Berta has been most appreciated.

This work has benefited from the use of the Intense Pulse Neutron Source at Argonne National Laboratory, which is funded by the U.S Department of Energy, BES-Materials Science under Contract W-31-109-ENG-38. I thank Simine Short for her assistance with the neutron data collection. Neutron diffraction studies were also performed at the National Center for Neutron Research at the National Institute of

Standards and Technology. I acknowledge the support of the National Institute of Standards and Technology, U. S. Department of Commerce, in providing the neutron research facilities used in this work and thank Dr. Brian Toby for his assistance in the data collection and Dr. Qingzhen Huang for discussions. Many thanks also go to Dr. Julie Borchers for her collaboration in the small angle neutron diffraction studies.

I am also grateful for the help, assistance, and friendship of the past and present members of the Zhang Group. I especially thank Dr. Chao Liu and Dr. Adam Rondinone for getting me started in the lab and Dr. Anna Samia for her suggestions. Thanks are also extended to Qing Song for his helpful discussions and for providing me the nanocrystal samples that I used in Chapter 7. I also wish to acknowledge the contributions of Man Han to the variable chromium doping data presented Chapter 3. Thanks also to Eva Heintz for keeping me sane!

Funding for this work was provided from a number of sources including NSF (DMR-9875892), Sandia National Laboratory, the Beckman Young Investigator program of the Arnold & Mabel Beckman Foundation, and the PECASE program. I also acknowledge partial support of this project by the Georgia Institute of Technology Molecular Design Institute, under prime contract N00014-95-1-1116 from the Office of Naval Research. During my studies, I also received funding from a Georgia Institute of Technology Presidential Fellowship.

Last, but certainly not least, many thanks are extended to my family and close friends for their support and encouragement.

TABLE OF CONTENTS

Acknowledgements	iii
Table of Contents	v
List of Tables	xi
List of Figures	xiii
Summary	xx
Chapter 1 Introduction to Magnetism and Superparamagnetism	1
1.1 Introduction	1
1.2 Fundamentals of Magnetism	4
1.2.1 Magnetic Ordering	5
1.2.2 Exchange Interactions	10
1.2.2.1 Direct Exchange	10
1.2.2.2 Indirect Exchange	12
1.2.2.3 Superexchange	13
1.3 Single Domain Theory and Superparamagnetism	16
1.3.1 Single Domain Particles	16
1.3.2 Stoner-Wohlfarth Theory	19
1.3.3 Néel Theory	20
1.4 Superparamagnetism and Implications upon Applications	23

1.4.1 Data Storage	23
1.4.2 Magnetic Resonance Imaging (MRI) Contrast Agents	23
1.4.3 Magnetic Refrigeration	25
1.5 Anisotropy Mechanisms	26
1.5.1 Magnetocrystalline and Shape Anisotropy	26
1.5.2 Surface Anisotropy	28
1.5.3 Interparticle Interactions	30
1.6 References	33
Chapter 2 Spinel Ferrites and Instrumentation	39
2.1 Spinel Ferrites	39
2.1.1 Spinel Structure	39
2.1.2 Magnetic Properties	41
2.2 Synthesis of Spinel Ferrites Using Microemulsion Methods	43
2.2.1 Normal Micelle (Oil-in-Water)	46
2.2.1.1 Synthesis Overview	46
2.2.1.2 Size Control	48
2.2.2 Reverse Micelle (Water-in-Oil)	51
2.2.2.1 Synthesis Overview	51
2.2.2.2 Size Control	52
2.3 Instrumentation	53
2.3.1 Powder X-Ray Diffraction	53
2.3.2 Powder Neutron Diffraction	56
2.3.3 SQUID Magnetometry	64

2.3.4 Transmission Electron Microscopy	67
2.3.5 Photoacoustic Infrared Spectroscopy	67
2.3.6 Thermal Analysis	68
2.4 References	69
Chapter 3 Synthesis of Chromium-doped Cobalt Ferrite Nanoparticles using Microemulsion Methods and Size Dependent Studies of Their Magnetic Properties	73
3.1 Introduction	74
3.2 Experimental	77
3.2.1 Nanoparticle Synthesis	77
3.2.2 Instrumentation	78
3.3 Results and Discussion	79
3.3.1 Nanoparticle Synthesis and Size Dependent Characterization	79
3.3.2 Studies of Nanoparticles Regarding Anomalous Bulk Properties	90
3.3.3 Compositional Dependent Characterization	92
3.4 Conclusions	97
3.5 References	98
Chapter 4 Neutron Diffraction Studies of the Anomalous Magnetic Properties of Cobalt Chromium Iron Oxide Prepared from Nanoparticulate Precursor	100
4.1 Introduction	101
4.2 Experimental	103
4.3 Results and Discussion	104
4.3.1 Magnetic Measurements	104
4.3.2 Neutron Diffraction Studies	107
4.4 Conclusions	112

4.5 References	114
Chapter 5 Effects of Surface Coordination Chemistry on the Magnetic Properties of Manganese Ferrite Nanoparticles	115
5.1 Introduction	116
5.2 Experimental	119
5.3 Results and Discussion	120
5.3.1 FTIR-PAS and TGA/DSC	120
5.3.2 Magnetic Properties	126
5.4 Conclusions	139
5.5 References	141
Chapter 6 Comparing the Effects of Surface Chemistry on the Magnetic Properties of Cobalt Ferrite, Magnetite, and Manganese Ferrite Nanoparticles	143
6.1 Introduction	144
6.2 Experimental	145
6.3 Results and Discussion	146
6.4 Conclusions	156
6.5 References	157
Chapter 7 Effects of Interparticle Interactions upon the Magnetic Properties of Cobalt Ferrite and Manganese Ferrite Nanoparticles	159
7.1 Introduction	160
7.2 Experimental	164
7.3 Results	165
7.4 Discussion	169
7.5 Conclusions	175
7.6 References	176

Chapter 8 Synthesis of Polystyrene Coating Manganese Ferrite Nanoparticles Using Atom Transfer Radical Polymerization	178
8.1 Introduction	179
8.2 Experimental	181
8.3 Results and Discussion	182
8.4 Conclusions	189
8.5 References	192
Chapter 9 Magnetic Properties of Manganese Ferrite/Polystyrene Core/Shell Nanoparticles: A Non-Dilution Approach to Investigate Interparticle Interaction Effects	194
9.1 Introduction	195
9.2 Experimental	197
9.3 Magnetization Results	198
9.4 Discussion	201
9.5 Conclusions	205
9.6 References	206
Chapter 10 Synthesis and Magnetic Characterization of Manganese and Cobalt Spinel Ferrite-Silica Nanoparticles with Tunable Magnetic Core	209
10.1 Introduction	210
10.2 Experimental	212
10.3 Results and Discussion	213
10.4 Conclusions	221
10.5 References	222
Appendix A Synthesis of Magnesium Aluminum Oxide/Cobalt Ferrite Core/Shell Nanoparticles and Their Magnetic Characterization	225
A.1 Introduction	226

A.2 Experimental	227
A.2.1 MgAl ₂ O ₄ Nanoparticle Synthesis	227
A.2.2 Synthesis of MgAl ₂ O ₄ /CoFe ₂ O ₄ Core/Shell Nanoparticles	228
A.2.3 Instrumental	229
A.3 Results and Discussion	229
A.3.1 Synthesis and Characterization of MgAl ₂ O ₄	229
A.3.2 Preliminary Characterization of Core/Shell Nanoparticles	237
A.4 Conclusions	241
A.5 References	243
Appendix B Characterization of Cobalt-Zinc Ferrite/Zinc Ferrite Core/Shell Nanoparticles Using Small Angle Neutron Scattering	244
B.1 Introduction	245
B.2 Experimental	246
B.3 Results and Discussion	247
B.4 Conclusions	254
B.5 References	255
Vita	256

LIST OF TABLES

Table 1.1	Comparison of Magnetization Behavior for Differing Magnetic Ordering	8
Table 1.2	Critical size, Easy Axis, and Magnetocrystalline Anisotropy of Common Magnetic Materials	18
Table 2.1	Estimated and Experimental Single Domain Critical Size for Common Magnetic Materials	46
Table 2.2	Synthesis Conditions for the Preparation of Ferrite Nanoparticles	47
Table 4.1	Structural Parameters from Rietveld Refinement of Neutron Diffraction Data for Bulk CoCrFeO_4 Prepared from Nanoparticle Precursor	109
Table 4.2	Comparison of Sublattice and Net Magnetic Moment from Néel's Collinear Ferrimagnetic Model and Experimental Neutron Diffraction Data	109
Table 5.1	Grafting Density of Selected Ligands on Surface of MnFe_2O_4 Nanoparticles Determined from TGA/DSC Data	125
Table 5.2	Percentage Decrease in Coercivity from Surface Modification by <i>para</i> -Substituted Benzoic Acid Ligands with Respect to the Native 4 nm MnFe_2O_4 Nanoparticles	129
Table 5.3	Percentage Decrease in Coercivity from Surface Modification by Benzene Derivatives with Respect to the Native 4 nm MnFe_2O_4 Nanoparticles	129
Table 5.4	Percentage Decrease in Coercivity of Variable Sized Modified Nanoparticles with Respect to the Corresponding Native 4, 12, and 25 nm MnFe_2O_4 Nanoparticles	130
Table 6.1	Comparison of the Effects of Ligands Upon the Decrease in Coercivity with Respect to Native 30 nm Fe_3O_4 and 25 nm MnFe_2O_4 Nanoparticles	148

Table 6.2	Comparison of the Effects of Ligands Upon the Decrease in Coercivity with Respect to Native 4 nm CoFe_2O_4 and 4 nm MnFe_2O_4 Nanoparticles	149
Table 7.1	Effects of Increased Interparticle Interactions Upon the Blocking Temperature T_B , Néel's Relaxation time τ , the Coercivity H_C , and the Reduced Remanence M_R/M_S for a Variety of Magnetic Samples	163
Table A.1	d-spacing Comparison for Initial Precipitate and $\text{MgAl}_2(\text{OH})_8$	231
Table A.2	d-spacing Comparison for Spinel Samples	232
Table B.1.	Summary of the R_g determined from the Guinier region of the SANS Data with x-ray (and TEM) determined particle size	253

LIST OF FIGURES

Figure 1.1	Ancient Chinese spoon compass composed of magnetite rotated on a brass plate and stopped in the North-South direction and is one of the first known applications for a magnetic material	2
Figure 1.2	Survey of magnetization processes from meso- to nanoscale dimension	3
Figure 1.3	Magnetic moment orientations for various types of magnetic ordering (a) paramagnetic, (b) ferromagnetic, (c) antiferromagnetic, and (d) ferrimagnetic	7
Figure 1.4	Direct exchange for (a) small interatomic distances yields antiparallel alignment of spins, while (b) large interatomic distances result in parallel alignment	11
Figure 1.5	Bethe-Slater curve showing positive and negative exchange integral for assorted transition metals. Negative interactions yield antiferromagnetic order, while positive exchange J gives rise to ferromagnetic ordering	11
Figure 1.6	Exchange integral for RKKY exchange shows damped oscillatory response. Magnetic ordering dependent upon ion spacing.	12
Figure 1.7	Schematic of MnO unit cell with antiferromagnetic ordering shown	13
Figure 1.8	Schematic of superexchange interaction in MnO	14
Figure 1.9	(a) Bulk magnetic materials reverse through domain wall movement, while (b) the magnetization direction in single domain particles may reverse through coherent rotation (left) or curling (right)	17
Figure 1.10	Potential well schematic of Stoner-Wohlfarth anisotropy barrier for magnetization reversal	19

Figure 1.11	Schematic of particle moment with blocking temperature T_B and measurement time τ . Below T_B , the particles moment points along its easy axis. Above T_B , the moments can overcome the energy barrier E_A and flip orientations between any crystallographic direction. Figure from reference 3.	22
Figure 1.12	Schematic of magnetization for iron measured in a field of 80 Oe as a function of crystallographic orientation. Figure modeled from reference 35.	27
Figure 2.1	Schematic of spinel structure $A^{II}B_2^{III}O_4$. Metal cations are located tetrahedral (A) and octahedral (B) coordination sites within an FCC lattice of oxygen. Magnetic moments between the A and B sites are arranged antiparallel yielding ferrimagnetic ordering for the system.	40
Figure 2.2	Schematic of (a) normal micelle structure and (b) reverse micelle Structure	45
Figure 2.3	Three-dimensional cross section showing effects of metal cations [S(M)] and methylamine [A(M)] concentration on nanoparticle size. ³³	50
Figure 2.4	Three-dimensional cross section showing effects of metal cation concentration (S) and reaction temperature (T) on nanoparticle size. ³³	50
Figure 2.5	Schematic of x-ray tube	53
Figure 2.6	Schematic of crystal planes and Bragg's law. Figure from http://hyperphysics.phy_astr.gsu.edu/hbase/quantum/bragg.html	54
Figure 2.7	Comparison of nuclear reaction sources (left) and spallation sources (right) for the generation of neutrons	58
Figure 2.8	(a) X-ray and (b) neutron scattering factors. X-rays scale with Z, while neutrons vary	59
Figure 2.9	Schematic of scattering contrast for x-rays and neutrons	60
Figure 2.10	Neutron diffraction pattern of MnO (top) below the Curie temperature and (bottom) above the Curie temperature	61
Figure 2.11	Schematic of the SEPD instrument at IPNS	62
Figure 2.12	Schematic of the BT-1 powder diffractometer at NIST. The diffractometer radius is ~ 1 m	63
Figure 2.13	Comparison of magnetic field of different objects	65

Figure 2.14	Schematic of superconducting coil with two Josephson junctions (A and B)	66
Figure 3.1	X-ray diffraction pattern of 11 nm CoCrFeO ₄ nanoparticles	80
Figure 3.2	TEM micrograph of CoCrFeO ₄ nanoparticles with an average size of ~ 6 nm	80
Figure 3.3	TEM size distribution histogram with a size distribution of ~14%	81
Figure 3.4	Neutron diffraction pattern of 10 nm CoCrFeO ₄ nanoparticles at room temperature. The “goodness of fit” χ^2 is 1.44 and $R(f^2)$ for the data fitting is 0.0348. Below the pattern the first row of tick marks the peaks from the magnetic scattering. The second row of ticks corresponds to the peaks from the nuclear scattering	82
Figure 3.5	Temperature dependence of ZFC susceptibility for CoCrFeO ₄ nanoparticles of various sizes under a magnetic field of 100 G	83
Figure 3.6	Size dependence of blocking temperature under a 100G field for nanoparticles prepared by the normal and reverse micelle procedures	84
Figure 3.7	Field dependent magnetization of CoCrFeO ₄ nanoparticles with various sizes at 5K	85
Figure 3.8	(a) Size dependence of remnant magnetization for CoCrFeO ₄ nanoparticles; (b) Size dependence of saturation magnetization; (c) Size dependence of coercivity. The open circles (○) represent nanoparticles prepared by the reverse micelle procedure and open squares (□) represent nanoparticles synthesized by the normal micelle procedure	86
Figure 3.9	Saturation magnetization as a function of temperature for ~10 nm CoCrFeO ₄ nanoparticles	91
Figure 3.10	Temperature dependent susceptibility under 100G field for variable chromium compositions	93
Figure 3.11	Compositional dependence of the blocking temperature for 8 nm Nanoparticles	94
Figure 3.12	Hysteresis curves at 5K for 8 nm nanoparticles	94
Figure 3.13	Compositional dependence of saturation magnetization (top), remnant magnetization (middle) and coercivity (bottom) for 8 nm nanoparticles	95

Figure 4.1	Hysteresis measurements for bulk CoCrFeO_4 from 20 – 380 K in 40 K increments (top to bottom). Inset shows temperature dependence of saturation magnetization (M_s)	105
Figure 4.2	Temperature dependent susceptibility under a 100G applied field. Inset displays high temperature measurements	105
Figure 4.3	GSAS refinements of CoCrFeO_4 at 200K (top) and 350K (bottom) In the 200K pattern, the top set of tick marks represent calculated magnetic reflections and the bottom set of tick marks are the nuclear reflections. In the 350K, pattern, only the nuclear reflection ticks are present	108
Figure 4.4	A weak peak not corresponding to the spinel reflections or ferrimagnetic ordering appears $\sim 58^\circ 2\theta$ upon increasing the temperature from 200K (top) to 350K (bottom)	110
Figure 5.1	The spectra of surface Photoacoustic Infrared Spectroscopy (FTIR-PAS) for 4 nm MnFe_2O_4 nanoparticles with various ligands. The top curve is of the native 4 nm MnFe_2O_4 nanoparticles (a) followed by nanoparticles modified with aniline (b), benzoic acid (c), phenol (d), benzenesulfonic acid (e), and benzenethiol (e) respectively	121
Figure 5.2	FTIR-PAS spectra of 4 nm MnFe_2O_4 nanoparticles modified with benzoic acid	122
Figure 5.3	TGA (solid line) and DSC (dashed line) curves for (a) benzenesulfonic acid modified 4 nm MnFe_2O_4 nanoparticles and (b) benzenethiol modified nanoparticles	124
Figure 5.4	Field dependent magnetization at 5K for native 4 nm MnFe_2O_4 nanoparticles (dashed lines; \diamond) and 4 nm MnFe_2O_4 nanoparticles modified with benzoic acid (solid line; \square)	127
Figure 5.5	Top right quadrant hysteresis curve at 5 K for native 4 nm MnFe_2O_4 Nanoparticles and 4 nm MnFe_2O_4 nanoparticles modified with representative ligands. Inset shows magnification of coercivity region. The choice of functional group bound to the surface clearly results in distinctive differences in the magnitude of the coercivity changes	128
Figure 5.6	Theoretical model of surface anisotropy effects. (a) Calculated hysteresis curve for material with surface anisotropy and (b) calculated hysteresis curve for nanoparticle without surface anisotropy. From reference 25	132

Figure 5.7	(a) Ideal nanoparticle configuration has magnetic dipoles aligned ferrimagnetically throughout the entire particle volume. (b) Surface spin disorder is present in real nanoparticle systems. From reference 25	134
Figure 6.1	Hysteresis curve of native 30 nm Fe_3O_4 (solid line) and 30 nm Fe_3O_4 modified with benzenethiol (dashed line). Inset magnifies the coercivity region	146
Figure 6.2	Magnification of the coercivity at 5K for 30 nm Fe_3O_4 nanoparticles for the entire substituted benzene series	147
Figure 6.3	Hysteresis curves at 5K for native 4 nm CoFe_2O_4 (dashed lines) and aniline-modified 4 nm CoFe_2O_4 (solid line) nanoparticles	148
Figure 6.4	Comparison of the percentage decrease in coercivity upon ligand modification for 4 nm CoFe_2O_4 nanoparticles (dark bars) and 4 nm MnFe_2O_4 nanoparticles (light bars). BA = benzoic acid; BSA = benzenesulfonic acid	151
Figure 6.5	Comparison of the percentage decrease in coercivity upon ligand Modification for 30 nm Fe_3O_4 nanoparticles (light bars) and 25 nm MnFe_2O_4 nanopartilces (dark bars). BA = benzoic acid; BSA = benzenesulfonic acid	155
Figure 7.1	Temperature dependent susceptibility measurements for various dilutions from 100% to 0.05% (wt%) of 8.5 nm CoFe_2O_4 nanoparticles	165
Figure 7.2	Plot of blocking temperature T_B as a function of dilution percentage for 8.5 nm CoFe_2O_4 nanoparticles. The line serves only to guide the eye.	166
Figure 7.3	Plot of reduced remanence M_R/M_S as a function of dilution percentage for 8.5 nm CoFe_2O_4 nanoparticles. The line serves only to guide the eye	167
Figure 7.4	Temperature dependent susceptibility measurements for various dilutions of 8.5 nm MnFe_2O_4 nanoparticles	167
Figure 7.5	Effect of dilution upon the blocking temperature of 8.5 nm MnFe_2O_4 nanoparticles. The line serves only to guide the eye	168
Figure 7.6	Effect of dilution upon the reduced remanence M_R/M_S of 8.5 nm nanoparticles. The line serves only to guide the eye	168

Figure 7.7	Comparison of dilution effects upon the blocking temperature for 8.5 nm MnFe_2O_4 (■, solid line) and 8.5 nm CoFe_2O_4 (◆, dashed line)	170
Figure 8.1	Schematic of polystyrene coating procedure	183
Figure 8.2	Photoacoustic infrared spectroscopy of as synthesized MnFe_2O_4 nanoparticles (top), particles modified with 3-chloropropionic acid (middle), and after polymerization (bottom)	184
Figure 8.3	TEM image of ~ 16 nm MnFe_2O_4 /polystyrene core/shell nanoparticles	185
Figure 8.4	TEM image of MnFe_2O_4 /polystyrene nanoparticles prepared using (A) 3-chloropropionic acid and (B) 2-chloropropionic acid. The inset in A shows a magnification of a core/shell particles in A and the scale bar represents 25 nm	187
Figure 8.5	Schematic of synthesis routes to biologically active surface	191
Figure 9.1	Expanded region of hysteresis curve at 5K for polystyrene coated (- -, ○) and native 18.5 nm MnFe_2O_4 (-, □)	198
Figure 9.2	Percentage decrease in coercivity of polystyrene coated MnFe_2O_4 nanoparticles (■) and 3-chloropropionic acid modified MnFe_2O_4 (●) with respect to native 18.5 nm MnFe_2O_4 . The line serves only to guide the eye	199
Figure 9.3	Variation of reduced remanence (M_R/M_S) for native 18.5 nm MnFe_2O_4 nanoparticles (▲), 3-chloropropionic acid modified nanoparticles (●) and polystyrene coated nanoparticles (■). The line serves only to guide the eye	200
Figure 10.1	Powder x-ray diffraction pattern for (a) native 12 nm CoFe_2O_4 nanoparticles and (b) 13 nm CoFe_2O_4 nanoparticles coated with silica	214
Figure 10.2	TEM micrograph of silica- MnFe_2O_4 particles. Inset shows a higher magnification of a silica-ferrite nanoparticle with diameter 79 nm	215
Figure 10.3	Field dependent magnetization at 5K for 13 nm CoFe_2O_4 nanoparticles before and after silica coating	217
Figure 10.4	Field dependent magnetization at 5K for 12 nm MnFe_2O_4 nanoparticles before and after silica coating	217

Figure A.1	X-ray diffraction patterns for (a) the initial precipitated white powder and (b) 8 nm MgAl_2O_4 nanoparticles formed after annealing the powder sample shown in (a)	230
Figure A.2	TEM micrograph of 13 nm MgAl_2O_4 nanoparticles	233
Figure A.3	TGA (solid line) and DSC (dashed line) curves for precipitated Powders	234
Figure A.4	TGA (solid line) and DSC (dashed line) curves for $\text{Al}(\text{OH})_3$ standard	235
Figure A.5	TGA (solid line) and DSC (dashed line) curves for $\text{Mg}(\text{OH})_2$ standard	235
Figure A.6	X-ray diffraction patterns for (top) MgAl_2O_4 core and (bottom) same core after seed-mediated synthesis	237
Figure A.7	TEM-EDS spectrum taken near edge of nanoparticle	238
Figure A.8	TEM-EDS spectrum taken at center of nanoparticle	238
Figure A.9	Blocking temperature of $\text{MgAl}_2\text{O}_4/\text{CoFe}_2\text{O}_4$ core/shell nanoparticles as a function of saturation magnetization (M_S)	239
Figure A.10	Coercivity as a function of saturation magnetization (M_S) for $\text{MgAl}_2\text{O}_4/\text{CoFe}_2\text{O}_4$ core/shell nanoparticles	240
Figure B.1	Effect of ZnFe_2O_4 shell thickness upon the blocking temperature	247
Figure B.2	Effect of ZnFe_2O_4 shell thickness upon saturation Magnetization (M_S)	248
Figure B.3	Example of raw SANS data for core nanoparticle sample	249
Figure B.4	Scattering intensity as a function of temperature for core nanoparticle	249
Figure B.5	SANS measurements at 300K for the $\text{Zn}_{0.05}\text{Co}_{0.95}\text{Fe}_2\text{O}_4$ core (◆), the core with a 2.5 nm shell (■) and the core with a 4.5 nm shell (●)	250
Figure B.6	Identification of regions in which data analysis can be performed	251
Figure B.7	Example of Porod plot for the core sample	252
Figure B.8	Example of Guinier plot for the core sample	253

SUMMARY

The relationship between macroscopic magnetic properties and magnetic couplings is investigated using various spinel ferrite nanoparticles. The results of this thesis contribute to the knowledge of nanomagnetism in spinel ferrites by systematically investigating the effects of magnetocrystalline anisotropy, exchange coupling interactions, surface chemistry and anisotropy, and interparticle interactions upon the magnetic properties of spinel ferrite nanoparticles. In **Chapter 3**, the synthesis of $\text{CoCr}_x\text{Fe}_{2-x}\text{O}_4$ nanoparticles with variable size and composition is described and the magnetic characterization performed as a function of size and composition. This serves as an example of the effects of exchange energy and magnetocrystalline anisotropy. **Chapter 4** details neutron diffraction studies of bulk CoCrFeO_4 prepared from nanoparticles precursors and provides a further example of the effect of exchange energy upon the magnetic structure and properties. **Chapter 5** describes the effects of surface ligand modification upon the magnetic properties of MnFe_2O_4 nanoparticles, while **Chapter 6** provides further surface chemistry studies on CoFe_2O_4 and Fe_3O_4 nanoparticles. These studies are the first experiments that systematically vary the surface chemistry in order to deduce a correlation between surface ligands and magnetic properties. **Chapter 7** describes the dilution studies of CoFe_2O_4 and MnFe_2O_4 nanoparticles in eicosane and provides a general understanding of the effects of

interparticle interactions for differing ferrite systems. In **Chapter 8**, the synthesis of MnFe_2O_4 /polystyrene core/shell nanoparticles is described, while the interparticle interaction effects as a function of shell thickness are addressed in **Chapter 9**. **Chapter 10** describes the synthesis and magnetic characterization of silica coated CoFe_2O_4 and MnFe_2O_4 nanoparticles. The magnetic properties of this materials system result primarily from the contributions of magnetocrystalline anisotropy and surface chemistry.

Appendix A summarizes the synthesis and characterization of MgAl_2O_4 , a nonmagnetic spinel and introduces the preliminary work on the synthesis and magnetic characterization of $\text{MgAl}_2\text{O}_4/\text{CoFe}_2\text{O}_4$ core/shell ferrites, which were prepared in order to isolate the influence of surface interactions upon the magnetic properties of ferrite nanoparticles. **Appendix B** describes the preliminary temperature dependent small angle neutron scattering (SANS) experiments on $\text{Zn}_{0.05}\text{Co}_{0.95}\text{Fe}_2\text{O}_4/\text{ZnFe}_2\text{O}_4$ core/shell nanoparticles.

CHAPTER 1

INTRODUCTION TO MAGNETISM AND SUPERPARAMAGNETISM

1.1 Introduction

The mineral magnetite (Fe_3O_4) was perhaps the first magnetic material to be exploited for its magnetic properties. The ancient Chinese spoon compasses shown in Figure 1.1 were made of spoon-shaped magnetite that rotated on polished “earth plates” and stopped in the North-South direction.¹ From this ancient device, navigational compasses were developed. Today magnetite is still used in many applications such as laser printing technologies.² Its uses continue to expand when the materials dimensions are reduced to the nanoscale. For example, ultra-small, less than 20 nm, magnetite particles are the lead materials investigated in biomedical applications such as magnetically targeted drug delivery and magnetic resonance imaging (MRI) contrast agents.³⁻⁸ While magnetic materials of all types have been used for centuries for a wide range of applications, due to the unique size and physical properties when materials dimensions are reduced to the nanometer length, many new avenues for diverse applications have been opened.

Over the past 70 years efforts have been devoted to understanding the unique physical phenomenon appearing in nanosize particle systems. The motivation for such

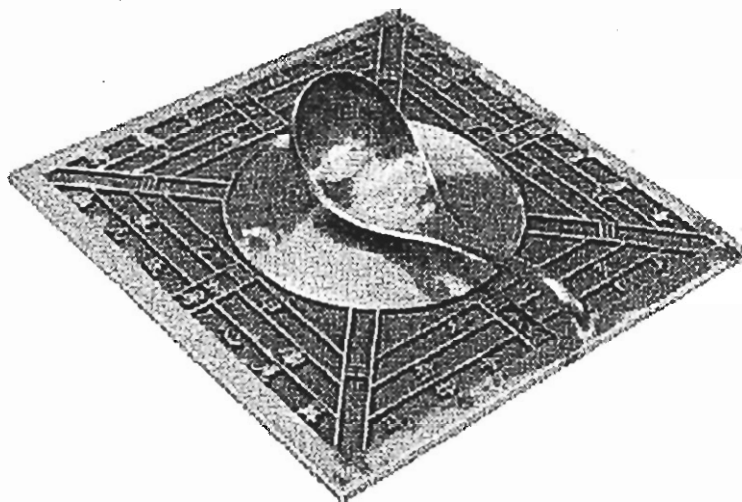


Figure 1.1 Ancient Chinese spoon compass composed of magnetite rotated on a brass plate and stopped in the North-South direction and is one of the first known application for a magnetic material.

attention is the changes in physical properties that occur when the critical length governing some phenomenon (magnetic, electric, transport, etc) is comparable to the nanoparticle size. Often novel size dependent properties are found in nanoscale materials, which may be dramatically different from those of their bulk counterparts.⁹⁻¹² The behavior of bulk magnetic materials is determined and influenced by the formation of domains and domain wall movement. As a result, interpreting the magnetic response of bulk materials is complicated by the fact that domain wall moment can be impeded or pinned by impurities, grain boundaries, etc. in the sample, and a direct correlation between the observed magnetic feature and the quantum origins of magnetism is not readily achievable. Below a critical size, domain formation is no longer energetically

favored and the particles exist in a single domain state.^{13,14} As a result new magnetic physical parameters emerge and gives rise to new magnetic features. Some of the unique and/or enhanced magnetic properties that may occur when the material dimensions are reduced to the nanoscale are giant magnetoresistance (GMR), coercivity enhancement, magnetocaloric effect enhancement, superparamagnetism and quantum tunneling of magnetization.¹⁵⁻²² Figure 1.2 outlines the changes in magnetic behavior over a variety of length scales.²³

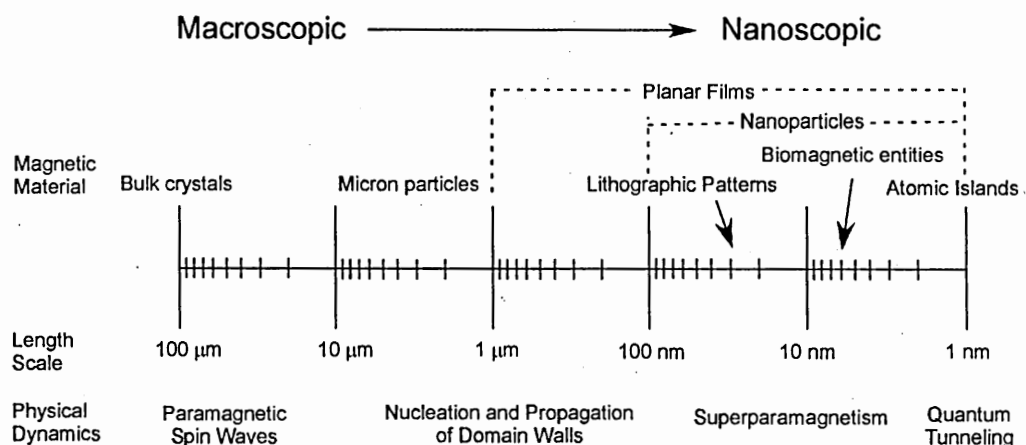


Figure 1.2 Survey of magnetization processes from meso- to nanoscale dimensions

Fundamentally, due to the single domain nature of magnetic materials below a critical size, magnetic nanoparticles provide a unique opportunity to understand and measure the quantum origins of magnetism. As a result of their novel magnetic properties magnetic nanoparticles also offer attractive potentials not only for fundamental

science value but also for technological innovations. While magnetic information storage is perhaps the most familiar application associated with magnetic nanoparticles, other unique uses for magnetic particle impact everyday life. For example, magnetic nanoparticles are used in industrial applications such as magnetic sensors, refrigerant materials, permanent magnets, and toner.²⁴⁻²⁸ Other applications include ferrofluids, catalysts, cell separation, magnetically guided drug delivery, and MRI contrast enhancement agents.^{3-8,29-33}

This chapter provides an overview of general magnetism fundamentals and a description of issues important to magnetism on the nanoscale - superparamagnetism, single domain theory, and anisotropy mechanisms.

1.2 Fundamentals of Magnetism³⁴⁻³⁶

A magnetic field is produced whenever there is an electrical charge in motion. In atoms, the magnetic moment originates from the motion of the electron spin and the orbital angular momentum around the nucleus. When a material is placed in a magnetic field, the flux density (or magnetic induction **B**) is given by

$$\mathbf{B} = \mathbf{H} + 4\pi \mathbf{M} \quad (1.1)$$

where **H** is the magnetic field and **M** is the magnetization. The *susceptibility* of a material χ is the ratio between the magnetization and the field given by

$$\chi = \mathbf{M} / \mathbf{H} \quad (1.2)$$

The *permeability* of a material relates the magnetic induction to the field by

$$\mathbf{B} = \mu \mathbf{H} \quad (1.3)$$

and relates to the magnetic susceptibility by

$$\mu = \mu_0(1+\chi) \quad (1.4)$$

where μ_0 is the vacuum permeability. When characterizing magnetic properties, the susceptibility is the main parameter that is usually considered as it provides a measure of the response of the sample to an applied magnetic field. The differences in magnetic behavior of materials are most often described in terms of the temperature and field dependence of the susceptibility.

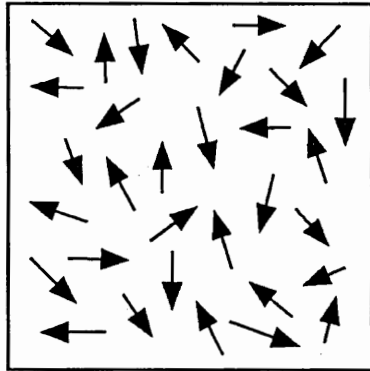
1.2.1 Magnetic Ordering³⁴⁻³⁶

Magnetic materials can essentially be divided into two groups. Diamagnetic and paramagnetic materials belong in the first group, in which there is no interaction between individual magnetic moments and each moment acts independently of one another.

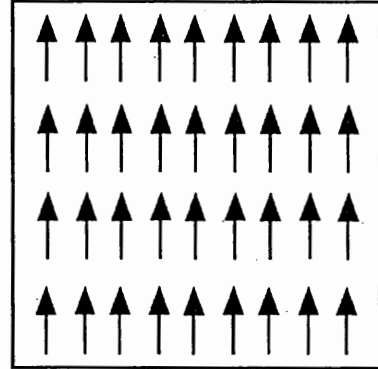
Diamagnetic materials have no unpaired electrons and hence no moment. Copper, bismuth, boron, phosphorous, sulfur, and N_2 are all diamagnetic. Most organic compounds are also diamagnetic. *Paramagnetic* materials have an unpaired electron oriented randomly within the sample (Figure 1.3a). Examples of paramagnetic materials include O_2 , NO, and chromium. In the second group, the magnetic moments couple with

one another and form magnetically ordered states. Magnetic ordering can take the form of ferromagnetism, antiferromagnetism, or ferrimagnetism. When magnetic interactions favor parallel alignment of the spins (Figure 1.3b), the material is called *ferromagnetic*, and the material exhibits net magnetization even in the absence of an external magnetic field. Common examples of materials with ferromagnetic ordering include iron, nickel, and cobalt. *Antiferromagnetic* materials have their magnetic spins aligned antiparallel (Figure 1.3c). These materials do not have a net magnetization in the absence of an external magnetic field. Many transition metal compounds such as CoO, MnO, NiO, and CuCl₂ are antiferromagnets. The final class of magnetic materials with ordered moments are *ferrimagnets*. Like antiferromagnets, ferrimagnetic materials have their magnetic moments aligned antiparallel. However, the magnitude of the magnetic dipole or the number of moments pointing in one direction differs from the magnitude or number pointing in the opposite direction (Figure 1.3d). Hence a net magnetization is present in the absence of an external magnetic field. Spinel ferrites, the materials investigated in this thesis, are the most common example of ferrimagnetic materials.

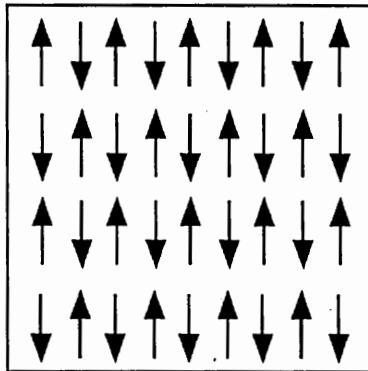
The magnetic response of materials with differing magnetic ordering is summarized in Table 1.1. Diamagnetic materials have a small, negative magnetic susceptibility, while paramagnetic materials have a small, positive magnetic susceptibility. Ferro- and ferrimagnetic materials have large, positive magnetic susceptibilities, while antiferromagnetic materials, have small magnetic susceptibilities comparable to paramagnetic materials. As a result of their differing susceptibilities, diamagnetic materials are repelled by an external magnetic field, paramagnetic and antiferromagnetic



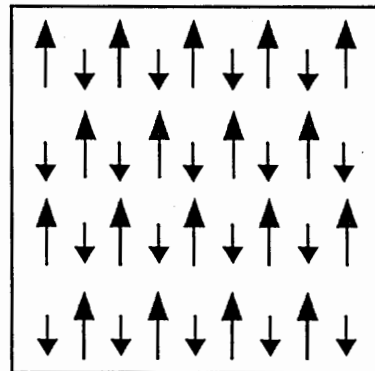
a



b



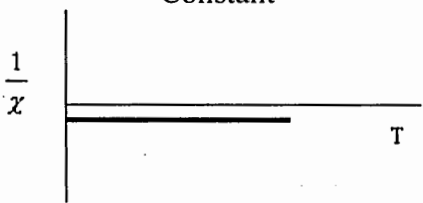
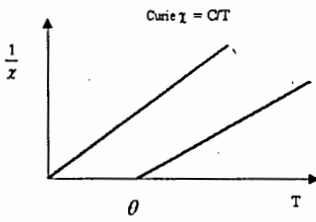
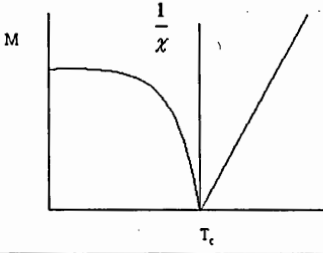
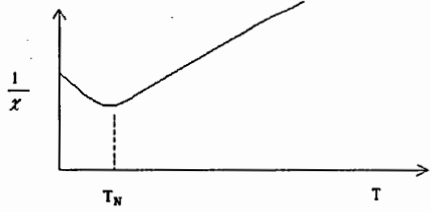
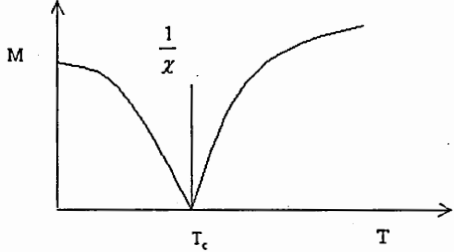
c



d

Figure 1.3 Magnetic moment orientations for various types of magnetic ordering (a) paramagnetic, (b) ferromagnetic, (c) antiferromagnetic, and (d) ferrimagnetic.

Table 1.1 Comparison of Magnetization Behavior for Differing Magnetic Ordering³⁴

Class	Critical Temperature	Magnitude of χ	Temperature Variation of χ
Diamagnetic	None	-10^{-6} to -10^{-5}	<p>Constant</p> 
Paramagnetic	None	10^{-5} to 10^{-3}	<p>$\chi = C/T$</p> 
Ferromagnetic	Curie Temperature	Large below T_C	<p>Above T_C : $\chi = C/(T-\Theta)$</p> 
Antiferromagnetic	Néel Temperature	10^{-5} to 10^{-3}	<p>Above T_N : $\chi = C/(T\pm\Theta)$</p> 
Ferrimagnetic	Curie Temperature	Large below T_C	<p>Above T_C : $\chi \cong C/(T\pm\Theta)$</p> 

materials are somewhat attracted by a magnetic field, and ferromagnetic and ferrimagnetic materials are strongly attracted by an applied magnetic field.

Materials with differing magnetic ordering also display varying temperature dependences of the susceptibility. Paramagnetic materials obey the Curie law, given in Equation 1.5,

$$\chi = C/T \quad (1.5)$$

where C is the Curie constant. Although the magnetic moments do not interact in paramagnetic materials, they do align in a magnetic field. With increasing temperature, alignment is more difficult, and hence from 1.5, the susceptibility decreases with temperature. For ferromagnetic ordering, the temperature dependence follows the Curie-Weiss law

$$\chi = C/(T-\theta) \quad (1.6)$$

where θ is the Weiss constant. For ferromagnetic materials, the Weiss constant and the Curie temperature are nearly identical. At and below the temperature T_C the materials magnetically order. Above this temperature, they lose their magnetic ordering and display paramagnetic behavior.

1.2.2 Exchange Interactions³⁴⁻³⁷

Two factors are primarily responsible for the magnetic properties of materials - exchange interactions and spin-orbit (L-S) couplings. Exchange interactions determine the magnetic ordering of a material, while spin-orbit couplings determine the magnetization orientation within a material (further detail in Section 1.5.1). The nature and magnitude of exchange interactions between neighboring magnetic ions determines how the individual moments will align and will force the moments to align either parallel (positive exchange) or antiparallel (negative exchange) to its neighbors. The exchange energy U is dependent upon the orbital overlap of electron spins S_i and S_j and is given by

$$U_{ij} = -2 J_{ij} S_i S_j \quad (1.7)$$

where J is the exchange integral relating the degree of orbital overlap. Three types of exchange energy are known - direct exchange, indirect exchange, and superexchange.

1.2.2.1 Direct Exchange

Direct exchange occurs between moments that are close enough to have sufficient overlap of their wavefunctions. When the atoms are very close together the Coulomb interaction is minimized when the electrons reside between the nuclei (Figure 1.4a). By Pauli's exclusion principle, the electrons must have opposite spin, giving rise to antiparallel (antiferromagnetic) ordering. If the atoms are far apart, the electrons are localized far from one another in order to minimize electron-electron repulsion, giving rise to parallel (ferromagnetic) alignment (Figure 1.4b). For direct exchange the

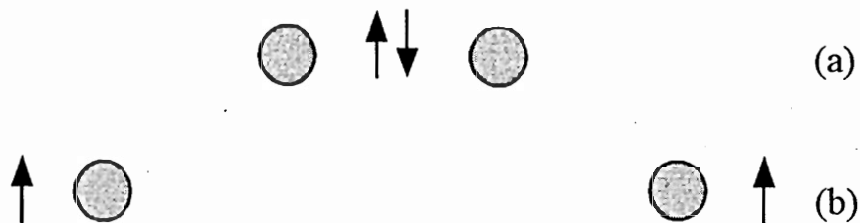


Figure 1.4. Direct exchange for (a) small interatomic distances yields antiparallel alignment of spins, while (b) large interatomic distances result in parallel alignment.

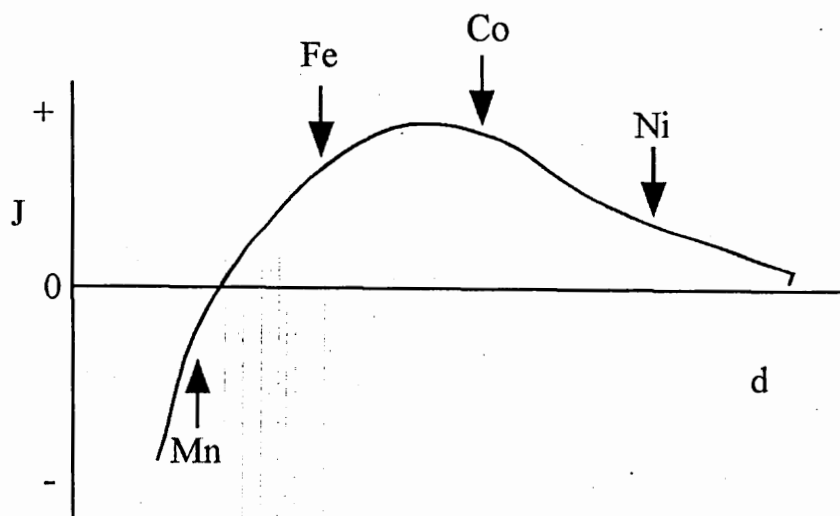


Figure 1.5. Bethe-Slater curve showing positive and negative exchange integral for assorted transition metals. Negative interactions yield antiferromagnetic order, while positive exchange J gives rise to ferromagnetic ordering.

exchange coefficient J can be positive or negative depending on the balance between Coloumb and kinetic energies. The Bethe-Slater curve shown in Figure 1.5 represents the magnitude of direct exchange as a function of atomic spacing. Iron, cobalt, and nickel all have positive exchange and thus ferromagnetic ordering, while manganese has negative exchange and thus displays antiferromagnetic ordering.

1.2.2.2 Indirect Exchange

Indirect exchange couples moments over relatively large distances via conduction electrons. It is the dominant exchange interaction in metals where there is little to no direct overlap between neighboring magnetic electrons. Indirect exchange, more commonly known as the RKKY interaction (named after Ruderman, Kittel, Kasuya, and Yosida), is the primary exchange mechanism for rare-earth metals. The exchange coefficient J for RKKY interactions oscillates between positive and negative with a dampening as shown in Figure 1.6. Therefore, the magnetic ordering could either be ferromagnetic or antiferromagnetic depending upon the ion separation.

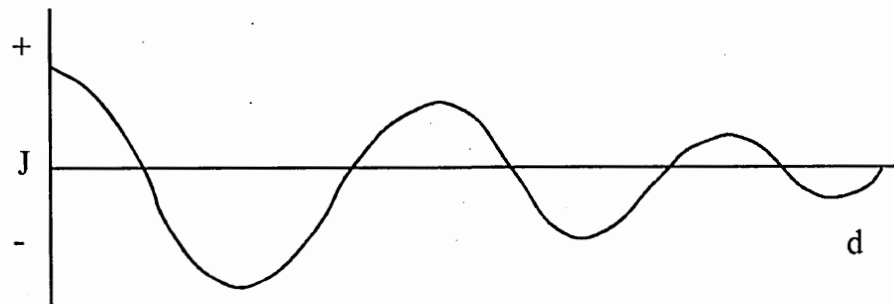


Figure 1.6. Exchange integral for RKKY exchange shows damped oscillatory response. Magnetic ordering dependent upon ion spacing.

1.2.2.3 Superexchange

Superexchange involves the interactions between moments that are too far apart to couple via direct exchange. Instead coupling occurs through a non-magnetic material, such as oxygen. The exchange integral J depends upon the distance between the ions and the symmetry and arrangement of the cation and anion orbitals. The simplest view of superexchange is when the orbital symmetry is 180° (this arrangement also yields the strongest superexchange). An example of a material meeting this requirement is MnO, an antiferromagnet whose rock salt structure is shown in Figure 1.7. A schematic of the $3d_{x^2-y^2}$ and $2p_x$ orbitals involved in the superexchange in MnO are shown in Figure 1.8.

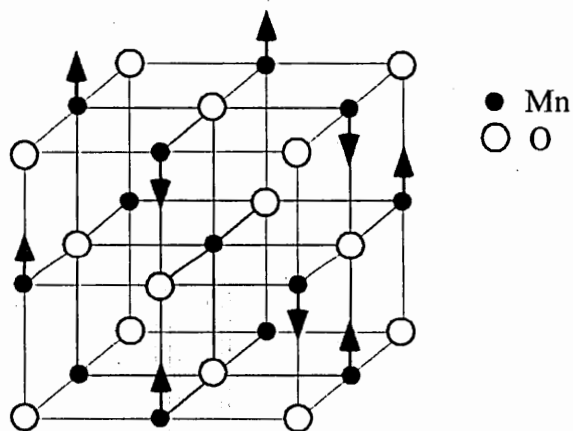


Figure 1.7. Schematic of MnO unit cell with antiferromagnetic ordering shown

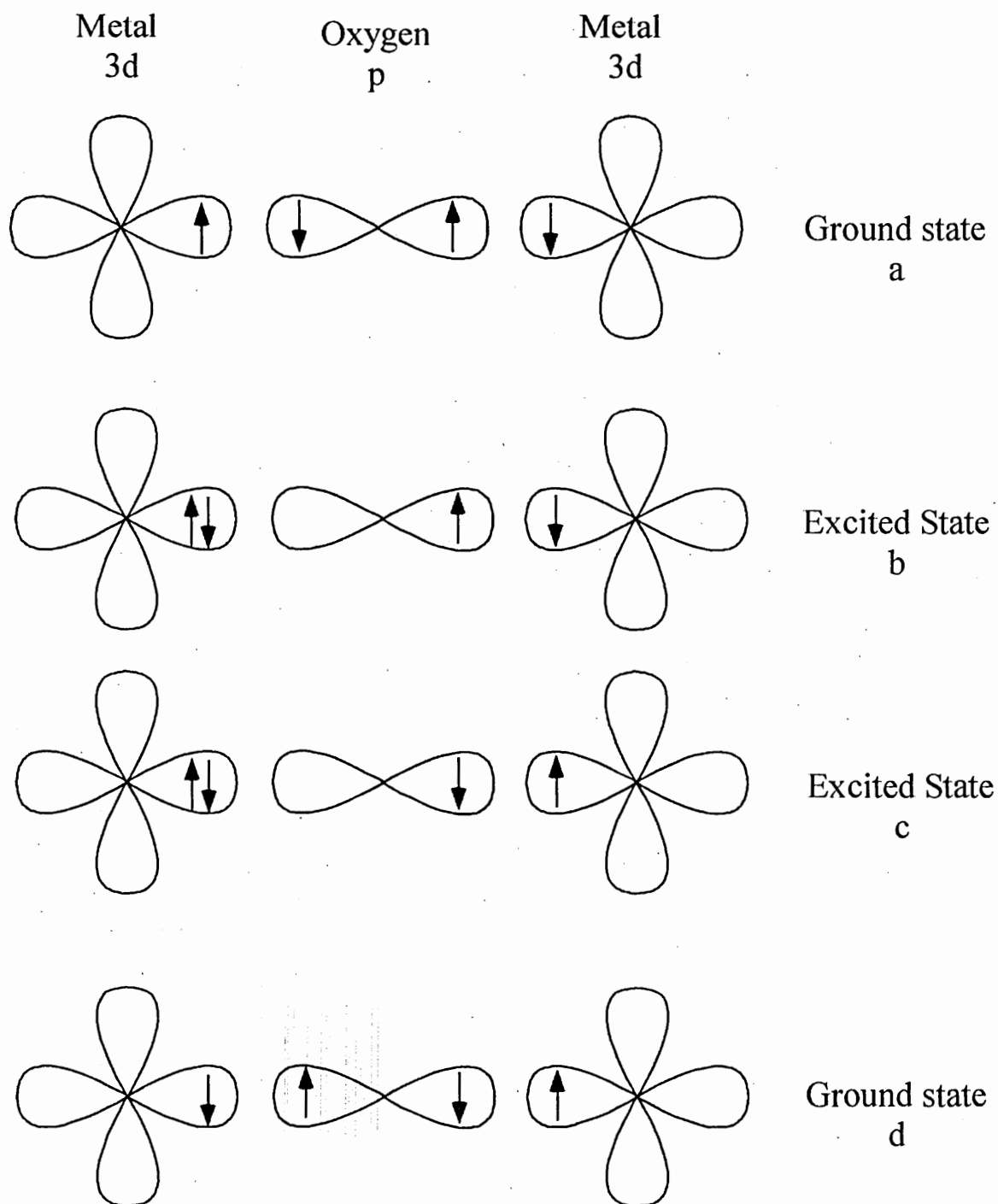


Figure 1.8. Schematic of superexchange interaction in MnO.

the metal 3d orbital. The 3d and p orbitals exchange electrons by exciting one of the p_x electrons into an empty d state, forming a (p-d) σ or σ^* bond (Figure 1.8b). When the p electron is excited into the empty d state, the remaining electron of opposite spin may now exchange with the other metal orbitals (Figure 1.8c). The complete exchange of the electrons is accomplished by Figures 1.8 c&d. For d ions with the same ground state configuration (in this example d^5), antiferromagnetic coupling results.

The magnetic ordering in spinel ferrites occurs via superexchange. In ferrites, three exchange interactions J_{A-A} , J_{B-B} , and J_{A-B} are present due to the two lattice sites (A and B) in the crystal structure (see Chapter 2). Interestingly, the exchange integral is negative for all three interactions, meaning antiparallel alignment of spins for all the sublattices is preferred, an orientation which cannot occur. However, superexchange is dependent upon the symmetry of the orbitals, their spatial orientation, and the distance between ions. A 180° linear arrangement as described above for MnO yields the strongest overlap and exchange. In spinels the A-O-B bond angle is 125° , the B-O-B bond angle is 90° , the A-O-A bond angle is 79° (and the A-A separation is $\sim 4\text{\AA}$).³⁷ Due to the degree of orbital overlap resulting from these geometrical considerations, the J_{A-B} exchange integral is the dominant exchange, followed in magnitude by J_{B-B} , then J_{A-A} . As a result, the arrangement of spins between the A and B lattice sites is antiparallel, thereby forcing the spin arrangement on the A and B sites to (unfavorably) be parallel.

1.3 Single Domain Theory and Superparamagnetism

1.3.1 Single Domain Particles

Bulk magnetic materials contain magnetic domains, consisting of groups of spins all pointing in the same direction. The domains are separated by domain walls which form to minimize magnetostatic energy and have a characteristic width.^{38a} Magnetization reversal occurs through the nucleation and movement of the domain walls shown in Figure 1.9a. Below a critical length scale, the energy required to produce a domain wall becomes greater than the corresponding reduction in magnetostatic energy. As a result domain formation is no longer supported and the particle becomes a single domain.¹³ Magnetization reversal may occur by coherent rotation of spins, curling, or quantum tunneling of the magnetization vector (Figure 1.9b).^{38b}

In 1930, Frenkel and Dorfman first predicted the existence of single domain particles,¹³ while, Kittel in 1946 provided the first estimates of the critical size for the existence of a single domain.¹⁴ The critical diameter (D_{cr}) depends upon the saturation magnetization (M_S), the anisotropy energy density (K), and the exchange energy density (A) as given in Equation 1.8.^{38c35}

$$D_{cr} = 36 (KA)^{1/2} / \mu_0 M_S^2 \quad (1.8)$$

The values of D_{cr} cover a wide size range – from 10 – 800 nm, though for most materials it falls below 100 nm. Table 1.2 lists the critical diameter for a number of common magnetic materials.^{24,39-41}

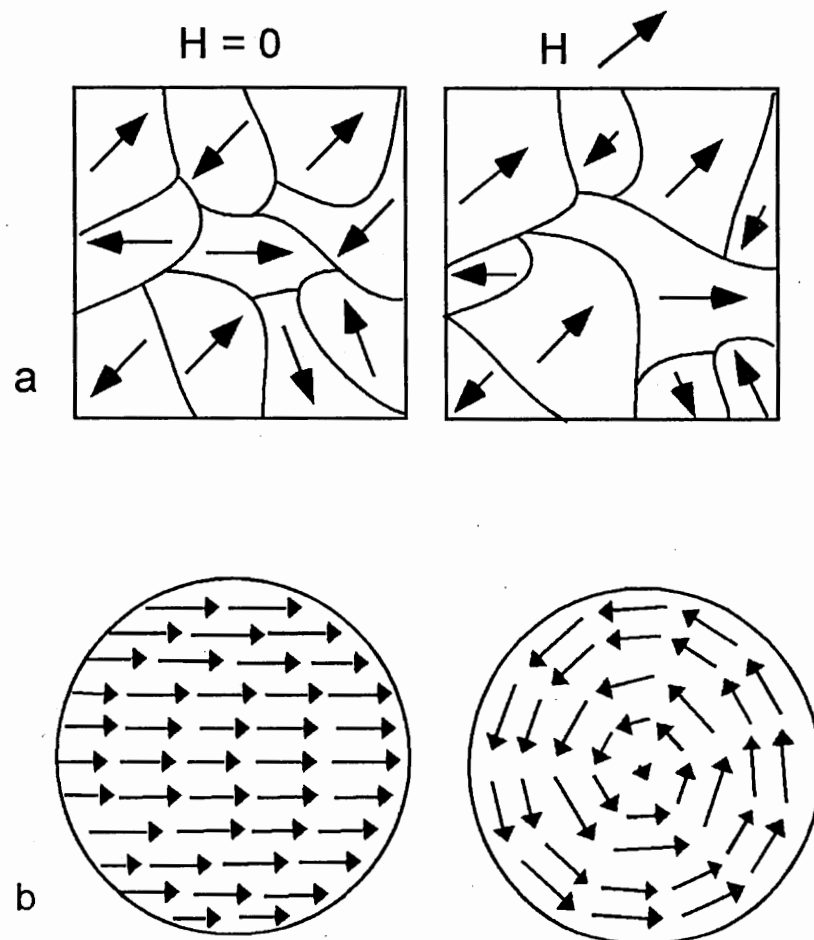


Figure 1.9. (a) Bulk magnetic materials reverse through domain wall movement, while (b) the magnetization direction in single domain particles may reverse through coherent rotation (left) or curling (right).

When $D < D_{cr}$ the material will be uniformly magnetized. The magnetic moments in each particle will point to the same preferred direction known as the *easy axis*. The easy axis is usually a preferred crystallographic direction determined by the magnetocrystalline anisotropy (K) of the material, which arises from spin-orbit couplings. The easy axis is given for a material and is independent of shape.³⁹ Table 1.2 also lists the easy axis directions and magnetocrystalline anisotropy for common magnetic materials.

Table 1.2. Critical Size, Easy Axis, and Magnetocrystalline Anisotropy of Common Magnetic Materials

Material	D_{cr} (nm)	Easy Axis	$ K_1 $ (erg/cm ³) x 10 ⁵
Co (hcp)	60	0001	53
Fe (bcc)	15	100	5
Ni (fcc)	55	100	0.5
Nd ₂ Fe ₁₄ B	230	001	500
SmCo ₅	750	0001	1700
FePt (L10)	340	001	660-1000
CoFe ₂ O ₄	50	100	18
Fe ₃ O ₄	128	111	1.2
MnFe ₂ O ₄	50	111	0.25

1.3.2 Stoner-Wohlfarth Theory

In 1948, Stoner and Wohlfarth described the case of magnetization reversal through the coherent rotation of the magnetization vector for an assembly of single domain, non-interacting particles with uniaxial anisotropy.⁴² In the simplest form, the energy barrier for coherent magnetization reversal of single domain magnetic nanoparticles is given as

$$E_A = KV \sin^2 \theta \quad (1.9)$$

where E_A is the energy barrier, K is the magnetic anisotropy of the particle, V is the particle volume, and θ is the angle between the magnetic moment and the easy axis of the particle. The anisotropy energy barrier E_A may be viewed as a simple potential well model as shown in Figure 1.10. In reality, there may be many minima, corresponding to

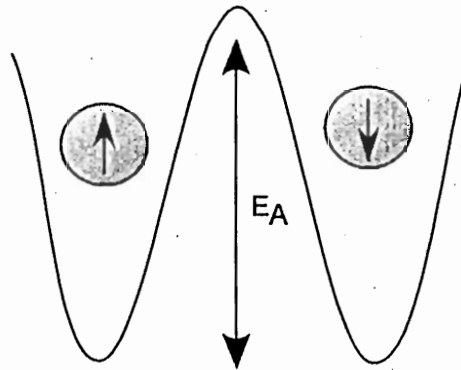


Figure 1.10. Potential well schematic of Stoner-Wohlfarth anisotropy energy barrier for magnetization reversal.

differing crystallographic directions, in which the magnetization vector may point. In thermal equilibrium, the resulting magnetization of the particle will point along the direction that will minimize the total anisotropy energy (typically the easy axis). If a magnetic field H is applied along the easy axis direction, the energy of the particles becomes

$$E_A = KV \sin^2 \theta - \mu H \cos \theta \quad (1.10)$$

where μ is the total magnetic moment of the particle.²⁰

The energy barrier E_A may become comparable to the thermal energy $k_B T$, where k_B is the Boltzmann constant, when K or V is decreased to a critical value. At this point, the magnetic moment can overcome the energy barrier separating the easy directions. As a result, the direction of the particles moment fluctuates and behaves like a paramagnetic material. However, instead of a single magnetic moment per atom as in the case of a paramagnetic material, each particle contains many spins magnetically coupled. Therefore the particle behaves as a ‘superspin’ with a relatively enormous moment per particle. Bean coined the term *superparamagnetism* to differentiate and describe such behavior.⁴³ Further details on the ‘discovery’ and developments in superparamagnetism can be found in classic reviews by Bean and Livingston¹⁹ and Jacobs and Bean.²⁰

1.3.3 Néel Theory

In 1949, Néel described the rate at which the magnetic vector of single domain particles will overcome the energy barrier E_A as

$$\tau = \tau_0 \exp (E_A/k_B T) \quad (1.11)$$

where τ_0 is the attempt frequency for the magnetization vector to flip.⁴⁴ τ_0 depends upon a number of factors including temperature, the gyromagnetic ratio, saturation magnetization, applied field, particle volume, and damping constant, but is typically considered a constant. Néel's calculations for τ_0 was 10^{-9} s, although in recent years 10^{-10} s has been used as the accepted theoretical value.⁴⁵ Experimental values ranging from $10^{-9} - 10^{-14}$ s have been reported.⁴⁶⁻⁵⁰

If the characteristic measurement time of an experiment is much shorter than τ at a fixed temperature, then the particle moments are said to remain *blocked* during the observation period, i.e. the magnetic moments do not relax. When the measurement time window is longer than τ , rapid fluctuation of the particle moment occurs, and the particles behave superparamagnetically. The *blocking temperature* is defined as the temperature for a given measurement time at which the moments are no longer blocked and are able to overcome the energy barrier E_A . (See Figure 1.11) For measurement times of 1 – 1000 s and $\tau_0 = 10^{-9} - 10^{-10}$ s, E_A ranges from $21k_B T$ to $30k_B T$. From equation 1.9, the conditions for superparamagnetism relates to the particles properties and become

$$KV = N k_B T \quad (1.12)$$

where N is the appropriate scalar for the respective measurement time. As a common measurement time for dc magnetization measurements is 100 s, traditionally the condition for superparamagnetism is cited as $KV = 25 k_B T$.¹⁹

For practical engineering applications such as data storage, the time the magnetization of a system remains in a certain state at a given temperature is critically important. For example, an iron particle of size 11.5 nm has a relaxation time of 0.1 s at room temperature and will therefore reach thermal equilibrium almost immediately. On the other hand if the size is 15.0 nm, the room temperature relaxation time for the iron particle is 10^9 s, and the magnetization will be extremely stable.⁴⁵

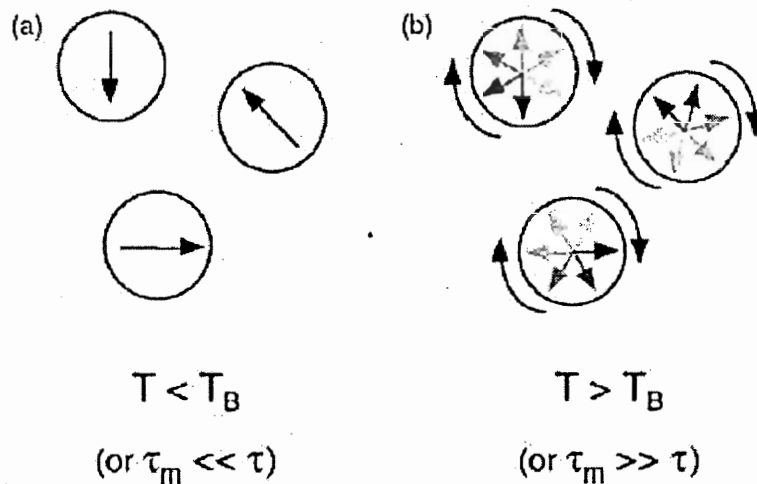


Figure 1.11 Schematic of particle moment with blocking temperature T_B and measurement time τ . Below T_B , the particles moment points along its easy axis. Above T_B , the moments can overcome the energy barrier E_A and flip orientations between any crystallographic direction. Figure from reference 3.

1.4 Superparamagnetism and Implications upon Applications

1.4.1 Data Storage

In 1956, IBM introduced the first commercial hard drive using 1-2 μ m γ -Fe₂O₃ particles. The total storage capacity was 5MB with an aerial density of 2 kbit/in².⁵¹ Through the reduction of particulate size, larger areal densities have been achieved. Currently by using CoPtCr granular media, areal densities are on the order of Gbit/in².⁵¹ However, continued growth in areal density is limited by the onset of superparamagnetism. By Stoner-Wohlfarth theory as the volume of the magnetic particles decreases, the energy barrier for magnetization reversal also decreases. Upon decreasing the particles volume to a critical size, thermal activation is significant enough to overcome the anisotropy energy barrier and the particles display superparamagnetism. Hence the magnetization direction will rapidly fluctuate from one direction to another, and data integrity is lost. To push the superparamagnetic limit materials with larger K are being developed to counteract the effect of decreasing V upon the energy barrier E_A. However, materials with larger K require larger write fields, which then present new issues to be addressed in the information storage industry. Extensive reviews on developing materials for information storage have been recently published.⁵¹⁻⁵⁴

1.4.2 Magnetic Resonance Imaging (MRI) Contrast Agents

Image contrast in MRI is a result of the different signal intensity each tissue produces in response to a particular sequence of applied radiofrequency (RF) pulses and is dependent on proton density and magnetic relaxation times.³³ The magnetic relaxation

times for MRI are described by the time constants T1 (longitudinal – resulting from the relaxation of the proton nuclei to the lowest energy state of alignment with the applied magnetic field B_0) and T2 (transverse – resulting from the decay of echo amplitudes of the transverse magnetic precession about B_0).³³ Contrast agents generally achieve enhancing effects by modifying these characteristic relaxation times. If the fractional decrease in T1 is greater than T2, the intensity of the MRI image increases, and the material is said to be a positive contrast agent. If the fractional decrease for T1 is less than T2, the intensity of the MRI image decreases and the material is said to be a negative contrast agent.

Most contrast agents are traditionally paramagnetic ions, where the unpaired electrons act as small magnets within the main magnetic field to effect the relaxation of T1 and T2. Above the blocking temperature, superparamagnetic nanoparticles behave like paramagnetic materials, but with an extremely large moment and are expected to create larger local field inhomogeneities and influence the magnetic relaxation times.³³ In 1978, dextran-coated superparamagnetic iron oxide (Fe_3O_4) were shown to be extremely effective T2 proton relaxation enhancers.⁵⁵ In fact superparamagnetic iron oxide has demonstrated a very high relaxivity, even surpassing that of current paramagnetic contrast agents.⁸ For example, superparamagnetic iron oxide particles relaxivity is 100 l/mmol Fe s compared to monomolecular gadolinium complexes (5 l/mmol Gd s) or macromolecular gadolinium contrast agents (20 l/mmol Gd s).⁶ Due to the lack of hysteresis in superparamagnetic materials (above their blocking temperature), advantages of using magnetic nanoparticles in superparamagnetic regime include the lack of remanence in the magnetic material upon removal of the magnetic fields used in MRI.^{6,7}

Iron oxide nanoparticles are the most commonly used magnetic nanoparticle contrast agent and are currently available commercially. Lumirem[®] and Resovit[®], are magnetic contrast agents of maghemite ($\gamma\text{-Fe}_2\text{O}_3$) used for gastro-intestinal tract imaging and for the detection of liver or spleen lesions/tumors respectively.^{3,7}

1.4.3 Magnetic Refrigeration

The technology of magnetic refrigeration depends upon the magnetocaloric effect, which was discovered in pure iron by Warburg in 1881.⁵⁶ The *magnetocaloric effect* is a materials adiabatic temperature change upon application of a magnetic field and is an intrinsic property of a magnetic solid. Application of a magnetic field causes the materials magnetic moments to align and the magnetic entropy is lowered. Under adiabatic conditions the total entropy change is zero, and thus the sample heats up. When the field is removed the resulting reduction in magnetic spin alignment means the magnetic entropy is increased and hence the temperature is lowered.⁵⁷

In the early 1990s, Shull, et.al. predicted that superparamagnetic materials would show an enhanced magnetocaloric effect.⁵⁸ Superparamagnetic materials are essentially an assembly of spins and the entropy of the group of spins, for certain ranges of size, temperature, and applied fields, may be more easily changed by an application of a field than paramagnetic systems. Furthermore, calculations predict that superparamagnetic materials may be used at lower applied fields and higher temperatures, which would improve the operation capability of magnetic refrigerators.⁵⁹ Experimentally, it was found that the superparamagnetic magnetic nanocomposite $\text{Gd}_3\text{Ga}_{5-x}\text{Fe}_x\text{O}_{12}$ displays

magnetocaloric effects 3-4 times larger than those of $\text{Gd}_3\text{Ga}_5\text{O}_{12}$, the most commonly used low temperature paramagnetic refrigerant.¹⁸

1.5 Anisotropy Mechanisms

Magnetic nanoparticles have use in a range of applications from high-density information storage to magnetically guided drug delivery and each application demands unique often vastly different magnetic properties as illustrated by the examples outlined above. Improving such applications requires understanding and controlling the fundamental magnetic properties of the nanoparticles, such as superparamagnetism. In this study, the relationship between macroscopic magnetic properties and magnetic couplings is investigated using various spinel ferrite nanoparticles. Specifically, the effects of magnetocrystalline anisotropy, exchange energy, surface chemistry, and interparticle interactions upon the superparamagnetic properties of the nanoparticles are examined. A brief description of anisotropy mechanisms responsible for the magnetic properties of nanoparticles is outlined here.

1.5.1 Magnetocrystalline and Shape Anisotropy

Magnetocrystalline and shape anisotropy were the anisotropy mechanisms considered in the development of Stoner-Wohlfarth and Néel theory as described above. Magnetocrystalline anisotropy arises from spin-orbital couplings from the interactions of the magnetic moments with the crystal lattice symmetry. While exchange interactions determine the magnetic ordering of a material, the magnetocrystalline anisotropy determines the magnetic orientation in a material. The specific crystallographic direction

that gives rise to the lowest magnetocrystalline anisotropy energy is called the easy axis. Moving the moment away from the easy axis increases the anisotropy energy. An example of the impact of the magnetocrystalline energy upon the magnetization of Fe is presented in Figure 1.12. The (100) direction is the easy axis for Fe, and hence it is easy to magnetize Fe in that direction (i.e. a large $M(H)$ value). The (111) direction of iron is the hard axis and therefore it is difficult to align the magnetic moment along the (111) direction. As a result, the value of the magnetization under the same applied magnetic field is lower than that of the magnetization along the (100) direction.

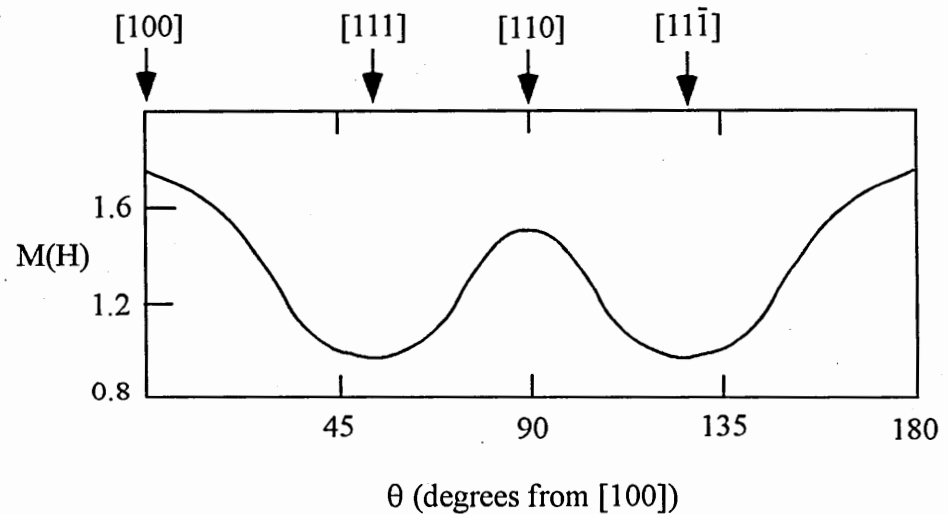


Figure 1.12 Schematic of magnetization for iron measured in a field of 80 Oe as a function of crystallographic orientation. Figure modeled from reference 35.

The magnetocrystalline anisotropy is intrinsic to the material and its magnitude affects the hysteresis response of the material. Magnetic materials with large magnetocrystalline energy are classified as hard magnetic materials and display large coercivity. Materials with weak magnetocrystalline anisotropy energy have small coercivity and are called soft magnetic materials.

Shape anisotropy results from magnetostatic energy and is an extrinsic property^{38f,40} Spherical shapes do not produce any shape anisotropy. The shape anisotropy (K_f) affects the demagnetization energy (E_d) within samples and for spheroids is given by

$$E_d = K_f \sin^2 \theta + (1/2) N_i \mu_0 M_s^2 \quad (1.13)$$

where M_s is the saturation magnetization and N_i is the demagnetization factor along the i direction. For infinite wires $K_f = \mu_0 M_s^2 / 4$, and for infinite disks $K_f = \mu_0 M_s^2 / 2$.⁴⁰ Both circular and ellipsoidal shapes were considered by Stoner-Wohlfarth theory.

1.5.2 Surface Anisotropy

The surface chemistry is of great importance to the chemical and physical properties of nanoparticles. Surface effects become more significant as the size of nanoparticles decreases, due to the increased volume ratio of surface atoms to the total number of atoms in the particle. Néel first proposed the concept of surface anisotropy arising from the reduced coordination and lower symmetry of surface atoms with respect to the core of the nanoparticle in 1954.⁶⁰ The surface anisotropy had a crystal-field

nature and the symmetry breaking at the surface as well as the atomic disorder induces local crystal fields with easy axis normal to the surface of the particle.²⁴ As a result of the local crystal fields, the lower coordination number of metal ions at the surface, and the broken magnetic exchange bonds, spins at the particle surface are often canted and/or disordered and do not align with the core spins of the particle.^{61,62}

Due to the size dependence of the surface effects, often the effects of particle size (V in equation 1.9) and surface effects are mixed and difficult to isolate. An effective anisotropy constant (K_{net}) is used to describe the additional anisotropy due to the surface. For spherical particles, K_{net} is given by

$$K_{\text{net}} = K_{\text{xtal}} + (6/d) K_S \quad (1.14)$$

where K_S is the surface anisotropy, K_{xtal} is the magnetocrystalline anisotropy, and d is the diameter of the particle. In general, the surface anisotropy causes the surface to be magnetically harder than the core of the particle.

Many unique magnetic properties of magnetic nanoparticles have been attributed to the surface anisotropy and its effects. The reduction in the saturation magnetization, observed for nearly all magnetic nanoparticle systems, is usually attributed to the magnetic “dead-layer” consisting of randomly canted spins caused by the surface anisotropy. Monte Carlo simulations performed by Kachkachi, et.al. confirm the reduced saturation magnetization results from surface anisotropy.^{63,64} Néel’s early calculations as well as several recent theoretical studies, have pointed out that increases in coercivity are expected if the surface anisotropy is increased.^{60-62,65} The atypical trend of increases in

coercivity with decreasing particle size are suggested to result from increasing contributions of surface anisotropy as the particle size is reduced.⁶⁵⁻⁶⁷ Calculations by Iglesias and Labarta investigating changes in shape of hysteresis loops with particle size show that the reversal of the particle moment is strongly influenced by the reduced atomic coordination and disorder at the surface.⁶⁸ As a result of the misaligned surface spins, the ideal model of Stoner-Wohlfarth of magnetization reversal by the coherent rotation of all spins pointing along one direction is no longer valid.

1.5.3 Interparticle Interactions^{24,69,70}

Interparticle interactions are known to affect the magnetic properties of materials and will contribute to the magnetic response in the powder samples reported here. Interparticle interactions may arise from dipole-dipole interactions or exchange interactions between surface ions of neighboring particles. When a capping surfactant such as oleic acid is used, the exchange interactions become negligible and the primary interaction is due to dipole-dipole coupling.⁷¹ The energy associated with dipole-dipole interactions (E_{d-d}) given by

$$E_{d-d} = - (\mu_0 m_o^2) / (4\pi l^3) \quad (1.15)$$

where μ_0 is the permeability, m_o is the magnetic moment, and l is the particle-particle separation. This energy modifies the anisotropy energy barrier for magnetization reversal E_A and is argued to introduce local minima in the energy barrier.²⁴ Although it is generally understood that particle-particle interactions affect the magnetic properties of

nanoparticles, correlating the effects of interparticle interactions with observed magnetic properties has still provided a challenge.

Three primary theoretical models developed for understanding the effects of interparticle interactions exist: the Shtrikman-Wohlfarth (SW) model developed in 1981, the Dormann-Bessais-Fiorani (DBF) model developed in 1998, and the Mørup-Tronc model developed in 1994. Both the SW and DBF models show that increasing interparticle interactions will lead to an increase in the energy barrier, E_A by

$$E_A = KV \sin^2\theta + B_i \quad (1.16)$$

where B_i is the interaction term, whose form varies according to the respective model and their subsequent revisions. The MT model however, indicates that increased interparticle interactions should decrease the energy barrier. Considerable argument between the authors of these models as to the validity of their conclusions are present in the literature.^{69,70}

Experimentally, the effects of interparticle interactions are determined by varying the interparticle interactions through dilution of ferrofluid samples. Most studies show that the blocking temperature and coercivity decrease with dilution, i.e. weaker interparticle interactions. These findings collaborate the SW and BDF models that increasing interparticle interactions results in an increase of the energy barrier for magnetization reversal. However, other experimental results show mixed results. For example, SQUID relaxation measurements show that τ (see equation 1.11) increases with increasing interactions, which also further supports the SW and DBF models. However,

Mössbauer studies indicate that τ decreases with increasing interactions and these studies are cited as support for the MT model.

Other experimental results show inconsistency between the reduced remanence (M_R/M_S) and particle interactions. Held et.al. report that M_R/M_S decreases with increasing interactions, while studies reported in this thesis find that M_R/M_S can increase with increasing particle interactions.⁷¹ Other discrepancies include the correlation between particle size and interparticle interaction strengths. Most studies report that the interaction energy should decrease with increasing particle size since there is greater void space with increasing size, thereby increasing the particle-particle distance and decreasing the energy by equation 1.14. However, Taketomi and Shull point out that the moment per particle increases with size, and as such the interparticle energy should *increase* by two orders of magnitude by increasing the particle size from 3 nm to 10 nm.⁷² Although interparticle interactions are discussed as if they are well understood, insight as to the effects of interparticle interactions upon the observed magnetic properties has still not been achieved.

1.6 References

- (1) Livingston, J. D. *Driving Force: The Natural Magic of Magnets*; Harvard University Press: Cambridge, 1996.
- (2) Shimada, A.; Anzai, M.; Kakuta, A.; Kawanishi, T. *IEEE Trans. Ind. Appl.* **1987**, *IA-23*, 804.
- (3) Pankhurst, Q. A.; Connolly, J.; Jones, S. K.; Dobson, J. *J. Phys. D.: Appl. Phys.* **2003**, *36*, R167.
- (4) Lübke, A. S.; Bergemann, C.; Brock, J.; McClure, D. G. *J. Magn. Magn. Mater.* **1999**, *194*, 149.
- (5) Bonnemain, B. *J. Drug Targeting* **1998**, *6*, 167.
- (6) Kresse, M.; Wagner, S.; Taupitz, M. In *Scientific and Clinical Applications of Magnetic Carriers*; Häfeli, U., Schütt, W., Teller, J., Zborowski, M., Eds.; Plenum Press: New York, 1997, p 545.
- (7) Berry, C. C.; Curtis, A. S. G. *J. Phys. D.: Appl. Phys.* **2003**, *36*, R198.
- (8) Bulte, J. W. M.; Cuyper, M. d.; Despres, D.; Frank, J. A. *J. Magn. Res. Imaging.* **1999**, *9*, 329.
- (9) Trager, F. *Appl. Phys. B: Lasers and Optics* **2001**, *73*, 291.
- (10) Trindade, T.; O'Brien, P.; Pickett, N. L. *Chem. Mater* **2001**, *13*, 3843.
- (11) Link, S.; El-Sayed, M. A. *Int. Rev. Phys. Chem.* **2000**, *19*, 409.
- (12) Hahn, H. *NATO ASI Series E: Appl. Sci.* **1994**, *260*, 263.
- (13) Frenkel, J.; Dorfman, J. *Nature* **1930**, *126*, 274.

- (14) Kittel, C. *Phys. Rev* **1946**, 70, 965.
- (15) Knobel, M.; Ferrari, E. F.; Silca, F. C. S. *Mater. Sci. Forum* **1999**, 302-303, 169.
- (16) White, R. L. *IEEE Trans. Magn.* **1992**, 28, 2482.
- (17) Liou, S. H.; Huang, S.; Klimek, E.; Kirby, R. D.; Yao, D. *J. Appl. Phys.* **1999**, 85, 4334.
- (18) Shull, R. D. *IEEE Trans. Magn.* **1993**, 29, 2614.
- (19) Bean, C. P.; Livingston, J. D. *J. Appl. Phys.* **1959**, 30, 1205.
- (20) Jacobs, I. S.; Bean, C. P. In *Magnetism Vol. III*; Rado, G. T., Suhl, H., Eds.; Academic Press: New York, 1963, p 271.
- (21) Tejada, J.; Ziolo, R. F.; Zhang, X. X. *Chem. Mater.* **1996**, 8, 1784.
- (22) Wernsdorfer, W. In *Macroscopic Quantum Coherence and Quantum Computing*; D.V. Averin, B. R., P. Silvestrini, Ed.; Kluwer Academic: New York, 2001, p 195.
- (23) Awschalom, D. D.; DiVincenzo, D. P.; Smyth, J. F. *Science*. **1992**, 258, 414.
- (24) Battle, X.; Labarta, A. *J. Phys. D.: Appl. Phys.* **2002**, 35, R15.
- (25) Josephson, L.; Perez, J. M.; Weissleder, R. *Angew. Chem. In. Ed.* **2001**, 40, 3204.
- (26) Ziolo, R. F.; Giannelis, E. P.; Weinstein, B. A.; O'Horo, M. P.; Ganguly, B. N.; Mehrotra, V.; Russell, M. W.; Huffman, D. R. *Science* **1992**, 85, 219.
- (27) Bader, S. D. *Scripta Materialia* **2002**, 47, 527.
- (28) Hayashi, K.; Morii, H.; Tanka, Y.; Ishitani, S.: USA, 2002.

- (29) Raj, K.; Moskowitz, B.; Casciari, R. *J. Magn. Magn. Mater.* **1995**, *149*, 174.
- (30) Pileni, M. P. *Adv. Funct. Mater.* **2001**, *11*, 323.
- (31) Bell, A. T. *Science* **2003**, *299*, 1688.
- (32) Šafárik, I.; Šafáriková, M. In *Scientific and Clinical Applications of Magnetic Carriers*; Häfeli, U., Schütt, W., Teller, J., Zborowski, M., Eds.; Plenum Press: New York, 1997, p 323.
- (33) Bulte, J. W. M.; Brooks, L. A. In *Scientific and Clinical Applications of Magnetic Carriers*; Häfeli, U., Schütt, W., Teller, J., Zborowski, M., Eds.; Plenum Press: New York, 1997, p 527.
- (34) Jakubovics, J. P. *Magnetism and Magnetic Materials*; Institute of Metals: London, 1987.
- (35) O'Handley, R. C. *Modern Magnetic Materials: Principles and Applications*; John Wiley & Sons, Inc: New York, 2000.
- (36) Morrish, A. H. *The Physical Principles of Magnetism*; IEEE Press: New York, 2001.
- (37) Groenou, A. B. V.; Bongers, P. F.; Stuyts, A. L. *Mater. Sci. Engineer.* **1968/69**, *3*, 317.
- (38) Bertotti, G.; Academic Press: San Diego, 1998, p 10.
- (39) Leslie-Pelecky, D. L.; Rieke, R. D. *Chem. Mater.* **1996**, *8*, 1770.
- (40) Solzi, M. In *Fundamental Properties of Nanostructured Materials*; D. Fiorani, G. S., Ed.; World Scientific: River Edge, NJ, 1994, p 212.
- (41) Weller, D.; Moser, A.; Folks, L.; Best, M. E.; Lee, W.; Toney, M. F.; Schwickert, M.; Thiele, J.-U.; Doerner, M. F. *IEEE Trans. Magn.* **2000**, *36*, 10.

- (42) Stoner, E. C.; Wohlfarth, E. P. *Philosophical Transactions of the Royal Society A* **1948**, *240*, 599.
- (43) Bean, C. P. *J. Appl. Phys.* **1955**, *26*, 1381.
- (44) Néel, L. *Ann. Geophys (C.N.R.S.)* **1949**, *5*, 99.
- (45) Aharoni, A. In *Magnetic Properties of Fine Particles*; J.L. Dormann, D. F., Ed.; Elsevier Science Publishers: Amsterdam, 1992, p 3.
- (46) Dickson, D. P. E.; Reid, M. M. K.; Hunt, C.; Williams, H. D.; El-Hilo, M.; O'Grady, K. *J. Magn. Magn. Mater.* **1993**, *125*, 345.
- (47) Xiao, G.; Liou, S. H.; Levy, A.; Taylor, J. N.; Chien, C. L. *Phys. Rev. B* **1986**, *34*, 7573.
- (48) Dormann, J. L.; Fiorani, D.; Tholence, J. L.; Sella, C. *J. Magn. Magn. Mater.* **1983**, *35*, 117.
- (49) Rondinone, A. J.; Samia, A. C. S.; Zhang, Z. *J. Appl. Phys. Lett.* **2000**, *76*, 3624.
- (50) Rondinone, A. J.; Liu, C.; Zhang, Z. *J. Phys. Chem. B* **2001**, *105*, 7967.
- (51) Moser, A.; Takano, K.; Margulies, D. T.; Albrecht, M.; Sonobe, Y.; Ikeda, Y.; Sun, S.; Fullerton, E. E. *J. Phys. D.: Appl. Phys.* **2002**, *35*, R157.
- (52) Shen, J. X.; Shan, Z. S.; Wang, D.; Liu, Y.; Sellmyer, D. J. In *Handbook of Nanophase and Nanostructured Materials Volume III*; Wang, Z. L., Liu, Y., Zhang, Z., Eds.; Kluwer Academic: New York, 2003, p 269.
- (53) Weller, D.; Doerner, M. F. *Ann. Rev. Mater. Sci.* **2000**, *30*, 611.
- (54) Thompson, D. A.; Best, J. D. *IBM J. Res. Develop.* **2000**, *44*, 311.
- (55) Ohgushi, M.; Nagayama, K.; Wada, A. *J. Magn. Res. Imaging.* **1978**, *29*, 599.

- (56) Warburg, E. *Ann. Phys.* **1881**, *13*, 141.
- (57) Pecharsky, V. K.; Jr, K. A. G. *J. Magn. Magn. Mater.* **1999**, *200*, 44.
- (58) Shull, R. D.; Swartzendruber, L. J.; Bennett, L. H. In *Proceedings 6th International Cryocoolers Conference*; Green, G., Know, M., Eds.; David Taylor Research Center Publication #DTRC-91/002: Annapolis, 1991, p 231.
- (59) Shull, R. D.; McMichael, R. D.; Swartzendruber, L. J.; Bennett, L. H. In *Magnetic Properties of Fine Particles*; Dormann, J. L., Fiorani, D., Eds.; Elsevier Science Publishers: Amsterdam, 1992, p 161.
- (60) Néel, L. *Journal de Physics et la Radium* **1954**, *15*, 225.
- (61) Kodoma, R. H. *J. Magn. Magn. Mater.* **1999**, *200*, 359.
- (62) Kodoma, R. H.; Berkowitz, A. E. *Phys. Rev. B* **1999**, *59*, 6321.
- (63) Kachkachi, H.; Ezzir, A.; Nogues, M.; Tronc, E. *Eur. Phys. J. B* **2000**, *14*, 681.
- (64) Kachkachi, H.; Nogues, M.; Tronc, E.; Garanin, D. A. *J. Magn. Magn. Mater.* **2000**, *221*, 158.
- (65) Dimitrov, D. A.; Wysin, G. M. *Phys. Rev. B* **1994**, *50*, 3077.
- (66) Vestal, C. R.; Zhang, Z. J. *Chem. Mater.* **2002**, *14*, 3817.
- (67) Hocheplied, J. F.; Pileni, M. P. *J. Appl. Phys.* **2000**, *87*, 2472.
- (68) Iglesias, O.; Labarta, A. *Phys. Rev. B* **2001**, *63*, 184416.
- (69) Hansen, M. F.; Mørup, S. *J. Magn. Magn. Mater.* **1998**, *184*, 262.
- (70) Dormann, J. L.; Fiorani, D.; Tronc, E. *J. Magn. Magn. Mater.* **1999**, *202*, 251.

- (71) Held, G. A.; Grinstein, G.; Doyle, H.; Sun, S.; Murray, C. B. *Phys. Rev. B* **2001**, *64*, 012408.
- (72) Taketomi, S.; Shull, R. D. *J. Magn. Magn. Mater.* **2003**, *266*, 207.

CHAPTER 2

SPINEL FERRITES AND INSTRUMENTATION

2.1 Spinel Ferrites

2.1.1 Spinel Structure

Spinel ferrites (MFe_2O_4 ; $M = Mg, Co, Mn, \text{etc}$) are an ideal magnetic system for understanding and controlling superparamagnetic properties at the atomic level through chemical manipulations.¹ The spinel structure contains two cation sites for metal cation occupancy. (Figure 2.1). There are eight A sites in which the metal cations are tetrahedrally coordinated by oxygen, and sixteen B sites which possess octahedral coordination. Due to the exchange couplings, the magnetic moment of cations in the A sites are aligned parallel with respect to one another and all the magnetic moments of the cations in the B sites also align parallel, while between the A and B sites the arrangement is antiparallel (see Section 1.2.2). As there are twice as many B sites as A sites, there is a net moment of spins yielding ferrimagnetic ordering for the crystal.² When the A sites are occupied by M^{2+} cations and the B sites are occupied by Fe^{3+} cations, the ferrite is called a normal spinel. If the A sites are completely occupied by Fe^{3+} cations

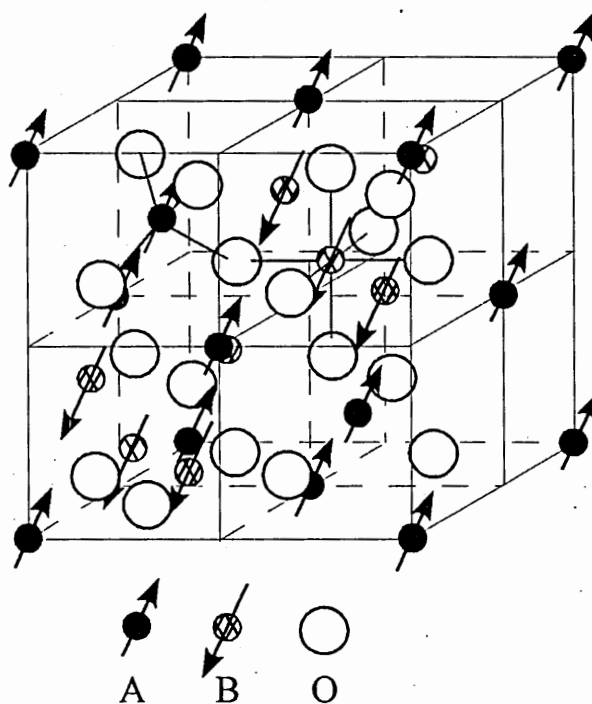


Figure 2.1 Schematic of spinel structure, $A^{II}B_2^{III}O_4$. Metal cations are located in tetrahedral (A) and octahedral (B) coordination sites within an FCC lattice of oxygen. Magnetic moments between the A and B sites are arranged antiparallel yielding ferrimagnetic ordering for the system.

and the B sites are randomly occupied by M^{2+} and Fe^{3+} cations, the structure is referred to as an inverse spinel. In most spinels, the cation distribution possesses an intermediate degree of inversion where both sites contain a fraction of the M^{2+} and Fe^{3+} cations. The choice of metal cation and cation distribution therefore offers a tunable magnetic system.

2.1.2 Magnetic Properties

Variation of the cation distribution between the A and B sites may lead to different magnetic properties even though the chemical composition may not change. $MnFe_2O_4$ nanoparticles are a prime example.³ $MnFe_2O_4$ nanoparticles with a 61% inversion for the cation distribution, or $(Mn_{0.39}Fe_{0.61})[Mn_{0.82}Fe_{1.18}]O_4$ where cations in parenthesis () represent A site occupancy and in brackets [] B site occupancy, have an A site moment of $3.2 \mu_B$ and B site moment of $2.5 \mu_B$ as determined from powder neutron diffraction. On the other hand $MnFe_2O_4$ nanoparticles with a 29% inversion for the cation distribution, i.e. $(Mn_{0.71}Fe_{0.29})[Mn_{0.50}Fe_{1.50}]O_4$, have an A site moment of $3.3 \mu_B$ and B site moment of $2.3 \mu_B$. These differences results in a blocking temperature change of $\sim 50^\circ C$.

The zinc-doped cobalt ferrite ($Co_{1-x}Zn_xFe_2O_4$) system illustrates the influence of choice of metal cation and cation site distribution upon magnetic properties. The saturation magnetization of $Co_{1-x}Zn_xFe_2O_4$ increases up to 50% zinc doping.⁴⁻⁶ These trends can be understood in terms of the distribution of cations between the A and B lattice sites. Due to site preferences, Zn^{2+} ions occupy the tetrahedral A sites. The replacement of Co^{2+} ($3\mu_B$) with nonmagnetic Zn^{2+} ($0\mu_B$) leads to a decrease in the A site moment. As the A and B lattices are coupled antiparallel, a decrease in the A site

moment causes the B site contribution to the magnetic moment of the unit cell to be more significant. Hence the saturation magnetization of the unit cell increases although a non-magnetic ion is introduced.

Zinc-doped cobalt ferrite ($\text{Co}_{1-x}\text{Zn}_x\text{Fe}_2\text{O}_4$) also serves to demonstrate the influence of choice of metal cation as a means to tune the magnetocrystalline anisotropy K . Co^{2+} contributes $3\mu_B$ and has a strong spin-orbital contribution while Fe^{3+} contributes five unpaired d electrons ($5\mu_B$) and has a moderately strong spin-orbital contribution. The resulting spin-orbital contributions from Co^{2+} and Fe^{3+} thus contribute to the value of K . On the other hand, Zn^{2+} has no unpaired electrons and does not contribute to the overall value of K . Therefore as Zn^{2+} replaces Co^{2+} in the crystal lattice, K is expected to decrease. The blocking temperature of $\text{Co}_{1-x}\text{Zn}_x\text{Fe}_2\text{O}_4$ particles decreased over the entire doping range $0 < x < 1$, which is consistent a reduction in E_A resulting from the lowering of K with increasing Zn^{2+} doping.⁶

For materials with similar cation distributions, such as CoFe_2O_4 and MgFe_2O_4 , a clear correlation between the spin-orbital couplings of the cations and superparamagnetic properties can be demonstrated.¹ The cation distributions determined from neutron diffraction are $(\text{Co}_{0.31}\text{Fe}_{0.69})[\text{Co}_{0.68}\text{Fe}_{1.32}]\text{O}_4$ and $(\text{Mg}_{0.32}\text{Fe}_{0.68})[\text{Mg}_{0.70}\text{Fe}_{1.30}]\text{O}_4$ where cations in parenthesis () occupy A sites and in bracket [] B sites.¹ The difference between CoFe_2O_4 and MgFe_2O_4 are the chemical components Co^{2+} and Mg^{2+} . Co^{2+} cations have seven d electrons, three of them unpaired, as well as a large spin-orbital coupling. Mg^{2+} has no unpaired electrons and hence contribute zero total electron spin. Recall that the magnetocrystalline anisotropy K comes from spin-orbit couplings (L-S couplings) in the crystal lattice. Due to the stronger L-S couplings in CoFe_2O_4 , a larger K

is expected for the material, which from Stoner-Wohlfarth theory would give rise to a larger anisotropy energy barrier E_A . For all sizes of CoFe_2O_4 and MgFe_2O_4 nanoparticles, the blocking temperature for CoFe_2O_4 is ~ 150 K larger than that of MgFe_2O_4 . This observation is consistent with an increase in E_A resulting from the stronger L-S couplings (K) in CoFe_2O_4 . Mössbauer experiments at 400 K, show only a sextet for CoFe_2O_4 , while for MgFe_2O_4 , the pattern is a doublet, with only a very weak small fraction of a sextet.¹ The existence of only a sextet at 400 K for CoFe_2O_4 indicates that the relaxation time τ is longer than the measurement time of 10 ns, while the presence of a doublet at 400 K for MgFe_2O_4 suggests that the relaxation time τ is shorter than 10 ns. From Néel theory, these observations are consistent with a larger K value for CoFe_2O_4 .

2.2 Synthesis of Spinel Ferrites Using Microemulsion Methods

In addition to microemulsion methods, spinel ferrite nanoparticles have been synthesized by a wide variety of methods including gas condensation, aerosol reduction, chemical precipitation, sol-gel processing, thermal decomposition of organometallic precursors, and continuous hydrothermal processing.^{3,7-15} Although these methods are able to produce nanoscale ferrites, often the quality of the nanoparticles is poor – in many cases a large size distribution is reported and size control is arbitrary. In many of these procedures size variation is achieved through post-synthesis annealing at various temperatures. Zhang, et. al. have demonstrated that although nanoparticle size changes according to the annealing temperature, the cation distribution between A and B lattice

sites also is affected by annealing temperature.³ As discussed above, the magnetic properties of the spinel ferrites are highly dependent upon the distribution of cations between the A and B sites. Therefore when annealing temperature is used to control nanoparticle size, a direct correlation between size effect and magnetic response is not possible due to the extra variable of cation re-distribution. If multiple sizes are produced through the synthesis without thermal annealing or without varying thermal annealing temperature, often large changes in the synthesis procedure are needed.

In order to correlate size effects with changes in magnetic properties it is critical to have a synthesis method that allows for control over the nanoparticle size and yields nanoparticles with a narrow size distribution.¹⁶ Microemulsion methods are suitable for such purposes. Microemulsion procedures have been commonly used over the past 20 years to form high quality metal and semiconductor nanoparticles with a small size distribution.¹⁷⁻²⁰ Furthermore, by minor adjustments to the synthesis conditions, size control is readily achievable. Microemulsion methods can be classified into normal micelle methods also called oil-in-water (o/w) methods and reverse micelle methods also referred to as water-in-oil (w/o) methods. In both cases surfactants are used and the surfactant molecules aggregate to form micelles, whose size typically ranges from 10 – 100 nm, when their concentration is above the critical micelle concentration (cmc).^{18,19} Normal micelles are shown in Figure 2.2a, and reverse micelles are shown in Figure 2.2b. Normal micelles form with the oily chain the surfactant molecule pointing to the inside of the micelle, with the polar end directed outwards towards the aqueous solvent. Reverse micelles contain the polar end of the surfactant molecule directed in towards the hydrophilic water interior and the oily chain directed outward towards the organic

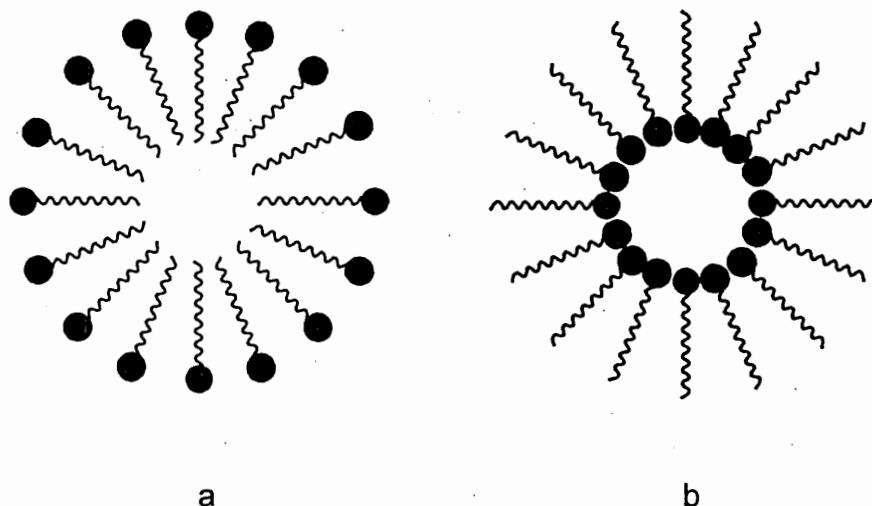


Figure 2.2 Schematic of (a) normal micelle structure and (b) reverse micelle structure.

solvent. The first report of utilizing microemulsion methods for the synthesis of nanoparticles was in 1982 by Boutonnet et. al. who prepared 3 – 5 nm samples of Pt, Pd, Rh, and Ir nanoparticles by a reverse micelle method.¹⁷ Since that time, reverse micelle methods have been used to form high quality Cu, Ni, Fe, and Co metallic nanoparticles; semiconductor nanoparticles such as CdS and $\text{Cd}_{1-y}\text{Mn}_y\text{S}$; and Y-Ba-Cu-O superconductors.^{18,20} Normal micelles have been used to prepare Cu and CdS nanoparticles.^{18,21}

This section covers some results from the synthesis of a variety of spinel ferrite nanoparticles using both normal and reverse micelle microemulsion methods. The sizes of the nanoparticles all fall well below the critical diameter listed in Table 2.1 and therefore are single domain. The conditions required for size control as a function of synthesis method are addressed.

Table 2.1. Estimated and Experimental Single Domain Critical Size for Common Magnetic Materials

Estimated		Experimental	
Material	D _{crit} (nm)	Material	D _{crit} (nm)
Co	70, ²² 55 ²³	NiFe ₂ O ₄	40-60 ^{24,25}
Fe	14, ²² 20 ²⁶	CoFe ₂ O ₄	50 ^{24,25}
Ni	55, ²² 65 ²⁷	Fe ₃ O ₄	< 100 ²⁸
γ - Fe ₂ O ₃	166 ²²		
Fe ₃ O ₄	128, ²² 50 ²⁸		

2.2.1 Normal Micelle (Oil – in – Water)

2.2.1.1 Synthesis Overview

Normal micelle methods have been used to prepare a wide range of spinel ferrite nanoparticles including iron oxides, cobalt ferrite, and cobalt ferrites doped with various cations such as chromium, zinc, and the lanthanides. For quick comparison, Table 2.2 summarizes the general reaction conditions such as microemulsion method, surfactant system, and choice of iron salt for all ferrite synthesis using microemulsion methods. As seen in Table 2.2, the most common surfactant for normal micelle procedures is sodium dodecylsulfate (SDS, CH₃(CH₂)₁₀CH₂OSO₃Na). In these reactions, the metal cations (e.g. Fe²⁺, Co²⁺) are associated at the polar head of the surfactant chain and above the

Table 2.2. Synthesis Conditions for the Preparation of Ferrite Nanoparticles.

Ferrite	Microemulsion Method ^a	Surfactant ^b	Oxidation State of Iron Salt	Size (nm)
$\text{Fe}_3\text{O}_4 / \gamma - \text{Fe}_2\text{O}_3$	nm	SDS	+ 2	3 – 12 ^{29,30}
	rm	AOT	+ 2	5 ¹⁶
		Brij	+ 2 ; +3	2 – 7 ³¹
CoFe_2O_4	nm	SDS	+ 2	3 – 35 ^{21,32,33}
			+ 3	4 – 10 ³⁴
	rm	AOT	+ 2	12 – 18 ³⁵
MnFe_2O_4	rm	DBS	+ 3	4 – 15 ³⁶
		AOT	+ 2	5, 10 ^{16,37}
MgFe_2O_4	rm	DBS + CTAB	+ 3	2 – 45 ¹
CoCrFeO_4	nm	SDS	+ 3	6 – 20 ³⁸
	rm	DBS	+ 3	4 – 11 ³⁸
$\text{Co}_{1-x}\text{Zn}_x\text{Fe}_2\text{O}_4$	nm	SDS	+ 2	3 – 4, 15 ^{4,6}
$\text{CoLn}_x\text{Fe}_{2-x}\text{O}_4$	nm	SDS	+ 2	20 ³⁹

^anm and rm represent normal and reverse micelle method respectively

^bSDS = sodium dodecylsulfate; AOT = sodium bis(2-ethylhexyl) sulfosuccinate

CTAB = cetyl trimethyl ammonium bromide; DBS = sodium dodecylbenzene sulfonate

critical micelle concentration, the surfactant molecules aggregate to form micelles. Examples of the critical micelle concentration are 1.52×10^{-3} M for $\text{Co}(\text{DS})_2$ and 1.56×10^{-3} M for $\text{Fe}(\text{DS})_2$ at 25°C .⁴⁰ Such a low concentration for micelle formation, with the metal cations “confined” in solution, allows for much lower reactant concentrations to be used compared to co-precipitation methods. At concentrations below the cmc, spinel ferrite formation does not occur.²⁹ In order to vary the size of the nanoparticles, minor adjustments to the synthesis procedure are generally made as micelles can increase in size with addition of salts, an increase of surfactant concentration, and/or addition of alcohols.¹⁸

2.2.1.2 Size Control

Rondinone, et. al. used chemometric modeling to quantitatively correlate the effects of experimental conditions with nanoparticle size.³³ Over forty reactions were performed in which surfactant concentration, metal salt concentration, methylamine concentration, and reaction temperature were individually varied. The range of conditions studied yielded nanoparticles with sizes 5 – 32 nm. From this study, the effect of surfactant concentration was determined to be negligible. This observation is in agreement with other reports that varying the SDS concentration while maintaining a constant concentration of $\text{Co}(\text{DS})_2$ and $\text{Fe}(\text{DS})_2$ only marginally decreased the size of CoFe_2O_4 nanoparticles. For example, the CoFe_2O_4 nanoparticle size decreases from 2.8 nm when 1.56 M SDS is used to 2.4 nm after the SDS concentration was dramatically increased to 16.5 M.⁴¹

Other results from the chemometric study included correlations between increases in nanoparticle size and increases in reaction temperature, metal cation concentration, and methylamine concentration. The model's findings are consistent with other reported experimental data. For example, a reaction temperature of 25°C, 50°C or 80°C results in Fe₃O₄ nanoparticle size of 5.6 nm, 6.8 nm, and 8.3 nm respectively.²⁹ For room temperature reactions, increasing the Fe(DS)₂ concentration by a factor of 2 and 4 alters the size of Fe₃O₄ nanoparticle from 3.7 nm to 5.6 nm and 7.4 nm respectively.²⁹ Performing the synthesis at 80°C results in Fe₃O₄ particles with size 6.6, 8.3, and 11.6 nm upon increasing the concentration again by a factor of 2 and 4.²⁹ Similarly, an increase the concentration of Fe(DS)₂ by a factor of 2 while maintaining a 2:1 molar ratio with Co(DS)₂ increases the size of CoFe₂O₄ nanoparticles from 2 nm to 3 nm, while increasing the Fe(DS)₂ concentration by a factor of 4 increases the size to 5 nm.^{41,42} X-ray absorption near edge spectroscopy (XANES) and small angle x-ray scattering (SAXS) studies indicated the oxidation state of iron and cobalt ions increase when the Fe(DS)₂ concentration is increased. Furthermore, an increase in micelle size is reported when Fe(DS)₂ concentration is increased. These factors are suggested to induce an increase in the number of nuclei formed thus favoring the formation of larger particles.⁴¹

By plotting the three-dimensional cross sections of the chemometric model, correlations between the experimental conditions and nanoparticle size are available.³³ For example, the 3-D surface plot comparing effects of the metal cation and methylamine concentrations at constant temperature (Figure 2.3) shows a saddle shape, indicating strong interactions between the metal salts and methylamine. This means that the nanoparticle size could either increase OR decrease with increasing metal salt

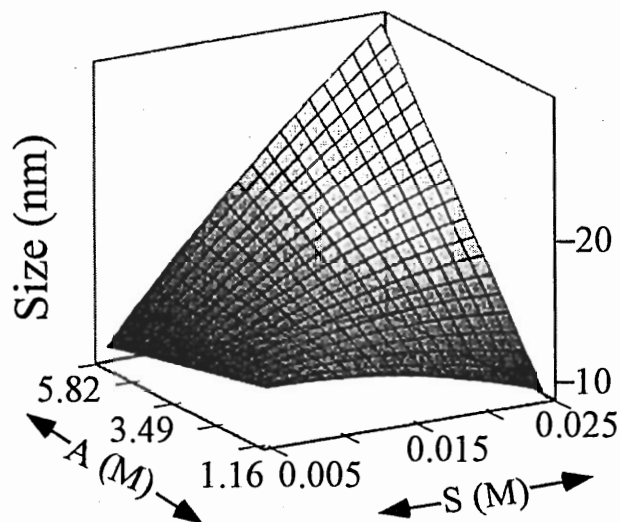


Figure 2.3 Three-dimensional cross section showing effects of metal cation $[S(M)]$ and methylamine $[A(M)]$ concentration on nanoparticle size.³³

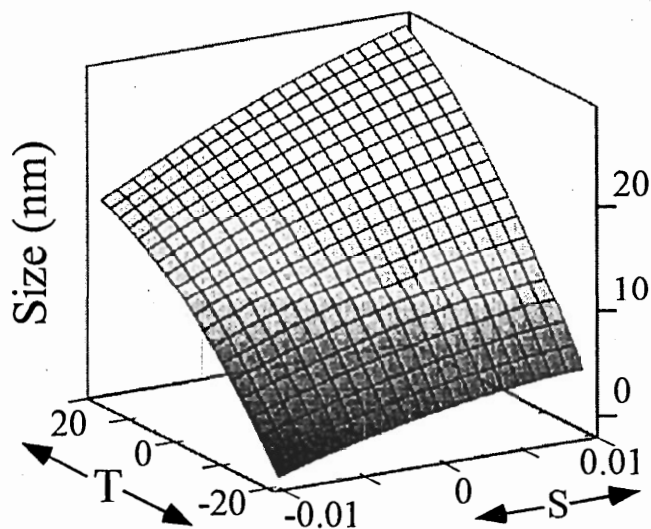


Figure 2.4 Three-dimensional cross section showing effects of metal cation concentration (S) and reaction temperature (T) on nanoparticle size.³³

concentration depending on the methylamine concentration for that reaction. In another cross sectional plot shown in Figure 2.4, the effect of temperature and metal salt concentration were compared at constant methylamine concentrations. The shape of the surface curve indicates the factors are independent of one another. Therefore if the reaction temperature increases, the nanoparticle size increases at any choice of metal salt concentration and vice versa, increasing the metal salt concentration yields larger sized nanoparticles at all choices of reaction temperature.

From this model the best approach to varying nanoparticle size is suggested to be varying the metal salt concentration and the reaction temperature.³³ Because the rate of size change is different for these two factors, adjusting the reaction temperature should be used for rough tuning of the nanoparticle size as changing this factor results in large changes in nanoparticle size. Adjusting the metal salt concentration effects smaller changes in particle size and therefore should be used for fine-tuning of nanoparticle size. The model was tested on subsequent CoFe_2O_4 synthesis as well as the synthesis of $\text{Co}_{1-x}\text{Zn}_x\text{Fe}_2\text{O}_4$ and ZnFe_2O_4 nanoparticles. By using specified reaction conditions, the size of the prepared nanoparticles agreed with the models predictions $\pm 1 - 3 \text{ nm}$.³³

2.2.2 Reverse Micelle (Water – in – Oil)

2.2.2.1 Synthesis Overview

As shown in Table 2.2, a wide variety of surfactants have been used in the reverse micelle synthesis to form various spinel ferrite nanoparticles. Many ferrites such as CoFe_2O_4 , CoCrFeO_4 , and Fe_3O_4 have been synthesized by both normal and reverse

micelle methods. Interestingly, there are a few spinel ferrite nanoparticles that can only be formed by reverse micelle methods. For example, to date attempts at forming MnFe_2O_4 and CuFe_2O_4 have proven unsuccessful using normal micelle methods.⁴³

2.2.2.2 Size Control

Most reverse micelle syntheses report varying the size of nanoparticle by varying the water/surfactant or water/dispersing solvent ratio, thereby changing the diameter of the water droplet. The most common surfactant for reverse micelle procedures is Na(AOT) principally because the Na(AOT)-water-isooctane phase diagram shows a large size range (0.5 – 18 nm) for the diameter of the water droplets.¹⁸ The size of the water droplet is related to the ratio of water to surfactant ($w = [\text{H}_2\text{O}] / [\text{AOT}]$) by

$$D \text{ (nm)} = 0.3 w \quad (2.1)$$

MnFe_2O_4 nanoparticles prepared with AOT/isooctane with a size of 10 nm are formed when $w = 10$, while 5 nm MnFe_2O_4 nanoparticles are reported when $w = 0.01$.^{16,37}

Other surfactant systems show similar observations between changing the water pool diameter and the nanoparticle size. A size of 8 nm is obtained when the water/toluene ratio was 5/100 for MnFe_2O_4 nanoparticles prepared with DBS in toluene.³⁶ Adjusting the ratio of cyclohexane/water using the relation $(93-x)/7/x$ (cyclohexane/ Brij /aqueous iron solution) results in Fe_3O_4 nanoparticle sizes ranging from 1.9 nm, 2.4 nm, 3.6nm, 5.6 nm, and 7.3 nm when x varies as 1, 1.5, 2, 2.5, and 3 respectively.³¹ It is interesting to note that changing the surfactant concentration affects the size of the

nanoparticles in the reverse micelle synthesis, while this factor had no effect on size in the normal micelle synthesis. Certainly it appears that the mechanism for nanoparticle formation and thus size control is different between the two microemulsion procedures. A systematic model detailing the effects of specific experimental conditions as developed for normal micelle reactions has not been conducted for reverse micelles synthesis.

2.3 Instrumentation

2.3.1 Powder X-Ray Diffraction^{44,45}

X-ray diffraction was a primary tool used for the characterization of the spinel ferrite nanoparticles. For all experiments reported here, a Bruker D8 Advance x-ray diffractometer with Cu K α radiation was used. To produce the x-rays, a current is passed through a tungsten filament causing the filament to heat and thermionic emission of electrons occurs. These electrons are directed at a copper target, which has an applied voltage of 40 kV. (See Figure 2.5) The tube current (the flow of electrons from the

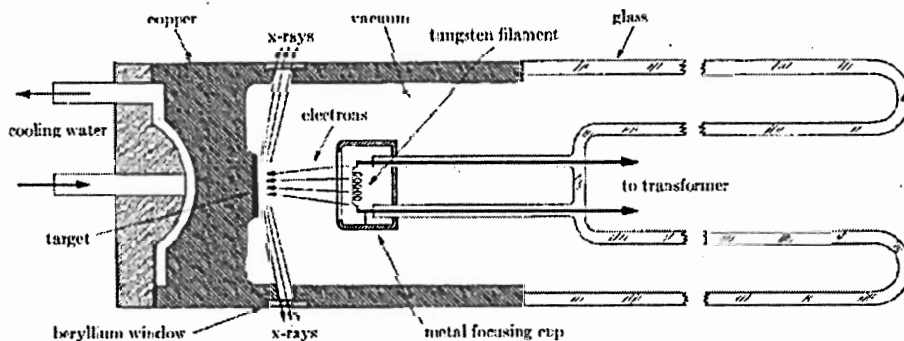


Figure 2.5 Schematic of x-ray tube

filament to the copper target) is maintained at 40 mA. The electrons hit the copper target with high velocity. If the electrons have sufficient energy, they may knock an electron of the copper target out of its orbital. As an outer electron falls from its orbital into the vacancy it emits x-ray radiation. Depending upon the target anode, x-rays characteristic of target are generated. Here Cu K_{α} radiation was used, which has a wavelength of 1.54 Å.

The x-ray radiation will diffract from the powder sample following Bragg's law. W.L. Bragg demonstrated that diffraction could be visualized as x-rays "reflecting" off of crystal planes as shown in Figure 2.6. The difference in path length traveled through the crystal and/or the phase differences between the incident and scattered beams gives rise to scattered waves that are in phase or out of phase. A diffracted beam is essentially a

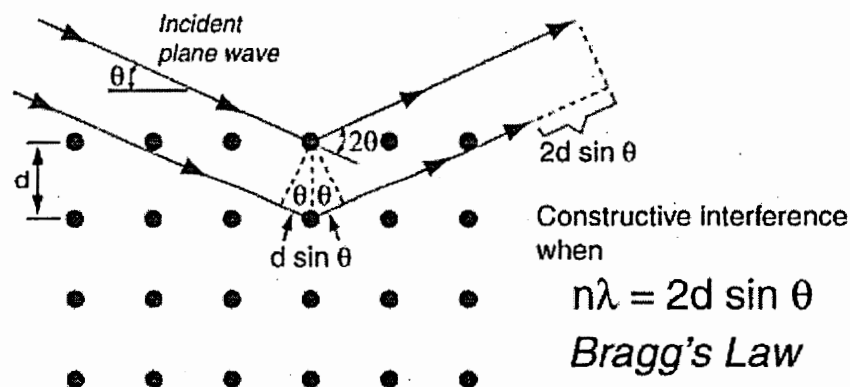


Figure 2.6 Schematic of crystal planes and Bragg's Law. Figure from <http://hyperphysics.phy-astr.gsu.edu/hbase/quantum/bragg.html>

group of scattered x-rays from the crystal that mutually reinforce on another. Bragg's law accounting for the diffraction physics is given in equation 2.2

$$n\lambda = 2d \sin \theta \quad (2.2)$$

where λ is the wavelength, d is the plane spacing and θ is the angle shown in Figure 2.6.

The recorded diffraction pattern essentially is composed of peaks at specific angles and with varying intensity. Crystal symmetry, the space group symmetry and the unit cell dimensions determine the peak position. The peak intensity is primarily determined by the contents of the unit cell and can be determined by the structure factor F_{hkl} .

$$F_{hkl} = \sum_1^n f_n e^{2\pi i(hu_n + kv_n + lw_n)} \quad (2.3)$$

where f_n is the electron scattering density for element n , hkl are the Miller indices, and uvw , are the coordinates of element n . Other factors may contribute to the intensity of the diffraction pattern as shown in equation 2.4

$$I = |F|^2 p \left(\frac{1 + \cos^2 2\theta}{\sin^2 \theta \cos \theta} \right) e^{-2M} \quad (2.4)$$

where F is the structure factor given in 2.3, p is the multiplicity, the Lorentz-polarization factor is in parenthesis, and the temperature factor e^{-2M} . Phase identification for all samples here was performed by matching the peak positions and intensities in the experimental diffraction pattern to those patterns in the JCPDS (Joint Committee on Powder Diffraction Standards) database.⁴⁶

In addition to providing information about phase purity, the x-ray diffraction pattern can provide information about crystallite size. Diffraction peaks for crystals smaller than 0.1 μm will show broadening of the peak. The size broadening of the diffraction peak can be related to the crystallite size by the Scherrer equation, given in equation 2.5

$$B = 0.9\lambda / t \cos\theta \quad (2.5)$$

B is the broadening of the x-ray diffraction peak measured at half max (*in radians*), λ is the wavelength, t is the diameter of the particle, and θ is the diffraction angle.

2.3.2 Powder Neutron Diffraction

In addition to x-rays, neutrons may be used as a probing wavelength for diffraction. Neutrons can be generated by nuclear reactors or by spallation sources. Neutrons are produced from nuclear reactors from the fission reactions of ^{235}U . Nuclear reactors yield 2-3 neutrons/fission at 2MeV kinetic energies. Moderators such as D_2O or H_2O are used to slow down the neutrons to thermal (0.025eV) energies. At nuclear

reactors, the neutrons supply is continuous and a wide range of energies is produced. By using monochromators, a small energy is selected for the diffraction wavelength. For example, at the BT-1 powder diffractometer at NIST, wavelengths of 2.0784 Å, 1.5401 Å, and 1.5903 Å, can be selected by using a Ge(311), Cu(311), or Si(531) monochromator.⁴⁷ In spallation sources, a pulsed high energy proton beam is smashed into a heavy metal target such as ^{183}W or ^{238}U , generating bursts of neutrons. In general, spallation sources produce about 10-30 neutrons/proton with energies about 1 MeV. These neutrons are then moderated as is usually done in a nuclear reactor. Spallation sources operate in pulses, and the intensity of neutrons is not constant as for nuclear reactors. As a result, the whole range of energies that is generated with each burst of neutrons is used in the diffraction experiments. Figure 2.7 compares the two neutron production methods.

Neutron diffraction will occur in accordance with Bragg's law detailed above for x-rays. However, while x-rays are scattered by electrons, neutrons are scattered by the nucleus of the atoms. As a result, neutron scattering varies irregularly with atomic number Z of the scattering angle, while x-rays scatter linearly with Z (See Figure 2.8). Therefore, atoms that are nearly indistinguishable by x-ray may be analyzed using neutron scattering. This is show schematically in Figure 2.9. This contrast enhancement is useful in investigating the cation distribution of transition metal ions between the A and B lattice sites in spinel ferrite nanoparticles.

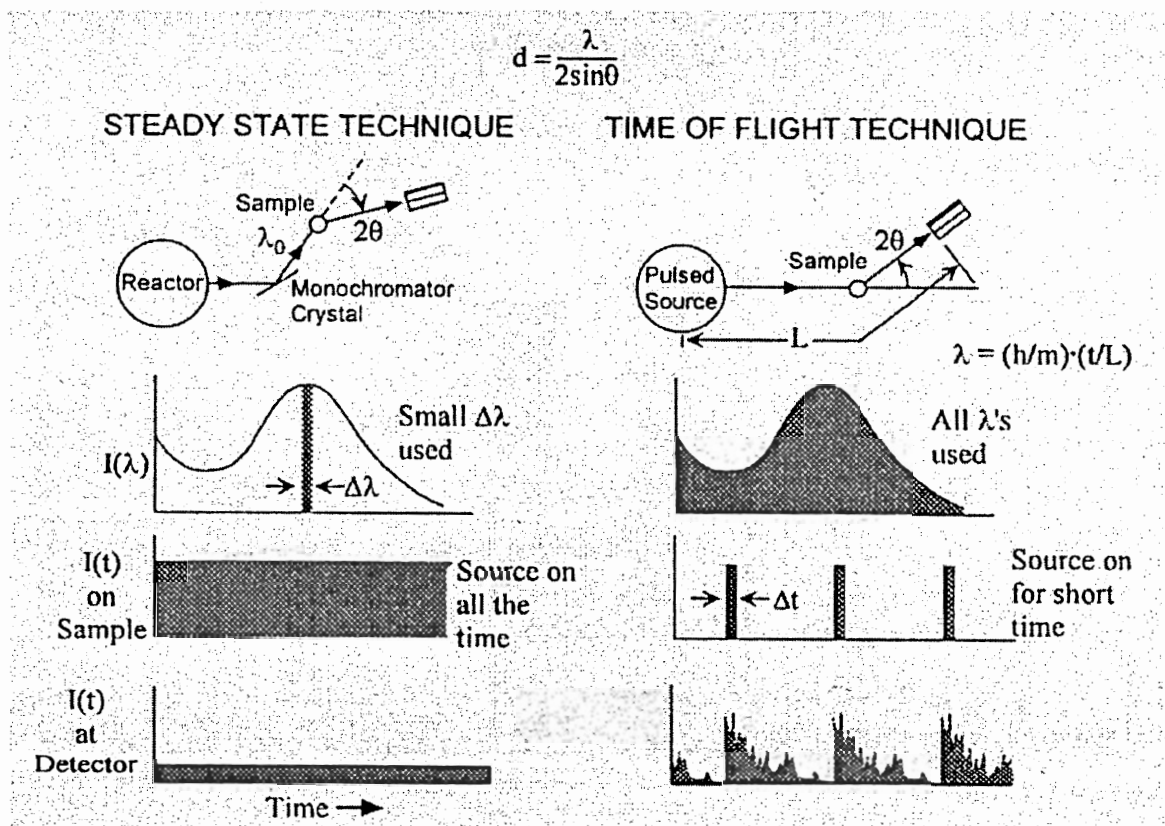


Figure 2.7. Comparison of nuclear reactor sources (left) and spallation sources (right) for the generation of neutrons.

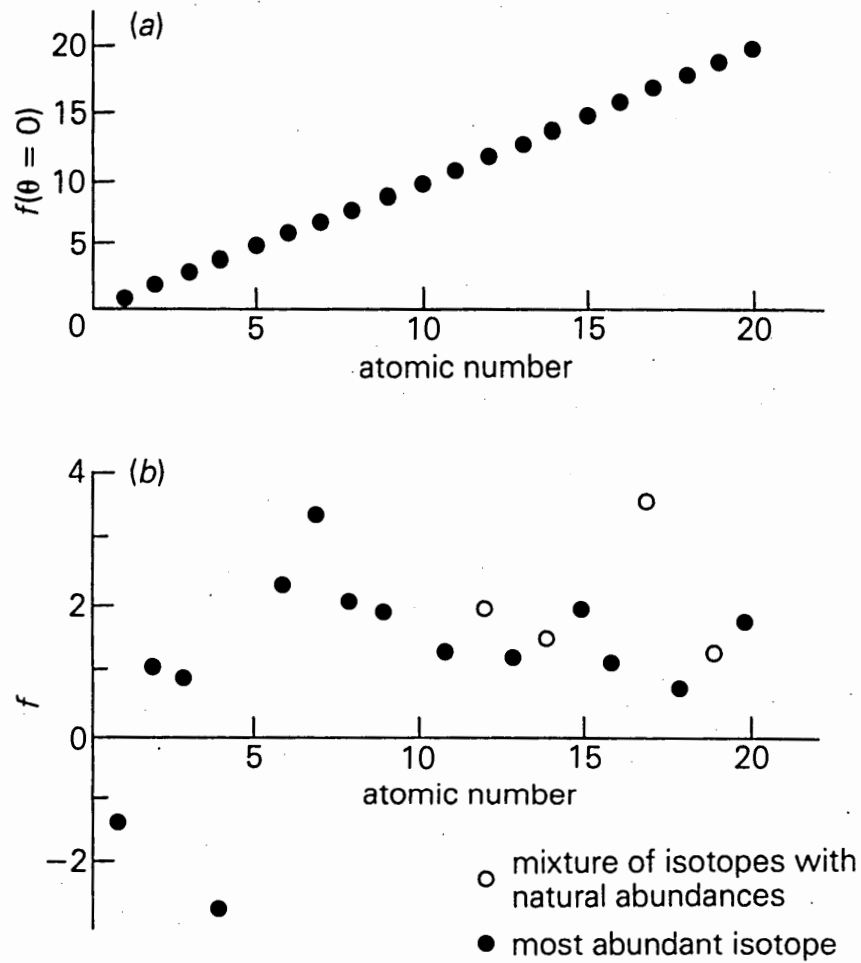
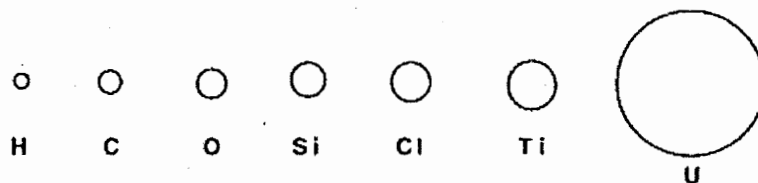


Figure 2.8. (a) X-ray and (b) neutron scattering factors. X-rays scale with Z , while neutrons vary.

ATOMS SEEN BY X-RAYS



NUCLEI SEEN BY NEUTRONS

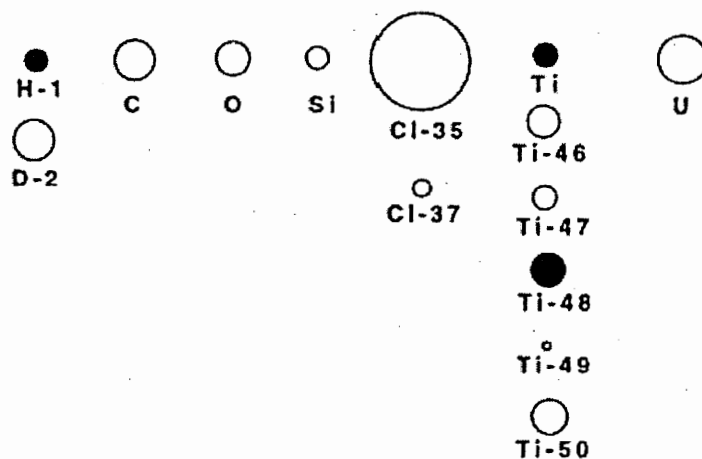


Figure 2.9 Schematic of scattering contrast for x-rays and neutrons.

Neutrons also have a small magnetic moment. When a neutron interacts with an atom with a net magnetic moment, the two interact and the total scattering is affected. As a result, peaks due to magnetic scattering may be present in the diffraction pattern (or intensities of nuclear peaks may be increased due to the magnetic scattering). An example of a neutron diffraction pattern for antiferromagnetic MnO is shown in Figure 2.10. The bottom pattern was collected above the Curie temperature of MnO. Therefore no magnetic ordering is present and only nuclear reflections are observed. In the top pattern, taken below the Curie temperature, magnetic ordering occurs, and new peaks reflecting the magnetic structure appear. The technique of neutron diffraction provided the first concrete evidence that the proposed antiparallel alignment of magnetic moments in antiferromagnets really existed.

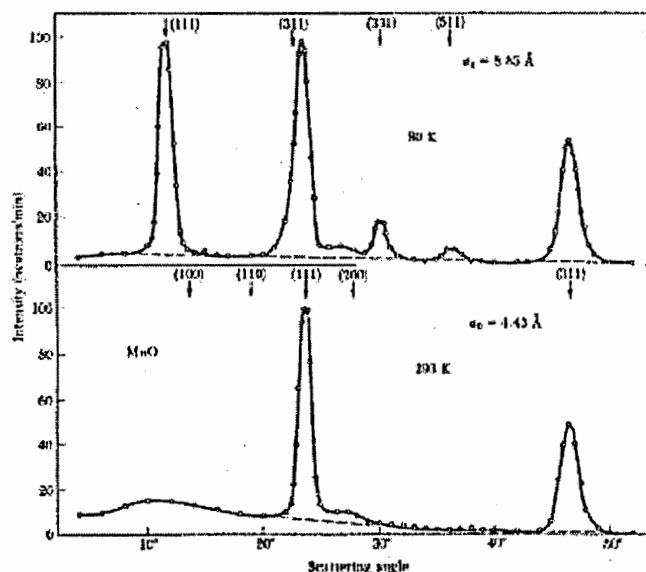


Figure 2.10 Neutron diffraction pattern of MnO (top) below the Curie temperature and (bottom) above the Curie temperature.

In this thesis neutron diffraction studies were carried out both at a spallation facility and at a reactor facility. Neutron diffraction studies reported in Chapter 3 were performed on the Special Environment Powder Diffractometer (SEPD) at the Intense Pulsed Neutron Source (IPNS) at Argonne National Laboratory. A schematic of the instrument is shown in Figure 2.11. Like most experiments performed at spallation sources, the experiment is a time of flight design. Since the neutrons with a range of energies come in pulses, their energy (and thus their wavelength) can be determined by measuring the time it takes for the neutron to reach the detector bank. Data from multiple detector banks, such as the backscatter detector at 145° (Bank 1) and the Bank 3 detectors at 44° are used in the Rietveld refinement. Using multiple banks allows for a wide range of d-spacing to be analyzed ($0.33 - 4.02 \text{ \AA}$ for Bank 1 and $0.85 - 10.21 \text{ \AA}$ for Bank 3).⁴⁸

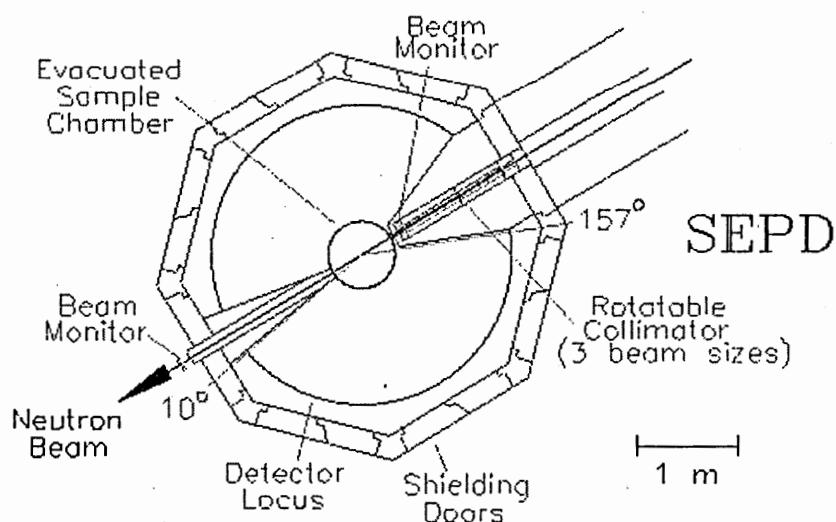


Figure 2.11 Schematic of the SEPD instrument at IPNS.

Neutron diffraction data reported in Chapter 4 were collected on the BT-1 powder diffractometer at the National Center for Neutron Research (NCNR) at NIST. A schematic of the instrument is shown in Figure 2.12. A bank of detectors measures the scattered beams and intensities as a function of scattering angle are recorded. The Ge(311) monochromator with 15' arcmin of inpile collimation was used to select an incident wavelength of 2.0784 Å. This monochromator setting was selected as it provided the highest neutron intensity and the largest diffraction intensities and is widely used for magnetic scattering. The high diffraction intensity is required for nanoparticle samples as peak broadening effects generally lower the maximum intensity of the diffraction peaks.

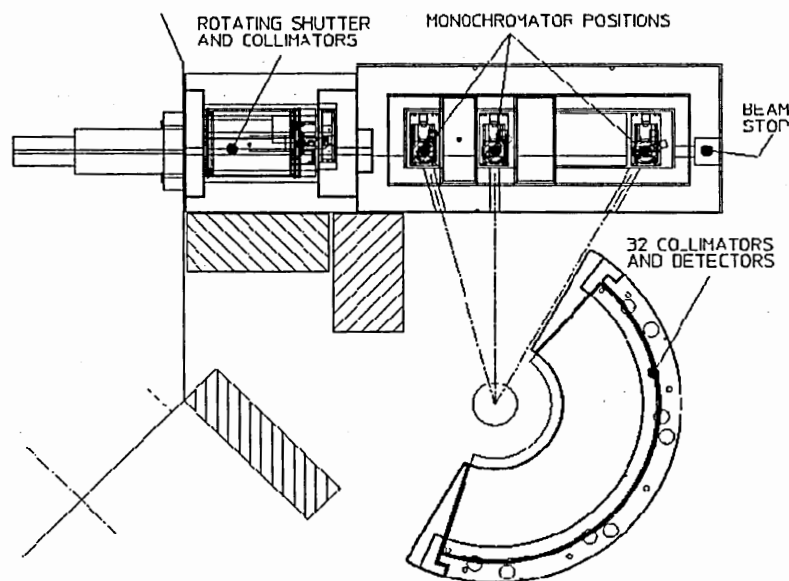


Figure 2.12 Schematic of the BT-1 powder diffractometer at NIST. The diffractometer radius is ~ 1m.

2.3.3 SQUID Magnetometry^{49,50}

Superconducting quantum interference devices (SQUIDs) are the most sensitive instrument for the measurement of magnetic fields. In fact, SQUID magnetometry can even detect neuromagnetic fields in the brain. The threshold resolution for the SQUID is ~ 1 fT. The magnetic field of the heart is 50,000 fT and the magnetic field of the brain is a few fT. Figure 2.13 summarizes the range of magnetic fields for various objects and the SQUID noise levels.

The SQUID operates on two principles – quantization of magnetic flux in a superconducting ring and the Josephson junction. A Josephson junction consists of a thin insulating material between two superconductors where the insulating material is thin enough that the electron wave propagating in the superconducting material can tunnel through the insulating layer and overlap with the electron wave in the other superconductor. In the SQUID coil, two Josephson junctions are used as shown in Figure 2.14. As a magnetic sample is moved through the coils, it induces an electric current in the coils. When the current changes in response to the magnetic flux from the sample, phase differences across the Josephson junction occur. Because the current through the superconducting circuit is quantized, interference between the current in the two sides of the superconducting ring will occur and the total current through the superconducting circuit will change. These detectable changes in current can be correlated to the magnetic flux.

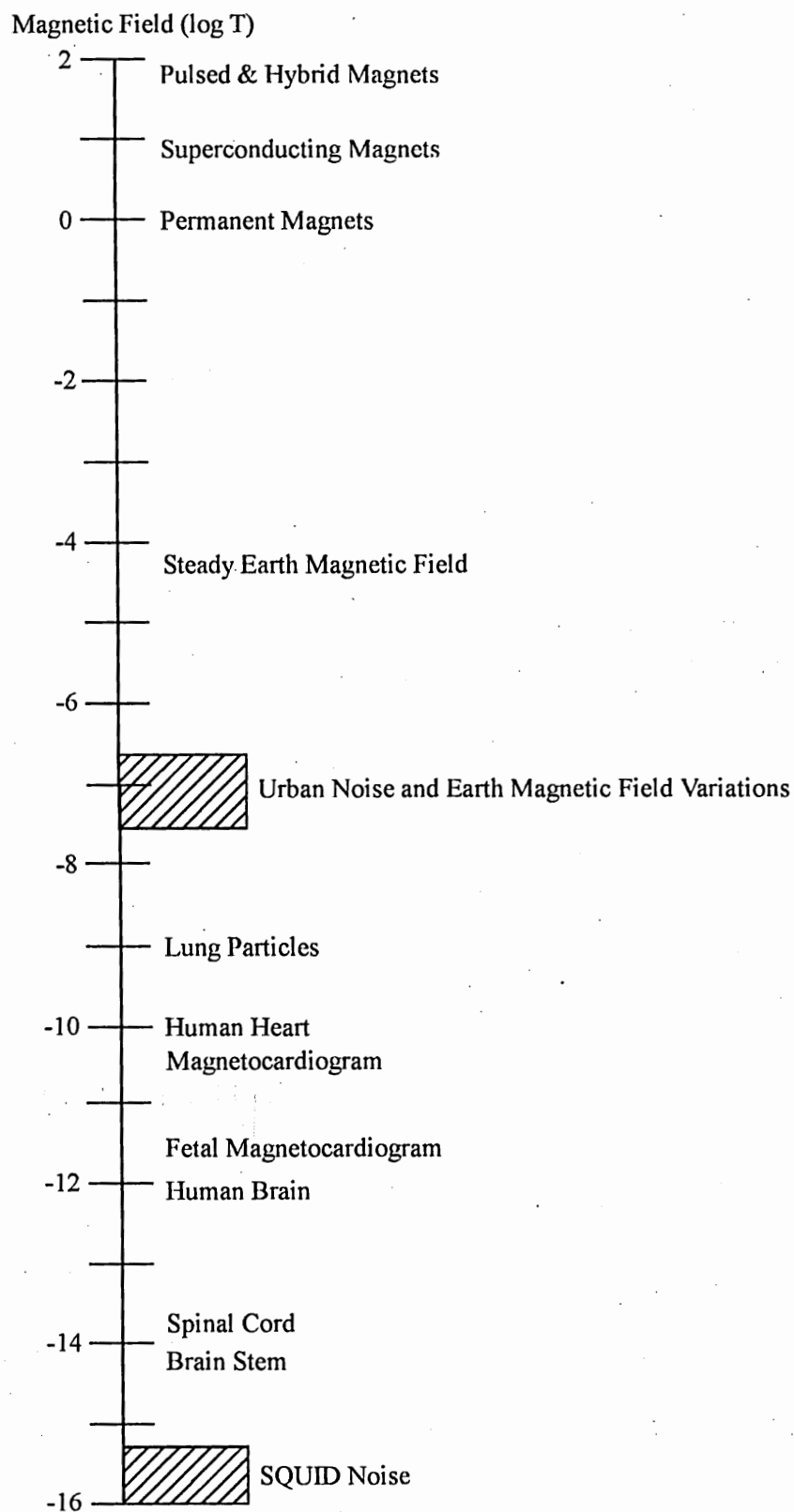


Figure 2.13. Comparison of magnetic field of different objects

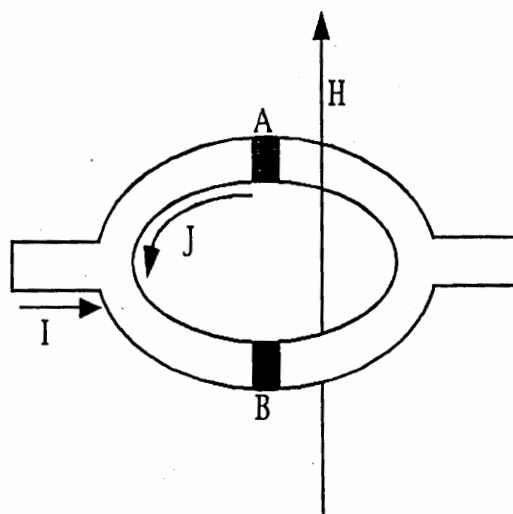


Figure 2.14 Schematic of superconducting coil with two Josephson junctions (A and B).

Two types of magnetic measurements can be performed using the SQUID magnetometer. The first measurement is the field dependence of the magnetic material at constant temperature $M(H)$ and the second is the temperature dependence of the material under constant field $M(T)$. Two types of temperature dependent measurements are typically performed – zero field cooled (ZFC) and field cooled (FC). In zero field-cooled measurements, the sample is cooled from room temperature in the absence of a magnetic field. A weak magnetic field is applied, and the magnetization recorded as the temperature is increased. In field-cooled measurements, the sample is cooled from room temperature under an applied magnetic field. In this thesis, measurements are performed

on a Quantum Design MPMS-5S SQUID magnetometer. Temperature dependence was measured from 5 – 780K and field dependence with applied fields up to ± 5 T.

2.3.4 Transmission Electron Microscopy (TEM)

Transmission electron microscopy (TEM) is a useful tool for the characterization of nanoparticles. While x-ray diffraction can provide information about the average particle size of the crystallites from the peak broadening information, TEM is useful for the visualization of the nanoparticle size and morphology. Furthermore, TEM studies provide pertinent information about the particle size distribution. Here, TEM studies were performed on a JEOL 100C operating at 100kV at the Georgia Institute of Technology Microscopy Center. Samples were dispersed onto holey carbon grids. Over 100 particles were counted by hand for the particle size distribution measurements.

2.3.5 Photoacoustic Infrared Spectroscopy⁵¹

Photoacoustic infrared spectroscopy (PAS-IR) is a useful alternative to transmission infrared spectroscopy techniques for samples that are highly absorbing. Additionally, the spectra can be obtained without modifying the sample and does not require sample preparation such as pressing pellets. The ferrite powder samples are placed into an aluminum cup, which is then placed into a chamber containing nitrogen. Modulated infrared radiation is focused on the sample and the radiation is absorbed by the sample and is converted into heat. The heat diffuses to the surface and then into the

surrounding nitrogen atmosphere. The heating of the gas causes expansion. As the infrared signal is modulated, intermittent thermal expansion of the gas occurs which generates pressure waves. These waves are detected using a microphone and converted into a PAS signal. In this thesis, photoacoustic infrared spectra were collected in the frequency range of 400 to 4000 cm^{-1} using a Biorad FTS-6000 Fourier transform infrared (FTIR) spectrometer equipped with a MTEC model 300 photoacoustic (PAS) detector.

2.3.6 Thermal Analysis

Two thermal analysis methods were utilized – thermogravimetric analysis (TGA) and differential scanning calorimetry (DSC). In TGA experiments, the mass of a sample is recorded as the temperature of the sample is increased. TGA measurements are used here to investigate the mass loss resulting from the decomposition of surface bound ligands in order to determine the grafting density of the ligands onto the nanoparticles. TGA measurements (in conduction with DSC) also provided information about the possible mechanism for the conversion of $\text{MgAl}_2(\text{OH})_8$ to MgAl_2O_4 reported in Appendix A. In DSC experiments, heat flow into a sample and into a reference material as a function of temperature is measured. Separate heaters are used to keep the temperature of the sample and reference equal. The difference in power required to keep the reference and sample at the same temperature is measured and plotted as a function of the sample temperature. Information about endothermic and exothermic reaction processes can be determined.

2.4 References

- (1) Liu, C.; Zou, B.; Rondinone, A. J.; Zhang, Z. J. *J. Am. Chem. Soc.* **2000**, *122*, 6263.
- (2) Groenou, A. B. V.; Bongers, P. F.; Stuyts, A. L. *Mater. Sci. Engineer.* **1968/69**, *3*, 317.
- (3) Zhang, Z. J.; Wang, Z. L.; Chakoumakos, B. C.; Yin, J. S. *J. Am. Chem. Soc.* **1998**, *120*, 1880.
- (4) Hocheplied, J. F.; Pileni, M. P. *J. Appl. Phys.* **2000**, *87*, 2472.
- (5) Hocheplied, J. F.; Bonville, P.; Pileni, M. P. *J. Phys. Chem. B* **2000**, *104*, 905.
- (6) Samia, A. C. S. Ph.D. Thesis. Georgia Institute of Technology, **2002**.
- (7) Hyeon, T.; Lee, S. S.; Park, J.; Chung, Y.; Na, H. B. *J. Am. Chem. Soc.* **2001**, *123*, 12798.
- (8) Hyeon, T.; Chung, Y.; Park, J.; Lee, S. S.; Kim, Y. W.; Park, B. H. *J. Phys. Chem. B* **2002**, *106*, 6831.
- (9) Kagawa, M.; Kikuchi, M.; Ohno, R.; Nagae, T. *J. Am. Ceramic Soc.* **1974**, *53*, 6263.
- (10) Nininger, R. C.; Schroeder, D. J. *J. Phys. Chem. Solids* **1978**, *39*, 137.
- (11) Blesa, M. A.; Matijevic, C. *Adv. Colloid. Interfac. Sci* **1985**, *29*, 173.
- (12) Xiong, G.; Mai, Z.; Xu, M.; Cui, S.; Ni, Y.; Zhao, Z.; Wang, X.; Lu, L. *Chem. Mater* **2001**, *13*.
- (13) Cote, L. J.; Teja, A. S.; Wilkinson, A. P.; Zhang, Z. J. *J. Mater. Res.* **2002**, *17*, 2410.

- (14) Chen, Q.; Zhang, Z. J. *Appl. Phys. Lett.* **1998**, *73*, 3156.
- (15) Cabanas, A.; Poliakoff, M. *J. Mater. Chem.* **2001**, *11*, 1408.
- (16) Seip, C. T.; Carpenter, E. E.; O'Conner, C. J. *IEEE Trans. Magn.* **1998**, *34*, 1111.
- (17) Boutonnet, M.; Kizling, J.; Stenius, P.; Maire, G. *Colloids Interf. Sci.* **1982**, *5*, 209.
- (18) Pileni, M. P. In *Nanoparticles and Nanostructured Films*; Fendler, J. H., Ed.; Wiley - VCH: Weinheim, 1997, p 71.
- (19) Pillai, V.; Shah, D. O. *J. Magn. Magn. Mater.* **1996**, *163*, 243.
- (20) Li, Y.; Park, C. W. *Langmuir* **1999**, *15*, 952.
- (21) Petit, C.; Jain, T. K.; Billoudet, F.; Pileni, M. P. *Langmuir* **1994**, *10*, 4446.
- (22) Leslie-Pelecky, D. L.; Rieke, R. D. *Chem. Mater.* **1996**, *8*, 1770.
- (23) Sato, M.; Ishii, Y. *J. Appl. Phys.* **1983**, *54*.
- (24) Berkowitz, A. E.; Schuele, W. J. *J. Appl. Phys* **1959**, *30*, 1345.
- (25) Schuele, W. J.; Deet Sreek, V. D. In *Ultrafine Particles*; Kuhn, W. E., Lamprey, H., Sheer, C., Eds.; Wiley: New York, 1963, p 219.
- (26) Sato, M.; Ishii, Y.; Nakae, M. *J. Appl. Phys.* **1982**, *53*, 6331.
- (27) Du, Y.; Xu, M.; Wu, J.; Shi, Y.; Lu, H.; Xue, R. *J. Appl. Phys.* **1991**, *70*, 5903.
- (28) Morrish, A. H.; Yu, S. P. *Phys. Rev* **1956**, *102*, 670.
- (29) Feltin, N.; Pileni, M. P. *Langmuir* **1997**, *13*, 3927.

- (30) Feltin, N.; Pileni, M. P. *J. Phys. IV* **1997**, 7, C1.
- (31) López-Perez, J. A.; López-Quintela, M. A.; Mira, J.; Rivas, J.; Charles, S. W. *J. Phys. Chem. B* **1997**, 101, 8045.
- (32) Moumen, N.; Veillet, P.; Pileni, M. P. *J. Magn. Magn. Mater.* **1995**, 149, 67.
- (33) Rondinone, A. J.; Samia, A. C. S.; Zhang, Z. J. *J. Phys. Chem. B* **2000**, 104, 7919.
- (34) Liu, C.; Rondinone, A. J.; Zhang, Z. J. *Pure Appl. Chem.* **2000**, 72, 37.
- (35) Li, S.; Liu, L.; John, V. T.; O'Conner, C. J.; Harris, V. G. *IEEE Trans. Magn.* **2001**, 37, 2350.
- (36) Liu, C.; Zou, B.; Rondinone, A. J.; Zhang, Z. J. *J. Phys. Chem. B* **2000**, 104, 1141.
- (37) Carpenter, E. E.; O'Conner, C. J.; Harris, V. G. *J. Appl. Phys.* **1999**, 85, 5175.
- (38) Vestal, C. R.; Zhang, Z. J. *Chem. Mater.* **2002**, 14, 3817.
- (39) Kahn, M. L.; Zhang, Z. J. *Appl. Phys. Lett.* **2001**, 78, 3651.
- (40) Moumen, N.; Lisiecki, I.; Pileni, M. P.; Briois, V. *Supramolecular Science* **1995**, 2, 161.
- (41) Moumen, N.; Pileni, M. P. *J. Phys. Chem.* **1996**, 100, 1867.
- (42) Pileni, M. P.; Moumen, N.; Hochepped, J. F.; Bonville, P.; Veillet, P. *J. Phys. IV* **1997**, 7, C1.
- (43) Liu, C.; Vestal, C. R. *unpublished results*.
- (44) Cullity, B. D. *Elements of X-ray Diffraction Second Edition*; Addison-Wesley Publishing Co: Reading, 1978.

- (45) Snyder, R. L. In *Materials Science and Technology: Characterization of Materials*; Chan, R. W., Haasen, P., Kramer, E. J., Eds.; VCH: Weinham, 1992; Vol. 2A, pp 251.
- (46) JCPDS International Center for Diffraction Data: Swarthmore, PA.
- (47) Toby, B. <http://www.ncnr.nist.gov/instruments/bt1/>.
- (48) Jorgensen, J. D.; Jr., J. F.; Carpenter, J. M.; Crawford, R. K.; Haumann, J. R.; Hitterman, R. L.; Kleb, R.; Ostrowski, G. E.; Rotella, F. J.; Worlton, T. G. *J. Appl. Cryst.* **1989**, 22, 321.
- (49) Jenks, W. G.; Thomas, I. M.; Wikswo, J. J. P. In *Encyclopedia of Applied Physics, Vol 19*; VCH Publishers, Inc: New York, 1997, p 457.
- (50) Rondinone, A. J.; Zhang, Z. J. In *Handbook of Nanophase and Nanostructured Materials. Volume III: Materials Systems and Applications I*; Wang, Z. L., Liu, Y., Zhang, Z., Eds.; Kluwer Academic: New York, 2003; Vol. III, pp 252.
- (51) McClelland, J. F.; Jones, R. W.; Bajic, S. J. In *Handbook of Vibrational Spectroscopy*; Chalmers, J. M., Griffiths, R. R., Eds.; John Wiley & Sons, Ltd: New York, 2002.

CHAPTER 3

SYNTHESIS OF CHROMIUM-DOPED COBALT FERRITE NANOPARTICLES USING MICROEMULSION METHODS AND SIZE DEPENDENT STUDIES OF THEIR MAGNETIC PROPERTIES

Abstract

Normal and reverse micelle microemulsion methods were used to synthesis single phase CoCrFeO_4 nanoparticles with controlled size range of 6-16 nm and with a size distribution of 14%. The size dependent magnetic properties were characterized and found to agree well with Stoner-Wohlfarth theory. The results from nanoparticles prepared by the normal micelle and reverse micelle microemulsion methods were consistent with each other. The CoCrFeO_4 nanoparticles did not display the types of anomalous magnetic properties reported for their bulk phase material. Room temperature neutron diffraction studies confirm their superparamagnetic behavior. The compositional influence ($\text{CoCr}_x\text{Fe}_{2-x}\text{O}_4$; $0 < x < 1$) upon the magnetic properties is consistent with the effects of the magnetocrystalline anisotropy energy in Stoner-Wohlfarth theory.

3.1 Introduction

Nanometer scale materials have generated considerable interest due to their unique relationship between size and physical properties.¹ Superparamagnetism is an interesting phenomena that occurs usually in magnetic nanoparticles.^{2,3} Understanding and controlling this behavior is critically important in the technological applications of magnetic nanoparticles such as data storage,⁴ magnetocaloric refrigeration,⁵ drug delivery,⁶ and magnetic resonance imaging (MRI) contrast enhancement.⁷ From a fundamental standpoint, magnetic nanoparticles below a critical diameter possess a single domain magnetic structure which may provide insights to the quantum origins of magnetism arising from magnetic couplings at the atomic level such as the coupling between the spin of electron and quantum momentum of its atomic orbital (L-S coupling).

Spinel ferrite MFe_2O_4 ($M = Mn, Co, Ni, Zn$ etc.) nanoparticles are an ideal system for investigating the relationship between magnetic properties and crystal chemistry of materials.⁸ The spinel structure contains two cation sites for metal cation occupancy. There are eight A sites in which the metal cations are tetrahedrally coordinated by oxygen, and sixteen B sites which possess octahedral coordination. When the A sites are occupied by M^{2+} cations and the B sites are occupied by Fe^{3+} cations, the ferrite is called a normal spinel. If the A sites are completely occupied by Fe^{3+} cations and the B sites are randomly occupied by M^{2+} and Fe^{3+} cations, the structure is referred to as an inverse spinel. In most spinels, the cation distribution possesses an intermediate degree of inversion where both sites contain a fraction of the M^{2+} and Fe^{3+} cations. Magnetically, spinel ferrites display ferrimagnetic ordering. The magnetic moment of cations in the A

sites are aligned parallel with respect to one another and all the magnetic moments of the cations in the B sites also align parallel. Between the A and B sites the arrangement is antiparallel and as there are twice as many B sites as A sites, there is a net moment of spins yielding ferrimagnetic ordering for the crystal. The choice of metal cation and the distribution of ions between the A and B sites therefore offers a tunable magnetic system.

A type of interesting nanoparticle for investigating the changes of magnetization in a single domain magnetic structure is the mixed spinel ferrite CoCrFeO_4 in which Fe^{3+} is partially replaced by Cr^{3+} . Cr^{3+} ions usually occupy the octahedral B sites in spinels.⁹ A decrease in the total magnetic moment at the B-sites is expected as Cr^{3+} has a weaker magnetic moment ($3 \mu_B$) than Fe^{3+} ($5 \mu_B$). Cr^{3+} has an electron configuration of $t_{2g}^3 e_g^0$ in the spinel structure, which theoretically has no orbital angular momentum. Fe^{3+} at the B site has $t_{2g}^3 e_g^2$ in the spinel structure, which also theoretically has a zero orbital angular momentum. Therefore substitution of Fe^{3+} by Cr^{3+} will not offer information on the contribution from the orbital angular momentum towards the magnetic properties. However, such substitutions can introduce variations of the exchange coupling into this mixed spinel ferrite system. Therefore, the collinear model may not be correct, and triangular or spiral arrangement may dominate the magnetic order.¹⁰⁻¹² Cr^{3+} substitution could be complicated since the exchange couplings between Cr^{3+} ions display a large negative exchange constant (J_{B-B}).⁹ A strong negative J_{B-B} interaction favors antiparallel alignment of spins on the B sites. Such an arrangement is typically hindered in spinel ferrites due to the dominance of the large negative J_{A-B} couplings (which gives rise to the net ferrimagnetic ordering for the system), but it could disrupt the parallel alignment of spins on the B sites to various extents and lead to spin canting. In the case where Cr has

completely replaced Fe (CoCr_2O_4), the antiferromagnetic alignment between the A and B sites is completely destroyed and the system displays a screw ordering.⁹ When Fe is partially replaced by Cr (CoCrFeO_4), the bulk magnetic properties have been reported to be anomalous due to a frustrated magnetic structure.¹³ Examples of the anomalous behavior include sharp decreases in the saturation magnetization versus temperature curve at ~ 100 K and at 330 K. Also, a cusp in the susceptibility curve is usually observed at 330 K, just before the reported Curie transition temperature, T_C of CoCrFeO_4 .^{13, 14} The decrease at ~ 100 K was believed to be a result of a transition from a sperimagnetic phase (a frustrated structure) into a cluster spin glass. The anomaly at 330 K is a transition from cluster spin glass to a paramagnetic state. To further complicate the issues, a wide range of Curie temperatures of 330-360 K, 475 K, and 780 K have also been reported.¹³⁻¹⁵

CoCrFeO_4 nanoparticles should have a single domain magnetic structure, which may offer a simpler system for understanding the magnetic behavior of CoCrFeO_4 materials. Xiong, et. al. have recently reported the synthesis and magnetic characterization of CoCrFeO_4 nanoparticles with a size of 8.1 nm by using a sol-gel method.¹⁵ However, the size dependence of magnetic properties and the issues regarding to the anomalous behavior remain untouched. Although a variety of spinel ferrite nanoparticles have been synthesized by various methods¹⁶⁻²¹ microemulsion methods provide a synthetic approach that allows for making high quality nanoparticles with a narrow size distribution. Furthermore, by minor adjustments to the synthesis conditions, this approach easily allows for controlling the size of nanoparticles by means other than thermal annealing of nanoparticles at various temperatures.^{21, 22} Variable temperature annealing of samples not only changes the size of the nanoparticles, but may also result in

different cation redistribution depending upon the annealing temperature.²³ The magnetic properties of spinel ferrites closely relate to the magnetic couplings between the magnetic cations at the A and B sites. They are affected by redistribution of cations between these two sites. Therefore, a direct correlation between magnetic properties and the size of spinel ferrite nanoparticles is not straightforward when variable temperature annealing is used to control the size variation.

This chapter reports the use of microemulsion methods to synthesize CoCrFeO_4 nanoparticles with controlled sizes ranging from 6 to 16 nm and a size distribution of 14%. Their corresponding magnetic properties as a function of size have also been studied. The CoCrFeO_4 nanoparticles did not display the types of anomalous magnetic properties reported for their bulk material.

3.2 Experimental

3.2.1 Nanoparticle Synthesis

Both normal and reverse micelle microemulsion methods were used to synthesize CoCrFeO_4 spinel ferrite nanoparticles. Aqueous solutions containing $\text{CoCl}_2 \cdot 6\text{H}_2\text{O}$ (Fisher, 98%), $\text{CrCl}_3 \cdot 6\text{H}_2\text{O}$ (Aldrich, 98+%), and $\text{Fe}(\text{NO}_3)_3 \cdot 9\text{H}_2\text{O}$ (Alfa Aesar, 98+%) were mixed in an equimolar ratio. To form the normal micelles, an aqueous solution of sodium dodecyl sulfate (Aldrich, 98%) was added to the cation mixture and stirred constantly. A dark slurry was formed after the addition of methylamine (Acros, 40% in water). Following the chemometric model developed by Rondinone, et.al., the size of the CoCrFeO_4 nanoparticles was controlled by adjusting the temperature at which the

mixture was heated and stirred over the next several hours.²² To form the reverse micelles, an aqueous solution of sodium dodecylbenzenesulfonate (Aldrich, 98%) was added to the equimolar cation solution, followed by a large volume of toluene (JT Baker, ACS grade). The solution was stirred overnight to complete the formation of reverse micelles. Methylamine was added to precipitate the nanoparticles followed by refluxing the solution for several hours. Varying the water to toluene ratio controlled the size of the nanoparticles. In both microemulsion procedures, the samples were washed with ethanol and water to remove excess surfactant. Then, the nanoparticles were collected by centrifugation. The samples were heated to 600 °C in air for 20 hours to form crystalline nanoparticles.

3.2.2 Instrumentation

X-ray diffraction data were collected with a Bruker D8 ADVANCE X-ray diffractometer using Cu K- α radiation. Particle sizes were determined from the average peak broadening of the five strongest diffraction peaks by using the commercial program TOPAS.

Transmission electron microscopy (TEM) study has been performed using a JEOL 100C operating at 100 kV. Nanoparticles were dispersed onto a holey carbon grid. Particle size distributions were determined by manually counting over 100 particles.

Magnetic measurements were performed with a Quantum Design MPMS-5 SQUID magnetometer. Zero field cooled (ZFC) susceptibility measurements were conducted by cooling the sample from room temperature to 5 K under no applied field. Then, a field of 100 G was applied and the change in magnetization recorded as the

nanoparticles were slowly warmed up. Field cooled (FC) susceptibility experiments were performed by applying a 100 G field before cooling the sample to 5 K. Hysteresis measurements were carried out at 5 K and 300 K in applied fields up to 5 Tesla. In the low temperature hysteresis measurements, the nanoparticles were mixed with eicosane ($C_{20}H_{42}$, Aldrich) to prevent physical shifting of nanoparticles.

Room temperature neutron diffraction studies were performed on the Special Environment Powder Diffractometer (SEPD) at the Intense Pulse Neutron Source (IPNS) at Argonne National Laboratory. The magnetic and nuclear structures were determined by Rietveld refinement using the General Structure Analysis System (GSAS) program.

3.3 Results and Discussion

3.3.1 Nanoparticle Synthesis and Size Dependent Characterization

Both normal and reverse micelle microemulsion methods produced $CoCrFeO_4$ nanoparticles consisting of a pure spinel phase as indicated by the results from X-ray diffraction studies (Figure 3.1). Average particle sizes were determined from the broadening of X-ray diffraction peaks using Scherrer equation and found to range from 8 – 16 nm when the normal micelle method was employed, and from 6 – 11 nm when the reverse micelle method was used. Particle sizes were confirmed using TEM (Figure 3.2) and the size distribution was ~14% (Figure 3.3). Advantages of using the reverse micelle method include being able to form smaller sized particles and also the relative ease in control over the size of nanoparticles. However, the reverse micelle synthesis involves handling and disposal of large quantities of organic wastes. The normal micelle method

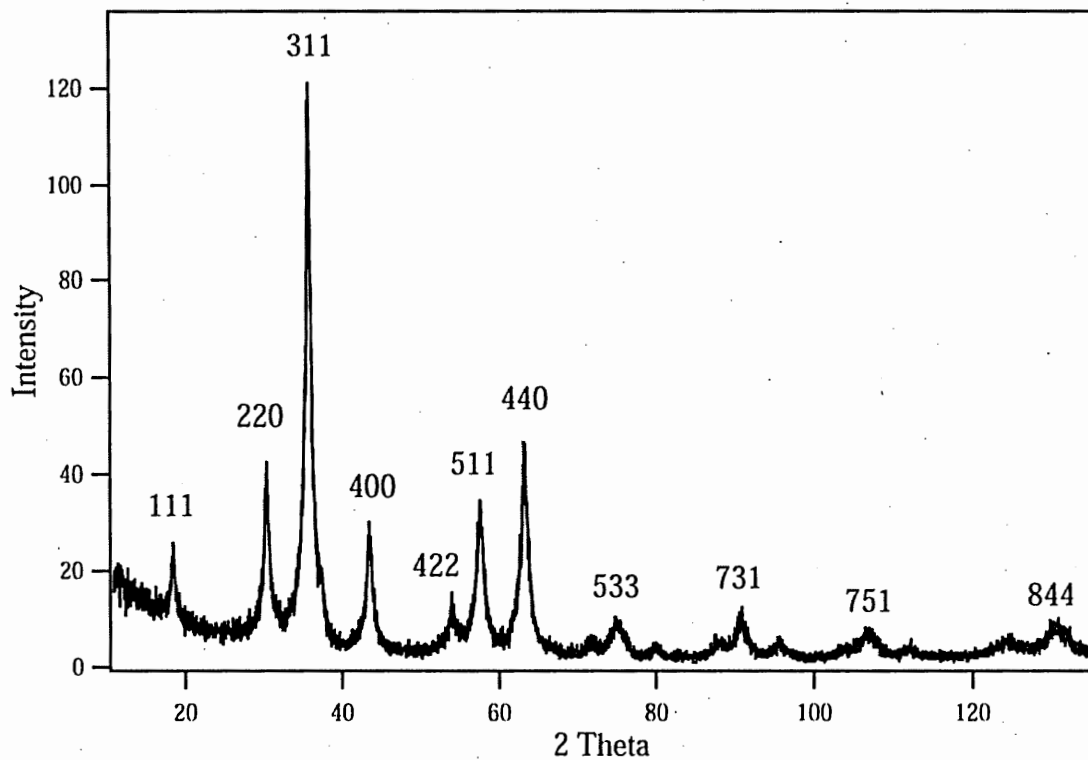


Figure 3.1 X-ray diffraction pattern of 11 nm CoCrFeO_4 nanoparticles

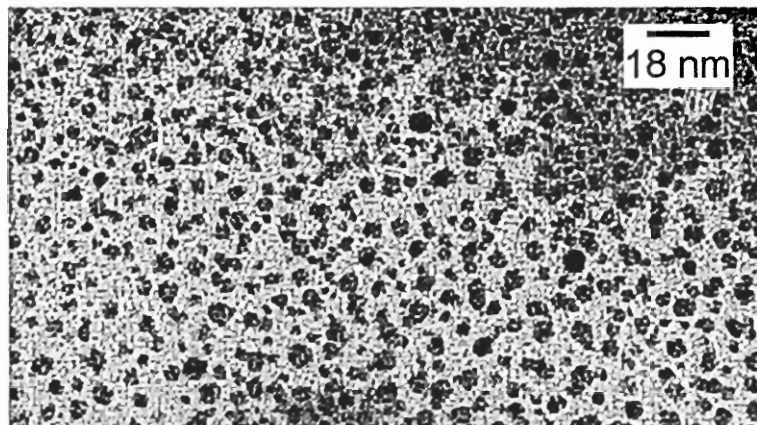


Figure 3.2 TEM micrograph of CoCrFeO_4 nanoparticles with an average size of ~ 6 nm

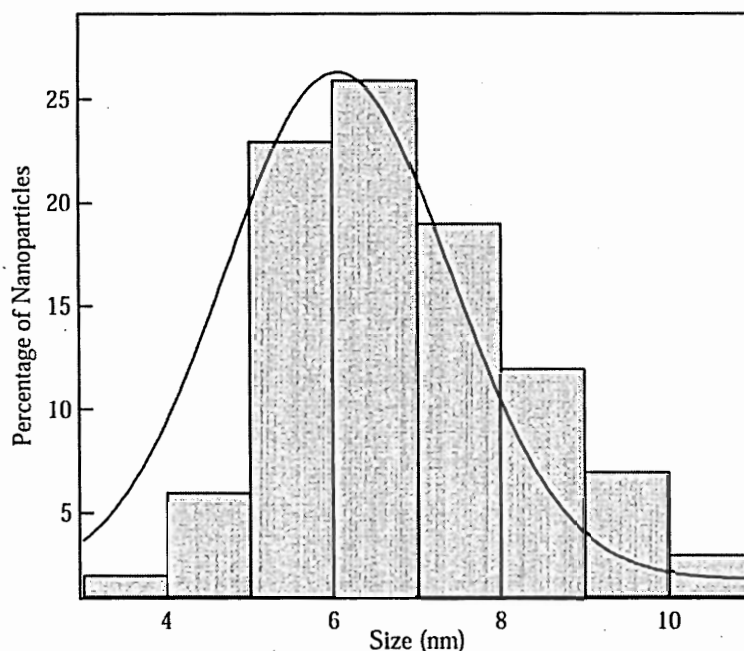


Figure 3.3 TEM size distribution histogram with a size distribution of ~14%.

allows for easier formation of larger sized nanoparticles and a 'green' cleanup. In terms of quality of the nanoparticles such as size distribution, these two methods generated similar results. Elemental analysis by inductively coupled plasma atomic emission spectroscopy (ICP-AES) confirmed an equimolar ratio of metal cations in the nanoparticles and provided a chemical composition of $\text{CoFe}_{1.01 \pm 0.03}\text{Cr}_{1.00 \pm 0.03}\text{O}_4$.

A room temperature neutron diffraction pattern is shown in Figure 3.4 for 10 nm CoCrFeO_4 nanoparticles. Although Co^{2+} and Fe^{3+} distribute at both the A and B sites, Cr^{3+} cations occupy only the B sites. From the Rietveld refinement fit, the site

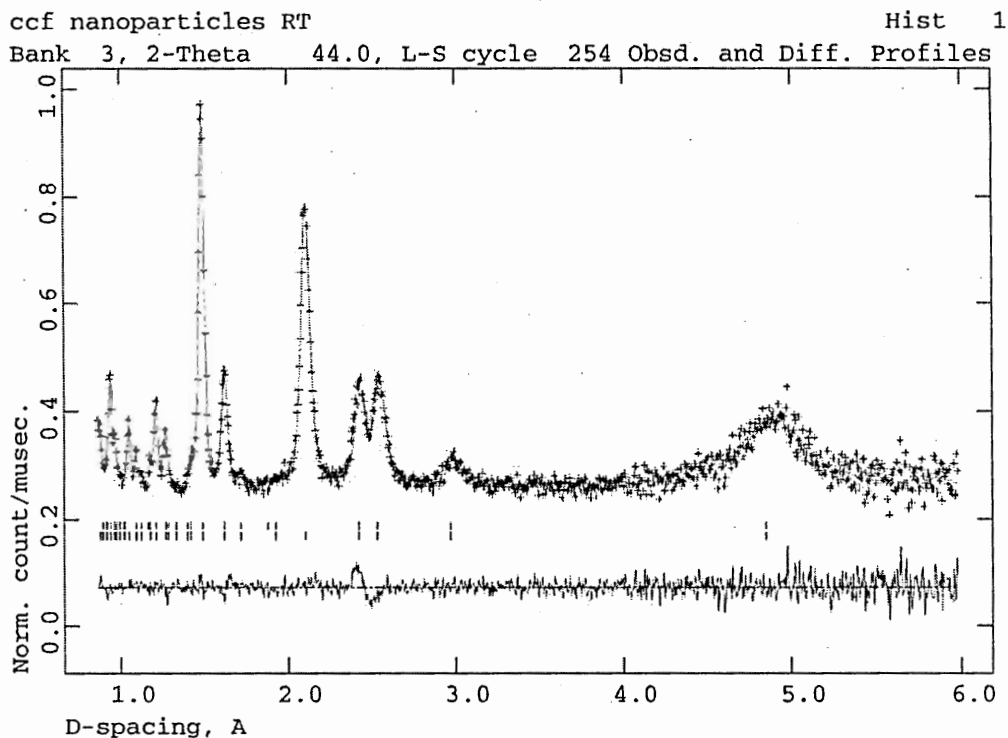


Figure 3.4 Neutron diffraction pattern of 10 nm CoCrFeO_4 nanoparticles at room temperature. The “goodness of fit” χ^2 is 1.44 and $R(f^2)$ for the data fitting is 0.0348. Below the pattern the first row of ticks marks the peaks from the magnetic scattering. The second row of ticks corresponds to the peaks from the nuclear scattering.

occupancy is $(\text{Co}_{0.76}\text{Fe}_{0.24})[\text{Co}_{0.12}\text{Fe}_{0.38}\text{Cr}_{0.5}]_2\text{O}_4$ where the cations in parentheses () occupy the tetrahedral A sites and cations in brackets [] occupy the octahedral B sites. The lattice constant for the cubic spinel unit cell is 8.347 Å at room temperature. The average magnetic moment is $-1.3(3) \mu_B$ at the A sites and $1.4(5) \mu_B$ at the B sites.

The temperature dependent ZFC measurement of magnetic susceptibility for CoCrFeO_4 nanoparticles with varying sizes is shown in Figure 3.5. For all samples, the magnetic susceptibility initially increases as temperature increases and at a certain temperature reaches a maximum. This maximum point is referred to as the blocking temperature, T_B . At temperatures above the blocking temperature the magnetization decreases, and nanoparticles display paramagnetic behavior. Figure 3.6 shows the

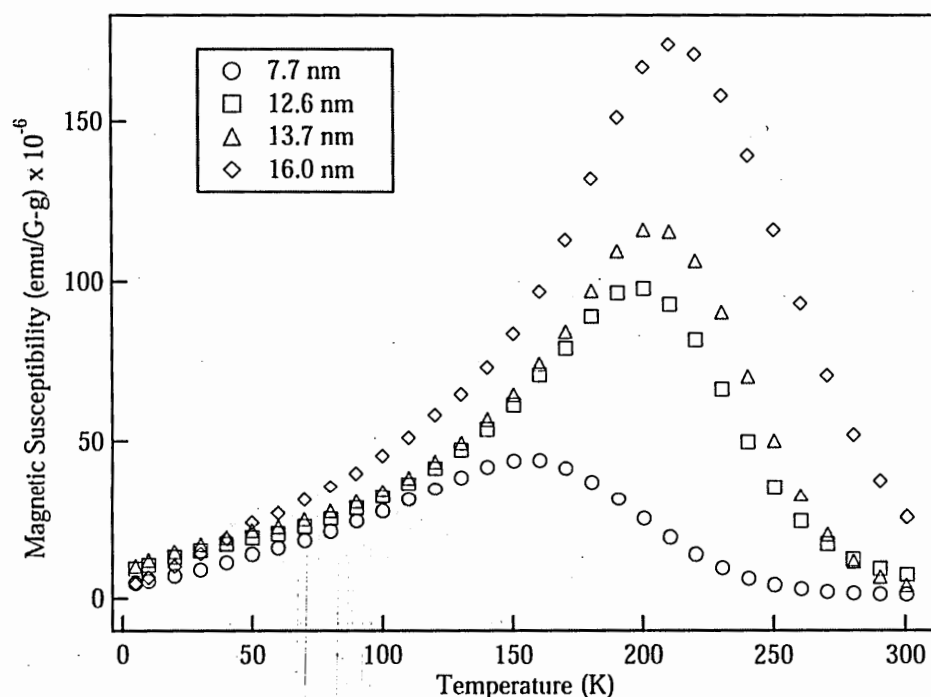


Figure 3.5 Temperature dependence of ZFC susceptibility for CoCrFeO_4 nanoparticles of various sizes under a magnetic field of 100 G.

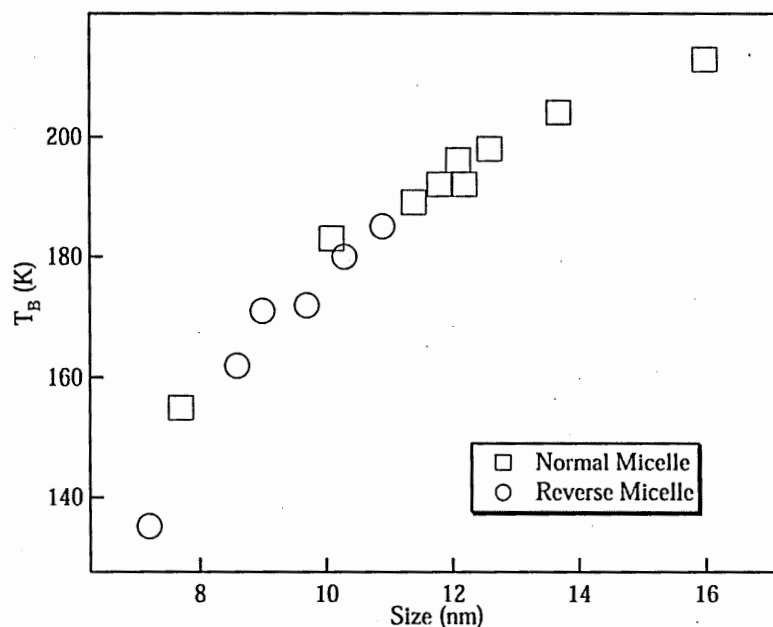


Figure 3.6 Size dependence of blocking temperature under a 100 G field for nanoparticles prepared by the normal and reverse micelle procedures

blocking temperature increasing as the size of the nanoparticles increases and also the good agreement between the results for the particles synthesized by the reverse micelle method and by the normal micelle method.

At temperatures below the blocking temperature, the field dependent magnetization of CoCrFeO_4 nanoparticles displays hysteresis. Figure 3.7 shows the hysteresis curves at 5 K for CoCrFeO_4 nanoparticles with different sizes. The remnant

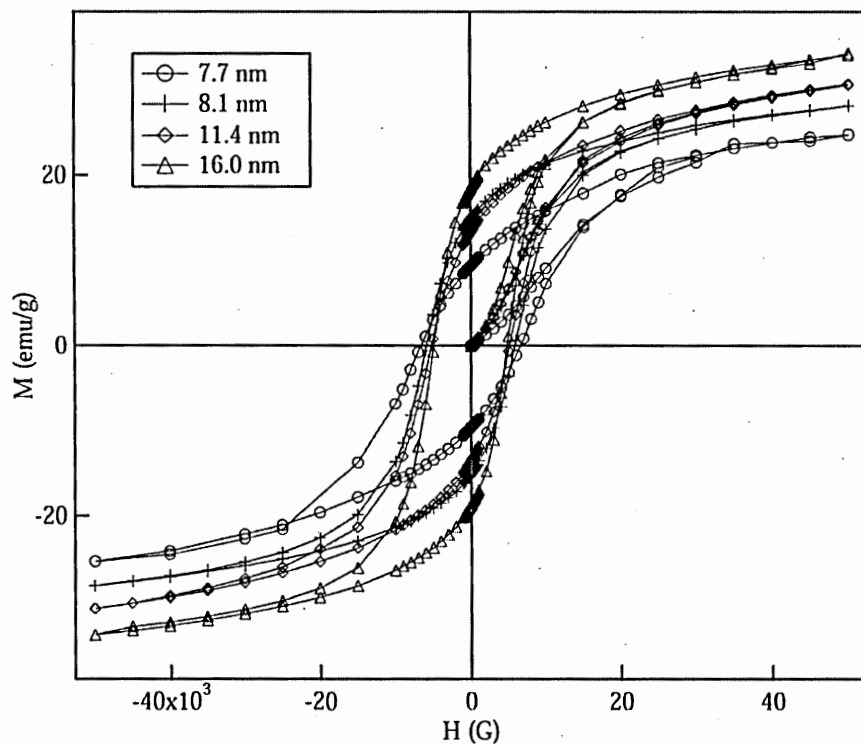


Figure 3.7 Field dependent magnetization of CoCrFeO_4 nanoparticles with various sizes at 5 K

magnetization (M_R) clearly increases as size increases as shown in Figure 3.8a.

Furthermore, there is good agreement between the results for the samples synthesized by the two microemulsion methods. Although there is a bit more scatter in the saturation magnetization (M_S) and coercivity (H_C) trends, it is clear that the saturation magnetization increases as a function of size while the coercivity decreases (Figures 3.8b & c). In all samples, the hysteresis disappears at temperatures above the blocking temperature.

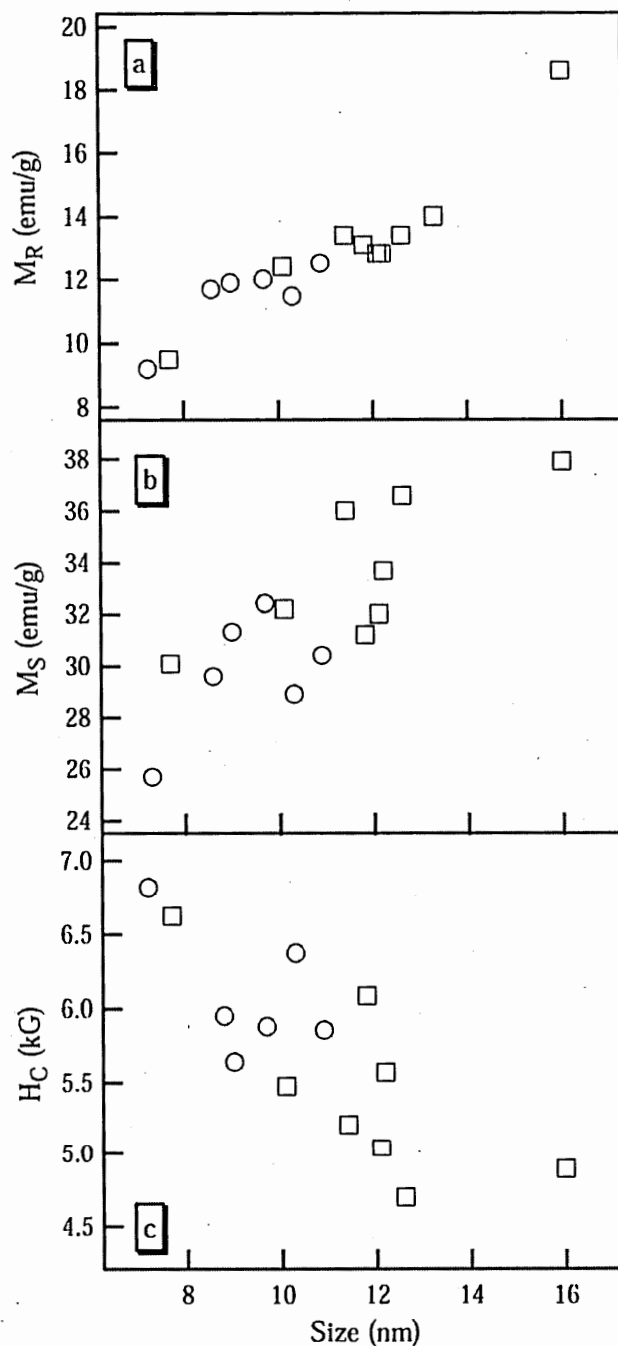


Figure 3.8 (a) Size dependence of remnant magnetization for CoCrFeO₄ nanoparticles; (b) Size dependence of saturation magnetization; (c) Size dependence of coercivity. The open circles (○) represent nanoparticles prepared by the reverse micelle procedure and open squares (□) represent nanoparticles synthesized by the normal micelle procedure.

The size dependent relationship of the blocking temperature (Figure 3.7) is consistent with the size dependence of the magnetocrystalline anisotropy energy (E_A). According to Stoner-Wohlfarth theory, E_A of a single domain particle is given by

$$E_A = KV \sin^2\theta \quad (3.1)$$

where K is the anisotropy energy constant and reflects the strength of the L-S couplings, V is the volume of the nanoparticle, and θ is the angle between the applied magnetic field and the easy axis of nanoparticles.²⁴ Below a critical size the magnetocrystalline anisotropy energy becomes comparable with the thermal activation energy, $k_B T$, where k_B is the Boltzman constant, and the magnetization direction of the nanoparticle can easily be moved away from its easy axis by thermal activation. T_B represents the point at which thermal activation is strong enough to overcome the anisotropy energy, E_A . Since E_A increases with increasing size of the nanoparticles, more energy is needed to overcome this increasing energy barrier, and hence the threshold point of thermal activation (T_B) increases with nanoparticle size (Figure 3.7).

A blocking temperature of 249 K in a 100 G field was reported by Xiong, et.al. for their 8.1 nm CoCrFeO_4 nanoparticles synthesized by the sol-gel method.¹⁵ This temperature is ~90 K above our nanoparticles with a similar size. Although the exact reasons for this discrepancy are not clear, it is well known that particles produced by different synthesis routes may show different magnetic and structural properties due to a

variety of reasons including whether kinetic versus thermodynamic control is affecting cation distributions in the chosen synthesis route.²⁵ In addition, post-synthesis annealing may also change cation distribution and hence affect the magnetic results.²³ In the current case, 600 °C was used to anneal our nanoparticles while Xiong, et.al. have annealed their samples at 500 °C.

The cation distribution was approximated from SQUID susceptibility measurements using equation 3.2

$$\chi = \sigma_s \mu / (3k_B T) \quad (3.2)$$

where σ_s is the saturation magnetization and μ is the magnetic moment.²⁶ It was assumed that all Cr^{3+} ions occupied octahedral sites as reported for chromium containing spinel ferrites⁹ and also that the distribution followed Néel's two-sublattice model for ferrimagnetism. Using the above conditions, the distribution was approximated to be $(\text{Co}_{0.42}\text{Fe}_{0.58})[\text{Co}_{0.57}\text{Fe}_{0.43}\text{Cr}]\text{O}_4$ where the cations in parenthesis occupy A sites and the cations in brackets occupy B sites. This distribution is within the range that has been reported for the bulk systems.^{13, 14} Since Xiong, et.al. did not provide information on cation distribution of their nanoparticles, a direct comparison can not be conducted. The "true" cation distribution and magnetic order was determined by neutron diffraction studies. The observation of magnetic ordering above the blocking temperature unambiguously shows that these magnetic nanoparticles are truly superparamagnetic.

The Cr^{3+} ions indeed have partially replaced the Fe^{3+} cations at the octahedral sites. The small moment at the B site suggests that the strong $J_{\text{B-B}}$ couplings may have caused the magnetic dipoles at the B sites to become canted, and consequently, the moment was reduced. The discrepancies between the cation distributions determined from magnetization data and neutron diffraction data are likely due to strong couplings between chromium ions on the octahedral sites ($J_{\text{B-B}}$). Since Cr^{3+} containing spinel ferrites often have canted magnetic spins, and deviations from Néel's model are common,⁹ the cation distribution from the magnetization approximations are not valid. The cation distributions of the bulk CoCrFeO_4 were derived from magnetization data and are likewise expected to be inaccurate representation of the true cation distribution.

The hysteresis behavior of the CoCrFeO_4 nanoparticles is also consistent with the temperature dependence of the magnetocrystalline anisotropy energy. Since the magnetocrystalline anisotropy is overcome at temperatures above the blocking temperature, the nanoparticle magnetization direction changes concurrently with the direction of applied field. As a result, the hysteresis disappears. The size dependent trends for the field dependent magnetization agree well with Stoner-Wohlfarth theory for the coercivity H_C of a single-domain nanoparticle, which is presented as the following:

$$H_C = 2K / (\mu_0 M_S) \quad (3.3)$$

where μ_0 is a universal constant of permeability in free space and M_S is the saturation magnetization of the nanoparticle.²⁷ Figure 3.8b shows that the saturation magnetization of the CoCrFeO_4 nanoparticles increases as the size increases. From the inverse relationship between saturation magnetization and coercivity (Equation 3.3) and assuming the magnetocrystalline anisotropy constant remains constant, it is expected the coercivity should decrease as size increases. This trend indeed is observed in Figure 8c. Certainly, it is highly questionable that the anisotropy constant K would remain unchanged as the size of nanoparticles changes. However, as long as the K value does not change drastically, the trend should still be consistent with the prediction of Stoner-Wohlfarth theory.

3.3.2 Studies of Nanoparticles Regarding Anomalous Bulk Properties

The field dependent magnetization of CoCrFeO_4 nanoparticles with a size of ~ 10 nm was measured over a temperature range of 5 – 180 K (The blocking temperature for these nanoparticles was 180 K). Figure 3.9 shows the saturation magnetization decreasing smoothly with increasing temperature. The more rapid decrease at very low temperature suggests that the Bloch's $T^{3/2}$ Law is not followed, which is commonly observed in nanoparticulate magnetic systems. High temperature susceptibility measurements indicate that the Curie temperature of these nanoparticles is ~ 780 K.

Previous studies on the magnetic properties of bulk CoCrFeO_4 materials have reported some interesting but complex anomalous magnetic properties. The most distinctive features include a cusp in the susceptibility measurements at ~ 330 K, just

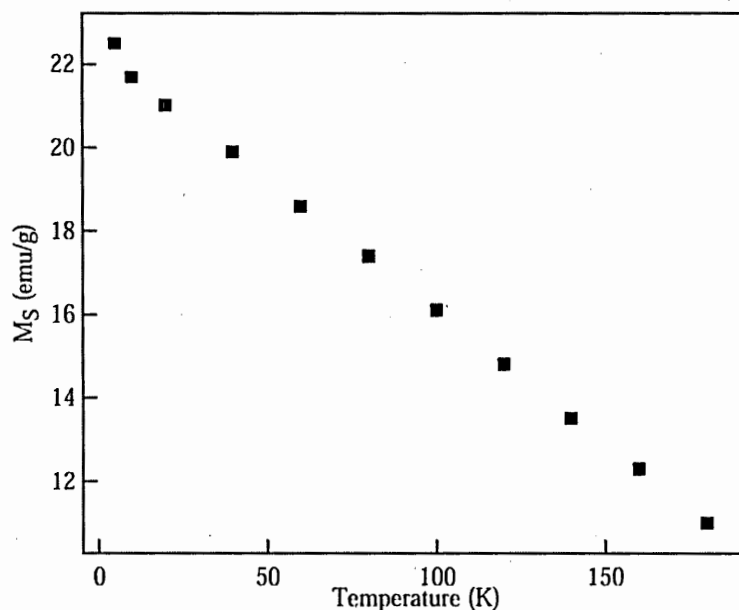


Figure 3.9 Saturation magnetization as a function of temperature for ~10 nm CoCrFeO_4 nanoparticles

before the reported Curie transition temperature 358 K. Also the saturation magnetization versus temperature curve usually shows sharp decreases at 100 K and at this cusp temperature of ~330 K.^{13, 14} It was reasoned that these anomalous properties are due to the magnetic transitions related to the frustrated structure in CoCrFeO_4 material. In some types of frustrated magnetic structures, spontaneously separated regions exist and each region has its own distinct magnetic phase. Magnetic ordering does not go through the whole sample space. Sperrimagnetic materials possess one type of frustrated structure in which the isolated regions display ferrimagnetic ordering. CoCrFeO_4 bulk materials have been considered to have the sperimagnetic structure. CoCrFeO_4 contains three different magnetic cations, and therefore, various combinations of magnetic

exchange interaction between lattice sites can occur. The magnitude of magnetic exchange interactions can vary greatly. For instance, the exchange coupling between Cr^{3+} cations at B lattice sites has a large negative exchange constant $J_{\text{B-B}}$. Moreover, different magnetic cations also possess different anisotropy strengths. Co^{2+} cation usually acts as a highly anisotropic ion. Due to the presence of such metal cations with different anisotropic strength and very diverse exchange couplings, different magnetic states may exist in mixed spinel ferrite CoCrFeO_4 and result in a frustrated magnetic structure.^{28,29} The anomalous properties have been considered as the indications of such a frustrated structure. The transition at ~ 100 K was reported to be the result of a magnetic transition from a sperimagnetic phase into a cluster spin glass. The anomaly around 330 K was believed as a transition between cluster spin glass and a paramagnetic state.

Interestingly, none of these anomalous properties are observed in CoCrFeO_4 nanoparticles. It is highly likely that the limited size and also the single magnetic domain nature of magnetic nanoparticles severely restrict the formation of isolated regions with different magnetic orderings as observed in typical frustrated materials. Due to the lack of observable anomalous properties, the magnetic moments in CoCrFeO_4 nanoparticles probably do not order into a frustrated structure.

3.3.3 Compositional Dependent Characterization

$\text{CoCr}_x\text{Fe}_{2-x}\text{O}_4$ ($0 < x < 1$) were prepared using normal micelle methods detailed above, but varying the molar ratios of $\text{Cr}^{3+} : \text{Fe}^{3+}$ in the cation solution. Figure 3.10 shows the temperature dependent magnetic susceptibility of $\text{CoCr}_x\text{Fe}_{2-x}\text{O}_4$ nanoparticles

with varying Cr composition. Figure 3.11 clearly indicated that the blocking temperature decreases with increasing Cr^{3+} . Figure 3.12 shows the field dependent magnetization of 8 nm $\text{CoCr}_x\text{Fe}_{2-x}\text{O}_4$ with variable Cr^{3+} doping, while Figure 3.13 displays the composition dependence of the magnetization parameters.

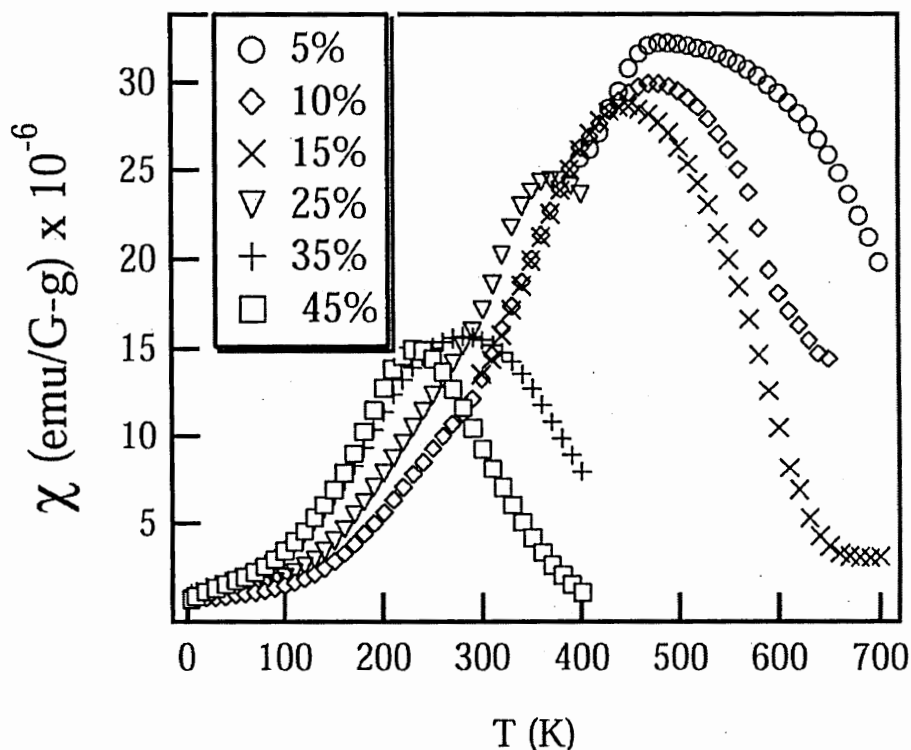


Figure 3.10 Temperature dependent susceptibility under 100G field for variable chromium compositions

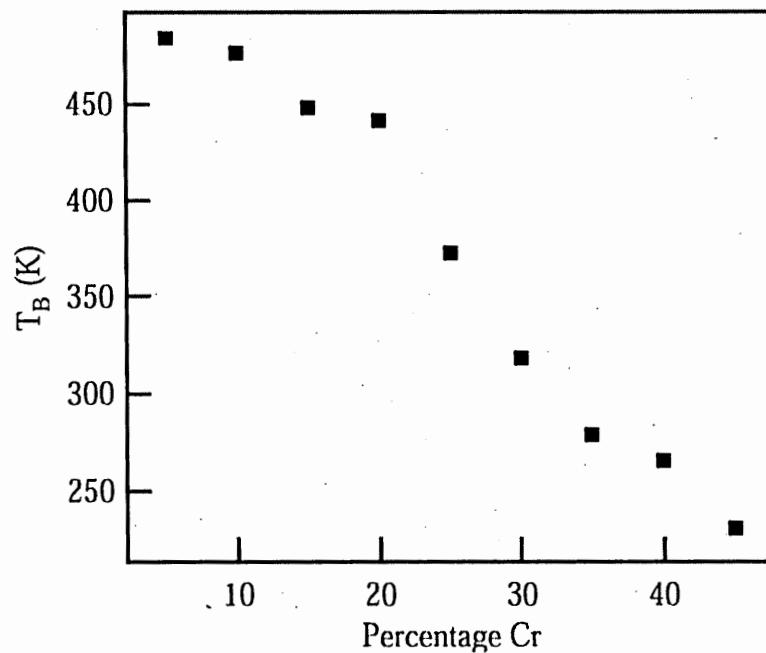


Figure 3.11 Compositional dependence of the blocking temperature for 8 nm nanoparticles

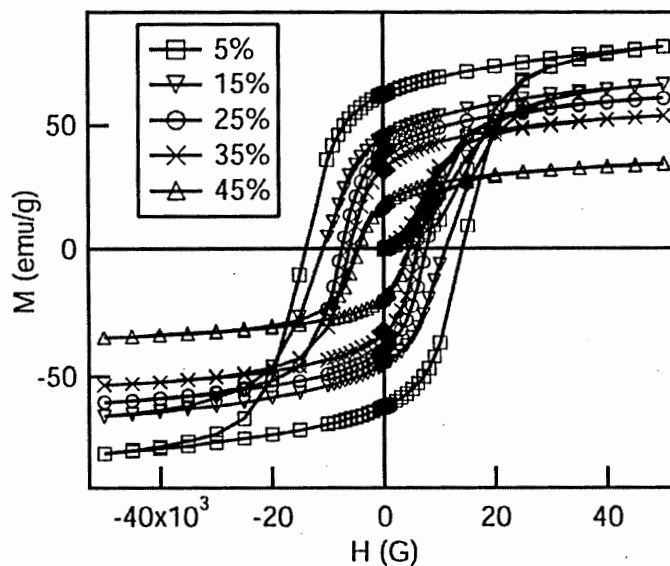


Figure 3.12 Hysteresis curves at 5K for 8 nm nanoparticles

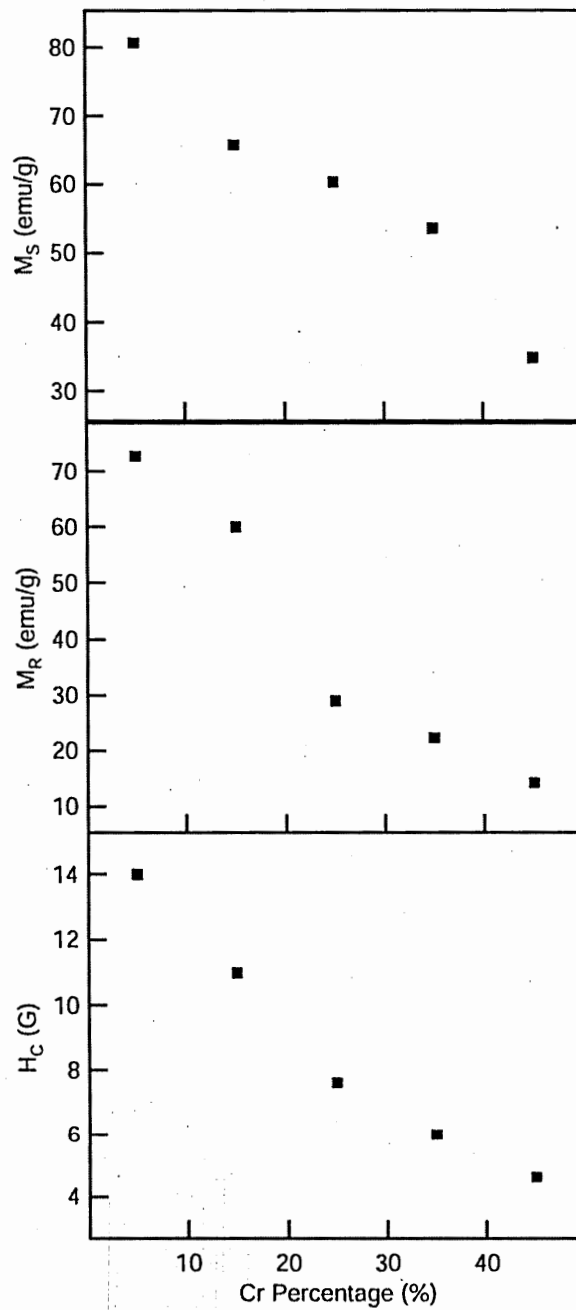


Figure 3.13 Compositional dependence of saturation magnetization (top), remnant magnetization (middle) and coercivity (bottom) for 8 nm nanoparticles

The observed decrease in T_B upon increasing the Cr^{3+} concentration implies a reduction in E_A (equation 3.1) resulting from the weakened L-S couplings (weaker K). Incorporation of more Cr^{3+} ions into the B sites weakens the L-S couplings due to the weaker magnetic moment of Cr^{3+} compared to Fe^{3+} as well as the strong negative J_{B-B} coupling. The reduced J_{A-B} causes spin canting and the collinearity between the A and B lattice sites is somewhat disrupted. This weakening of the magnetic ordering within the crystal will weaken the L-S couplings and hence the energy barrier E_A will decrease.

The observed decrease in the coercivity (Figure 3.13c) can be explained by a reduction of L-S coupling strength as well. The magnitude of the coercivity can be considered as a measure of the magnetic field strength that is required to overcome the anisotropy energy barrier in order to change the magnetization direction in a material. The lowering of the coercivity upon doping agrees with a reduction of the magnetization reversal energy barriers as discussed above. The decrease in the saturation and remnant magnetization (Figure 3.13a & b) upon incorporation of more Cr^{3+} is consistent with a decrease in the new magnetic moment as a result of substitution of Fe^{3+} ($5\mu_B$) with a magnetically weaker Cr^{3+} ($3\mu_B$) and increasing the canting of magnetic dipoles because of the strong negative J_{B-B} contribution.

3.4 Conclusions

Microemulsion methods were used to synthesize single phase CoCrFeO_4 nanoparticles over a size range of 6-16 nm. The size dependent magnetic properties were characterized and found to agree well with size dependence of the anisotropy energy in Stoner-Wohlfarth theory. Room temperature neutron diffraction confirms their

superparamagnetic behavior and suggests spin canting is present. The CoCrFeO_4 nanoparticles did not display the types of anomalous magnetic properties reported for the bulk CoCrFeO_4 materials. Due to the weaker magnetic moment of Cr^{3+} and the strong negative $J_{\text{B-B}}$ couplings, substitution of Cr^{3+} for Fe^{3+} weakens the L-S couplings. The magnetic properties of the nanoparticles upon doping with chromium are consistent with a weakening of the anisotropy constant K in Stoner-Wohlfarth theory.

3.5 References

- (1) Service, R.F. *Science* 1996, 271, 920.
- (2) Awschalom, D.D. and DiVincenzo, D.P. *Phys. Today* 1995, 48 (4), 43.
- (3) Aharoni, A. *Introduction to the Theory of Ferromagnetism*. Oxford University Press: New York, 1996; p.92.
- (4) Sun, S.; Murray, C.B.; Weller, D.; Folks, L.; and Moser, A. *Science*. 2000, 287, 1989.
- (5) McMichael, R.D.; Shull, R.D.; Swartzendruber, L.J.; and Bennett, L.H. *J. Magn. Magn. Mater.* 1992, 111, 29.
- (6) Häfeli, U.; Schütt, W.; Teller, J.; and Zborowski, M. Eds. *Scientific and Clinical Applications of Magnetic Carriers*. Plenum: New York, 1997.
- (7) Mitchell, D.G. *J. Magn. Reson. Imaging*. 1997, 7, 1.
- (8) Liu, C.; Zou, B.; Rondinone, A.J.; Zhang, Z.J. *J. Am. Chem. Soc.* 2000, 122, 6263
- (9) Broese Van Groenou, A.; Bongers, P.F.; and Stuyts, A.L. *Mater. Sci. Eng.* 1968/69, 3, 317.
- (10) Yafet, Y.; Kittel, C. *Phys. Rev.* 1952, 87, 290.
- (11) Kaplan, T.A. *Phys. Rev.* 1960, 116, 888.
- (12) Kaplan, T.A.; Dwight, K.; Lyons, D.H.; Menyuk, N. *J. Appl. Phys.* 1961, 32, 13S.
- (13) Belov, K.P.; Goryaga, A.N.; Annaev, R.R.; Kokorev, A.I.; and Lyamzin, A.N. *Sov. Phys. Solid. State*. 1989, 31, 785.
- (14) Mohan, H.; Shaikh, I.A.; Kulkarni, R.G. *Physica B*. 1996, 217, 292.
- (15) Xiong, G.; Mai, Z.; Xu, M.; Cui, S.; Ni, Y.; Zhao, Z.; Wang, X.; and Lu, L. *Chem. Mater.* 2001, 13, 1943.
- (16) Moumen, N. and Pileni, M.P. *Chem. Mater.* 1996, 8, 1128.
- (17) Pileni, M.P. and Moumen, N. *J. Phys. Chem. B*. 1996, 100, 1867.

- (18) Perez, J.A.L.; Quintela, M.A.L.; Mira, J.; Rivas, J.; and Charles, S.W. *J. Phys. Chem. B.* 1997, *101*, 8045.
- (19) Chen, Q. and Zhang, Z.J. *Appl. Phys. Lett.* 1998, *73*, 3156.
- (20) Chen, Q.; Rondinone, A.J.; Chakoumakos, B.C.; and Zhang, Z.J. *J. Magn. Magn. Mater.* 1999, *194*, 1.
- (21) Liu, C.; Zou, B.; Rondinone, A.J.; and Zhang, Z.J. *J. Phys. Chem. B.* 2000, *104*, 1141.
- (22) Rondinone, A.J.; Samia, A.C.S.; and Zhang, Z.J. *J. Phys. Chem. B.* 2000, *104*, 7919.
- (23) Zhang, Z.J.; Wang, Z.L.; Chakoumakos, B.C.; and Yin, J.S. *J. Am. Chem. Soc.* 1998, *120*, 1800.
- (24) Stoner, E.C. and Wohlfarth, E.P. *Phil. Trans. R. Soc. A.* 1948, *240*, 599; reprinted in *IEEE Trans. Magn.* 1991, *27*, 3475.
- (25) Pandya, P.B.; Joshi, H.H.; and Kulkarni, R.G. *J. Mater. Sci. Letters.* 1991, *10*, 474.
- (26) Chen, J.P.; Sorenson, C.M.; Klabunde, K.J.; and Hadjipanayis, G.C. *Phys. Rev. B.* 1995, *51*, 11527.
- (27) McCurrie, R.A. *Ferromagnetic Materials – Structure and Properties*; Academic: London, 1994; p.16.
- (28) Shellmyer, D.J. and Nafis, S. *J. Appl. Phys.* 1985, *57*, 3584.
- (29) Chudnovsky, E.M. *J. Appl. Phys.* 1988, *64*, 5770.

CHAPTER 4

NEUTRON DIFFRACTION STUDIES ON THE ANOMALOUS MAGNETIC PROPERTIES OF COBALT CHROMIUM IRON OXIDE PREPARED FROM NANOPARTICULATE PRECURSOR

Abstract

Bulk CoCrFeO_4 has been prepared using nanoparticulate precursors. The temperature dependence of the saturation magnetization does not display the anomalous properties reported for bulk CoCrFeO_4 prepared by conventional ceramic methods, while temperature dependent susceptibility measurements show transitions at 287 K and at 780 K. Powder neutron diffraction shows ferrimagnetic ordering present below 295 K. However, the spins are highly non-collinear. Above 295 K, ferrimagnetic ordering is no longer observed, but a new peak at 58° 2-Theta appears. The transition at 287 K is suggested to be from an 'unstable' ferrimagnet to cluster spins, while the transition at 780 K is the Curie transition temperature.

4.1 Introduction

Spinel ferrites, MFe_2O_4 ($M = Zn, Co, Ni, \text{etc.}$), have been widely employed as electronic materials over the past half-century.¹ The magnetic properties of spinel ferrites can be controlled through chemical composition and bonding.² The spinel structure contains two cation sites in the lattice; the A sites are tetrahedrally coordinated by oxygen, and the B sites have octahedral coordination. The magnetic properties of spinels are determined by the exchange interactions of the metal cations on the A and B sites and can therefore be manipulated through choice of cation and the cation occupancy site. For most of the commonly used ferrites (e.g. $CoFe_2O_4$, $MnFe_2O_4$), the magnetization is ferrimagnetic - the net moment is a result of antiparallel arrangement of magnetic moments of the cations between the A and B sites.² However, the probability of forming frustrated magnetic structures is increased in systems that contain two or more types of metal cations.^{3,4} Bulk $CoCrFeO_4$ prepared by traditional ceramic routes in which stoichiometric ratios of CoO , Cr_2O_3 , and Fe_2O_3 are annealed at 1000 – 1200 °C for 12 - 24 hours have been reported by various groups to display anomalous magnetic properties resulting from such a frustrated magnetic structure.^{5,6} Examples of reported anomalies include a sharp decrease in the saturation magnetization versus temperature curve at ~ 100 K and at 330 K.⁵ Furthermore, a cusp in the susceptibility curve is usually observed at 330 K, just before the reported Curie transition temperature, T_C of $CoCrFeO_4$ (although a wide range of Curie temperatures of 330-360 K, 475 K, and 780 K have been reported).⁵⁻⁸

Due to strong couplings between chromium ions on the octahedral sites (J_{B-B}), chromium containing spinels often have canted magnetic spins and deviations from

Néel's collinear ferrimagnetic ordering model are common.² The increased canting of the magnetic spin away from the longitudinal direction (z-axis) has been suggested to cause magnetic frustration by preventing long range ordering, which reduces the system into finite regions of spin clusters.⁶ The lower temperature transition observed in the magnetization data for bulk CoCrFeO_4 prepared by conventional ceramic methods has been interpreted Mohan, et.al. as a transition between finite regions of these cluster spins into an unstable ferrimagnetic state and the higher transition temperature as a transition between the unstable ferrimagnetic state to a paramagnetic state.⁶ On the other hand, Belov, et. al. suggest that the decrease observed in the temperature dependent saturation magnetization at ~ 100 K is a result of a transition from a sperimagnetic phase (a frustrated structure) into a cluster spin glass and the anomaly at 330 K is a transition from a cluster spin glass to a paramagnetic state.⁵ The correlations between the anomalous magnetic data and the proposed magnetic ordering were determined through interpretations of Mössbauer and magnetization data and their consistency (or lack thereof) with Néels ferrimagnetism model as well as through similarities between the observed magnetization measurements and reported characteristics of spin glasses.

Recently the synthesis and magnetic characterization of CoCrFeO_4 nanoparticles was reported.⁸ Interestingly, none of the anomalous features reported for bulk CoCrFeO_4 prepared by conventional ceramic methods were observed for the nanoparticles, which suggests that the magnetic moments in CoCrFeO_4 nanoparticles probably do not order into a frustrated structure. Due to their limited size and also the single magnetic domain nature of magnetic nanoparticles, the formation of isolated regions with different magnetic orderings as observed in typical frustrated materials may be restricted in

nanoparticles. However, bulk CoCrFeO_4 samples prepared using the CoCrFeO_4 nanoparticles as a precursor do show some unusual features, although they differ from the features observed for the bulk ferrite prepared by conventional ceramic methods.⁸ In order to understand the correlations between magnetic ordering and the magnetization properties in the nanoparticle and bulk CoCrFeO_4 samples, powder neutron diffraction studies were performed. Herein the findings of the neutron diffraction studies as well as magnetic characterization of the bulk CoCrFeO_4 samples prepared from the nanoparticle precursors are reported.

4.2 Experimental

CoCrFeO_4 nanoparticles were prepared using reverse micelle microemulsion methods described previously.⁸ To prepare the bulk phase, nanoparticles with size ~ 10 nm were annealed at 1100°C for 24 hours.

Magnetic measurements were performed on a Quantum Design MPMS-5S SQUID magnetometer. Temperature dependent susceptibility measurements were conducted from 5 – 780 K under an applied field of 100 G. Field dependent hysteresis measurements were performed from 5 – 400 K in applied fields up to 5 T.

Neutron powder diffraction data were collected using the BT-1 32 detector neutron powder diffractometer at the National Center for Neutron Research (NCNR) at NIST. A Ge(311) monochromator with a 75° take-off angle, $\lambda = 2.0775(2)$ Å, and in-pile collimation of 15 minutes of arc were used. Data were collected over the range of 1.3 - $166.3^\circ 2\theta$ with a step size of 0.05° . The instrument is described in the NCNR WWW site (<http://www.ncnr.nist.gov/>). The CoCrFeO_4 sample was sealed in a vanadium

container of length 50 mm and diameter 6.0 mm inside a dry He-filled glovebox. A closed-cycle He refrigerator was used for temperature control. The nuclear and magnetic structures of the sample were refined using the General Structure Analysis System (GSAS) program.⁹ In the Rietveld refinement, Cr^{3+} cations were confined to the octahedral (B) sites as this occupancy preference is well established for chromium containing spinels.²

4.3 Results and Discussion

4.3.1 Magnetic Measurements

Variable temperature hysteresis measurements from 5 – 400 K for bulk CoCrFeO_4 prepared by annealing CoCrFeO_4 nanoparticles to 1100 °C for 24 hours are presented in Figure 4.1. No unusual features are apparent in the hysteresis curves. Furthermore, the inset in Figure 4.1 shows that the temperature dependence of the saturation magnetization clearly decreases in a smooth manner. No sharp decreases at 100 K and 330 K as reported for the bulk CoCrFeO_4 prepared by conventional ceramic methods are observed. Figure 4.2 displays the temperature dependent susceptibility under an 100 G applied field for bulk CoCrFeO_4 prepared from the nanoparticulate precursor. A peak at 287 K is evident in the low temperature region, while the inset of high temperature measurements shows a Curie transition temperature ≥ 780 K. Interestingly the temperature dependence of the saturation magnetization (inset of Figure 4.1) does not show any features reflecting the transition at 287 K. For comparison, temperature dependent susceptibility measurements under an applied field of 100 G for 10 nm CoCrFeO_4 nanoparticles used as

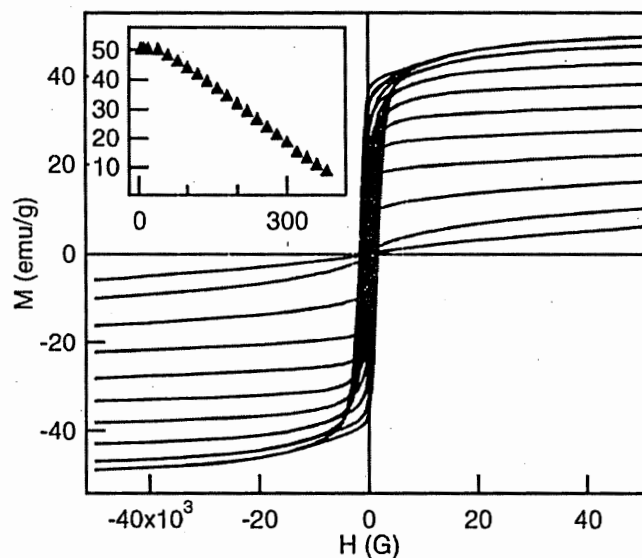


Figure 4.1. Hysteresis measurements for bulk CoCrFeO_4 from 20 – 380 K in 40 K increments (top to bottom). Inset shows temperature dependence of saturation magnetization (M_s).

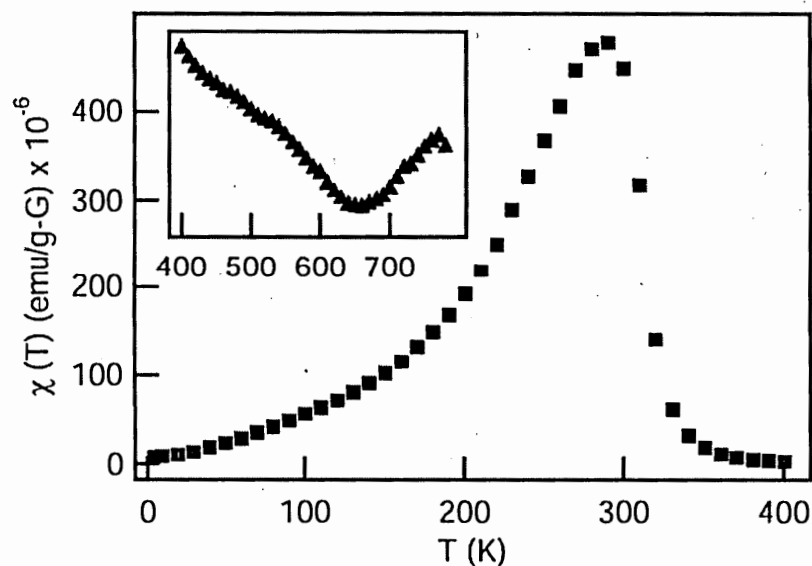


Figure 4.2. Temperature dependent susceptibility under a 100G applied field. Inset displays high temperature measurements.

the precursor show superparamagnetic behavior with a blocking temperature $T_B \sim 180$ K and a Curie temperature of ~ 780 K.⁸

It is very intriguing that the CoCrFeO_4 sample with a bulk phase prepared from CoCrFeO_4 nanoparticles did not display the same anomalous properties as reported for the bulk materials made by the ceramic routes. Unlike the ceramic bulk materials that displayed a sharp decrease of saturation magnetization at 100 K and 330 K, the saturation magnetization versus temperature trend decreases smoothly in the bulk material here (Figure 4.1). A peak at 287 K in the low temperature susceptibility measurement was found, which may be comparable to the cusps at 330 K for the ceramic bulk CoCrFeO_4 . However, it is interesting that no consequence of this transition is observable around this temperature in the temperature dependent saturation magnetization trend. The differences between the bulk samples prepared from nanoparticles versus conventional ceramic methods may be the consequence of a lack of frustrated structure in the precursor nanoparticles. When the nanoparticles were heated at 1100 °C, the crystal grains were homogenous and the magnetic structure was always similar. In the bulk materials different magnetic structure may have formed due to the inherent inhomogeneity of the process, i.e. one magnetic structure may have initially formed at the $\text{CoO}/\text{Fe}_2\text{O}_3$ interface while another type of ordering may have occurred at the $\text{Cr}_2\text{O}_3/\text{Fe}_2\text{O}_3$ grain interface. Certainly, it is not clear solely from the magnetization data the exact nature of the magnetic ordering, nor the reasoning for the differences in the magnetic behavior between bulk CoCrFeO_4 prepared from nanoparticle precursors versus conventional ceramic methods.

4.3.2 Neutron Diffraction Studies

Powder neutron diffraction was utilized in order to determine the magnetic structure of CoCrFeO_4 over the temperature range in which the anomalous magnetic features were observed in the SQUID magnetometry experiments. Figure 4.3 shows examples of the Rietveld refinements for diffraction patterns collected at 200 K and 350 K. A refinement of the 50 K neutron diffraction pattern suggests a formula $(\text{Co}_{0.85}\text{Fe}_{0.15})[\text{Co}_{0.08}\text{Fe}_{0.42}\text{Cr}_{0.5}]_2\text{O}_4$ where cations in parenthesis () occupy the tetrahedral A sites of the spinel structure and the cations in brackets [] occupy the octahedral B sites. This distribution is similar to the cation distribution reported by Mohan determined from a combination of x-ray diffraction, magnetization and Mössbauer results $\{(\text{Co}_{0.7}\text{Fe}_{0.3})[\text{Co}_{0.15}\text{Fe}_{0.35}\text{Cr}_{0.5}]_2\text{O}_4\}$,⁶ but differs from the distribution suggested by Bela, et.al. from magnetization results $\{(\text{Co}_{0.5}\text{Fe}_{0.5})[\text{Co}_{0.25}\text{Fe}_{0.25}\text{Cr}_{0.5}]_2\text{O}_4\}$.⁵ Table 4.1 summarizes the structural parameters determined from the Rietveld refinements for all of the temperatures studied. As seen in Table 4.1, the cation distribution did not vary with temperature. On the other hand, the magnitude of the magnetic moment clearly decreases with increasing temperature. The refinement of the 50 K neutron diffraction pattern shows a clear ferrimagnetic ordering, while at temperatures above room temperature, no ferrimagnetic ordering is observed (also see Figure 4.3). For comparison, room temperature neutron diffraction for CoCrFeO_4 nanoparticle samples with size ~ 10 nm clearly shows ferrimagnetic ordering well above the blocking temperature ($T_B \sim 180$ K), which confirms the observed transition at 180 K is a superparamagnetic transition.¹⁰

Further study of the neutron diffraction patterns reveals a small peak at $\sim 58^\circ 2\theta$, which begins to emerge in the room temperature diffraction pattern, although it is

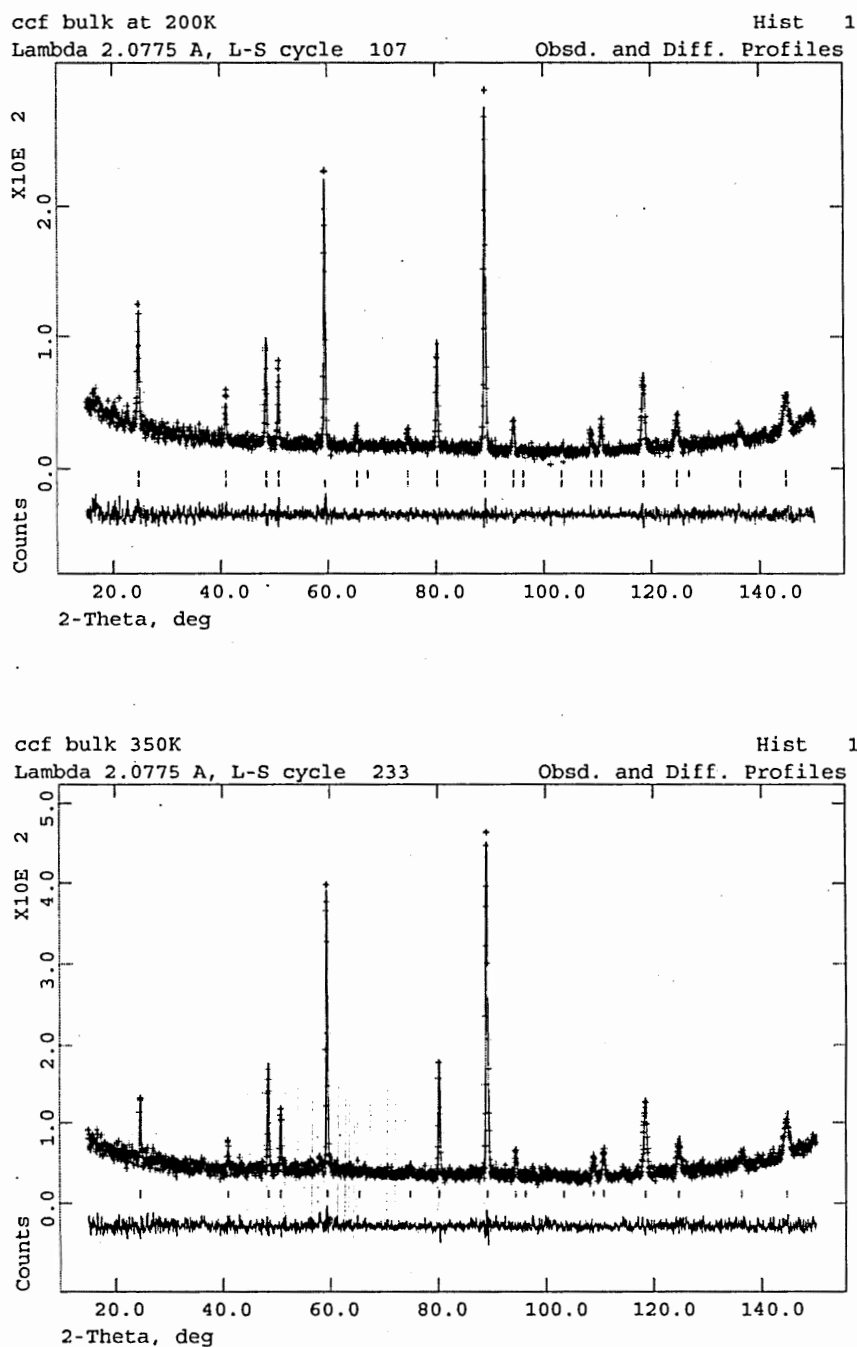


Figure 4.3. GSAS refinements of CoCrFeO_4 at 200K (top) and 350K (bottom). In the 200K pattern, the top set of tick marks represent calculated magnetic reflections and the bottom set of tick marks are the nuclear reflections. In the 350K pattern, only the nuclear reflection ticks are present.

Table 4.1. Structural Parameters from Rietveld Refinement of Neutron Diffraction Data for Bulk CoCrFeO_4 Prepared from Nanoparticle Precursor

T (K)	cation distribution ^a		x (O)	Moment (μ_B)		a (Å)	R (F^2)
	A Sites	B Sites ^b		A site	B site		
50	$\text{Co}_{0.85}\text{Fe}_{0.15}$	$\text{Co}_{0.08}\text{Fe}_{0.42}\text{Cr}_{0.5}$.2595(3)	-2.6(6)	1.8(2)	8.365(3)	.0717
200	$\text{Co}_{0.83}\text{Fe}_{0.17}$	$\text{Co}_{0.09}\text{Fe}_{0.41}\text{Cr}_{0.5}$.2589(3)	-2.3(2)	1.2(4)	8.369(3)	.0729
295	$\text{Co}_{0.84}\text{Fe}_{0.16}$	$\text{Co}_{0.08}\text{Fe}_{0.42}\text{Cr}_{0.5}$.2598(3)	-1.3(1)	0.6(2)	8.375(4)	.1020
350	$\text{Co}_{0.83}\text{Fe}_{0.17}$	$\text{Co}_{0.09}\text{Fe}_{0.41}\text{Cr}_{0.5}$.2598(2)	na	na	8.375(3)	.0455
450	$\text{Co}_{0.82}\text{Fe}_{0.18}$	$\text{Co}_{0.09}\text{Fe}_{0.41}\text{Cr}_{0.5}$.2598(3)	na	na	8.380(3)	.0576

^a Estimated standard uncertainties for site occupancies are ± 0.01 .

^b Cr occupancy fixed in B site

Table 4.2. Comparison of Sublattice and Net Magnetic Moments from Néel's Collinear Ferrimagnetic Model and Experimental Neutron Diffraction Data

T (K)	A Site		B Site		Net Moment	
	Calc	Expt	Calc	Expt	Calc	Expt
50	-3.3 μ_B	-2.6 μ_B	3.8 μ_B	1.8 μ_B	4.3 μ_B	1 μ_B
200		-2.3 μ_B		1.2 μ_B		0.1 μ_B
295		-1.3 μ_B		0.6 μ_B		-0.1 μ_B

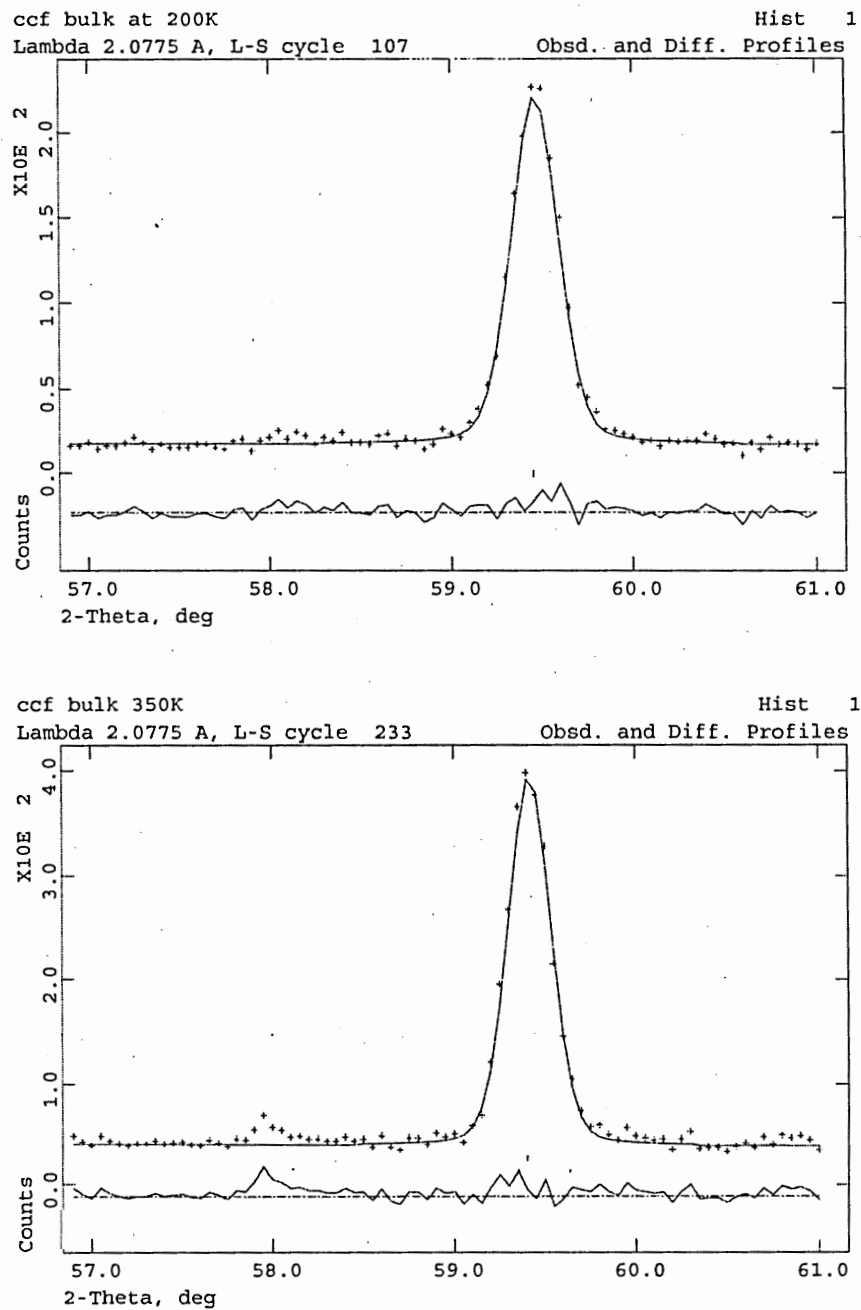


Figure 4.4. A weak peak not corresponding to the spinel reflections or ferrimagnetic ordering appears $\sim 58^\circ 2\theta$ upon increasing the temperature from 200K (top) to 350K (bottom).

not significantly above signal-to-noise. The peak is evident in the 350 K neutron diffraction pattern, but then disappears at 450 K. Figure 4.4 shows a magnified view of the refinement for neutron diffraction data collected at 200 K and 350 K showing the emergence of the peak at $\sim 58^\circ$ 2-Theta. No other new peaks were observed.

Using Néel's collinear ferrimagnetic model for magnetic ordering, the ideal magnetic moment of each sublattice can be determined from the free ion moments of the metal cations and the lattice site distributions in Table 4.1. Table 4.2 compares the calculated magnetization using Néel's model to the values determined from the Rietveld refinements. From Table 4.2, it is clear that the experimental values of the magnetic moment are substantially smaller than the estimated values, which indicates that the moments are highly non-collinear. Due to the strong negative J_{B-B} couplings of Cr^{3+} , the exchange coupling between the A and B lattice sites (J_{A-B}), which is responsible for ferrimagnetic ordering, is weakened. As a consequence deviations from collinearity are common in chromium containing spinels.² In this case, the degree of spin canting increases with temperature and above room temperature the canting becomes severe enough to disrupt ferrimagnetic ordering. Because non-collinear spins inhibit cooperative long range ordering and leave spins in a frustrated state, this observed increase in spin canting will enhance the frustration and thus clusters of magnetic spins form.^{6, 11} Although such clusters should give rise to diffuse scattering at very small q 's,^{11, 12} in the q range studied here such diffuse scattering is not observed.

Additionally in systems with non-collinear spin, in which the magnetic spin cants away from the longitudinal z direction, spatial ordering of the transverse spins ($x \leftrightarrow y$) may occur. Such ordering would give rise to a (200) Bragg magnetic reflection,^{11, 12}

which would be present at $\sim 29^\circ$ 2-Theta under the conditions used in these neutron diffraction experiments. However, no (200) reflection is observed at any temperature, indicating the spins are randomly canted.

The new peak at 58° 2-Theta, which first emerges at 295 K, may be a reflection of the 287 K transition observed in Figure 4.2. Because this peak begins to emerge at temperatures in which ferrimagnetic ordering disappears, the presence of this peak may suggest a new magnetic ordering or phase. However, with no other peaks to assist in indexing and modeling this peak, no conclusions about the origins of this peak can be made at this time.

The combination of SQUID magnetometry and neutron diffraction suggests transitions between a ferrimagnetic state with a high degree of canting and an unknown phase of magnetic clusters formed through the decreased long range ordering resulting from the increased canting with temperature. The transition observed at 287 K in the SQUID susceptibility measurements is likely a transition from an “unstable” canted ferrimagnetic state into cluster spins, while the transition at 780 K is a “Curie temperature” transition to paramagnetic ordering.

4.4 Conclusions

Bulk CoCrFeO_4 nanoparticles prepared from single-domain nanoparticulate precursors display magnetic properties that differ from both the nanoparticle precursor and from bulk CoCrFeO_4 prepared by conventional ceramic methods. No unusual features are present in the temperature dependent saturation magnetization, while susceptibility measurements show two peaks at 287 K and 780 K. From neutron powder

diffraction ferrimagnetic ordering is clear below 295 K. However, the spins are highly non-collinear. The ferrimagnetic ordering is destroyed above 295 K due to the increased spin canting. Such an increasing degree of spin canting likely leads to the formation of spin clusters. The transition at 287 K is suggested to be a transition between an 'unstable' ferrimagnet into cluster spins and the transition at 780 K is the Curie transition temperature.

4.5 References

- (1) Sugimoto, M. *J. Am. Ceram. Soc.* **1999**, *82*, 269.
- (2) Van Groenou, A.B.; Bongers, P.F.; Stuyts, A.L. *Mater. Sci. Eng.* **1968/69**, *3*, 317.
- (3) Shellmyer, D.J.; Naffis, S. *J. Appl. Phys.* **1985**, *57*, 3584.
- (4) Chudnovsky, E.M. *J. Appl. Phys.* **1988**, *64*, 5770.
- (5) Belov, K.P.; Goryoga, A.N.; Annaev, R.R.; Kokorev, A.I.; Lyamzin, A. *Sov. Phys. Solid State.* **1989**, *31*, 785.
- (6) Mohan, H.; Shaikah, I.A.; Kulkarni, R.G. *Physica B.* **1996**, *217*, 292.
- (7) Xiong, G.; Mai, Z.; Xu, M.; Cui, S.; Ni, Y.; Zhao, Z.; Wang, X.; Lu, L. *Chem. Mater.* **2001**, *13*, 1943.
- (8) Vestal, C.R.; Zhang, Z.J. *Chem. Mater.* **2002**, *14*, 3817.
- (9) Larson, A.C.; von Dreele, R.B. General Structure Analysis System (GSAS); Los Alamos National Laboratory Report, LAUR 86-748, 2000.
- (10) Han, M.; Vestal, C.R.; Zhang, Z.J. *J. Phys. Chem. B.* **2004**, *108*, 583.
- (11) Chakravarthy, R.; Rao, L.M.; Paranjpe, S.K.; Kulshreshtha, S.K.; Roy, S.B. *Phys. Rev. B.* **1991**, *43*, 6031.
- (12) Yunus, S.M.; Shim, H.S.; Lee, C.H.; Asgar, M.A.; Ahmed, F.U.; Zakaria, A.K.M. *J. Magn. Magn. Mater.* **2002**, *241*, 40.

CHAPTER 5

EFFECTS OF SURFACE COORDINATION CHEMISTRY ON THE MAGNETIC PROPERTIES OF MANGANESE FERRITE NANOPARTICLES

Abstract

In order to understand the influence of surface chemistry upon the magnetic properties of magnetic nanoparticles, the surface of manganese ferrite, MnFe_2O_4 , nanoparticles have been systematically modified with a series of *para* - substituted benzoic acid ligands ($\text{HOOC-C}_6\text{H}_4\text{-R}$; $\text{R} = \text{H}, \text{CH}_3, \text{Cl}, \text{NO}_2, \text{OH}$) and substituted benzene ligands ($\text{Y-C}_6\text{H}_5$, $\text{Y} = \text{COOH}, \text{SH}, \text{NH}_2, \text{OH}, \text{SO}_3\text{H}$). The coercivity of magnetic nanoparticles decreases up to almost 50% upon the coordination of the ligands on the nanoparticle surface while the saturation magnetization increases. The percentage coercivity decrease of the modified nanoparticles with respect to the native nanoparticles strongly correlates with the crystal field splitting energy (CFSE) Δ evoked by the coordination ligands. The ligand inducing the largest CFSE results in the strongest effect on the coercivity of the magnetic nanoparticles. The correlations suggest a decrease in spin-orbital couplings and surface anisotropy of magnetic nanoparticles due to the surface coordination.

5.1 Introduction

Surface chemistry is of great importance to the chemical and physical properties of nanoparticles. As the size of nanoparticles decreases, surface effects could become more significant due to the increased volume fraction of surface atoms within the whole particle. The symmetry is reduced for the chemical surroundings of magnetic metal cations at the surface due to the incomplete coordination sphere. Consequently, the magnetic structure at the surface layer usually is greatly different from that in the body of nanoparticle, and the magnetic interactions in the surface layer could have a notable effect on the magnetic properties of the nanoparticle.¹⁻⁶ Understanding the influence of surface chemistry on the magnetic properties of nanoparticles certainly facilitates our fundamental understanding of the unique magnetic behavior in nanoparticles such as the quantum origin of hysteresis in single domain magnetic nanoparticles. Furthermore, understanding and controlling the effects of surface chemistry on magnetic properties has become increasingly important for the technological applications of magnetic nanoparticles such as high density magnetic storage media, medical imaging, and drug delivery. In the information storage industry, the drive for higher density by greatly shrinking the size of data bits means surface effects become more dominant as smaller magnetic particles are employed.⁷ For practical implementation in biomedical applications of nanoparticles such as magnetically guided site specific drug delivery and magnetic resonance imaging (MRI) contrast enhancement agents, the surface of the nanoparticles have to be modified with biocompatible ligands and/or polymer matrices that also serve as drug carrying vehicles.⁸⁻⁹ Once internalized, the surfaces of nanoparticles are inevitably encapsulated with biological ligands that are associated with

the body's defense system.¹⁰ Understanding the changes in magnetic behavior from these chemical interactions at surface is critical for developing magnetic nanoparticles in biomedical techniques.

Early reports on the influence of surface interactions upon the magnetic properties of nanoparticles arose from the desire to understand the role of adsorbate and metal surface interactions in catalysis. Selwood, investigating the effects of adsorbed gases such as N₂, H₂, and O₂ upon magnetic properties of Ni nanoparticles, first reported such interactions.¹¹ A 50% decrease on the saturation magnetization of 6.4 nm Ni nanoparticles was reported when the ratio of O₂ pressure to the weight of Ni was 60 cm³/g at 300 K. When the adsorbate was H₂, the saturation magnetization of Ni, Ni-Si, and Ni-Cu alloy nanoparticles decreased to various extents. Compared to O₂, a ratio of 17 cm³ H₂/g caused a 13% decrease on the saturation magnetization of Ni nanoparticles. On the other hand, the adsorption of H₂ increased the saturation magnetization of 1.5 nm Fe nanoparticles.¹¹ The reasons are not understood for such effects on the magnetic properties of metallic nanoparticles by gas adsorption.

The effect upon the magnetic properties of oxide nanoparticles has not been well established for ligands that are chemically bound to the particle surface. Tronc and Jolivet demonstrated that magnetic anisotropy constant of 10 nm γ -Fe₂O₃ nanoparticles changes slightly with different surface chemical treatments such as NO₃⁻, ClO₄⁻, and SO₄²⁻,¹² while Ngo et. al. recently reported that the anisotropy constant of 3 nm cobalt ferrite nanoparticles coated with citrate did not change at all with respect to an uncoated sample. At the same time, the saturation magnetization decreased 9.3% after citrate coating.¹³ Berkowitz et. al. have compared the magnetic response of bare nanoparticles

versus those with attached ligands on ~10 nm NiFe_2O_4 and CoFe_2O_4 nanoparticles. A 20% increase in saturation magnetization was observed for bare NiFe_2O_4 nanoparticles. However, the bare particles in these studies were prepared by annealing the coated samples at 700 °C.¹⁴ Annealing treatments will not only remove the ligand and thus create bare particles, but may lead to increase in nanoparticle size, cation re-distribution, and “healing” effect of defects on the nanoparticle surface. Not surprisingly, the size of the NiFe_2O_4 nanoparticles was reported to increase from 10 nm to 14 nm after the thermal annealing.¹⁴ Therefore, as Kodoma and Berkowitz et.al. have pointed out later, annealing treatment complicated the direct correlations of magnetic properties to ligand surface effects.⁴ Overall, the effects of surface bound ligands upon the magnetic properties are not clear and the origins of such effects certainly are not understood.

To study the effects of bound surface ligands upon the magnetic properties of nanoparticles, a series of MnFe_2O_4 nanoparticles was prepared with which the nature of the surface ligands was varying systematically. MnFe_2O_4 nanoparticles prepared by reverse micelle microemulsion methods serve as a reference and aliquots of the nanoparticles from the same batch were subsequently modified with ligands, thereby reducing errors resulting from possible batch dependent variations upon shape, cation distribution, and size. The ligands chosen for the study offer selectivity in the surface binding moiety and the “body” (the part of the ligand not involved in surface binding) components. Substituted benzoic acid ligands ($\text{HOOC-C}_6\text{H}_4\text{-R}$; $\text{R} = \text{H}, \text{CH}_3, \text{Cl}, \text{NO}_2, \text{OH}$) were chosen to investigate the effects due to the electron donating or withdrawing capability from the ligands with the same surface binding group (COO^-). Certainly, the dipole moment of the ligand can be tuned through the choice of the *para* R group and in

fact such an approach has been used to tune the electronic properties of semiconductor surfaces.¹⁵ To compare the effects of the binding moiety, while maintaining a consistent “body”, substituted benzenes ($\text{Y-C}_6\text{H}_5$, $\text{Y} = \text{COOH}$, SH , NH_2 , OH , SO_3H) were investigated. This chapter reports the effects of these ligands on the magnetic properties of 4, 12, and 25 nm MnFe_2O_4 nanoparticles with emphasis on coercivity. The change on coercivity clearly correlates with the coordination chemistry features of surface bound ligands.

5.2 Experimental

MnFe_2O_4 nanoparticles were prepared by reverse micelle methods with controllable size and a size distribution less than 15%.¹⁶ Mean sizes of 4 nm, 12 nm, and 25 nm MnFe_2O_4 nanoparticles were used in this study. Benzoic acid (Aldrich, 99%), benzenesulfonic acid (Aldrich, 90%), aniline (Aldrich, 95%), phenol (Fisher, Purified Grade), benzenethiol (Aldrich, 97%), 4-chlorobenzoic acid (Aldrich, 99%), 4-hydroxybenzoic acid (Aldrich, 99%), *p*-toluic acid (Aldrich, 98%), and 4-nitrobenzoic acid (Aldrich, 98%) were used as received. Each of these ligands were chemically bound to the nanoparticle surfaces by stirring ~ 20 mg MnFe_2O_4 nanoparticles overnight in 0.1M ethanol solutions of the respective ligand. The nanoparticles were collected with a magnet and washed with ethanol 3-5 times to remove excess ligands. The samples were then allowed to air dry at room temperature.

Magnetic measurements were performed with a Quantum Design MPMS-5S SQUID magnetometer. Zero-field cooled (ZFC) susceptibility measurements were performed under an applied field of 100 G. Hysteresis measurements were performed at

5 K with applied fields up to 5 T. For the hysteresis measurements, the nanoparticles were mixed with eicosane ($C_{20}H_{42}$, Aldrich) to prevent physical shifting of the nanoparticles.

Thermogravimetric analysis (TGA) and differential scanning calorimetry (DSC) were collected from room temperature to 1000 °C at a heating rate of 17 °C /min using a Netzsch Luxx STA 409 PG. Surface photoacoustic infrared spectra were collected in the frequency range of 400 to 4000 cm^{-1} using a Biorad FTS-6000 Fourier transform infrared (FTIR) spectrometer attached with a MTEC model 300 photoacoustic (PAS) detector. Transmission electron microscopy (TEM) studies were performed on a JEOL 100C operating at 100 kV.

5.3 Results and Discussion

5.3.1 FTIR-PAS and TGA/DSC

Figure 5.1 presents a series of surface photoacoustic infrared spectra (FTIR-PAS) for 4 nm $MnFe_2O_4$ nanoparticles modified with benzoic acid and benzene derivatives ($Y-C_6H_5$; $Y=COOH$, SH , NH_2 , etc). Peaks corresponding to the characteristic stretching frequencies of the respective ligand are evident for each sample and clearly differ from the native $MnFe_2O_4$ nanoparticle reference. Figure 5.2 shows a specific example of the FTIR-PAS spectra in which the IR stretching frequencies from benzoic acid-modified $MnFe_2O_4$ nanoparticles are identified. Strong bands at 1640 cm^{-1} and 1410 cm^{-1} result from the skeleton C-C vibrations of the benzene ring and the symmetric carboxyl COO^- stretch respectively. A weak band at 1540 cm^{-1} indicates the asymmetric carboxyl COO^-

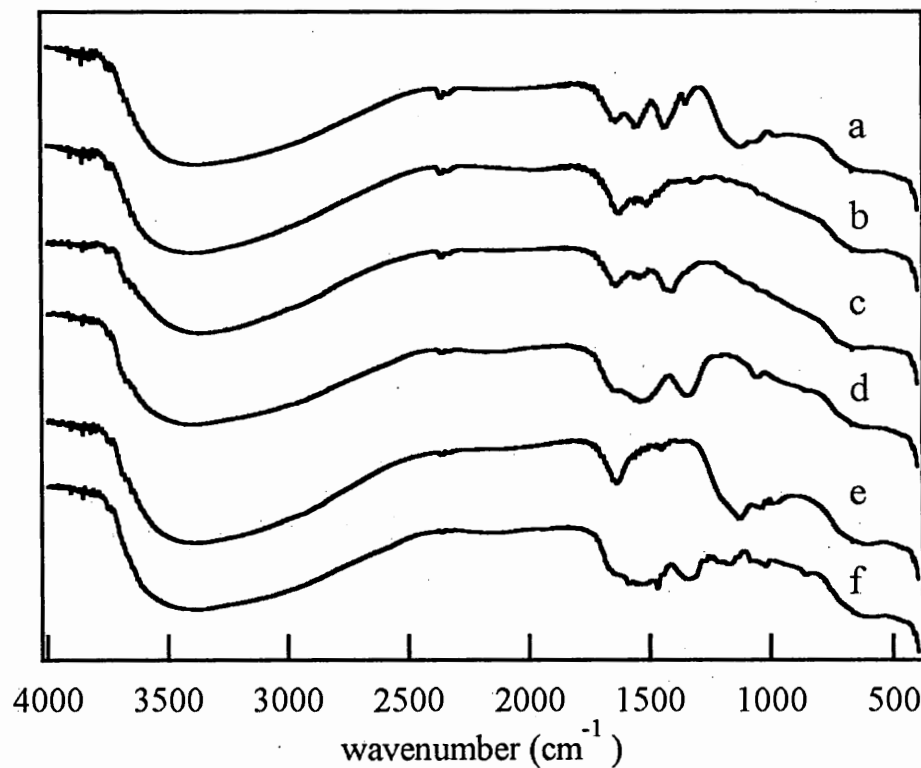


Figure 5.1 The spectra of surface Photoacoustic Infrared Spectroscopy (FTIR-PAS) for 4 nm MnFe_2O_4 nanoparticles with various ligands. The top curve is of the native 4 nm MnFe_2O_4 nanoparticles (a) followed by nanoparticles modified with aniline (b), benzoic acid (c), phenol (d), benzenesulfonic acid (e), and benzenethiol (f) respectively.

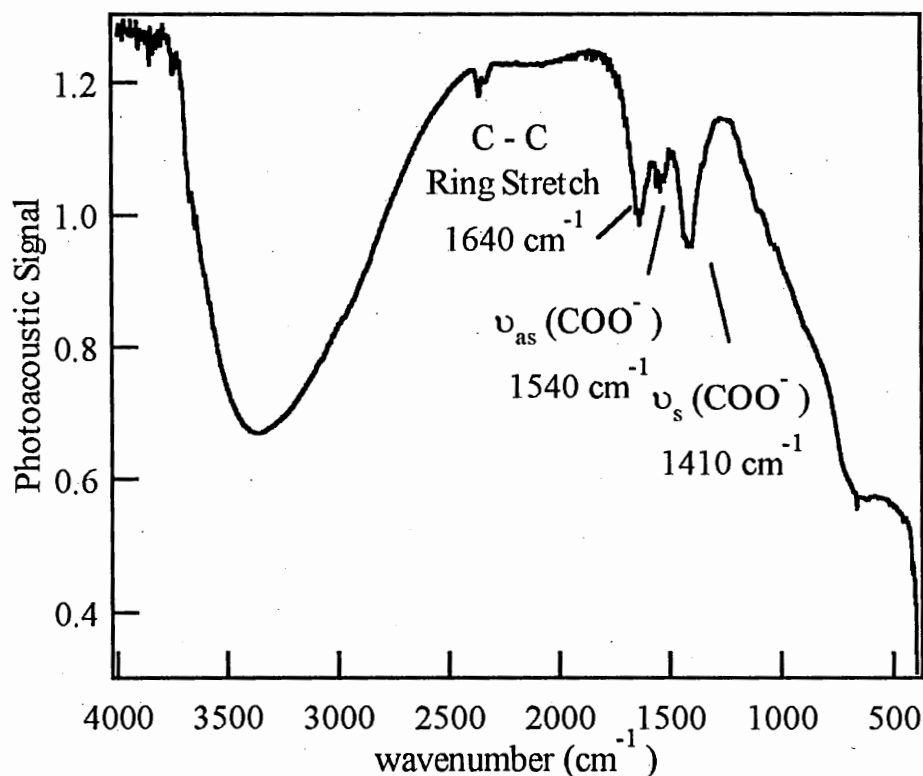


Figure 5.2 FTIR-PAS spectra of 4 nm MnFe₂O₄ nanoparticles modified with benzoic acid.

stretch. However, the C=O stretching frequency of the parent benzoic acid ligand usually at $\sim 1700\text{ cm}^{-1}$ is not observed in the spectrum. Such a disappearance of the C=O stretching band has been observed in *p*-nitrobenzoic acid adsorbed onto silver; benzoic acid, *m*-hydroxy benzoic acid, or *p*-hydroxybenzoic acid adsorbed onto stainless steel; and benzoic acid onto α -FeOOH.¹⁷⁻¹⁹ The disappearance has been suggested to result from the surface binding of the ligands through the COOH group by release of a proton. The lack of a band at 1700 cm^{-1} in our spectra of benzoic acid derivatives is thereby attributed to the benzoic acid ligand chemically bound to the nanoparticle surface through the COO⁻ functionality. Similar results of missing and/or distorted bands comparable to

literature reports for adsorbed aniline and/or benzenethiol are observed. These results indicate that the ligands indeed are chemically bound to the nanoparticle surface.²⁰⁻²¹ Comparison studies by TEM analysis before and after surface modification have shown that the nanoparticle size is not reduced, which indicates that there is no possible dissolving of surface layers during the surface modification processes.

TGA and DSC studies have been carried out for the nanoparticles modified with various ligands. Each ligand modification case gives its distinctive TGA and DSC curves, which certainly indicates that the respective ligands are truly bound onto the surface of nanoparticles in contrast with the ligands simply depositing onto the surface. As representative examples, Figure 5.3 shows the TGA and DSC curves of nanoparticles modified with benzenethiol and benzenesulfonic acid. Since the size of nanoparticles and the molecular weight of ligands are well defined, the grafting density of the ligands on nanoparticle surface can be estimated from the TGA/DSC data. Table 5.1 lists the grafting density of representative ligands determined from the TGA/DSC data. These results are in good agreement with the literature data of benzoic acid derivatives adsorbed onto micron size particles of stainless steel. For instance, the grafting density was 1.17 molecules/nm², 1.16 molecules/nm², and 1.28 molecules/nm² on 8-10 μ m stainless steel particles for benzoic acid, *m*-hydroxybenzoic acid, and *p*-hydroxybenzoic acid

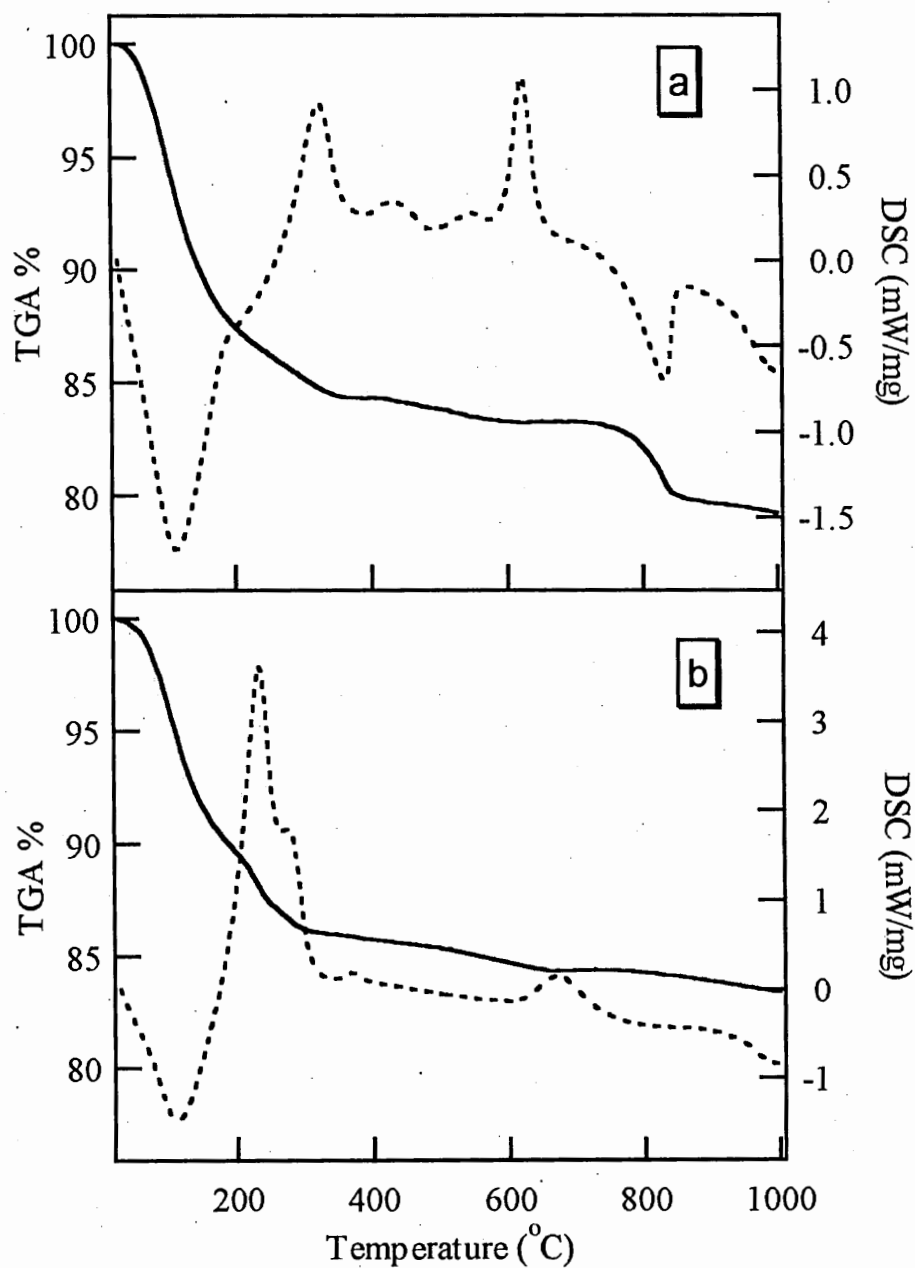


Figure 5.3 TGA (solid line) and DSC (dashed line) curves for (a) benzenesulfonic acid modified 4 nm MnFe_2O_4 nanoparticles and (b) benzenethiol modified nanoparticles.

respectively.¹⁸ Furthermore, Table 5.1 clearly shows that the grafting density on our nanoparticle surface is comparable among all the surface modification ligands that we have used. The comparable grafting density allows for meaningful comparisons among various surface-coordinating ligands. Vastly differing coverage density would represent different surface environments and therefore will introduce uncertainty to the magnetic response of nanoparticles after the surface modification.

Table 5.1. Grafting Density of Selected Ligands on Surface of MnFe₂O₄ Nanoparticles Determined from TGA/DSC Data

Ligand	Grafting Density (molecules/nm ²)
benzoic acid	1.20
<i>p</i> -toluic acid	1.39
<i>p</i> -hydroxybenzoic acid	1.40
Benzenethiol	1.29
Aniline	1.52
benzenesulfonic acid	1.26
Phenol	1.19

5.3.2 Magnetic Properties

Zero field cooled (ZFC) susceptibility measurements reveal that the blocking temperature, T_B , of the native nanoparticles and the ligand modified nanoparticles remains constant without any change beyond experimental error. However, the hysteresis measurements show unmistakable changes upon surface coordination of ligands. Figure 5.4 shows a typical hysteresis measurement at 5 K for native 4 nm MnFe_2O_4 nanoparticles and the same nanoparticles modified with benzoic acid. Upon coating with benzoic acid, the coercivity of the particles is reduced. At the same time, the addition of benzoic acid to the nanoparticle surface increases the saturation magnetization. Table 5.2 lists the benzoic acid ligands with various *para* substituents and the percentage coercivity decrease of the modified MnFe_2O_4 nanoparticles with respect to the coercivity of the native nanoparticles. The experimental error in terms of reproducibility in coercivity measurement is $\pm 2\%$. It is clear from Table 5.2 that the coercivity of nanoparticles decreases after surface coordination by modification ligands. Furthermore, the percentage coercivity decrease gets smaller as the pK_a of the ligand decreases.

The nature of the moiety bound to the surface was also found to influence the hysteresis behavior of the nanoparticles. Figure 5.5 shows an example of the hysteresis measurements, for representative ligands attached to the surface of 4 nm MnFe_2O_4 nanoparticles. Like the substituted benzoic acid ligand series, the coercivity decreased and the saturation magnetization increased upon coating with various substituted benzene ligands. Table 5.3 lists the percentage coercivity decrease with respect to the native 4 nm MnFe_2O_4 nanoparticles due to the results of attaching benzenes derivatives on surface.

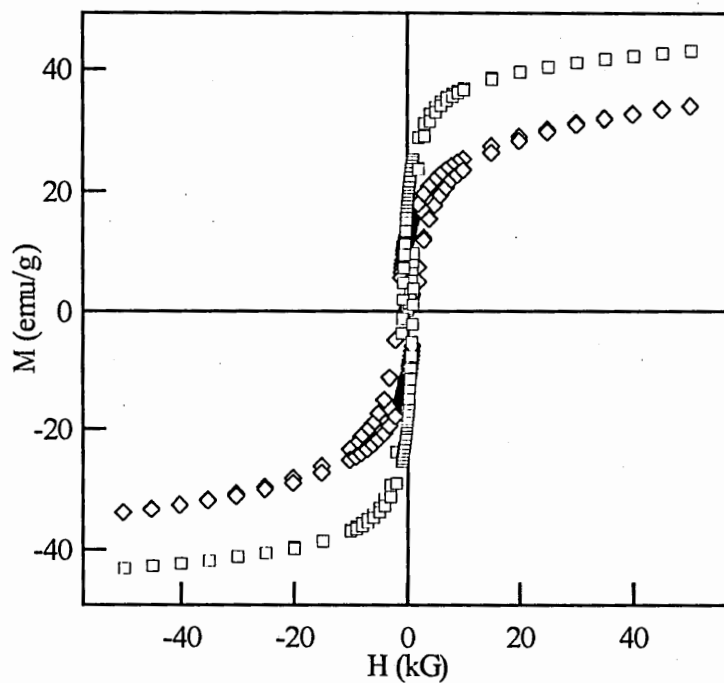
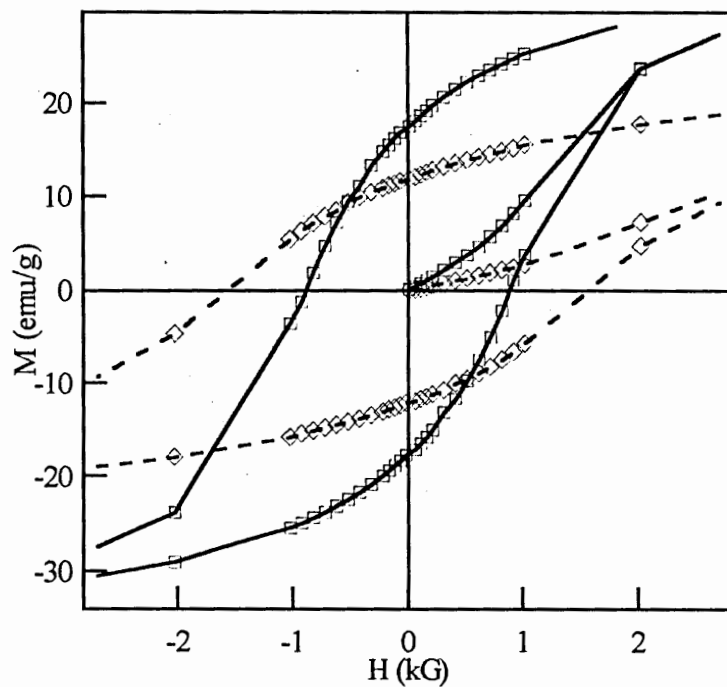


Figure 5.4. Field dependent magnetization at 5 K for native 4 nm MnFe_2O_4 nanoparticles (dashed lines; \diamond) and 4 nm MnFe_2O_4 nanoparticles modified with benzoic acid (solid line; \square).

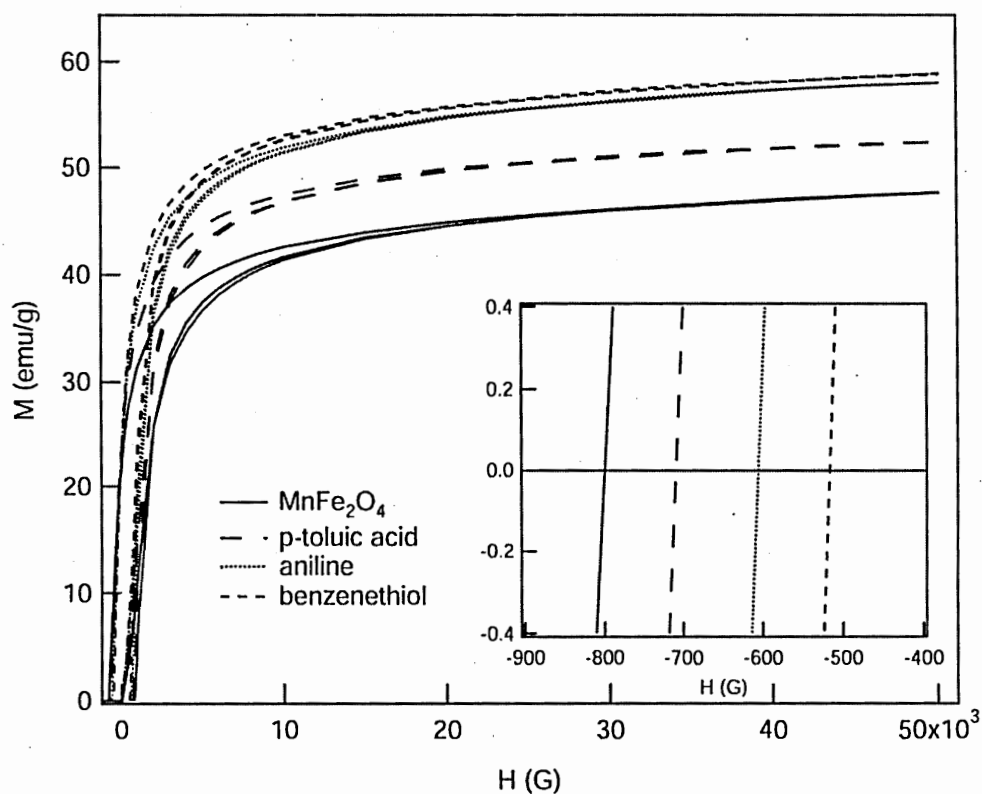


Figure 5.5 Top right quadrant hysteresis curve at 5 K for native 4 nm MnFe_2O_4 nanoparticles and 4 nm MnFe_2O_4 nanoparticles modified with representative ligands. Inset shows magnification of coercivity region. The choice of functional group bound to the surface clearly results in distinctive differences in the magnitude of the coercivity changes.

Table 5.2. Percentage Decrease in Coercivity from Surface Modification by *para* Substituted Benzoic Acid Ligands with Respect to the Native 4 nm MnFe₂O₄ Nanoparticles

Ligand	pK _a	H _C (G)	% H _C decrease
native 4nm MnFe ₂ O ₄	---	1563	---
<i>p</i> – hydroxybenzoic acid (R = OH)	4.48	808	48.3
<i>p</i> – toluic acid (R = CH ₃)	4.27	871	44.3
benzoic acid (R = H)	4.19	885	43.4
<i>p</i> – chlorobenzoic acid (R = Cl)	3.98	975	37.6
<i>P</i> – nitrobenzoic acid (R = NO ₂)	3.42	1058	32.3

Table 5.3. Percentage Decrease in Coercivity from Surface Modification by Benzene Derivatives with Respect to the Native 4 nm MnFe₂O₄ Nanoparticles

Ligand	H _C (G)	% H _C decrease
native 4 nm MnFe ₂ O ₄	1563	---
benzenethiol (Y = SH)	814	47.9
benzoic acid (Y = COOH)	885	43.4
benzenesulfonic acid (Y = SO ₃ H)	1005	35.7
aniline (Y = NH ₂)	1091	30.2
phenol (Y = OH)	1171	25.1

Similar results are observed for the hysteresis behavior of 12 and 25 nm MnFe₂O₄ nanoparticles. The influence on coercivity from representative ligands is listed in Table 5.4 for the three sizes of MnFe₂O₄ nanoparticles. Clearly, each ligand evokes a different response in the magnitude of coercivity decrease for each of the three sized nanoparticles. In addition, as the nanoparticle size increases, the percentage coercivity decrease from a particular ligand gets smaller. The magnitude of percentage coercivity decrease for the 12 nm and 25 nm MnFe₂O₄ nanoparticles coated with the benzene derivative ligand series follows the same trend as the 4 nm nanoparticles. The correlation between pK_a and percentage decrease observed for the substituted benzoic acid series in the larger sized

Table 5.4. Percentage Decrease in Coercivity of Variable Sized Modified Nanoparticles with Respect to the Corresponding Native 4, 12, and 25 nm MnFe₂O₄ Nanoparticles

Ligand	4 nm MnFe ₂ O ₄		12 nm MnFe ₂ O ₄		25 nm MnFe ₂ O ₄	
	H _C (G)	% H _C decrease	H _C (G)	% H _C decrease	H _C (G)	% H _C decrease
native MnFe ₂ O ₄	1563	---	799	---	354	---
<i>p</i> - hydroxybenzoic acid	808	48.3	678	15.2	310	12.4
<i>p</i> - toluic acid	871	44.3	690	13.6	313	11.5
benzenesulfonic acid	1005	35.7	598	25.1	301	15.0
Aniline	1091	30.2	602	24.7	314	11.3
Phenol	1171	25.1	767	4.0	345	2.5

nanoparticles is not as clear as the correlation in using 4 nm MnFe_2O_4 nanoparticles. The coercivity does decrease upon coating with these ligands; nevertheless, the percentage of coercivity decrease among all the ligands does not change as much as in smaller nanoparticles and does not clearly follow the pK_a values.

The observed decrease in coercivity of MnFe_2O_4 nanoparticles after a series of ligands are attached onto their surface is consistent with a reduction in the surface magnetic anisotropy of nanoparticles. Coercivity is certainly related to magnetocrystalline anisotropy of nanoparticles, which has been explained clearly by the Stoner-Wohlfarth model.²² In 1954, Néel introduced an additional anisotropy term, the surface anisotropy, to account for the effects of symmetry reduction at nanoparticle surfaces upon spin-orbit couplings.²³ Néel's early calculations as well as several recent theoretical studies, have pointed out that decreases in coercivity are expected if the surface anisotropy is decreased.²³⁻²⁵ Figure 5.6 is the results of theoretical calculations by Kodoma and Berkowitz for the effects of surface anisotropy upon the hysteresis of 4 nm $\gamma\text{-Fe}_2\text{O}_3$ nanoparticles. Clearly, the coercivity decreases when the surface anisotropy is reduced.

The oxygen coordination for metal cations in MnFe_2O_4 spinels is highly symmetrical in the forms of tetrahedron and octahedron. For metal cations at the surface, some coordination oxygen atoms are missing and the coordination symmetry is greatly reduced. Consequently, the magnetic structure at the surface layer could be drastically different than the one in the core of spinel nanoparticle and usually exhibits some degree of spin disorder and pinning. Qualitatively, adsorbed ligands can be viewed as effectively taking the positions of the missing oxygen atoms, which results in the

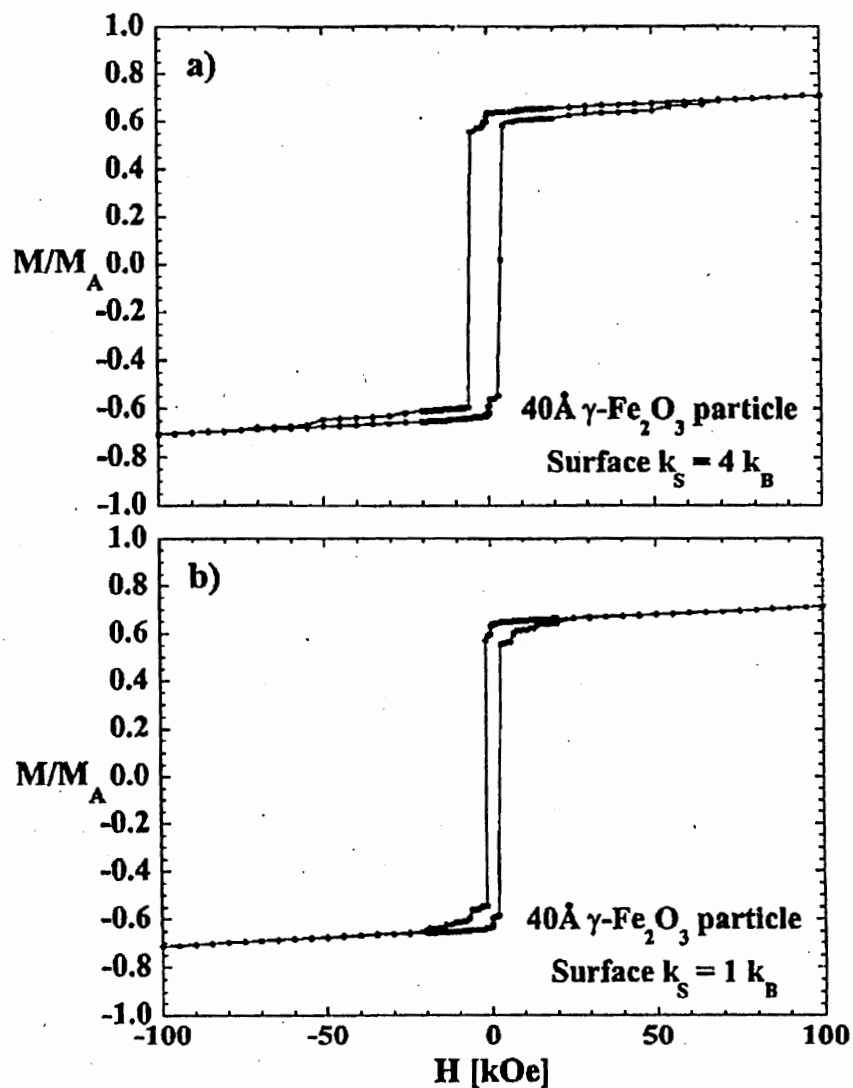
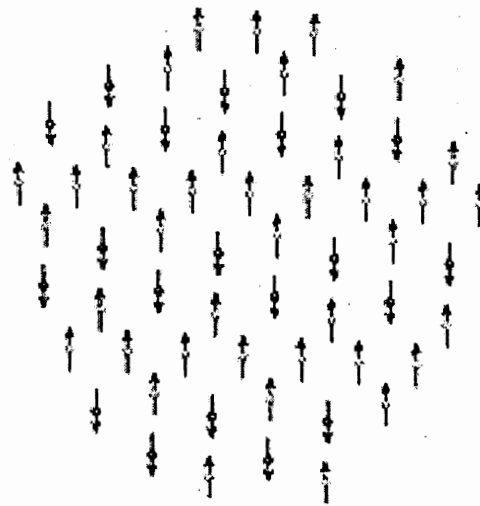


Figure 5.6 Theoretical model of surface anisotropy effects. (a) Calculated hysteresis curve for material with surface anisotropy and (b) calculated hysteresis curve for nanoparticle without surface anisotropy. From reference 25.

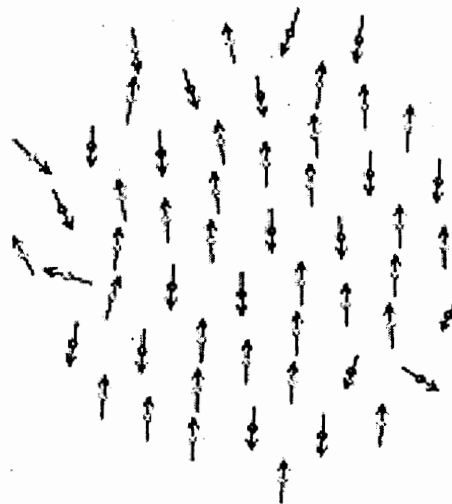
symmetry and crystal field of the surface metal ion more closely resembling that of the core, and therefore reduces the spin disorder and pinning.

The observed increase in the saturation magnetization in all of our nanoparticulate samples can also be considered in terms of reducing surface anisotropy. Surface anisotropy is often pictorially viewed in terms of the degree of spin disorder and/or spin pinning at the surface as seen in Figure 5.7. It appears that coating the surface with the ligands “frees” the surface spins, and hence they are more easily able to align with the overall magnetization direction of the nanoparticle. As a result of such increasing alignment, the magnetization of nanoparticles is observed to increase after surface modification. Contrary to our findings, Ngo, et. al. reported a decrease in saturation magnetization upon coating cobalt ferrite nanoparticles with citrate,¹³ while Spada, et. al. reported no change in saturation magnetization in polyphosphate treated $\gamma\text{-Fe}_2\text{O}_3$.⁵ The reasons for such discrepancies in the studies of saturation magnetization are not entirely clear. However, it is worth to notice the differences in the nanoparticulate samples used in these studies. Ngo, et. al. reported a change in the chemical composition of the CoFe_2O_4 nanoparticles after the surface modification, which was attributed to preferentially dissolving Co cations from the surface layer in the modification process and implied a completely different surface generated after the surface modification. In the studies by Spada, et. al., the samples were acircular with a size of ~ 23 nm by ~ 200 nm. Certainly, the surface atoms and therefore surface effects are much less dominant in the samples with such sizes.

Although inter-particle interactions contribute to the magnetic responses observed in our nanoparticles, the differences in magnetic response from various modified



(a) Ideal



(b) Real

Figure 5.7 (a) Ideal nanoparticle configuration has magnetic dipoles aligned ferrimagnetically throughout the entire particle volume (b) Surface spin disorder is present in real nanoparticle systems. From reference 25.

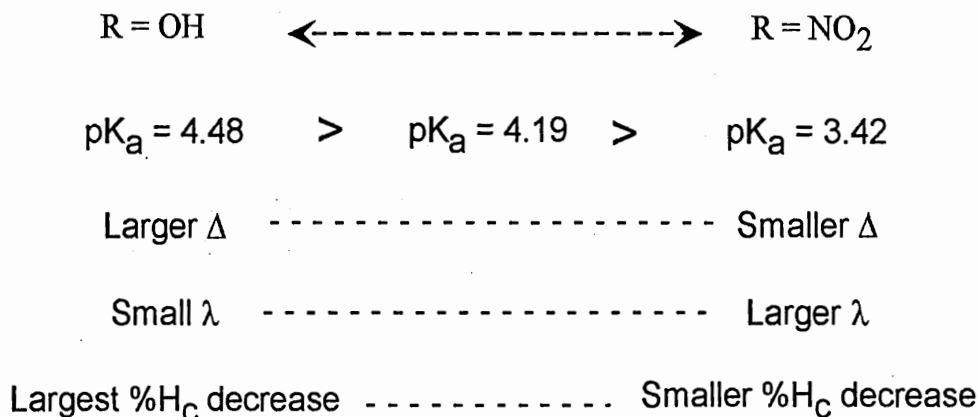
nanoparticles can not be attributed to the possible variation of inter-particle interactions because of the similar size, shape and grafting density of the ligand series chosen for this study. If the body of the ligands were allowed to vary in length, certainly inter-particle separation factors should be considered.

For both ligand series presented here, a correlation can be established between the percentage coercivity decrease of 4 nm MnFe_2O_4 nanoparticles and the crystal field splitting energy of the coordination ligands at the particle surface. When the surfaces of magnetic nanoparticles were coordinated by *para*-substituted benzoic acid ligand series (Table 5.2), the largest decrease in coercivity occurred with ligands having higher pK_a values. The great advantage of utilizing substituted benzoic acid ligands is from the existing correlation between the pK_a value of the ligand and the electron withdrawing/donating effects possessed by the R-substituent. The more electron donating the R-substituent is, the higher the pK_a value. As pK_a values increase, the substituted benzoic acid ligands become weaker acids.

Ligand field theory considers how the energy levels of d orbitals in transition metal are affected by the coordination of various ligands and the coordination symmetry. After ligand coordination, the previously degenerate d orbitals split into different levels according to the appropriate symmetry of the coordination environment. The magnitude of the energy difference between the energy levels of d orbitals is referred to as the crystal field splitting energy (CFSE) Δ and is determined by the ligands at a given coordination symmetry. Based upon ligand field theory, as a ligand becomes more basic, the strength of the metal-ligand σ bond increases, and consequently CFSE Δ associated with the ligand increases.²⁶ As the pK_a of the ligands increases in *para*-substituted

benzoic acid ligand series, the CFSE Δ induced by those ligands is expected to increase. Therefore, the trend in percentage decrease of coercivity with increasing pK_a of substituted benzoic acid ligands corresponds to the increase of CFSE Δ associated with the ligands that have coordinated onto the surface of the magnetic nanoparticles. Such correlations are depicted in Scheme 5.1.

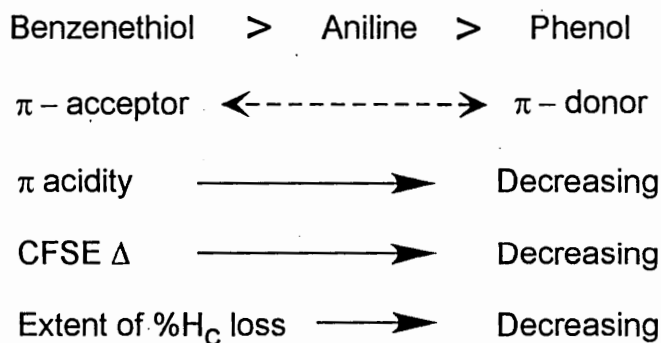
Scheme 5.1



The acidity of the coordination ligands is a major factor when different functional groups are chosen for the binding moiety onto the surface of the nanoparticles (Table 5.3). Using different binding group onto surface could be a little more complicated since different binding modes are likely present at the particle surface. For example, benzoic acid has been proposed in numerous reports to bind via chelation to surface cations.^{18-19,}

²⁷⁻²⁸ However, the non-chelating ligands of benzenethiol, aniline, and phenol offer a straight forward comparison in the CFSE Δ and the coercivity response. Benzenethiol is a strong π -acceptor, while phenol is a weak π -acceptor, but a strong π -donor.²⁹ In ligand field theory, it is well established that π -acceptors result in larger CFSE Δ than π -donors.²⁶ The CFSE decreases in the order of benzenethiol, aniline, and phenol. MnFe₂O₄ nanoparticles with benzenethiol as surface coordination ligand shows the largest coercivity decrease followed by aniline, then phenol in agreement with the decreasing CFSE Δ in these ligands. Such correlations are depicted in Scheme 5.2.

Scheme 5.2



In both coordination ligand series, the largest percentage decrease in coercivity is displayed in the nanoparticles with a surface coordinated by the ligands that evoke the biggest CFSE Δ . As ligand field theory has indicated, the transition metal having a larger d orbital energy level splitting due to ligand coordination should have a smaller spin-orbit

coupling parameter ξ , which measures the interaction strength of the spin and orbital angular momentum.²⁶ Magnetic anisotropy is generated by the spin-orbital couplings occurred at magnetic cations, and the anisotropy decreases with decreasing spin-orbital coupling.³⁰ When the metal cations at the surface layer of nanoparticles are coordinated with ligands, the spin-orbital coupling is reduced, and consequently the surface anisotropy decreases and the coercivity of nanoparticles is reduced. As the CFSE Δ resulted by the ligand gets larger, the spin-orbital coupling ξ becomes smaller. Therefore, the surface anisotropy is reduced further and the coercivity H_C becomes even less. The magnetic anisotropy in nanoparticles includes the anisotropy in the core and the surface anisotropy. The results here indicate that the blocking temperature of magnetic nanoparticles is predominately determined by the magnetic anisotropy in the core, while the surface anisotropy mainly has the effect on coercivity of nanoparticles. Certainly, the extent of the surface anisotropy effect shown here is astonishingly strong on magnetic coercivity.

The effects of percentage coercivity loss as a function of nanoparticle size (Table 5.4) are consistent with surface effects. For 4 nm nanoparticles, surface atoms make up ~50 % of the total volume of atoms and therefore contribute to the net magnetic response to a large degree. The volume fraction of atoms at the surface is reduced as nanoparticle size increases. As a result, the influence of atoms at the surface does not contribute to the total magnetic response of larger nanoparticles as strongly as to 4 nm nanoparticles. Hence for the same ligand, the coercivity does not decrease as dramatically when the size of nanoparticles is increased. The loss of a clear correlation between the pK_a of substituted benzoic acid ligands and the coercivity decrease in 12nm and 25nm

nanoparticulate samples may be attributed to the fact that the changes in surface coordination bonding evoked by changing the *para* substituent are quite subtle. At larger nanoparticle sizes, the overall surface influences are greatly weakened, and therefore these slight variations may not be observable. When the electronic nature of the binding moiety is more markedly changed, as in the case of the benzene derivatives in which the atom attached to the surface is different, the electronic effects are likely stronger and hence the variation in surface effects on the magnetic properties are still able to be observed in larger nanoparticles.

5.4 Conclusions

Three sizes of MnFe_2O_4 nanoparticles have been modified with a series of substituted benzoic acid and substituted benzene ligands. In all cases, the coercivity was found to decrease and the saturation magnetization increase upon coating with the ligand. Furthermore, a correlation between the nature of the bound surface ligand and magnetic response has been demonstrated. In both ligand series, the maximum coercive loss was found in nanoparticles modified with a surface coordination ligand that is able to evoke a larger degree of crystal field splitting energy. The extent of coercivity decrease correlates with the capability of inducing crystal field splitting energy by surface coordination ligand. Such correlations can be understood from the fact that the spin-orbit couplings of magnetic cations decrease with increasing crystal field splitting energy evoked by the coordination ligands. Certainly, the magnetic response of nanoparticles to the surface modification elucidates the quantum origins of magnetic properties such as hysteresis. Furthermore, the effects of surface coordination chemistry upon the magnetic

nanoparticles are important for the design of magnetoelectronic devices that make use of spin exchange at surfaces. The surface effects should also have impacts on the potential use of surface magnetism for tuning the magnetic properties of nanoparticles, and on the development of bioligand-modified magnetic nanoparticles for biomedical applications.

5.5 References

- (1) Gradmann, U. *J. Magn. Magn. Mater.* **1991**, *100*, 481
- (2) Kachkachi, H.; Ezzir, A.; Noguès, M.; Tronc, E. *Eur. Phys. J. B.* **2000**, *14*, 681
- (3) Gazeau, F.; Bacri, J.C.; Gendron, F.; Perzynski, R.; Raikher, Y.L.; Stepanov, V.I.; Dubois, E. *J. Magn. Magn. Mater.* **1998**, *186*, 175
- (4) Kodoma, R.H.; Berkowitz, A.E.; McNiff Jr., E.J.; Foner, S. *J. Appl. Phys.* **1997**, *81*, 5552
- (5) Spada, F.E.; Parker, F.T.; Nakakura, C.Y.; Berkowitz, A.E. *J. Magn. Magn. Mater.* **1993**, *120*, 129
- (6) Tronc, E.; Ezzir, A.; Cherkaoui, R.; Chanéac, C.; Noguès, M.; Kachkachi, H.; Fiorani, D.; Testa, A.M.; Grenèche, J.M.; Jolivet, J.P. *J. Magn. Magn. Mater.* **2000**, *221*, 63
- (7) Sugimoto, M. *J. Am. Ceram. Soc.* **1999**, *82*, 269
- (8) Mitchell, D.G. *J. Magn. Reson. Imaging.* **1997**, *7*, 1
- (9) *Scientific and Clinical Applications of Magnetic Carriers.* Häfeli, U.; Schütt, W.; Teller, J.; Zborowski, M., Eds. Plenum Press: New York, 1997
- (10) Davis, S.S.; Illum, L. *Biomaterials.* **1988**, *9*, 110
- (11) Selwood, P.W. *Chemisorption and Magnetization.* Academic Press: New York, 1975
- (12) Tronc, E.; Jolivet, J.P. *Hyperfine Inter.* **1986**, *28*, 525
- (13) Ngo, A.T.; Bonville, P.; Pileni, M.P. *Eur. Phys. J. B.* **1999**, *9*, 583
- (14) Berkowitz, A.E.; Lahut, J.A.; VanBuren, C.E. *IEEE Trans. Magn.* **1980**, *MAG-16*, 184
- (15) Ashkenasy, G.; Cahen, D.; Cohen, R.; Shanzer, A.; Vilan, A. *Acc. Chem. Res.* **2002**, *35*, 121
- (16) Liu, C.; Zou, B.; Rondinone, A.J.; Zhang, Z.J. *J. Phys. Chem. B.* **2000**, *104*, 1141
- (17) Osawa, M.; Ataka, K.; Yoshii, K.; Nishizawa, Y. *Appl. Spect.* **1993**, *47*, 1497

- (18) Suzuki, O.; Shibata, Y.; Inoue, M. *J. Colloid Interf. Sci.* **1997**, *193*, 234
- (19) Tejedor-Tejedor, M.I.; Yost, E.C.; Anderson, M.A. *Langmuir*, **1990**, *6*, 979
- (20) Tanaka, M.; Ogasawara, S. *J. Catalysis* **1972**, *25*, 111
- (21) Fauconnier, N.; Pons, J.N.; Roger, J.; Bee, A. *J. Colloid Interf. Sci.* **1997**, *194*, 427
- (22) Stoner, E.C. and Wohlfarth, E.P. *Phil. Trans. R. Soc. A.* **1948**, *240*, 599;
reprinted in *IEEE Trans. Magn.* **1991**, *27*, 3475
- (23) Néel, L. *J. Phys. Radium* **1954**, *15*, 225
- (24) Dimitrov, D.A.; Wysin, G.M. *Phys. Rev. B.* **1994**, *50*, 3077
- (25) Kodoma, R.H.; Berkowitz, A.E. *Phys. Rev. B.* **1999**, *59*, 6321
- (26) Figgis, B.N.; Hitchman, M.A. *Ligand Field Theory and Its Applications*. Wiley-VCH: New York, 2000
- (27) Evanko, C.R.; Dzombak, D.A. *J. Colloid Interf. Sci.* **1999**, *214*, 189
- (28) Fauconnier, N.; Bee, A.; Roger, J.; Pons, J.N. *J. Molecular Liq.* **1999**, *83*, 233
- (29) Huheey, J.E.; Keiter, E.A.; Keiter, R.L. *Inorganic Chemistry: Principles of Structure and Reactivity 4th Ed.* HarperCollins College Publishers: New York, 1993. p. 431
- (30) Liu, C.; Zou, B.; Rondinone, A.J.; Zhang, Z.J. *J. Am. Chem. Soc.* **2000**, *122*, 6263

CHAPTER 6

COMPARING THE EFFECTS OF SURFACE CHEMISTRY ON THE MAGNETIC PROPERTIES OF COBALT FERRITE, MAGNETITE, AND MANGANESE FERRITE NANOPARTICLES

Abstract

In order to understand the influence of surface chemistry upon the magnetic properties of magnetic nanoparticles, the surface of 4 nm cobalt ferrite (CoFe_2O_4) and 30 nm magnetite (Fe_3O_4) nanoparticles have been systematically modified with a series of substituted benzene ligands ($\text{Y-C}_6\text{H}_5$, $\text{Y} = \text{COOH}$, SH , NH_2 , OH , SO_3H). The coercivity decreased upon coating with the ligands for both particles. The maximum coercivity decrease for 4 nm CoFe_2O_4 nanoparticles was $\sim 7.5\%$, which occurred for the nanoparticle whose surface was modified with benzenethiol. Benzenethiol-modified magnetite nanoparticles also showed the largest effect upon the coercivity decrease. The effects upon the magnetic properties for cobalt ferrite and magnetite are compared to the results for manganese ferrite. The differences in magnetic response can be attributed to the magnetocrystalline anisotropy strength of the ferrite.

6.1 Introduction

Surface chemistry is of great importance to the chemical and physical properties of nanoparticles. The magnetic structure at the surface layer usually is greatly different from that in the body of nanoparticle, and the magnetic interactions in the surface layer often have a notable effect on the magnetic properties of the nanoparticle.¹⁻⁶

Understanding the influence of surface chemistry on the magnetic properties of nanoparticles not only facilitates our fundamental understanding of the unique magnetic behavior in nanoparticles, but also is important for the applications of magnetic nanoparticles such as medical imaging and drug delivery. For practical implementation in biomedical applications of nanoparticles such as magnetically guided site specific drug delivery and magnetic resonance imaging (MRI) contrast enhancement agents, the surface of the nanoparticles have to be modified with biocompatible ligands and/or polymer matrices that also serve as drug carrying vehicles.⁷⁻⁹ Once internalized, the surfaces of nanoparticles are inevitably encapsulated with biological ligands that are associated with the body's defense system.¹⁰ Understanding the changes in magnetic behavior from these chemical interactions at the surface is critical for developing magnetic nanoparticles in biomedical techniques.

Recently, Vestal and Zhang have reported a systematic study of the influence of surface chemistry upon the magnetic properties of manganese ferrite, MnFe_2O_4 , nanoparticles.¹¹ The surface of MnFe_2O_4 nanoparticles were modified with a series of *para* - substituted benzoic acid ligands ($\text{HOOC-C}_6\text{H}_4\text{-R}$; $\text{R} = \text{H, CH}_3, \text{Cl, NO}_2, \text{OH}$) and substituted benzene ligands ($\text{Y-C}_6\text{H}_5$, $\text{Y} = \text{COOH, SH, NH}_2, \text{OH, SO}_3\text{H}$). The coercivity of magnetic nanoparticles decreases up to almost 50% upon the

coordination of the ligands on the nanoparticle surface while the saturation magnetization increases. The percentage coercivity decrease of the modified nanoparticles with respect to the native nanoparticles strongly correlated with the crystal field splitting energy (CFSE) Δ evoked by the coordination ligands and the ligand inducing largest CFSE resulted in the strongest effect on the coercivity of magnetic nanoparticles. The correlations suggest a decrease in spin-orbital couplings and surface anisotropy of magnetic nanoparticles due to the surface coordination.

In this chapter, the effects of surface chemistry are investigated for other spinel ferrite nanoparticle systems. The surface of CoFe_2O_4 and Fe_3O_4 nanoparticles are modified using substituted benzene ligands ($\text{Y-C}_6\text{H}_5$, $\text{Y} = \text{COOH}$, SH , NH_2 , OH , SO_3H) and the magnetic properties, with a focus on coercivity, are investigated. The results are compared with the findings for MnFe_2O_4 .

6.2 Experimental

CoFe_2O_4 and Fe_3O_4 nanoparticles were prepared by normal micelle methods with controllable size and a size distribution less than 15%.¹² Mean sizes of 4 nm CoFe_2O_4 nanoparticles and 30 nm Fe_3O_4 nanoparticles were used in this study. Benzoic acid (Aldrich, 99%), benzenesulfonic acid (Aldrich, 90%), aniline (Aldrich, 95%), phenol (Fisher, Purified Grade), and benzenethiol (Aldrich, 97%) were used as received. Each of these ligands were chemically bound to the nanoparticle surfaces by stirring ~ 20 mg of MFe_2O_4 ($\text{M}=\text{Co}$ or Fe) ferrite nanoparticles overnight in 0.1M ethanol solutions of the respective ligand. The nanoparticles were collected with a magnet and washed with

ethanol 3-5 times to remove excess ligands. The samples were then allowed to air dry at room temperature.

Magnetic measurements were performed with a Quantum Design MPMS-5S SQUID magnetometer. Zero-field cooled (ZFC) susceptibility measurements were performed under an applied field of 100 G. Hysteresis measurements were performed at 5 K with applied fields up to 5 T. For the hysteresis measurements, the nanoparticles were mixed with eicosane ($C_{20}H_{42}$, Aldrich) to prevent physical shifting of the nanoparticles.

6.3 Results and Discussion

Figure 6.1 shows the hysteresis curves of 30 nm Fe_3O_4 before and after modification with benzenethiol. It is clear that the saturation magnetization increases

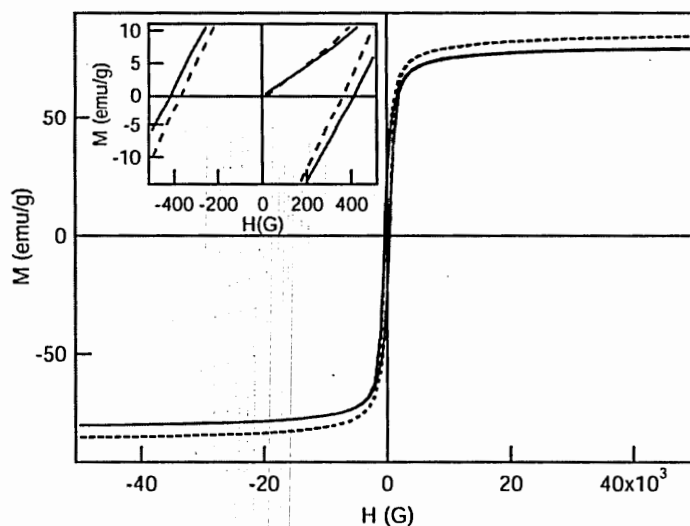


Figure 6.1 Hysteresis curve of native 30 nm Fe_3O_4 (solid line) and 30 nm Fe_3O_4 modified with benzenethiol (dashed line). Inset magnifies the coercivity regions.

and that the coercivity decreases slightly. The effect of the choice of ligand upon the coercivity of Fe_3O_4 nanoparticles is shown in Figure 6.2. For all samples the coercivity was reduced after ligand modification. The effect of the ligand upon the coercivity are summarized in Table 6.1. Figure 6.3 shows the results for 4 nm CoFe_2O_4 nanoparticles before and after coating with benzoic acid. Again the saturation magnetization increased, and the coercivity decreased slightly. The results of the effect of the ligand upon the coercivity are summarized in Table 6.2.

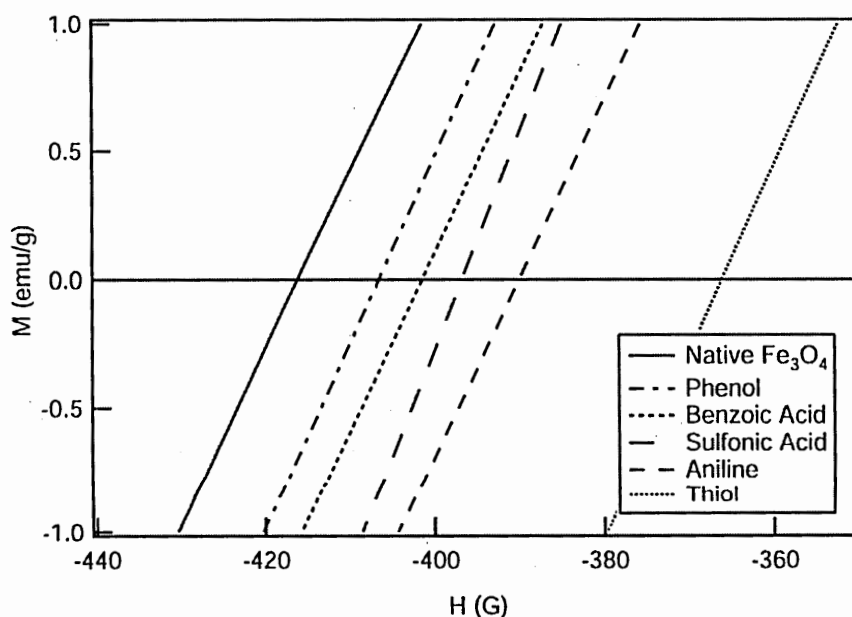


Figure 6.2 Magnification of the coercivity at 5 K for 30 nm Fe_3O_4 nanoparticles for the entire substituted benzene series.

Table 6.1 Comparison of the Effects of Ligands upon the Decrease in Coercivity with Respect to Native 30 nm Fe_3O_4 and 25 nm MnFe_2O_4 Nanoparticles.

Ligand	% H_C Decrease for 30 nm Fe_3O_4	% H_C Decrease for 25 nm MnFe_2O_4
Benzenethiol	11.3	13.0
Aniline	6.7	11.5
Benzenesulfonic acid	5.4	7.5
Benzoic Acid	3.8	12.0
Phenol	2.9	2.5

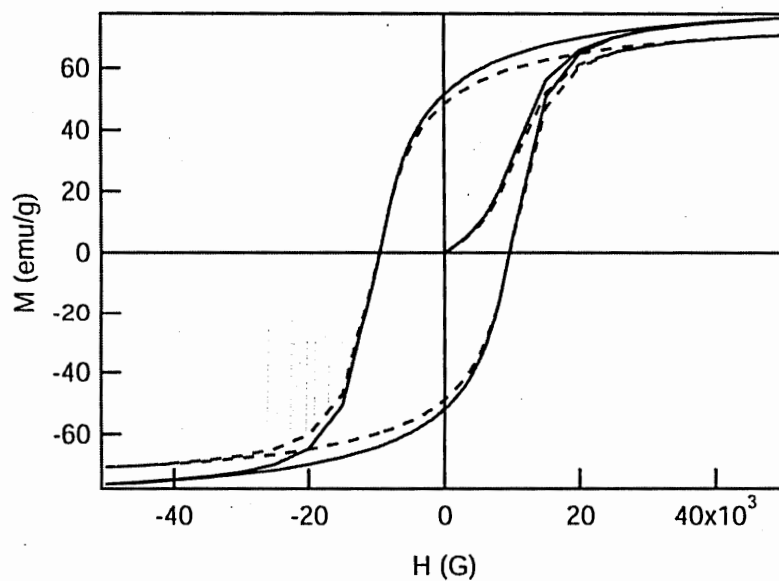


Figure 6.3 Hysteresis curves at 5 K for native 4 nm CoFe_2O_4 (dashed line) and aniline-modified 4 nm CoFe_2O_4 (solid line) nanoparticles.

Table 6.2 Comparison of the Effects of Ligands upon the Decrease in Coercivity with Respect to Native 4 nm CoFe₂O₄ and 4 nm MnFe₂O₄ Nanoparticles.

Ligand	% H _C Decrease for 4 nm CoFe ₂ O ₄	% H _C Decrease for 4 nm MnFe ₂ O ₄
Benzenethiol	7.5	47.9
Aniline	6.7	30.2
Benzoic Acid	6.4	43.4
Benzenesulfonic acid	1.2	35.7
Phenol	0.3	25.1

The observation that the saturation magnetization increased and the coercivity decreased after coating with a substituted benzene ligand agrees with results of MnFe₂O₄ nanoparticles modified with these ligands.¹¹ The observation of a decrease in the coercivity after ligand modification is consistent with a reduction in the surface anisotropy of the nanoparticles. Surface effects in nanoparticles result from the lack of translational symmetry at the boundary of the particle and a lower coordination number for the metal cations exists at the surface. The surface anisotropy is of a crystal field origin and results from this lower symmetry at the nanoparticle surface. Néel first described the origins and effects of surface anisotropy in 1954.¹³ Néel's early calculations as well as several recent theoretical studies, have pointed out that decreases in coercivity are expected if the surface anisotropy is decreased.^{4,13,14}

A further consequence of the lack of translational symmetry at the surface is the broken exchange interactions at the surface, which results in surface spin disorder. Another contribution to the surface anisotropy results from magnetostriction effects as result of strain related to lattice deformations at the surface.¹⁵ Jacobs, et.al. have shown that the surface sites of spinels are mainly the octahedral sites.¹⁶ Qualitatively, adsorbed ligands can be viewed as effectively binding to the octahedral cations, which results in the symmetry and crystal field of the surface metal ion more closely resembling the octahedral sites of the core. As a result, the surface anisotropy is reduced.

A comparison of the coercivity decrease resulting from bound ligands on 4 nm CoFe_2O_4 and 4 nm MnFe_2O_4 nanoparticles is shown in Figure 6.4 and in Table 6.2. Although the coercivity of 4 nm CoFe_2O_4 nanoparticles was reduced after modification with a ligand, the magnitude of the coercivity reduction was very small compared to the effects upon MnFe_2O_4 nanoparticles. For example, modification of 4 nm MnFe_2O_4 with benzenethiol resulted in a 47.9% decrease of the coercivity with respect to the native particle, while for 4 nm CoFe_2O_4 nanoparticles, the coercivity was reduced by only 7.5%. The response of the ligands follow a similar trend in the reduction of coercivity – benzenethiol evokes the largest decrease in coercivity, while modification with phenol yields the smallest response. However, the relationship of the response of aniline was larger for CoFe_2O_4 nanoparticles than for MnFe_2O_4 nanoparticles. In other words, the coercivity decreased as benzenethiol, aniline, benzoic acid, benzenesulfonic acid, phenol for CoFe_2O_4 nanoparticles, while it decreased as benzenethiol, benzoic acid, benzenesulfonic acid, aniline, phenol for MnFe_2O_4 nanoparticles.

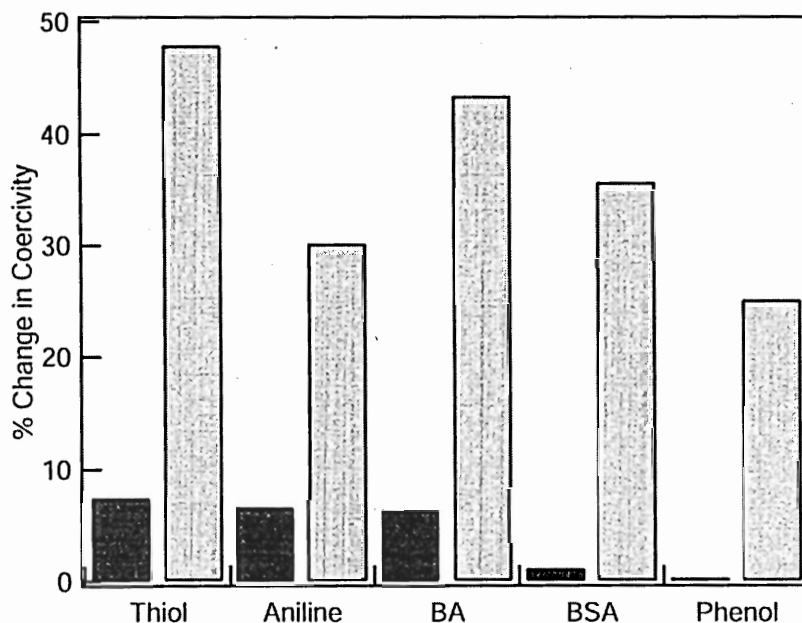


Figure 6.4. Comparison of the percentage decrease in coercivity upon ligand modification for 4 nm CoFe₂O₄ nanoparticles (dark bars) and 4 nm MnFe₂O₄ nanoparticles (light bars). BA = benzoic acid; BSA= benzenesulfonic acid.

The difference between the two spinel ferrite systems may originate from two factors. The first factor is the difference between the natures of the A²⁺ cation, such as the difference in ligand binding affinity for Co²⁺ and Mn²⁺ as well as the different single ion anisotropy of Co²⁺ and Mn²⁺. Co²⁺ atoms are known to have a much larger stability product for amines than Mn²⁺.¹⁷ This stronger affinity for the highly anisotropic Co²⁺ ion may be reflected in the larger decrease in the coercivity for aniline within the ligand series for CoFe₂O₄ than in MnFe₂O₄. The large difference in magnitude of the coercivity decrease between CoFe₂O₄ and MnFe₂O₄ for all of the

ligands could be a result of the different single ion anisotropies of Co^{2+} and Mn^{2+} . Mn^{2+} has an orbital angular momentum, L_z , equal to zero and also an L-S coupling of zero.¹⁸ Co^{2+} on the other hand has an $L_z \neq 0$ and a large single ion anisotropy. The weaker influence of the ligand crystal field upon the magnetic properties of CoFe_2O_4 may be a result of its large single ion anisotropy.

Although the single ion anisotropy of the surface ions likely play a role in the differences in the magnetic results, the primary contribution to the large difference in the coercivity response is due to the magnetocrystalline anisotropy difference between the two spinel ferrites. MnFe_2O_4 has a bulk magnetocrystalline anisotropy of 0.25×10^5 erg/cm³, while CoFe_2O_4 has a bulk magnetocrystalline anisotropy energy value of 18×10^5 erg/cm³.¹⁸ An effective anisotropy constant (K_{net}) is used to describe the additional anisotropy due to the surface for nanoparticles. For spherical particles, K_{eff} is given by

$$K_{\text{net}} = K_{\text{xtal}} + (6/d) K_S \quad (6.1)$$

where K_S is the surface anisotropy, K_{xtal} is the magnetocrystalline anisotropy, and d is the diameter of the particle. The anisotropy for 7.5 nm MnFe_2O_4 nanoparticles synthesized using reverse micelle microemulsion methods was found to be 5.6×10^5 erg/cm³ – a value 20 larger than the bulk magnetocrystalline anisotropy!!¹⁹ Using this value as a net anisotropy and the bulk magnetocrystalline anisotropy for MnFe_2O_4 , the surface anisotropy is calculated to be 0.066 erg/cm². In comparison, the net anisotropy for an 8.5 nm CoFe_2O_4 nanoparticle prepared using normal micelle microemulsion methods was determined to be 2.23×10^6 erg/cm³.²⁰ Using this value

and the bulk magnetocrystalline anisotropy for CoFe_2O_4 given above, the surface anisotropy was calculated as 0.061 erg/cm^2 . These values for the surface anisotropy are comparable with the surface anisotropy reported by Bakuzis and Morais at 100K for 6.6 nm MnFe_2O_4 nanoparticles prepared by co-precipitation of 0.053 erg/cm^2 as well as the value reported by Bødker, et.al. for 2.4 nm $\alpha\text{-Fe}$ nanoparticles of 0.09 erg/cm^2 .^{21,22} The largest surface anisotropy for magnetic nanoparticles was reported to be 1 emu/cm^2 .²¹

Because the surface anisotropy is comparable between CoFe_2O_4 and MnFe_2O_4 , any changes in the surface anisotropy as a result of coating with a ligand, will show a more pronounced effect in the MnFe_2O_4 nanoparticles due to its smaller magnetocrystalline anisotropy. For example, using equation 6.1, and assuming a complete reduction in the surface anisotropy (i.e. $K_s = 0$), the net magnetocrystalline of a 4 nm MnFe_2O_4 particle is reduced from $9.9 \times 10^5 \text{ erg/cm}^3$ (for $K_s = 0.066 \text{ erg/cm}^2$) to $0.25 \times 10^5 \text{ erg/cm}^3$ (for $K_s = 0$) – a 39.6 times decrease in the anisotropy of the nanoparticle. In contrast, for a 4 nm CoFe_2O_4 , nanoparticle, the anisotropy is reduced by only a factor of 1.5. By this argument, *any* reduction in K_s due to the ligand modification will have a larger effect upon MnFe_2O_4 nanoparticles than CoFe_2O_4 nanoparticles. As the coercivity is related to anisotropy of nanoparticles, which has been explained clearly by the Stoner-Wohlfarth model,²³ the effect of a reduction in the surface anisotropy term upon the coercivity will therefore be more pronounced for MnFe_2O_4 nanoparticles.

Comparing the response of Fe_3O_4 nanoparticles with the results found for MnFe_2O_4 tests the theory that the magnitude of the magnetocrystalline anisotropy is

primarily responsible for the coercivity response. These two ferrites have a similar magnitude of their bulk magnetocrystalline anisotropy energies, $0.25 \times 10^5 \text{ erg/cm}^3$ and $1.2 \times 10^5 \text{ erg/cm}^3$ for MnFe_2O_4 and Fe_3O_4 respectively.¹⁸ A comparison of the coercivity decrease due to ligand modification for 30 nm Fe_3O_4 and 25 nm MnFe_2O_4 nanoparticles is shown in Figure 6.5 and Table 6.1. Like MnFe_2O_4 and CoFe_2O_4 nanoparticles, the coercivity of 30 nm Fe_3O_4 nanoparticles was reduced after modification with a ligand, which is consistent with the theories of surface anisotropy. However, the magnitude of the coercivity decrease was comparable to the effects upon 25 nm MnFe_2O_4 nanoparticles within the error of measurement ($\pm 2\%$) and the slight differences in nanoparticle size and magnetocrystalline anisotropy. Modification of 25 nm MnFe_2O_4 with benzenethiol resulted in a 13.0 % decrease of the coercivity with respect to the native particle, while for 30 nm Fe_3O_4 nanoparticles, the coercivity was reduced by 11.3 %. The effect of reducing the surface anisotropy to zero following the calculations described above should result in a $\sim 7 \times$ decrease in the anisotropy for 25 MnFe_2O_4 nanoparticles, and a $\sim 2 \times$ decrease in the anisotropy for 30 nm MnFe_2O_4 nanoparticles. Therefore, the observation that the magnitude of the coercivity decrease for Fe_3O_4 nanoparticles, which is similar in magnitude yet always smaller, is consistent with the balancing effects of the magnetocrystalline anisotropy and the surface anisotropy contribution.

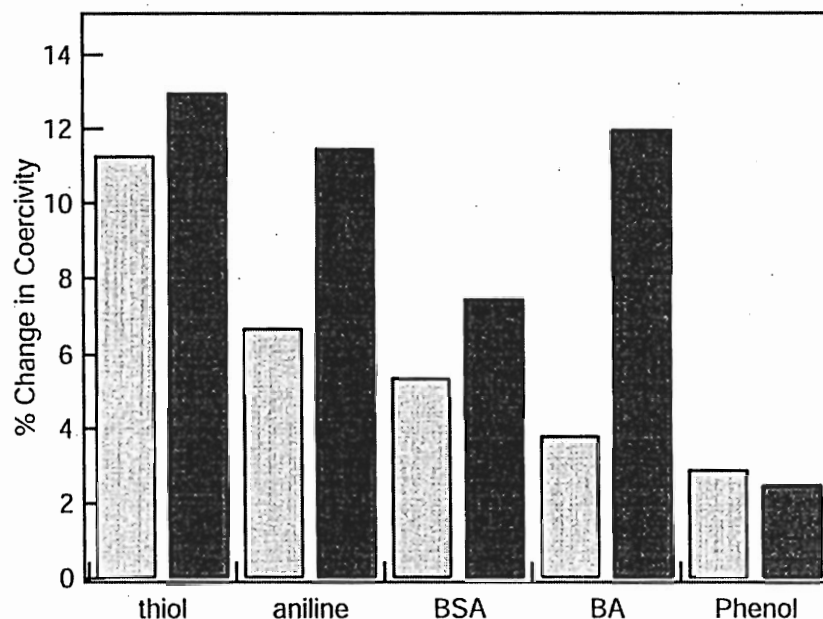


Figure 6.5. Comparison of the percentage decrease in coercivity upon ligand modification for 30 nm Fe₃O₄ nanoparticles (light bars) and 25 nm MnFe₂O₄ nanoparticles (dark bars). BA = benzoic acid; BSA= benzenesulfonic acid.

The coercivity response of the ligand series also follow a similar trend between the two ferrite systems – benzenethiol shows the largest decrease in coercivity, while modification with phenol exhibits the smallest response. However, the relationship of the response of aniline was again larger for Fe₃O₄ nanoparticles than for MnFe₂O₄ nanoparticles. The coercivity decreased as benzenethiol, aniline, benzenesulfonic acid, benzoic acid, phenol for Fe₃O₄ nanoparticles, while it decreased as benzenethiol, benzoic acid, aniline, benzenesulfonic acid, phenol for MnFe₂O₄ nanoparticles. Like CoFe₂O₄, the difference can likely be attributed to the higher affinity of amines for Fe²⁺ ions than Mn²⁺ ions.¹⁷

6.4 Conclusions

The surface of 4 nm CoFe_2O_4 nanoparticles and 30 nm Fe_3O_4 nanoparticles have been modified with a series of substituted benzene ligands ($\text{Y-C}_6\text{H}_5$, $\text{Y} = \text{COOH}, \text{SH}, \text{NH}_2, \text{OH}, \text{SO}_3\text{H}$) and their hysteresis curves measured. For both ferrite nanoparticle systems, the coercivity decreased after coating with a ligand, a finding consistent with previous reports for 4, 12 and 25 nm MnFe_2O_4 nanoparticles. The decrease in coercivity can be attributed to a reduction in the surface anisotropy of the nanoparticles in agreement with theory. The magnitude of the coercivity response was quite different for 4 nm CoFe_2O_4 and 4 nm MnFe_2O_4 nanoparticles, while the magnitude of the coercivity reduction was similar for 30 nm Fe_3O_4 and 25 nm MnFe_2O_4 nanoparticles. The difference in magnetic behavior can be attributed to the larger contribution of the bulk magnetocrystalline anisotropy of CoFe_2O_4 to the net anisotropy of the nanoparticles.

6.5 References

- (1) Gradmann, U. *J. Magn. Magn. Mater.* **1991**, *100*, 481.
- (2) Kachkachi, H.; Ezzir, A.; Nogues, M.; Tronc, E. *Eur. Phys. J. B* **2000**, *14*, 681.
- (3) Gazeau, F.; Bacri, J. C.; Gendron, F.; Perzynski, R.; Raikher, Y. L.; Stepanov, V. I.; Dubois, E. *J. Magn. Magn. Mater.* **1998**, *186*, 175.
- (4) Kodoma, R. H. *J. Magn. Magn. Mater.* **1999**, *200*, 359.
- (5) Spada, F. E.; Parker, F. T.; Nakakura, C. Y.; Berkowitz, A. E. *J. Magn. Magn. Mater.* **1993**, *120*, 129.
- (6) Tronc, E.; Ezzir, A.; Cherkaoui, R.; Chanéac, C.; Noguès, M.; Kachkachi, H.; Fiorani, D.; Testa, A. M.; Grenèche, J. M.; Jolivet, J. P. *J. Magn. Magn. Mater.* **2000**, *221*, 63.
- (7) Häfeli, U.; Schütt, W.; Teller, J.; Zborowski, M., Eds. *Scientific and Clinical Applications of Magnetic Carriers*; Plenum: New York, 1997.
- (8) Kim, D. K.; Zhang, Y.; Kehr, J.; Klason, T.; Bjelke, B.; Muhammed, M. *J. Magn. Magn. Mater.* **2001**, *225*, 256.
- (9) Berry, C. C.; Curtis, A. S. G. *J. Phys. D.: Appl. Phys.* **2003**, *36*, R198.
- (10) Davis, S. S.; Illum, L. *Biomaterials* **1988**, *9*, 110.
- (11) Vestal, C. R.; Zhang, Z. J. *J. Am. Chem. Soc.* **2003**, *125*, 9828.
- (12) Vestal, C. R.; Zhang, Z. J. *Int. J. Nanotech.* **2004**, *1*, 240.
- (13) Néel, L. *J. Phys. Radium* **1954**, *15*, 225.
- (14) Dimitrov, D. A.; Wysin, G. M. *Phys. Rev. B* **1994**, *50*, 3077.

- (15) Battle, X.; Labarta, A. *J. Phys. D.: Appl. Phys.* **2002**, *35*, R15.
- (16) Jacobs, J. P.; Maltha, A.; Reintjes, J. R. H.; Drimal, T.; Ponec, V.; Brongersma, H. H. *J. Catal.* **1994**, *147*, 294.
- (17) Sillen, L. G.; Martell, A. E. *Stability Constants of Metal-Ion Complexes*; The Chemical Society: London, 1964.
- (18) O'Handley, R. C. *Modern Magnetic Materials: Principles and Applications*; John Wiley & Sons, Inc: New York, 2000.
- (19) Rondinone, A. J.; Liu, C.; Zhang, Z. J. *J. Phys. Chem. B* **2001**, *105*, 7967.
- (20) Rondinone, A. J.; Samia, A. C. S.; Zhang, Z. J. *Appl. Phys. Lett.* **2000**, *76*, 3624.
- (21) Bakuzis, A. F.; Morais, P. C. *J. Magn. Magn. Mater.* **2001**, *226-230*, 1924.
- (22) Bødker, F.; Mørup, S.; Linderøth, S. *Phys. Rev. Letter* **1994**, *72*, 282.
- (23) Stoner, E. C.; Wohlfarth, E. P. *Phil. Trans. Royal Soc. A* **1948**, *240*, 599.

CHAPTER 7

EFFECTS OF INTERPARTICLE INTERACTIONS UPON THE MAGNETIC PROPERTIES OF COBALT FERRITE AND MANGANESE FERRITE

Abstract

Dilution experiments have been performed on 8.5 nm CoFe_2O_4 and MnFe_2O_4 spinel ferrite nanoparticles dispersed into eicosane. For both samples, the blocking temperature decreased with dilution, suggesting a decrease in the anisotropy energy barrier E_A . The blocking temperature for MnFe_2O_4 nanoparticles decreased continuously over the whole dilution range. However, the blocking temperature for CoFe_2O_4 remained constant until ~15% (wt%) below which the blocking temperature decreased. The reduced remanence (M_R/M_S) decreased with interparticle interactions for MnFe_2O_4 , while it increased for CoFe_2O_4 . The differences in magnetic response upon dilution between the two samples are attributed to the strength of the dipole interactions. The behavior of CoFe_2O_4 nanoparticle system is suggested to arise from the formation of nanoparticle clusters.

7.1 Introduction

Interest in nanosized magnetic particles has increased in the past few years due to their wide range of applications such as high density information storage, ferrofluid technology, magnetically guided drug delivery, and magnetic resonance imaging (MRI) enhancement.¹⁻⁶ Improving such applications requires control over the fundamental properties of the nanoparticles, such as superparamagnetism. The superparamagnetic state occurs when the anisotropy energy E_A of the nanoparticles is overcome thermally. This energy has been defined by Stoner and Wohlfarth as

$$E_A = KV \sin^2 \theta \quad (7.1)$$

where K is the anisotropy energy constant, V is the volume of the nanoparticle, and θ is the angle between the magnetization and the nanoparticles easy axis.⁷ The blocking temperature, T_B , represents the threshold of thermal activation and can be used as an indication of the superparamagnetic state. At temperatures above T_B the magnetic moment of each nanoparticle fluctuates with no preferred orientation and the assembly of nanoparticles behaves as a common paramagnetic material. Previous work by the Zhang group has established that modulating K through the use of crystal chemistry can control the energy barrier, E_A .⁸ Examples of the effects of size and magnetocrystalline anisotropy K upon the magnetic properties have been demonstrated in Chapter 3 using $\text{CoCr}_x\text{Fe}_{2-x}\text{O}_4$ spinel ferrite nanoparticles. In addition to crystalline anisotropy, other factors contribute to the observed magnetic properties of nanoparticles. For example, Chapters 5 & 6 demonstrate the effect of surface chemistry upon the magnetic properties

of various spinel ferrite nanoparticles. In the powder nanoparticle samples reported in this thesis, particle-particle interactions are likely to be present and contribute to the net magnetic properties.

Interparticle interactions are known to affect the magnetic properties of materials and may arise from dipole-dipole interactions or exchange interactions between surface ions of neighboring particles. When a capping surfactant such as oleic acid is used, the exchange interactions become negligible and the primary interaction is due to dipole-dipole coupling.⁹ The energy associated with dipole-dipole interactions (E_{d-d}) given by

$$E_{d-d} = - (\mu_0 m_o^2) / (4\pi l^3) \quad (7.2)$$

where μ_0 is the permeability, m_o is the magnetic moment, and l is the particle-particle separation. The dipole-dipole energy term modifies the anisotropy energy barrier for magnetization reversal E_A and is argued to introduce local minima in the energy barrier.¹⁰ Although it is generally understood that particle-particle interactions affect the magnetic properties of nanoparticles, correlating the effects of interparticle interactions with observed magnetic properties has still provided a challenge.

Three primary theoretical models have been developed to model the effects of interparticle interactions upon the magnetic properties of magnetic nanoparticles – the Shtrikman-Wohlfarth (SW) model developed in 1981, the Dormann-Bessais-Fiorani (DBF) model developed in 1998, and the Mørup-Tronc model developed in 1994. Both the SW and DBF models show that increasing interparticle interactions will lead to an increase in the energy barrier, E_A by

$$E_A = KV \sin^2\theta + B_i \quad (7.3)$$

where B_i is the interaction term, whose form varies according to the respective model and their subsequent revisions. The MT model however, indicates that increased interparticle interactions should decrease the energy barrier. Considerable argument between the authors of these models as to the validity of their conclusions are present in the literature.^{11,12}

Experimentally, the effects of interparticle interactions are determined by varying the particle-particle distance through dilution of ferrofluid samples or dispersion of nanoparticles into a non-magnetic matrix. Most studies show that the blocking temperature and coercivity decrease with dilution, i.e. weaker interparticle interactions. These findings collaborate the SW and DBF models that increased interparticle interactions results in an increase of the energy barrier for magnetization reversal. However, other experimental results show mixed results. For example, SQUID relaxation measurements show that τ (see equation 1.11) increases with increasing interactions, which also further supports the SW and DBF models. However, Mössbauer studies indicate that τ decreases with increasing interactions and these studies are cited as support for the MT model. A summary of the magnetic behavior of many magnetic samples as a function of increasing interparticle interactions is summarized in Table 7.1. Clearly there are discrepancies in the magnetization trends even for materials with the same composition! In this chapter, dilution measurements were performed on 8.5 nm CoFe_2O_4 and MnFe_2O_4 spinel ferrite nanoparticles. The effect of interparticle

Table 7.1 Effects of Increased Interparticle Interactions upon the Blocking Temperature T_B , Néel's Relaxation Time τ , the Coercivity H_C and the Reduced Remnance M_R/M_S for a Variety of Magnetic Samples.

Sample	T_B	τ	H_C	M_R/M_S	Ref.
$\gamma\text{-Fe}_2\text{O}_3$	Increases				11
$\gamma\text{-Fe}_2\text{O}_3$ in hydrocarbon oil	Increases				11
$\gamma\text{-Fe}_2\text{O}_3$ in silica	Constant		Increases	Decreases	13
$\gamma\text{-Fe}_2\text{O}_3$	Decreases				14
Fe_3O_4	Increases	Increases			11
Fe_3O_4	Increases				15
Fe_3O_4 (ac susceptibility)		Increases			16
Fe_3O_4 (Mössbauer)		Decreases			16
Fe_3O_4 in kerosene	Increases				17
Fe	Increases				14
$\epsilon\text{-Fe}_3\text{N}$	Increases				11
Co				Decreases	9

interactions upon these ferrite samples has not previously been reported. Specifically, the effect of interparticle interaction upon the blocking temperature and the reduced remanence is discussed.

7.2 Experimental

CoFe_2O_4 and MnFe_2O_4 spinel ferrite nanoparticles with size 8.5 nm were prepared by the thermal decomposition of metal-acetylacetonate complexes. Details of this synthesis method have been reported elsewhere.^{18,19} Advantages of this preparation method include a very narrow size distribution (< 5%) and an oleic acid coated surface. The capping of the nanocrystals by oleic acid facilitated their dispersion into eicosane $[\text{CH}_3(\text{CH}_2)_{18}\text{CH}_3]$ as well as eliminated exchange interactions between particles. The nanocrystalline samples used in this chapter were synthesized and provided by Qing Song. For the dilution measurements known amounts of eicosane were added to measured amounts of ferrite nanoparticles. The eicosane and nanocrystals were heated to 100°C, thereby melting the eicosane and allowing the ferrite nanocrystals to disperse into the liquid. The samples were then allowed to cool forming a solid eicosane matrix containing dispersed ferrite nanocrystals. Dilutions were performed down to 0.005 % (wt % of MFe_2O_4 in eicosane).

Magnetic measurements were performed on a Quantum Design MPMS-5S SQUID magnetometer. Hysteresis measurements were performed at 5K in applied field up to \pm 5T. Susceptibility measurements were performed from 5 – 300K under an applied field of 100G.

7.3 Results

The temperature dependent susceptibility measurements for 8.5 nm CoFe_2O_4 nanoparticles are shown in Figure 7.1. It is clear that the value of the susceptibility decreases with increasing dilution. A slight shift in the blocking temperature towards lower temperatures occurs with increasing nanoparticle dilution. The value of blocking temperature is plotted against dilution percentage in Figure 7.2. The blocking temperature remained at 236 ± 1 K down to a dilution of 15%. Below 15% dilution, the blocking temperature began to decrease and at 0.005 % reached 224 K. The effect of dilution upon the reduced remanence (M_R/M_S), which was determined from the hysteresis

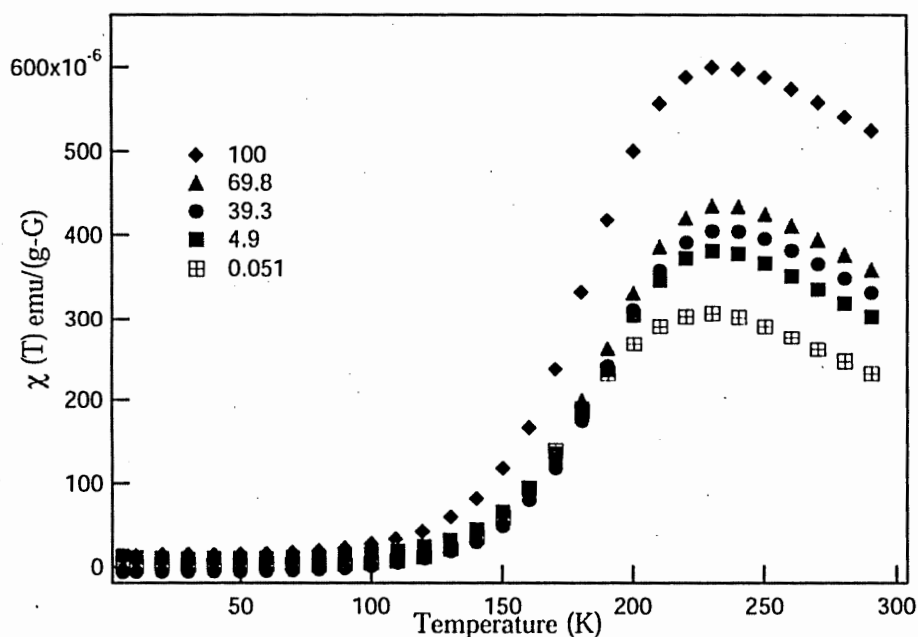


Figure 7.1 Temperature dependent susceptibility measurements for various dilutions from 100% to 0.05% (wt%) of 8.5 nm CoFe_2O_4 nanoparticles.

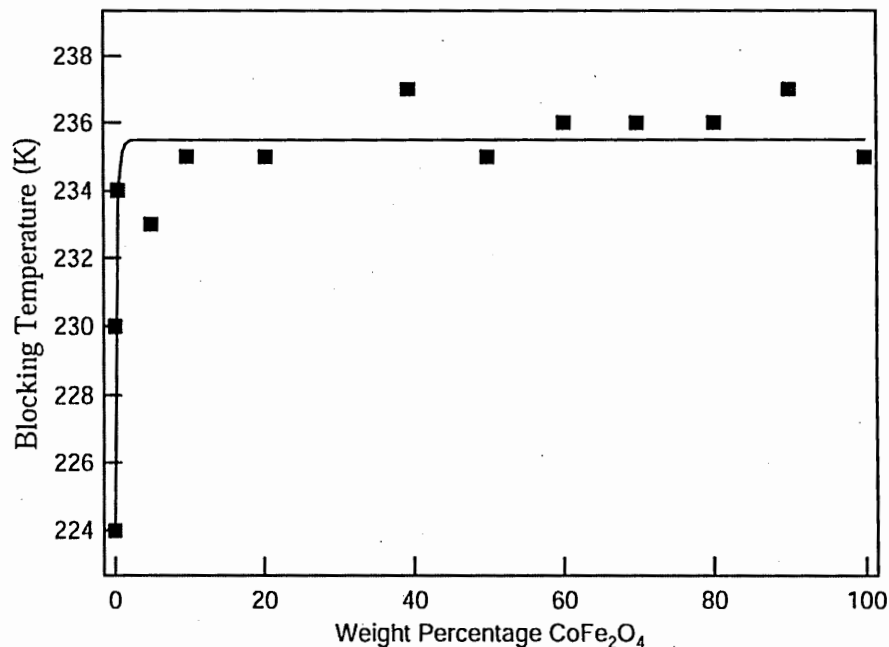


Figure 7.2. Plot of blocking temperature T_B as a function of dilution percentage for 8.5 nm CoFe_2O_4 nanoparticles. The line serves only to guide the eye.

measurements performed at 5 K, is shown in Figure 7.3. It is clear that the reduced remanence decreases with dilution.

The temperature dependent susceptibility for 8.5 nm MnFe_2O_4 samples is shown in Figure 7.4. Interestingly, the magnitude of the susceptibility varies with dilution percentage. The susceptibility initially increases with dilution, but then begins to *decrease* below 40% dilution! Despite the difference in the value of the susceptibility, the blocking temperature shifts to lower temperatures with increasing dilutions over the entire dilution range. Figure 7.5 shows that the blocking temperature as a function of dilution decreasing smoothly. The effect of dilution upon the reduced remanence (M_R/M_S) determined from hysteresis measurements at 5 K is shown in Figure 7.6. It is clear that the reduced remanence increases with dilution.

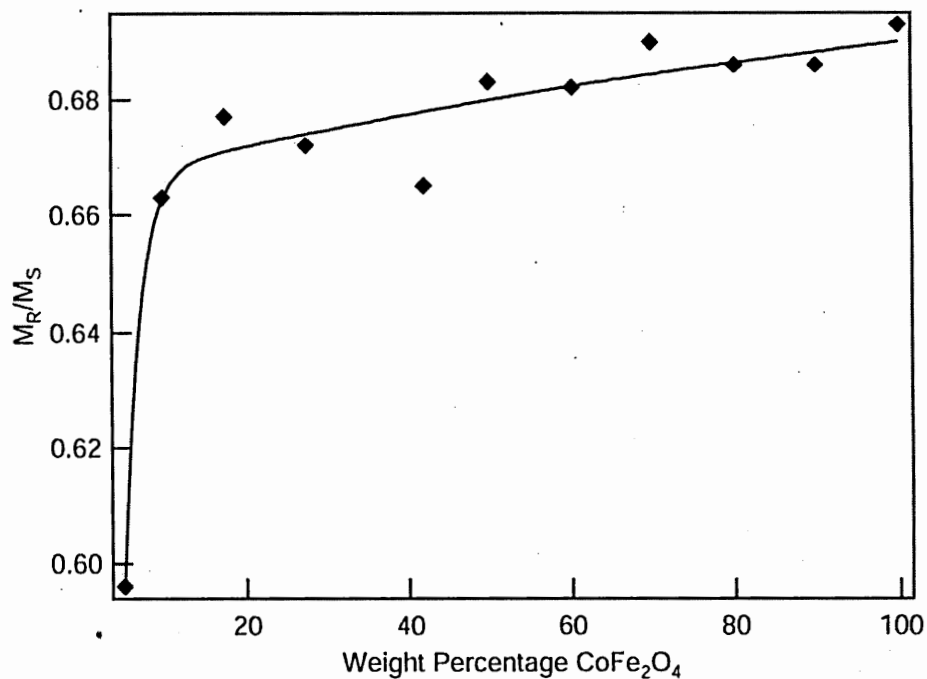


Figure 7.3 Plot of reduced remnance M_R/M_S as a function of dilution percentage for 8.5 nm CoFe_2O_4 nanoparticles. The line serves only to guide the eye.

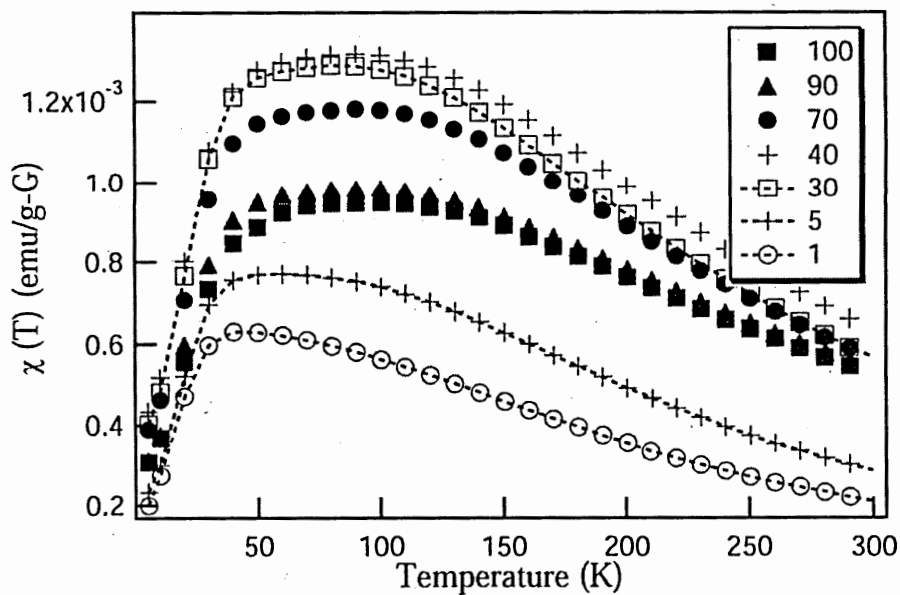


Figure 7.4. Temperature dependent susceptibility measurements for various dilutions of 8.5 nm MnFe_2O_4 nanoparticles

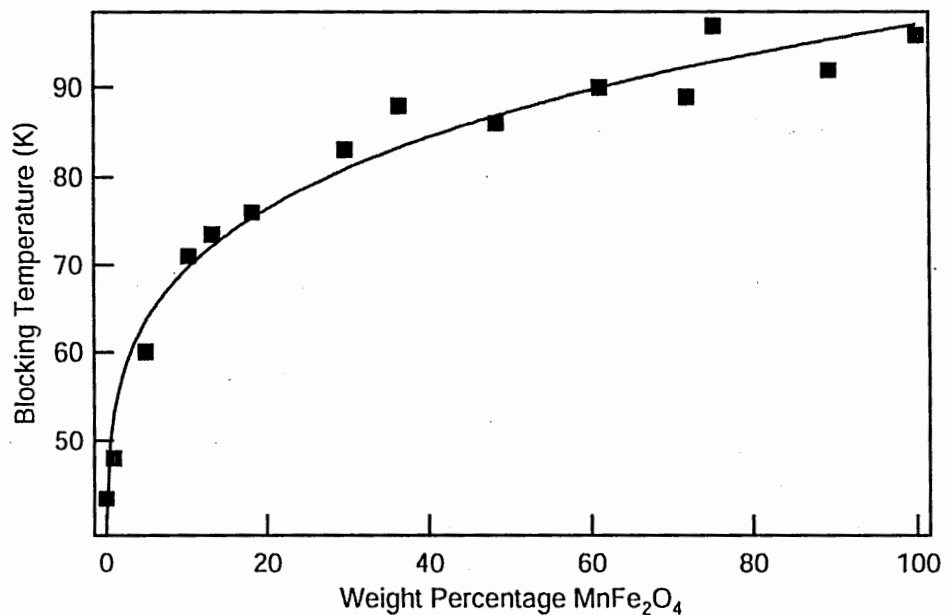


Figure 7.5. Effect of dilution upon the blocking temperature of 8.5 nm MnFe₂O₄ nanoparticles. The line serves only to guide the eye.

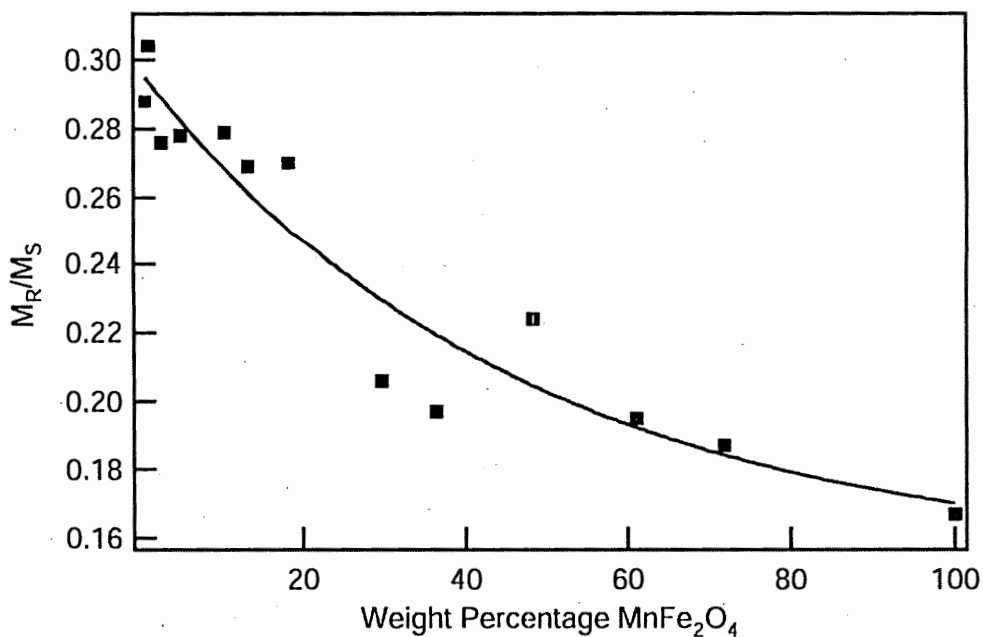


Figure 7.6. Effect of dilution upon the reduced remanence M_R/M_S of 8.5 nm MnFe₂O₄ nanoparticles. The line serves only to guide the eye.

7.4 Discussion

Changing the particle-particle interaction of CoFe_2O_4 and MnFe_2O_4 by dilution into eicosane affects the magnetic properties of the two samples quite differently. One similarity between the two samples is the fact that their blocking temperature decreases with dilution. A decrease in the blocking temperature suggests that the energy barrier for magnetization reversal E_A is lowered with decreasing interparticle interactions. These results are consistent with the Shtrikman-Wohlfarth (SW) and the Dormann-Bessais-Fiorani (DBF) models for interparticle interactions given in equation 7.3.¹¹ As a result, all data interpretation and discussions from this point forward will be based upon calculations by Dormann, et.al.

One difference between the $\chi(T)$ dilution measurements of CoFe_2O_4 and MnFe_2O_4 is the dependence of the blocking temperature “decay” with dilution percentage. Figure 7.7 overlays the blocking temperature data for the two samples. For CoFe_2O_4 nanoparticles, there is no change within experimental error in the blocking temperature, until ~15% dilution, while the blocking temperature for MnFe_2O_4 nanoparticles continuously decreases over the entire dilution range. The difference in the blocking temperature decay behavior with dilution for CoFe_2O_4 and MnFe_2O_4 nanoparticles can be understood in terms of their interaction strengths. The gradual decrease in T_B for MnFe_2O_4 nanoparticles is comparable to previous reports on Fe_3O_4 nanoparticles.¹⁵ Both of these materials have similar magnitude of their magnetocrystalline anisotropy energies, $0.25 \times 10^5 \text{ erg/cm}^3$ and $1.2 \times 10^5 \text{ erg/cm}^3$ respectively. CoFe_2O_4 on the other hand has a magnetocrystalline anisotropy energy value of $18 \times 10^5 \text{ erg/cm}^3$. MnFe_2O_4 and Fe_3O_4 nanoparticles behave as weakly

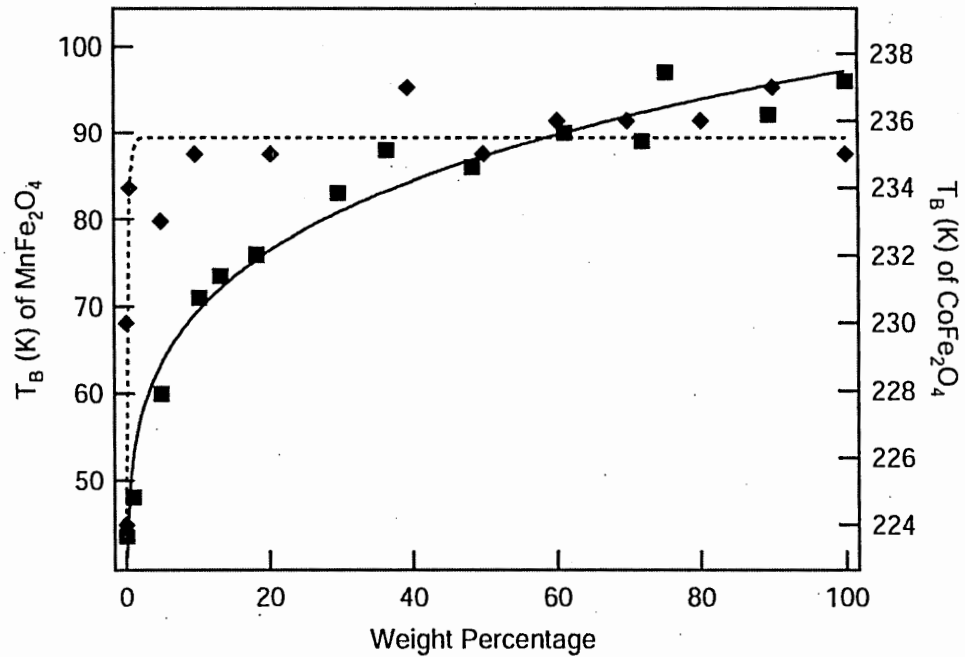


Figure 7.7. Comparison of dilution effects upon the blocking temperature for 8.5 nm MnFe_2O_4 (■, solid line) and 8.5 nm MnFe_2O_4 (◆, dashed line).

interacting systems; while CoFe_2O_4 nanoparticles are strongly interacting systems.

Dormann et.al. has described the effect of dipolar interaction strength upon magnetic properties for weakly and strongly coupled systems. The change in the energy barrier E_A for weakly interacting systems is given by¹⁵

$$E_A = KV + \frac{\langle n_1 \rangle M_s^4 V^4 \langle (3 \cos^2 \psi_1 - 1)^2 \rangle}{3k \langle d_1^6 \rangle} \quad (7.3)$$

where $\langle n_1 \rangle$ is the average number of next nearest neighbors, ψ_1 is the location of a first neighbor particle and d_1 is the average interparticle separation. Using this expression, the blocking temperature of a system of weakly interacting particles is then given by¹⁵

$$\langle T_B \rangle = \frac{\langle T_B \rangle}{2} + \frac{\langle T_B \rangle}{2} \sqrt{1 + \frac{4\xi_1 M_S^4 \ln(\tau_m \tau_o^{-1})}{3K}} \quad (7.4)$$

where ξ_1 is $\langle n_1 \rangle V^2 < (3 \cos^2 \psi_1 - 1)^2 \rangle / \langle d_1^6 \rangle$ and $\tau_m \tau_o^{-1}$ have been defined from the Néel equation (1.11). The non-interacting case is for $\xi_1 \rightarrow 0$. The blocking temperature for strongly coupled systems, such as CoFe_2O_4 nanoparticles, is given by¹⁵

$$\langle T_B \rangle = \frac{\left[\langle T_B \rangle + \frac{\langle n_1 \rangle M_S^2 V^2}{k \ln(\tau_m \tau_o^{-1})} < (3 \cos^2 \psi_1 - 1) \rangle \frac{1}{\langle d_1^3 \rangle} \right]}{\left[1 + \frac{\langle n_1 \rangle}{\ln(\tau_m \tau_o^{-1})} \right]} \quad (7.5)$$

The difference between the models is that the value of the blocking temperature at a given separation is different for weakly interacting versus strongly interacting systems. The “decay” behavior of the blocking temperature with increased interparticle separation d , however, is consistent between these two models.

An important feature of strongly interacting systems is that the majority of particles form clusters. Therefore two types of interactions are present – particle-particle interactions and cluster-cluster interactions.^{15,20} For highly concentrated samples cluster-cluster interactions are dominant and the blocking temperature is determined by the collective cluster behavior. The decay of the blocking temperature with separation for MnFe_2O_4 closely resembles that expected from equation 7.4. Because the blocking temperature of CoFe_2O_4 nanoparticles do not display the same fall off/decay behavior as

would be expected from equations 7.4 and 7.5 the difference is likely due to the presence of clusters of nanoparticles. As a result even upon dilution, interactions are present within the clusters and the blocking temperature remains $\sim 236\text{K}$. Below 15% dilution, the system may be dilute enough that the interparticle interaction effects are finally observable.

Another unique difference between the magnetic responses of the CoFe_2O_4 and MnFe_2O_4 is their reduced remanence trend. The reduced remanence for CoFe_2O_4 decreases with dilution (see Figure 7.3), while the reduced remanence for MnFe_2O_4 increases with dilution (see Figure 7.6). The value of M_R/M_S depends upon the symmetry of the easy axis and the orientation of the easy axis with respect to the applied magnetic field. For a particle with randomly oriented uniaxial easy axis, the value of M_R/M_S will be 0.5.⁷ For particles with cubic anisotropy and randomly oriented cubic easy axes, the value of M_R/M_S will be 0.83.⁷ The maximum value for the reduced remanence for MnFe_2O_4 was ~ 0.3 , well below the theoretical value of 0.5, while for CoFe_2O_4 , a material with a very strong cubic anisotropy, the maximum reduced remanence value also falls below the theoretical value. M_R/M_S values that fall below the theoretical reduced remanence are commonly observed in many magnetic nanoparticle samples and are attributed to frustration of surface spins.

An increase in the reduced remanence with dilution as observed for 8.5 nm MnFe_2O_4 has also been reported for 7 nm Co nanoparticles dispersed in paraffin and for 4 nm $\gamma\text{-Fe}_2\text{O}_3$ nanoparticles embedded into a silica matrix.^{9,13} The values of M_R/M_S increased from ~ 0.3 to 0.49 for Co dilutions of 100% and 2% respectively and from 0.37 to 0.45 for $\gamma\text{-Fe}_2\text{O}_3$ nanoparticle dilutions of 20% and 5% respectively.^{9,13} In both cases,

the M_R/M_S value approaches the theoretical value of 0.5. Monte-Carlo simulations by El-Hilo, et.al. show that dipolar interaction effects decrease the reduced remanence.²¹ Monte Carlo simulations by Kechrakos and Trohidou also show a decrease in M_R/M_S with increasing particle concentration for moderate dipolar interactions.²² This trend has been explained by Held, et.al.⁹ as a result of the frustration of the surface magnetic moments due to the competition between the interparticle dipolar interactions and the individual anisotropy energy of the nanoparticle. In the very dilute samples, the surface spins are not frustrated and the moment of the particle relaxes independently of its neighbors. However, for the higher concentrations, the moments are no longer independent and the spins relax to a local minimum in the energy barrier. As a result the moment of some particles may not lie along their easy axis. Since the moment must move greater than 90° , from geometric considerations, the value of M_R/M_S falls below 0.5. Such an argument could apply to the $MnFe_2O_4$ nanoparticles, which display increasing M_R/M_S values with increasing interparticle interactions.

The opposite trend in reduced remanence occurs in $CoFe_2O_4$. Compaction studies on maghemite have also demonstrated increases in the reduced remanence with particle concentration.²³ This opposite response was quite surprising, however, Monte Carlo simulations by Kechrakos and Trohidou demonstrates that the dependence of the reduced remanence with sample concentration may vary depending upon the competition between anisotropy and dipolar interactions.²² For example, a decrease in M_R/M_S with increasing particle concentration occurred for moderate dipolar interactions, while an increase in M_R/M_S with increasing particle concentration was observed for weakly interacting systems. While the $CoFe_2O_4$ nanoparticle system is certainly not a weakly interacting

system, another result from Kechrakos and Trohidou's Monte Carlo simulation was that dipole clusters also give rise to an increase in the reduced remanence of the magnetization. If the CoFe_2O_4 nanoparticles form clusters at high concentrations as suggested by their blocking temperature trend, such an increase in reduced remanence may be attributed to the cluster collective behavior.

One final difference between the magnetic response of CoFe_2O_4 and MnFe_2O_4 nanoparticles upon dilution in eicosane is the behavior of the magnitude of the susceptibility. The magnitude of the susceptibility decreases with dilution for CoFe_2O_4 while it increases then decreases with dilution for MnFe_2O_4 . Previous dilution studies on Fe_3O_4 ferrofluids show that the susceptibility increases with dilution.¹⁵ The decrease in susceptibility with increasing interactions was attributed to the increase in the energy barrier for magnetization reversal E_A thereby decreasing the fraction of particles that could overcome the energy barrier, thus lowering the susceptibility. This argument is not useful for the differences observed here and may not be valid. The blocking temperature data for both samples reported here show an increase in the energy barrier with interactions, yet their susceptibility behavior varies. Furthermore, the susceptibility generally increases with nanoparticles size (see Figure 3.5). By the argument of El-Hilo, the increasing energy barrier height resulting from the increased volume of the nanoparticles should lead to a decrease in the susceptibility, which is not observed in Figure 3.5. The fact that the susceptibility for CoFe_2O_4 decreases with dilution could be attributed to the cluster interactions. However, the unusual observation that the MnFe_2O_4 nanoparticles increases and then *decreases* (like CoFe_2O_4) at low concentrations suggests another origin. At this time though the reason for this behavior remains unclear.

7.5 Conclusions

The effects of interparticle interactions upon the magnetic properties of CoFe_2O_4 and MnFe_2O_4 nanoparticles have been investigated via the systematic dilution of the particles in eicosane. The blocking temperature for both spinel ferrite systems decreased with dilution, i.e. decreased interparticle interactions. This finding is consistent with Shtrikman-Wohlfarth (SW) and Dormann-Bessais-Fiorani (DBF) models which conclude that interparticle interactions lead to an increase in the anisotropy energy barrier for magnetization reversal E_A . The blocking temperature for MnFe_2O_4 nanoparticles decreased steadily with dilution, while the blocking temperature for CoFe_2O_4 nanoparticles remained constant until 15% at which point it then decreased with dilution. This finding suggests the formation of particle clusters in the strongly interacting CoFe_2O_4 system. The reduced remanence (M_R/M_S) decreased with interactions for MnFe_2O_4 nanoparticles, while it increased with interactions for CoFe_2O_4 nanoparticles. The increase in reduced remanence for CoFe_2O_4 nanoparticles is also consistent with the formation of nanoparticle clusters.

7.6 References

- (1) Berry, C. C.; Curtis, A. S. G. *J. Phys. D.: Appl. Phys.* **2003**, *36*, R198.
- (2) Bonnemain, B. *J. Drug Targeting* **1998**, *6*, 167.
- (3) Moser, A.; Takano, K.; Margulies, D. T.; Albrecht, M.; Sonobe, Y.; Ikeda, Y.; Sun, S.; Fullerton, E. E. *J. Phys. D.: Appl. Phys.* **2002**, *35*, R157.
- (4) Pankhurst, Q. A.; Connolly, J.; Jones, S. K.; Dobson, J. *J. Phys. D.: Appl. Phys.* **2003**, *36*, R167.
- (5) Shen, J. X.; Shan, Z. S.; Wang, D.; Liu, Y.; Sellmyer, D. J. In *Handbook of Nanophase and Nanostructured Materials Volume III*; Wang, Z. L., Liu, Y., Zhang, Z., Eds.; Kluwer Academic: New York, 2003, p 269.
- (6) Weller, D.; Moser, A.; Folks, L.; Best, M. E.; Lee, W.; Toney, M. F.; Schwickert, M.; Thiele, J.-U.; Doerner, M. F. *IEEE Trans. Magn.* **2000**, *36*, 10.
- (7) Stoner, E. C.; Wohlfarth, E. P. *Philosophical Transactions of the Royal Society A* **1948**, *240*, 599.
- (8) Liu, C.; Zou, B.; Rondinone, A. J.; Zhang, Z. J. *J. Am. Chem. Soc.* **2000**, *122*, 6263.
- (9) Held, G. A.; Grinstein, G.; Doyle, H.; Sun, S.; Murray, C. B. *Phys. Rev. B* **2001**, *64*, 012408.
- (10) Battle, X.; Labarta, A. *J. Phys. D.: Appl. Phys.* **2002**, *35*, R15.
- (11) Dormann, J. L.; Fiorani, D.; Tronc, E. *J. Magn. Magn. Mater.* **1999**, *202*, 251.
- (12) Hansen, M. F.; Mørup, S. *J. Magn. Magn. Mater.* **1998**, *184*, 262.
- (13) Tartaj, P.; González-Carreño, S.; Serna, C. J. *J. Phys. Chem. B* **2003**, *107*, 20.
- (14) Lu, J. L.; Deng, H. Y.; Huang, H. L. *J. Magn. Magn. Mater.* **2000**, *209*, 37.
- (15) El-Hilo, M.; O'Grady, K.; Chantrell, R. W. *J. Magn. Magn. Mater.* **1992**, *114*, 295.
- (16) Djurberg, C.; Svedlindh, P.; Nordblad, P.; Hansen, M. F.; Bødker, F.; Mørup, S. *Phys. Rev. Letter* **1997**, *79*, 5154.

- (17) Marin, C. N.; Malaescu, I.; Ercuta, A. *J. Phys. D.: Appl. Phys.* **2001**, *34*, 1466.
- (18) Sun, S.; Zeng, H.; Robinson, D. B.; Raoux, S.; Rice, P. M.; Wang, S. X.; Li, G. *J. Am. Chem. Soc.* **2004**, *126*, 273.
- (19) Song, Q.; Zhang, Z. J. *J. Am. Chem. Soc.* **2004**, *submitted*.
- (20) Trohidou, K. N.; Blackman, J. A. *Phys. Rev. B* **1995**, *51*, 11521.
- (21) El-Hilo, M.; Chantrell, R. W.; O'Grady, K. *J. Appl. Phys.* **1998**, *84*, 5114.
- (22) Kechrakos, D.; Trohidou, K. N. *Phys. Rev. B* **1998**, *58*, 12169.
- (23) Mørup, S.; Bødker, F.; Hendriksen, P. V.; Linderøth, S. *Phys. Rev. B* **1995**, *52*, 287.

CHAPTER 8

SYNTHESIS OF POLYSTYRENE COATED MANGANESE FERRITE NANOPARTICLES USING ATOM TRANSFER RADICAL POLYMERIZATION

Abstract

MnFe₂O₄/polystyrene core/shell nanoparticles have been prepared using atom transfer radical polymerization methods. When 3-chloropropionic acid is used as the surface initiator group, well-defined core-shell architecture is observed. On the other hand, when the particle is modified with 2-chloropropionic acid, a bimodal distribution of ~50 nm and ~70 nm polystyrene spheres containing 4-10 MnFe₂O₄ nanoparticles are produced. The difference in architecture corresponds with the stability and reaction rate of the generated free radical.

8.1 Introduction

In recent years there has been increased interest in coating surfaces of nanoparticles with a thin shell material in order to reduce the increased surface reactivity that occurs upon reduction of size, to tune the optical, magnetic, or catalytic properties of nanoparticles, and for the potential use of core-shell type materials in a wide range of applications such as ordered composite films for electronic applications to biomedical applications such as drug delivery.¹ Recently, methods to coat gold and silica nanoparticles with polymeric shells for organized assembly have been reported.^{2,3} Methods to coat magnetic nanoparticles with a controllable sized shell may aid in the development of ordered arrays of magnetic nanoparticles and may open avenues for exploring tunable magnetic properties for electronic applications. In electronic applications, magnetic couplings may be controlled through interparticle interactions and processable films with ordered assemblies of particles may be cast.^{2,3} For *in vivo* applications such as magnetic resonance imaging (MRI) contrast agents and magnetically guided drug delivery, coating with a polymer shell serves not only to protect the nanoparticle from biological degradation, but may also serve as a targeting agent and/or drug release matrix.^{4,5} To be viable for biomedical applications routes to improved polymeric coatings on magnetic nanoparticles are needed. Currently, methods to form magnetic polymer drug delivery systems results in particles that are too large to pass through cell membranes.^{6,7} The gaps in the endothelial lining of the blood vessels of the liver, through which nanoparticles could pass, for example have been estimated to range from 100-150 nm.⁸ Therefore, for biological applications, the net size of the magnetic nanoparticle/polymer structure should ideally be below 100 nm. For efficient diffusion through tissue for MRI applications, the size of the particles should be less than 20 nm.⁵

Previous studies prepared magnetic-polymer particles by using techniques such as emulsion polymerization and solvent evaporation.^{7,9} These methods yield polymer composites containing variable amounts of the magnetic nanoparticles and the size and shape of the magnetic polymer composites is inconsistent. Furthermore, most polymer coating studies on magnetic nanoparticles form the nanoparticle core (typically Fe, Fe₂O₃, or Fe₃O₄) in situ, which requires developing and/or testing new experimental conditions when another choice of magnetic core is desired.¹⁰⁻¹² In this study the MnFe₂O₄ nanoparticles were prepared by a reverse micelle microemulsion procedure, details of which have been previously reported.¹³ Like iron and iron oxide nanoparticles, spinel ferrite MnFe₂O₄ magnetic nanoparticles have a low blocking temperature that results in superparamagnetism being exhibited at room temperature, thereby making them useful for biomedical applications.^{13,14} Coating MnFe₂O₄ with polystyrene requires an additional synthesis step compared to the in situ reactions used to coat magnetic nanoparticles discussed above, but advantages of using spinel ferrite nanoparticles synthesized by microemulsion methods include forming higher quality nanoparticles with improved size distribution.^{13,15} Furthermore, by using microemulsion methods, a wide range of magnetic nanoparticle core materials may be designed with a specific superparamagnetic response.¹⁶

Von Werne and Patten have applied atom transfer radical polymerization (ATRP) methods to polymerize polymethylmethacrylate and polystyrene from the surface of silica nanoparticles, forming an inorganic core surrounded by the respectful polymer.^{3,17} In this method, polymerization initiators are chemically bound to the surface of the inorganic nanoparticles, and these modified particles are then used as macroinitiators in the polymerization reaction. ATRP offers several advantages over other polymerization

routes including surface initiation and control over molecular weight and molecular weight distribution.^{17,18} Furthermore, the polymers can be end-functionalized and/or block co-polymerized upon the addition of other monomers.¹⁸ Not only does this feature offer tailorability of the polymer coating with a wide range of possibilities for composition and functionality, but this feature may be important in biomedical applications in order to derivatize the polymer shell with biological moieties for specific cellular interactions.

This chapter discusses the synthesis of MnFe_2O_4 nanoparticles coated with polystyrene using atom transfer radical polymerization (ATRP) methods. The reaction conditions are important in developing core/shell structures. Differences in the core/shell structure are clear and are discussed in terms of radical concentration effects.

8.2 Experimental

MnFe_2O_4 nanoparticles were separately prepared using a reverse micelle microemulsion procedure.¹³ To modify the surface, ~ 9 nm MnFe_2O_4 nanoparticles were stirred in 1.0 M NaOH for 12 hours. The particles were collected using a magnet and the aqueous solution decanted. The particles were then re-suspended in a 1.0 M aqueous solution of either 3-chloropropionic acid (Aldrich, 98%) or 2-chloropropionic acid (Aldrich, 92%) and the pH adjusted to 4. After stirring overnight, the particles were collected with a magnet and washed 3-4 times to remove any excess ligand. Copper (I) chloride (0.3 mmol, J.T. Baker, 96%) and 4,4'-dinonyl-2,2'-dipyridyl (1.1 mmol, Aldrich, 97%) were dissolved in 4 mL *p*-xylene (Aldrich, 99%) or xylenes (Aldrich, AR). Dried modified nanoparticles and 8 mL styrene (J.T. Baker, 99%, inhibitors removed) were added to the xylene solution and the mixture heated to 130°C for 20-30 hours. All

experiments were conducted under nitrogen atmosphere. The particles were collected with a magnet and repeatedly washed with toluene.

Transmission electron microscopy was conducted using a JEOL 100C instrument operating at 100 kV. Samples suspended in toluene were dispersed onto a holey carbon grid. Particle sizes were determined by manually counting over 100 particles. Hysteresis measurements were performed at 5K in applied fields up to 5T using a MPMS-5S SQUID magnetometer. Thermogravimetric analysis (TGA) and differential scanning calorimetry (DSC) were collected from room temperature to 1000 °C at a heating rate of 17 °C /min using a Netzsch Luxx STA 409 PG.

8.3 Results and Discussion

A scheme of the polymerization method is outlined in Figure 8.1. Using carboxylic acid ligands that contain a chlorine functionality allows for binding of an initiator ligand onto the MnFe_2O_4 surface. Addition of $\text{Cu}^{\text{I}}\text{Cl}$ (stabilized by 4,4'-dinonyl-2,2'-dipyridyl) results in the extraction of the Cl group from the surface bound ligand, forming the more oxidatively stable $\text{Cu}^{\text{II}}\text{Cl}_2$ and leaving behind a free radical localized on the particle surface. This free radical will then initiate free radical polymerization with the styrene monomer. Initial polymerization experiments were performed using 3-chloropropionic acid as the surface initiator ligand and with xylenes as the solvent. Photoacoustic infrared spectroscopy of the native MnFe_2O_4 nanoparticles, the nanoparticles modified with 3-chloropropionic acid initiator ligand, and the nanoparticles at the end of the polymerization reaction are shown in Figure 8.2. The photoacoustic

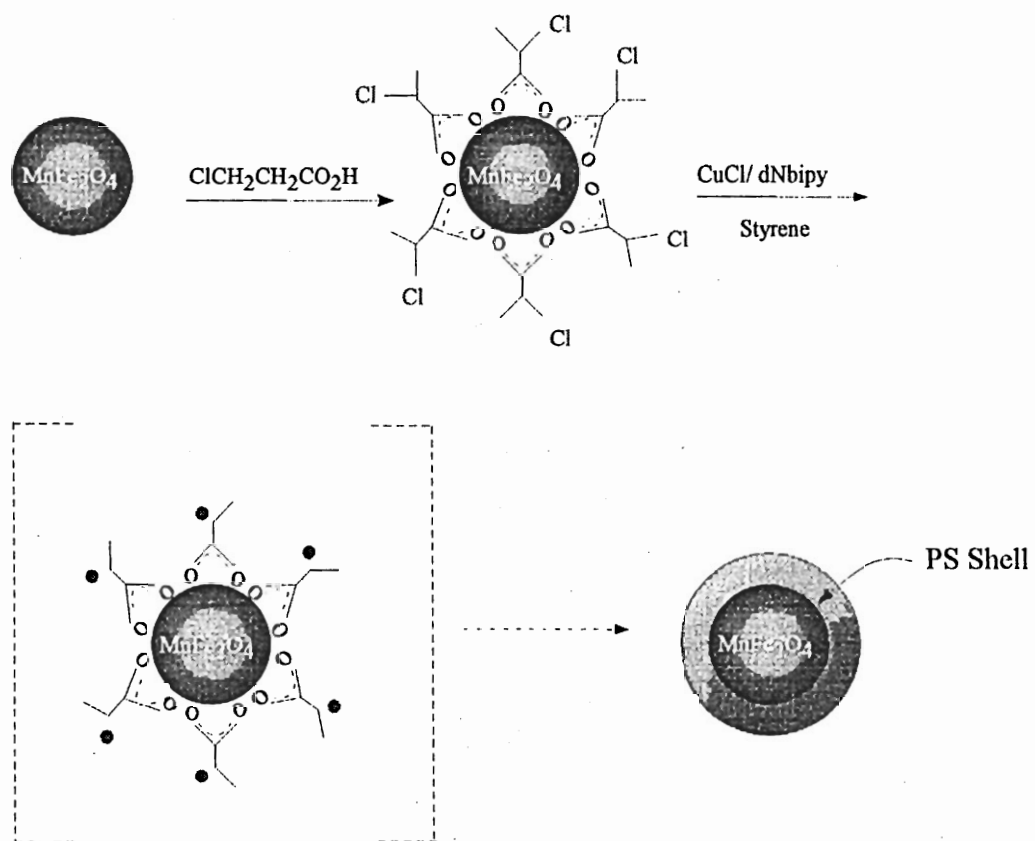


Figure 8.1 Schematic of polystyrene coating procedure

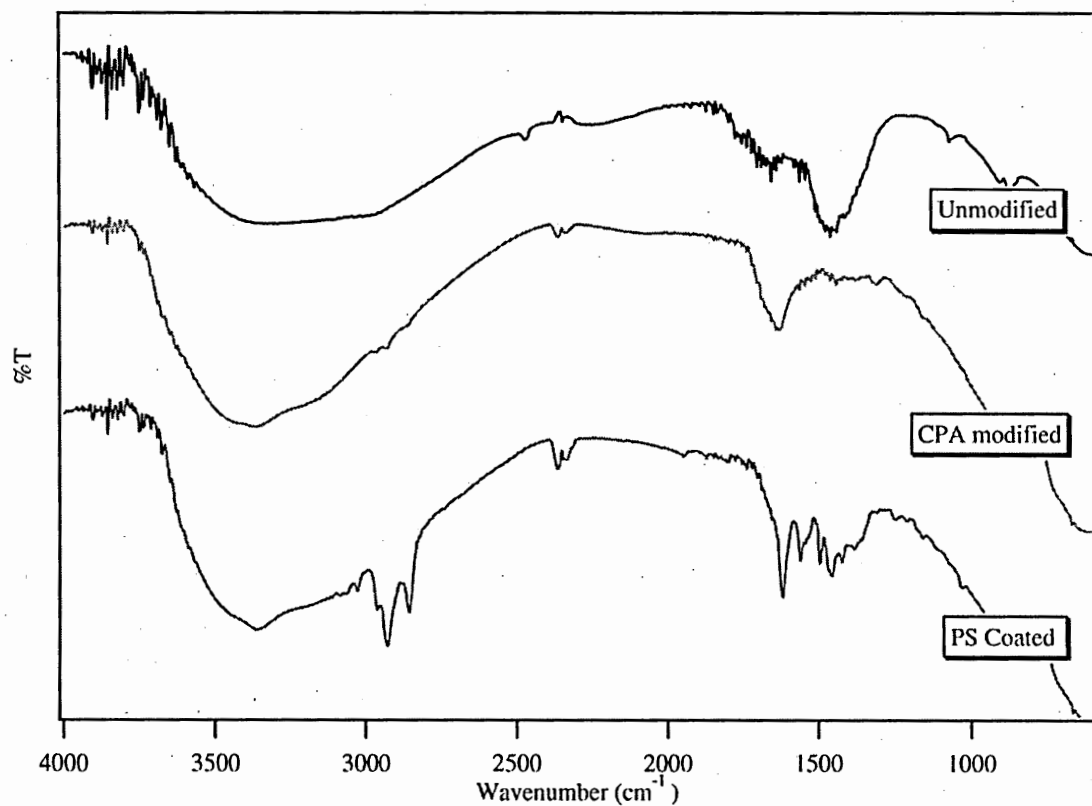


Figure 8.2. Photoacoustic infrared spectroscopy of as synthesized MnFe_2O_4 nanoparticles (top), particles modified with 3-chloropropionic acid (middle), and after polymerization (bottom)

infrared spectra clearly demonstrate that 3-chloropropionic acid is attached to the nanoparticle surface. After polymerization, the photoacoustic infrared spectra of the dried product confirm the presence of polystyrene. Characteristic peaks of polystyrene at $2700\text{--}3500\text{ cm}^{-1}$, $1000\text{--}1400\text{ cm}^{-1}$, and 700 cm^{-1} are observed in the coated product spectra that were not present in the spectra of the MnFe_2O_4 nanoparticle precursors.

The TEM micrograph for the coated products prepared under these conditions is presented in Figure 8.3. Individual MnFe_2O_4 particles coated with a thin polystyrene shell are observed. The average MnFe_2O_4 nanoparticle size was $9.3 \pm 1.5\text{ nm}$ with a $3.4 \pm 0.8\text{ nm}$ polystyrene shell. The few aggregates are likely due to chain entanglement during solvent evaporation.³ Polystyrene particles without a MnFe_2O_4 core were not observed.

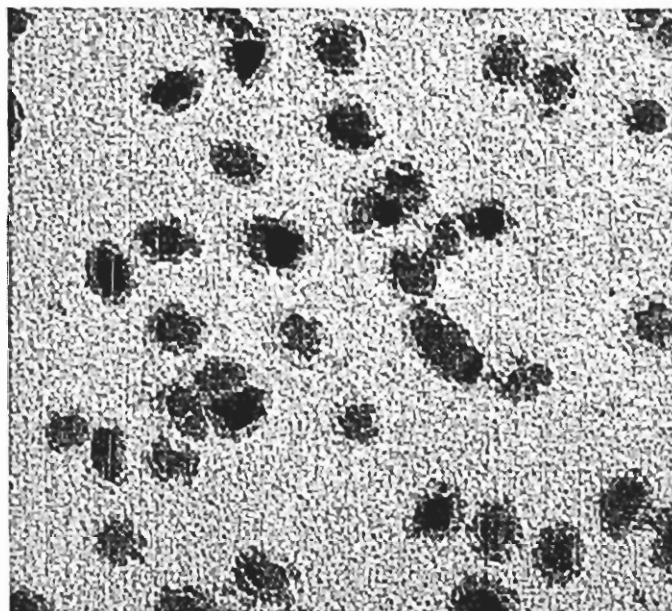


Figure 8.3. TEM image of $\sim 16\text{ nm}$ MnFe_2O_4 /polystyrene core/shell nanoparticles

Control experiments were performed in which MnFe_2O_4 nanoparticles that had not been modified with 3-chloropropionic acid were used in the polymerization reaction. Although thermal polymerization will occur at the temperatures used in this reaction, the control polymerization reactions using unmodified MnFe_2O_4 nanoparticles showed no observable polystyrene shell in the TEM micrographs. Furthermore, no characteristic polystyrene peaks were discernable in the photoacoustic infrared spectra.

In the above experiments, the 3-chloropropionic acid ligand was coupled to the nanoparticle surface, in which the chlorine is in the β position. However, it is well known that for atom transfer radical polymerizations, the best initiators are those alkyl halides with the substituent on the α – carbon.¹⁸ Therefore, synthesis of MnFe_2O_4 /polystyrene core/shell nanoparticles using 2-chloropropionic acid, an α – substituted ligand were subsequently performed. The results indicate that MnFe_2O_4 nanoparticles can be successfully coated with polystyrene using either 2- or 3-chloropropionic acid. However, the success in obtaining a discrete core/shell nanoparticle is dependent upon the initiator ligand. Figure 8.4 displays typical TEM images for MnFe_2O_4 /polystyrene core/shell samples prepared using 3-chloropropionic acid (Figure 8.4a) and 2-chloropropionic acid (Figure 8.4b) as the surface initiator groups. In both experiments, the solvent was *p*-xylene and the reaction length was 30 hours. It is clear that when 3-chloropropionic acid is used as the surface initiator group a well-defined core/shell architecture results. Figure 8.4a shows a single ~ 10 nm MnFe_2O_4 nanoparticle surrounded by an ~ 15 nm polystyrene shell, yielding a core/shell particle with size ~ 40 nm. However, when 2-chloropropionic acid is used as the surface bound group, no core/shell structure is observed. In Figure 8.4b, only a few nanoparticles consisting of a single MnFe_2O_4

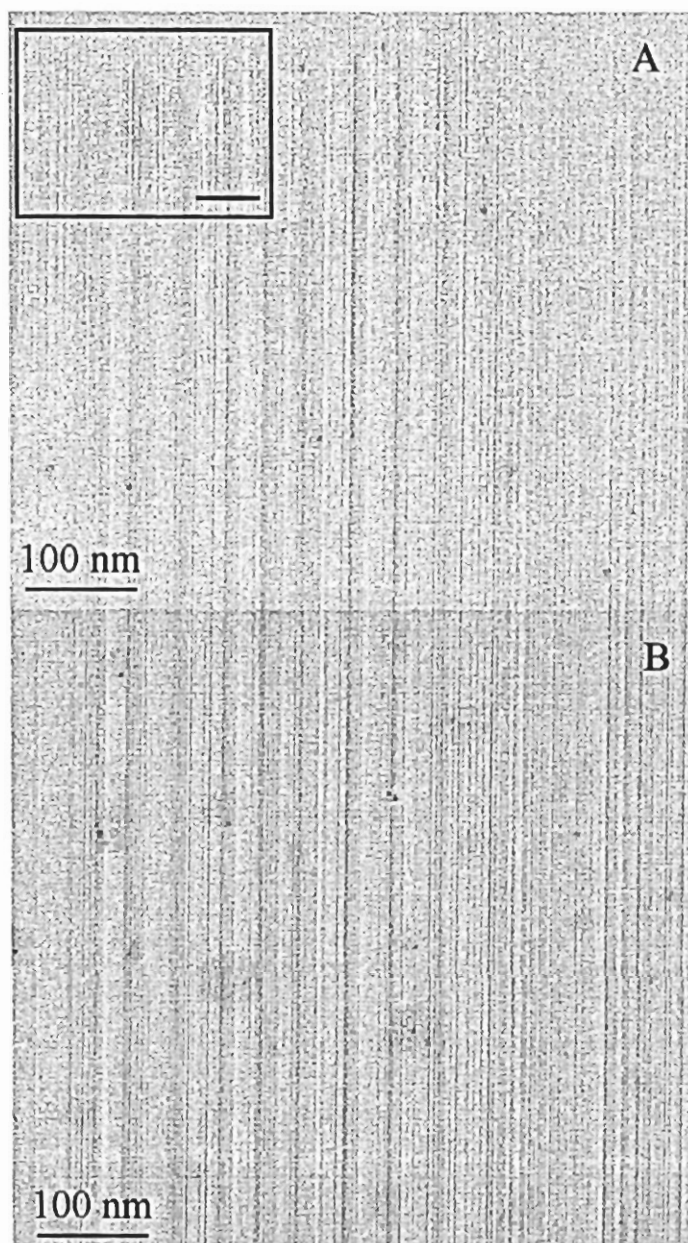


Figure 8. 4 TEM image of MnFe_2O_4 /polystyrene nanoparticles prepared using (A) 3-chloropropionic acid and (B) 2-chloropropionic acid. The inset in A shows a magnification of a core/shell particle in A and the scale bar represents 25 nm.

nanoparticle with a polystyrene shell are observed and the position of the MnFe_2O_4 is not centered within the polymer shell. Instead of the core/shell structure, a polystyrene sphere containing 4-10 MnFe_2O_4 nanoparticles is observed. Most of the MnFe_2O_4 /polystyrene composite particles are ~ 51 nm, but a small fraction are ~ 79 nm. Polystyrene spheres without magnetic nanoparticles incorporated are also found, which was not observed when 3-chloropropionic acid was used as the surface initiator group.

As the reaction conditions for preparing polystyrene coated MnFe_2O_4 nanoparticles reported here are identical except for the surface initiator group, the position of the chlorine (α or β) must account for the final architecture of the MnFe_2O_4 /polystyrene particles. The main role of the alkyl halide is to determine the number of initiated chains¹⁸ and as the formation of radicals is slow compared with propagation, it is the rate-determining step.¹⁸ The effect of the surface initiators upon the product properties has been demonstrated by von Werne and Patten. Surface polymerization of styrene from 75 nm SiO_2 particles show good molecular weight control while under the same conditions, poor molecular weight control was achieved when 300 nm SiO_2 particles were used.¹⁷ The difference was attributed to a smaller amount of initiator per gram of SiO_2 nanoparticles with increased particle volume.

The difference between the results of two differing initiator groups studied here is likely due to the stability of the radical group. Secondary radicals are more stable than primary radicals, have a faster reaction rate, and the transfer of the radical is more efficient in secondary radicals than the corresponding primary radical.¹⁹ 2-chloropropionic acid, with the chlorine in the α -position will produce a secondary free radical, while the nanoparticle with 3-chloropropionic acid coupled to the surface has the chlorine in the β -position and hence will form a primary radical. The larger net size of

the MnFe_2O_4 /polystyrene nanoparticles when 2-chloropropionic acid is used likely reflects this faster rate of reaction due to the increased radical stability. The probability of radical interaction also is correspondingly higher with increased free radical concentration.¹⁹ Due to the lower stability of the primary radical when 3-chloropropionic acid is used as the initiator species fewer radicals will exist. As a result, the probability of ‘unfavorable’ interactions such as interparticle termination routes decreases and well-defined core-shell structure is achieved. In the case of the α -linker, increased initiator concentrations may lead to interactions between growing chains from different nanoparticles and as such, large polystyrene particles which encapsulate many MnFe_2O_4 nanoparticles are formed. By adjusting the reaction conditions with respect to the initiator concentration, idealized core-shell samples may be achieved using the α -linker group. In the example of polystyrene grown from the surface 75 nm versus 300 nm SiO_2 nanoparticles, von Werne and Patten found that addition of a small amount of free initiator to the reaction solution of 300 nm SiO_2 nanoparticles improved the molecular weight control.¹⁷

8.4 Conclusion

In summary, spinel ferrite MnFe_2O_4 nanoparticles have been coated with a thin polystyrene shell using atom transfer radical polymerization. When the chlorine of the surface ligand is in the β position, well-defined core/shell architectures are observed. However, when the chlorine is in the α position, the idealized core/shell architecture is not achieved and a mixture of sizes of the MnFe_2O_4 /polystyrene composite is observed. Although MnFe_2O_4 nanoparticles were used in this study, the selection of the magnetic nanoparticle chosen for the core is dependent upon the desired superparamagnetic

properties for a specific application. For example, for data storage, the superparamagnetic state must be avoided in order to retain data integrity, while in MRI applications, superparamagnetism is crucial.^{20,21} Using ATRP to coat MnFe_2O_4 with polystyrene increases their potential for biomedical applications as the resulting core-shell nanoparticles are within the biological size restrictions. The polymer shell may also be easily modified for a particular biospecificity. Figure 8.5 demonstrates two routes for bioengineering the surface. In the first example, in which styrene- CH_2Cl is added during the polymerization, a chloromethylated polystyrene surface is created. The solid phase peptide synthesis technique developed by Merrifield to synthesize amino acids of any length from chloromethylated polystyrene can be followed in order to easily add peptides to the $\text{MnFe}_2\text{O}_4/\text{PS}$ nanoparticle surface.²² In the second example, a thiolated alkene is added during polymerization in order to create a thiol-rich surface. The using dithiol exchange techniques, DNA can be attached to the $\text{MnFe}_2\text{O}_4/\text{PS}$ nanoparticle surface.

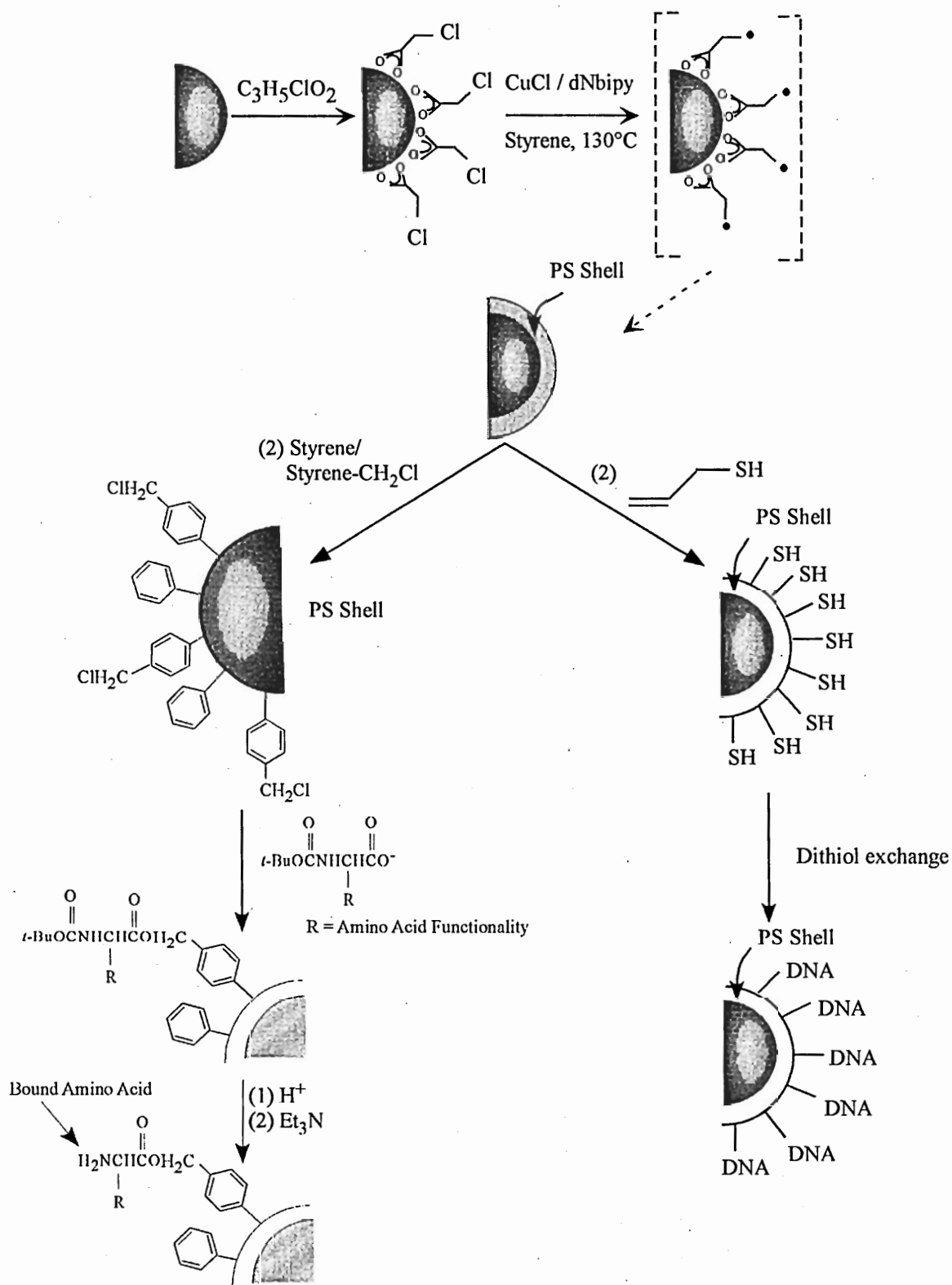


Figure 8.5 Schematic of synthesis routes to biologically active surface

8.5 References

- (1) Caruso, F. *Adv. Mater.* **2001**, *13*, 11.
- (2) Watson, K. J.; Zhu, J.; Nguyen, S. T.; Mirkin, C. A. *J. Am. Chem. Soc.* **1999**, *121*, 7409.
- (3) Von Werne, T.; Patten, T. E. *J. Am. Chem. Soc.* **1999**, *121*, 7409.
- (4) Landfester, K.; Ramirez, L. P. *J. Phys. Cond. Matter.* **2003**, *15*, S1345.
- (5) Portet, D.; Denizot, B.; Rump, E.; Lejeune, J. J.; Jallot, P. *J. Colloid Interf. Sci.* **2001**, *238*, 37.
- (6) Gómez-Lopera, S. A.; Plaza, R. C.; Delgado, A. W. *J. Colloid Interf. Sci.* **2001**, *240*, 40.
- (7) Ishii, F.; Takamura, A.; Noro, S. *Chem. Pharm. Bull.* **1984**, *32*, 678.
- (8) Davis, S. S.; Illum, L. *Biomaterials* **1988**, *9*, 110.
- (9) Bahar, T.; Çelebi, S. S. *J. Appl. Poly. Sci.* **1999**, *72*, 69.
- (10) Srikanth, H.; Hajndl, R.; Chirinos, C.; Sanders, J.; Sampath, A.; Sudarshan, T. S. *Appl. Phys. Lett.* **2001**, *79*, 3503.
- (11) López, S.; Cendoya, I.; Torres, F.; Tejada, J.; Mijangos, C. *Polym. Enginer. Sci.* **2001**, *41*, 1845.
- (12) Burke, N. A. D.; Stöver, H. D. H.; Dawson, F. P.; Lavers, J. D.; Jain, P. K.; Oka, H. *IEEE Trans. Magn* **2001**, *37*, 2660.
- (13) Liu, C.; Zou, B.; Rondinone, A. J.; Zhang, Z. J. *J. Phys. Chem. B* **2000**, *104*, 1141.
- (14) Liu, C.; Zhang, Z. J. *Chem. Mater.* **2001**, *13*, 2092.

- (15) Moumen, N.; Pileni, M. P. *J. Phys. Chem.* **1996**, *100*, 1867.
- (16) Liu, C.; Zou, B.; Rondinone, A. J.; Zhang, Z. J. *J. Am. Chem. Soc.* **2000**, *122*, 6263.
- (17) Von Werne, T.; Patten, T. E. *J. Am. Chem. Soc.* **2001**, *123*, 7479.
- (18) Patten, T. E.; Matyjaszewski, K. *Adv. Mater.* **1998**, *10*, 901.
- (19) Cowie, J. M. G. In *Polymers: Chemistry & Physics of Modern Materials*; Blackie Academic & Professional: London, 1991, pp 52.
- (20) Sun, S.; Murray, C. B.; Weller, D.; Folks, L.; Moser, A. *Science* **2000**, 287.
- (21) Häfeli, U.; Schütt, W.; Teller, J.; Zborowski, M., Eds, *Scientific and Clinical Applications of Magnetic Carriers*; Plenum: New York, 1997.
- (22) Streitwieser, A.; Heathcock, C. H.; Kosower, E. M. In *Introduction to Organic Chemistry 4th Edition*; Macmillan Publishing Company: New York, 1992, p 974.

CHAPTER 9

MAGNETIC PROPERTIES OF MANGANESE FERRITE/POLYSTYRENE CORE/SHELL NANOPARTICLES: A NON-DILUTION APPROACH TO INVESTIGATE INTERPARTICLE INTERACTION EFFECTS

Abstract

MnFe₂O₄/polystyrene core/shell nanoparticles with variable shell thickness were prepared using atom transfer radical polymerization methods. The magnetic properties have been characterized as a function of shell thickness. The saturation magnetization did not change upon coating, while the remnant magnetization and coercivity both decreased upon coating with thicker polystyrene shells. The decrease in coercivity with particle separation via thicker polystyrene shells is consistent with an decrease in the anisotropy energy barrier E_A . The increase in the reduced remanence with interactions is explained in terms of weakly interacting dipoles and Néel theory.

9.1 Introduction

Research into the properties of magnetic nanoparticles is of interest for both fundamental studies as well as for their applicability in a number of industries such as magnetic recording, voice coil motors, frictionless bearings, and biochemical separations.¹⁻⁴ Magnetic nanoparticles below a critical diameter exist as single domain and the magnetization vector no longer reverses by domain wall movement, but instead through the coherent rotation of the magnetization vector. Single domain theories describing the behavior of fine particle magnetic systems have been developed since the 1940s.⁵⁻⁷ Stoner and Wohlfarth first described the behavior of a single domain particle whose magnetization reverses through coherent rotation.⁵ The energy barrier for magnetization reversal E_A described by Stoner-Wohlfarth theory is

$$E_A = KV \sin^2\theta \quad (9.1)$$

where K is the magnetocrystalline anisotropy, V is the volume and θ is the angle between the easy axis of the nanoparticle and the magnetization direction. Control over the magnetic properties, such as the superparamagnetic state, can be achieved by varying the size of the nanoparticle or the magnetocrystalline anisotropy. Since the development of Stoner-Wohlfarth theory, many factors such as surface anisotropy and interparticle interactions have been found to contribute to the magnetic behavior of nanoparticles. Knowledge of how these factors contribute to or alter the magnetic properties of nanoparticles is essential for the practical implementation of magnetic nanoparticles in applications such as magnetically guided drug delivery or magnetic resonance imaging

(MRI) contrast enhancement agents that require a modified surface and/or variable concentration of particles in serum, for example.

Although interparticle interactions are known to affect the magnetic properties of magnetic nanoparticles, correlating the effect of particle-particle interactions with changes in magnetization has still provided a challenge. The effects of interparticle interaction upon the magnetic properties of nanoparticles vary depending upon the sample and in some cases, differing trends in magnetization with particle-particle separation are observed even for the same material.⁸⁻¹⁴ In Chapter 7 differing magnetic behavior was observed for 8.5 nm CoFe_2O_4 and 8.5 nm MnFe_2O_4 nanoparticles diluted into eicosane. The different magnetic response upon dilution can be attributed to the strength of the dipolar couplings. CoFe_2O_4 has a large magnetocrystalline anisotropy and is a strongly interacting system. In strongly interacting systems, clusters are known to form and the magnetic response of CoFe_2O_4 is suggested to result from collective cluster behavior. Although it is known that strongly interacting systems form clusters, recently there has been increased evidence of cluster formation in weakly interacting systems, such as magnetite and manganese zinc ferrite.¹⁵ The clusters form even at zero applied field and the nanoparticles arrange into a cluster such that a closed circuit or closed flux loop forms.^{15,16} Computer simulations by Chantrell, et.al. support this finding. The formation of closed chains of magnetic colloid particles was predicted even under zero field.^{17,18} Monte Carlo simulations by Kechrakos and Trohidou also show that around a percolation threshold, dipoles clusters form with a nose-to-tail ordering of their magnetic moments.¹⁹

Experimentally, the effects of interparticle interactions upon magnetic properties are typically investigated by dilution of ferrofluids. The rationale is that there exists a lower probability for particles to be located next to one another in the more diluted samples and therefore it is assumed that interparticle interactions decrease with increasing dilutions. However, the fact that even upon dilution, closed flux loop clusters may form in weakly interacting nanoparticle systems, suggests that dilution of magnetic nanoparticles may not provide true particle separation and cannot yield a straightforward analysis of interparticle interaction effects. In this chapter the magnetic properties of MnFe_2O_4 /polystyrene core/shell nanoparticles are reported. By adjusting the thickness of the polymer shell, the particles can be physically separated by variable amounts thereby providing a new approach for investigating interparticle interaction effects.

9.2 Experimental

MnFe_2O_4 /polystyrene core/shell nanoparticles were prepared using atom transfer radical polymerization methods reported elsewhere.²⁰ All samples were prepared using 3-chloropropionic acid and MnFe_2O_4 nanoparticle cores synthesized using reverse micelle microemulsion methods with size 18.5 nm. Shell thicknesses were varied by adjusting the reaction time, the choice of solvent, and the volume of solvent used in the synthesis. Transmission electron microscopy experiments were performed on a JEOL 100C operating at 100kV. Thermogravimetric analysis used to quantify the mass of polystyrene were collected from room temperature to 1000 °C at a heating rate of 17 °C/min using a Netzsch Luxx STA 409 PG. Hysteresis measurements were collected on a Quantum Design MPMS-5S SQUID magnetometer at 5 K with applied fields ± 5 T.

9.3 Magnetization Results

Figure 9.1 shows a typical hysteresis curve of 18.5 nm MnFe_2O_4 nanoparticles before and after coating with polystyrene. The magnetization has been corrected for polymer mass determined from thermogravimetric analysis (TGA) experiments and therefore is reported in emu/g of MnFe_2O_4 . It is clear that the saturation magnetization remains constant after addition of the polystyrene shell. However, from the inset, it is clear that the remnant magnetization and the coercivity decrease after coating with polystyrene. When the thickness of the polystyrene shell is allowed to vary, further

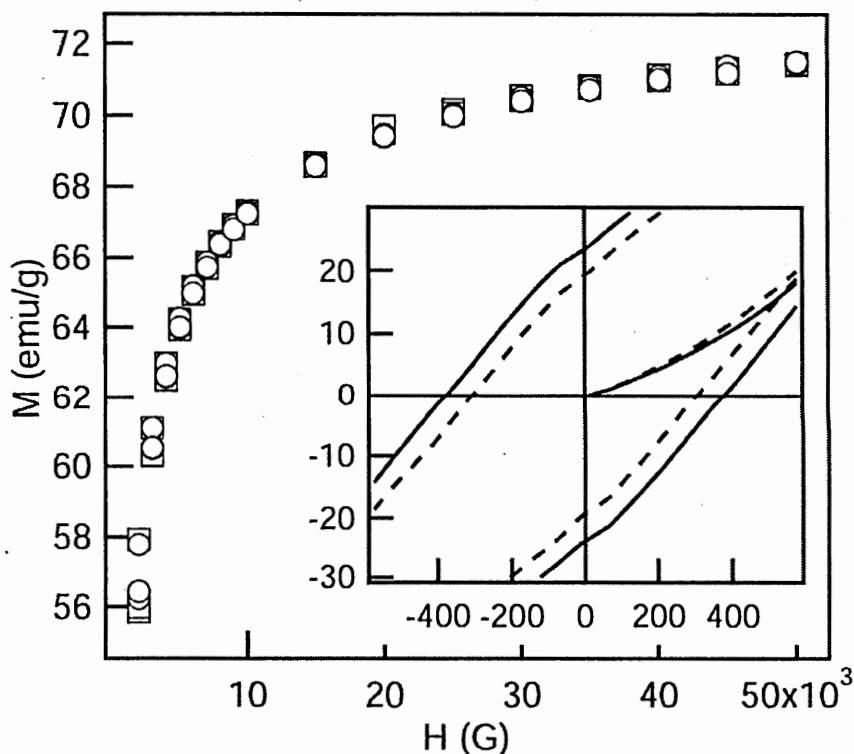


Figure 9.1. Expanded region of hysteresis curve at 5 K for polystyrene coated (---, \circ) and native 18.5 nm MnFe_2O_4 (—, \square).

decreases in the coercivity and remnant magnetization occur. The percentage decrease in the coercivity of the coated particles with respect to the native 18.5 nm MnFe_2O_4 nanoparticle for a number of samples is shown in Figure 9.2. Due to the fact that accurate measurements of small variations in shell thickness are difficult to achieve from our TEM studies, the data is plotted in terms of mass loss determined from TGA experiments. The coercivity of the MnFe_2O_4 nanoparticles decreases by $\sim 5\%$ upon attaching the surface initiators ligand, in this case, 3-chloropropionic acid. Upon coating with polystyrene, the percentage coercivity decrease jumps to 15–25 % in which the percentage coercivity decrease becomes larger with increasing mass loss (i.e. a thicker polystyrene shell).

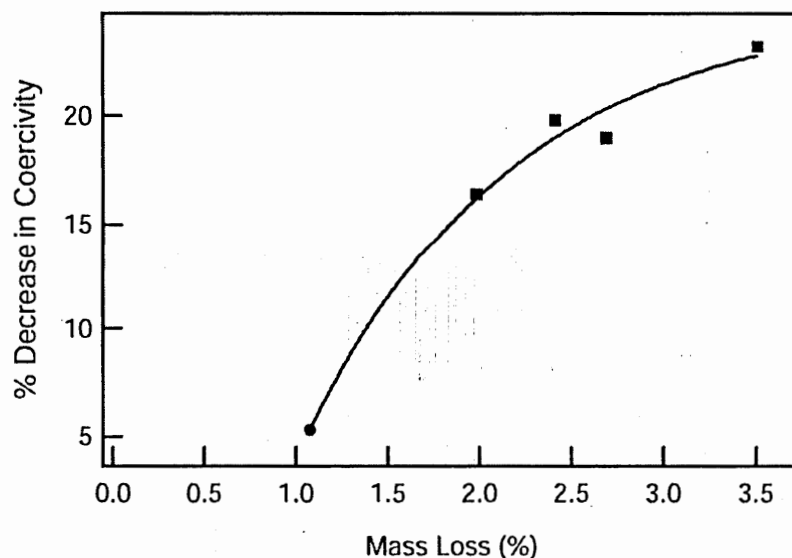


Figure 9.2 Percentage decrease in the coercivity of polystyrene coated MnFe_2O_4 nanoparticles (■) and 3-chloropropionic acid modified MnFe_2O_4 (●) with respect to native 18.5 nm MnFe_2O_4 . The line serves only to guide the eye.

The reduced remanence (M_R/M_S) of the magnetization determined from the hysteresis measurements at 5 K is shown as a function of polystyrene mass loss in Figure 9.3. The reduced remanence (M_R/M_S) decreases with increasing polymer coating, with values ranging from 0.33 for the native MnFe_2O_4 to 0.26 for the thickest coating of polystyrene on MnFe_2O_4 . These values clearly fall well below the ideal theoretical value of 0.5 for non-interacting randomly oriented particles.

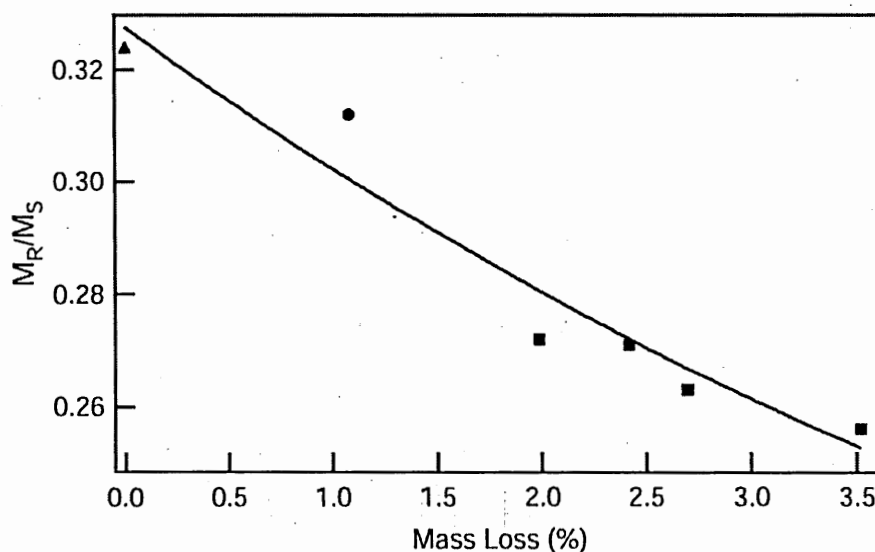


Figure 9.3 Variation of reduced remanence (M_R/M_S) for native 18.5 nm MnFe_2O_4 nanoparticles (▲), 3-chloropropionic acid modified nanoparticles (●) and polystyrene coated nanoparticles (■). The line serves only to guide the eye.

9.4 Discussion

The reduced coercivity for 3-chloropropionic acid – modified MnFe_2O_4 nanoparticles can be understood in terms of a reduction in surface anisotropy. Surface anisotropy in nanoparticles results from the reduced spin-orbital couplings at the particles surface due to the incomplete coordination sphere of the surface ions.²¹ Qualitatively, adsorbed ligands can be viewed as effectively taking the positions of the missing oxygen atoms, making the symmetry and crystal field of the surface metal ion to more closely resemble that of the core. Such changes certainly affect the surface anisotropy and consequently the coercivity of nanoparticles. Vestal and Zhang have recently reported a correlation between the magnitude of coercivity decrease and the crystal field stabilization energy evoked by the bound ligand.²² The results found here when 3-chloropropionic acid is attached to the surface of MnFe_2O_4 nanoparticles is consistent with the effects of substituted benzene ligands ($\text{Y-C}_6\text{H}_5$) attached to the surface of MnFe_2O_4 nanoparticles.²²

The further decrease in the coercivity by 10 – 15% after the subsequent coating with polystyrene is consistent with the effects of interparticle interaction. Several models have been developed to account for the effects of interparticle interactions upon magnetic properties.^{9,23} The majority of dilution studies investigating the effects of interparticle interaction show an increase in blocking temperature and coercivity with increasing interactions.^{12,13,23-29} This data supports the Shtrikman-Wohlfarth and Dormann-Bessais-Fiorani models for interparticle interactions. The results of these models suggest that the Stoner-Wohlfarth single domain energy barrier for magnetization reversal E_A increases due to the interparticle interactions as

$$E_A = KV \sin^2\theta + B_i \quad (9.2)$$

where B_i is the interaction term whose form varies from model to model. Therefore, increasing interparticle interactions would require higher temperatures and stronger fields to overcome the energy barrier, hence the blocking temperature and coercivity of the nanoparticles increases. The fact that the coercivity decrease observed here correlates with increasing particle separation resulting from a thicker polystyrene shell is consistent with equation 9.2 and interparticle interactions effects described by Dormann, et.al.

It is clear from Figure 9.3 that the reduced remanence (M_R/M_S) decreases with increasing polymer coating, with values ranging from 0.33 for the native $MnFe_2O_4$ to 0.26 for the thickest coating of polystyrene on $MnFe_2O_4$. These values clearly fall well below the ideal theoretical value of 0.5 for non-interacting randomly oriented particles. Reduced remanence values falling below 0.5 are commonly observed in many ferrite nanoparticle systems and are suggested to result from frustration induced by the effects of competition between interparticle interactions and intraparticle anisotropy on the spin relaxation process.⁸ The fact that the reduced remanence decreases with particle separation was surprising. The reduced remanence of Co and $\gamma\text{-Fe}_2\text{O}_3$ nanoparticles increases, approaching the theoretical value, when the interparticle interactions are reduced, by either reducing particle concentration or by dilution in a matrix.^{8,30,31} Furthermore, the results in Chapter 7 for dilution studies on 8.5 nm $MnFe_2O_4$ nanoparticles also show an increase in the reduced remanence with decreasing particle-particle interactions. An increase in reduced remanence with increased interactions like

that observed in Figure 9.3 was observed for 8.5 nm CoFe_2O_4 . However, the reasoning for such behavior was attributed to cluster phenomena. Here the particles are physically isolated from one another by the polystyrene shell and cluster behavior cannot account for the reduced remanence trend.

Monte Carlo simulations by Kechrakos and Trohidou show not only does cluster behavior give rise to an increased reduced remanence, but that the reduced remanence also increases with particle concentration for weakly interacting systems. This increase is only observed for a specific range of interaction strengths. For moderate interaction strengths, the reduced remanence decreases with particle interactions. The results of the Monte Carlo simulations agree with experimental reports. For example, experiments by Luo et.al. found that the reduced remanence of Fe_3O_4 nanoparticles decreased with interactions.²⁷ The interaction strength g/k (definitions not provided in the paper) for this nanoparticle's parameters was ~ 1 .¹⁹ At this value, the Monte Carlo simulation by Kechrakos and Trohidou predicted a decrease. On the other hand, the reduced remanence of $\gamma\text{-Fe}_2\text{O}_3$ nanoparticles reported by Mørup et.al. increased with interactions.³² The interaction strength corresponding to these particles was $g/k \sim 0.34$, which according to the simulation should yield an increase in the reduced remanence as was observed. The increase in reduced remanence for the polystyrene coating MnFe_2O_4 reported here might be a result of the weakly interacting dipolar strength. The difference between the trend reported here and that of 8.5 nm MnFe_2O_4 nanoparticles in Chapter 7 may result from the different synthesis methods used to prepare MnFe_2O_4 and the different size of the nanoparticles. Furthermore, the presence of the polystyrene shell may weaken the

exchange and dipolar interactions more than the oleic acid capping group and as a result, this system falls into the weakly interacting region described by Kechrakos and Trohidou.

The reduced remanence trend can also be understood in terms of the effects of the spin relaxation process. The relaxation of a magnetic moment has been described by Néel as

$$\tau = \tau_0 \exp(E_A/k_B T) \quad (9.3)$$

where τ_0 is the attempt time whose value ranges from 10^{-9} - 10^{-12} s, k_B is the Boltzmann constant, and E_A is the energy barrier defined in equation 9.1.³³ If E_A increases due to interparticle interactions as given in equation 9.2, the relaxation time τ must increase with increasing interparticle interactions.

Néel has also described the decay of the remnant moment of an assembly of single domain particles as

$$M_R(t) = M(0) \exp (-t/ \tau) \quad (9.4)$$

where $M_R(t)$ is the remnant magnetization at time t , and τ is the relaxation time given in equation 9.3. The increase in τ resulting from interparticle interactions as described above will thereby lead to an increase in $M_R(t)$ for a given measurement time. This result is experimentally observed here. In Figure 9.3 it is clear that M_R is larger for the native MnFe_2O_4 nanoparticle compared to the polystyrene-coated MnFe_2O_4 in which particle-particle interactions are reduced. Since the saturation magnetization M_S remains constant

even after coating with polystyrene, the reduced remanence (M_R/M_S) must scale with M_R . As such, for a consistent measurement time, the reduced remanence will decrease with decreasing interparticle interactions due to the impact upon relaxation times. This trend is observed in the polystyrene-coated $MnFe_2O_4$ samples.

9.5 Conclusions

Interparticle interaction effects were investigated using $MnFe_2O_4$ /polystyrene core/shell nanoparticles. The magnetic properties of the $MnFe_2O_4$ /polystyrene core/shell samples were dependent upon the shell thickness. The coercivity is increasingly reduced for samples with a thicker polystyrene shell. This observation is in accordance with interparticle interaction effects suggesting a decrease in the energy barrier for magnetization reversal with decreased interactions. The increasing reduced remanence trend with particle interactions observed here is consistent with Monte Carlo simulations for weakly interacting systems. Furthermore, as the saturation magnetization does not change upon coating, the reduced remanence trend can also be explained in terms of Néel's spin relaxation theory.

9.6 References

- (1) Jakubovics, J. P. *Magnetism and Magnetic Materials*; Institute of Metals: London, 1987.
- (2) Hadjipanayis, G. C. *J. Magn. Magn. Mater.* **1999**, *200*, 373.
- (3) Landfester, K.; Ramirez, L. P. *J. Phys. Cond. Matter.* **2003**, *15*, S1345.
- (4) Pankhurst, Q. A.; Connolly, J.; Jones, S. K.; Dobson, J. *J. Phys. D.: Appl. Phys.* **2003**, *36*, R167.
- (5) Stoner, E. C.; Wohlfarth, E. P. *Phil. Trans. Royal Soc. A* **1948**, *240*, 599.
- (6) Néel, L. *Comptes. rendus.* **1949**, *228*, 664.
- (7) Néel, L. *Ann. Geophys (C.N.R.S.)* **1949**, *5*, 99.
- (8) Held, G. A.; Grinstein, G.; Doyle, H.; Sun, S.; Murray, C. B. *Phys. Rev. B* **2001**, *64*, 012408.
- (9) Dormann, J. L.; Fiorani, D.; Tronc, E. *J. Magn. Magn. Mater.* **1999**, *202*, 251.
- (10) Tartaj, P.; González-Carreño, S.; Serna, C. J. *J. Phys. Chem. B* **2003**, *107*, 20.
- (11) Lu, J. L.; Deng, H. Y.; Huang, H. L. *J. Magn. Magn. Mater.* **2000**, *209*, 37.
- (12) El-Hilo, M.; O'Grady, K.; Chantrell, R. W. *J. Magn. Magn. Mater.* **1992**, *114*, 295.
- (13) Djurberg, C.; Svedlindh, P.; Nordblad, P.; Hansen, M. F.; Bødker, F.; Mørup, S. *Phys. Rev. Letter* **1997**, *79*, 5154.
- (14) Marin, C. N.; Malaescu, I.; Ercuta, A. *J. Phys. D.: Appl. Phys.* **2001**, *34*, 1466.
- (15) Taketomi, S.; Shull, R. D. *J. Magn. Magn. Mater.* **2003**, *266*, 207.

- (16) Bean, C. P.; Livingston, J. D. *J. Appl. Phys.* **1959**, *30*, 1205.
- (17) Chantrell, R. W.; Bradbury, A.; Popplewell, J.; Charles, S. W. *J. Phys. D.: Appl. Phys.* **1980**, *13*, L119.
- (18) Chantrell, R. W.; Popplewell, J.; Charles, S. W. *J. Appl. Phys.* **1982**, *53*, 2742.
- (19) Kechrakos, D.; Trohidou, K. N. *Phys. Rev. B* **1998**, *58*, 12169.
- (20) Vestal, C. R.; Zhang, Z. J. *J. Am. Chem. Soc.* **2002**, *124*, 14312.
- (21) Néel, L. *J. Phys. Radium* **1954**, *15*, 225.
- (22) Vestal, C. R.; Zhang, Z. J. *Journal of the American Chemical Society* **2003**, *125*, 9828.
- (23) Hansen, M. F.; Mørup, S. *Journal of Magnetism and Magnetic Materials* **1998**, *184*, 262.
- (24) Fiorani, D.; Dormann, J. L. In *Fundamental Properties of Nanostructured Materials*; D. Fiorani, G. S., Ed.; World Scientific: River Edge, NJ, 1994, p 193.
- (25) Battle, X.; Labarta, A. *Journal of Physics D: Applied Physics* **2002**, *35*, R15.
- (26) Dormann, J. L.; Bessais, L.; Fiorani, D. *J. Phys. C* **1988**, *21*, 2015.
- (27) Luo, W.; Nagel, S. R.; Rosenbaum, T. F.; Rosensweig, R. E. *Phys. Rev. Letter* **1991**, *67*, 2721.
- (28) Jonsson, T.; Mattsson, J.; Djurberg, C.; Khan, F. A.; Nordblad, P.; Svedlindh, P. *Physical Review Letters* **1995**, *75*, 4138.
- (29) Zhang, J.; Boyd, C.; Luo, W. *Physical Review Letters* **1996**, *77*, 390.
- (30) Tartaj, P.; González-Carreño, T.; Serna, C. J. *Journal of Physical Chemistry B* **2003**, *107*, 20.

- (31) Poddar, P.; Telem-Shafir, T.; Fried, T.; Markovich, G. *Physical Review B* **2002**, 66, 060403.
- (32) Mørup, S.; Bødker, F.; Hendriksen, P. V.; Linderøth, S. *Phys. Rev. B* **1995**, 52, 287.
- (33) Néel, M. L. *Annales de Geophysique* **1949**, 5, 99.

CHAPTER 10

SYNTHESIS AND MAGNETIC CHARACTERIZATION OF MANGANESE AND COBALT SPINEL FERRITE-SILICA NANOPARTICLES WITH TUNABLE MAGNETIC CORE

Abstract

A silica coating method on CoFe_2O_4 and MnFe_2O_4 spinel ferrite nanoparticles has been developed by using a reverse micelle microemulsion approach. Since magnetic nanoparticulate cores have been controllably synthesized prior to the encapsulation process, a great flexibility in tuning the magnetic properties of this magnetic nano-composite system can be achieved by independently controlling the magnetic properties of nanoparticulate cores. For these spinel ferrite nanoparticles, the saturation and remnant magnetizations decrease upon silica coating. The coercivity of silica-coated CoFe_2O_4 nanoparticles does not show any change after coating, while the coercivity of MnFe_2O_4 nanoparticles decreases by 10% after they have been coated with silica.

10.1 Introduction

The unique physical properties of nanoscale magnetic materials such as superparamagnetism have generated considerable interest for their use in a wide range of diverse applications from data information storage to in vivo magnetic manipulation in biomedical systems.^{1,2} Many technological applications require magnetic nanoparticles to be embedded in a non-magnetic matrix. Over the past few years, increased attention has been focused on the preparation of various nanostructures with magnetic nanoparticulate components and on understanding the magnetic behavior of nanoparticles due to new possible surface, inter-particle, and exchange interactions in a magnetic/non-magnetic matrix.³ Encapsulating magnetic nanoparticles in silica is a promising and important approach in the development of magnetic nanoparticles for technological and biomedical applications. For magneto-electronic applications, silica coated nanoparticles could be used to form ordered arrays with inter-particle magnetic couplings controlled through the silica shell thickness.⁴ The rich and well documented biocompatible chemistry of silica colloids may allow for practical implementation of magnetic nanoparticles in magnetically guided drug delivery, tumor targeting, and magnetically assisted chemical separation of cells and/or proteins.⁵⁻⁷ The silica shell certainly provides a chemically inert surface for the nanoparticulate system in biological systems. Moreover, it greatly improves the hydrophilicity of the magnetic nanoparticles.

Methods to coat magnetic nanoparticles with silica that have been reported over the past decade include sol-gel, aerosol pyrolysis, and Stöber processes.⁷⁻¹⁵ Many of the early reported methods produced a mixture of coated and uncoated particles.¹³ Very recently, the preparation of magnetic nanoparticle-silica core-shell architectures has been

reported by using surfactant microemulsion.^{16,17} Although advances have been achieved in preparing silica-magnetic nanoparticle composites, the magnetic nanoparticles used in the studies (typically Fe, Fe₂O₃, or Fe₃O₄) are often prepared *in situ*.^{8,9,14,17} The *in situ* preparation of nanoparticles often suffers in the poor quality of the magnetic core. A mixture of several iron oxide phases and poor crystallinity for the core, and a large dispersity in core nanoparticle size are commonly encountered in many of the synthesis procedures, which certainly muddle the interpretation of magnetic properties.^{7,9-13} Furthermore, if a different magnetic core is desired, a new set of reaction conditions are most likely required to be developed for each core material.

A two step Stöber process has generated magnetite silica core-shell nanostructure with good quality.¹⁵ But the magnetic features of this nanostructure were unknown since no magnetic characterization was provided for the core nanoparticles and the core-shell systems. There even was no crystallinity information for the core. The microemulsion method using surfactant sodium bis(2-ethyl) sulfosuccinate (AOT) or its mixture with polyoxyethylene(4)lauryl ether (Brij30) has shown that paramagnetic ZnFe₂O₄ nanoparticles can be coated with a silica shell. However, it is difficult to obtain discrete core-shell nanostructure.¹⁶ Under transmission electron microscopy (TEM), the silica shells seem more or less fused with each other between the core-shell nanoparticles. Using polyoxyethylene(15)cetyl ether for the synthesis, TEM has shown the good quality of core-shell nanostructure.¹⁷ Nevertheless, this synthesis method has been employed concurrently with *in situ* preparation of iron oxide or cobalt ferrite core and subsequently with thermal annealing at temperatures as high as 800-1000 °C. A variety of iron oxide

phases always co-exist in the core of this nanostructure, which make the core-shell nanoparticles magnetically poorly defined and their magnetic properties hard to control.

In this chapter the use of reverse micelle microemulsion method with the surfactant polyoxyethylene(5)nonylphenyl ether (Igepal CO-520) to prepare silica coated magnetic spinel ferrite nanoparticles (MFe_2O_4 ; $M = Co, Mn, Fe, Ni, Mg...$) with a tunable core is reported. High quality spinel ferrite nanoparticles with a narrow size distribution (typically 9-15%) are prepared prior to silica shell formation. Such two separate steps for the synthesis of core-shell nanostructure allow great flexibility in the selection of the magnetic core chosen for its desired magnetic response. There is no need for re-inventing the reaction procedure when a different magnetic core is chosen. This chapter demonstrates the ability to encapsulate two different spinel ferrite nanoparticles, $CoFe_2O_4$ and $MnFe_2O_4$ in silica and report the effects upon the magnetic properties of nanoparticles from silica shell.

10.2 Experimental

Both $CoFe_2O_4$ and $MnFe_2O_4$ nanoparticles were separately prepared prior to silica coating using microemulsion procedures. $CoFe_2O_4$ nanoparticles with a mean size of $\sim 4-25$ nm were prepared using normal micelle microemulsion methods.¹⁸ $MnFe_2O_4$ nanoparticles with size $\sim 8-25$ nm were prepared using reverse micelle microemulsion methods.¹⁹ To encapsulate the ferrite nanoparticles in silica, a reverse micelle microemulsion procedure was developed. The respective spinel nanoparticulate powder sample (100 mg) was mixed with concentrated NH_4OH (J.T. Baker, 3.5mL) and the slurry was sonicated (Fisher Scientific Solid State Ultrasonic F5-14) for ~ 15 minutes. To

form reverse micelles, 0.05M Igepal CO-520 in cyclohexane (Aldrich, 500 mL) was added to the base/nanoparticle mixture followed by tetraethylorthosilicate, TEOS (Aldrich, 3.0 mL). The solution was sonicated for ~30 minutes and then stirred for 5 days. The particles were collected by a magnet and the cyclohexane supernatant was decanted. The particles were washed with methanol then distilled water several times. Between each washing step, the particles were collected with a magnet.

X-ray diffraction studies were performed on a Bruker D8 Advance diffractometer with Cu K α radiation. SQUID magnetometry measurements were performed on a Quantum Design MPMS-5S SQUID magnetometer. TEM measurements were performed on a JEOL 100C TEM operating at 100 kV.

10.3 Results and Discussion

Typical x-ray diffraction patterns for the ferrite nanoparticles before and after silica coating are shown in Figure 10.1. As seen in Figure 10.1a, Bragg reflections for the ferrite nanoparticles can be indexed to a pure spinel phase. X-ray diffraction pattern remains identical in Figure 10.1b, indicating that the silica shell is amorphous and the crystallinity of the magnetic nanoparticulate core is retained after the coating procedure. BET N₂ adsorption experiments indicate that the silica shell is non-porous. Figure 10.2 shows a typical TEM micrograph for the spinel ferrite-silica nanoparticles. Samples were suspended in water and dispersed onto a holey carbon grid for TEM studies with a JEOL 100C operating at 100 kV. The average size of the ferrite-silica nanoparticles was 64.5 nm for coated 13 nm CoFe₂O₄ particles and 76.5 nm for coated 12 nm MnFe₂O₄ particles. Both nanoparticulate systems had a size distribution of ~15%. Occasionally non-coated

ferrite nanoparticles are observed under TEM, however they amount to less than 1% of the sample. Samples of similar quality are obtained when the ferrite core is varied between 4 - 20 nm. However, when the ferrite core is larger than 25 nm the fraction of uncoated particles increases greatly, reaching ~50%.

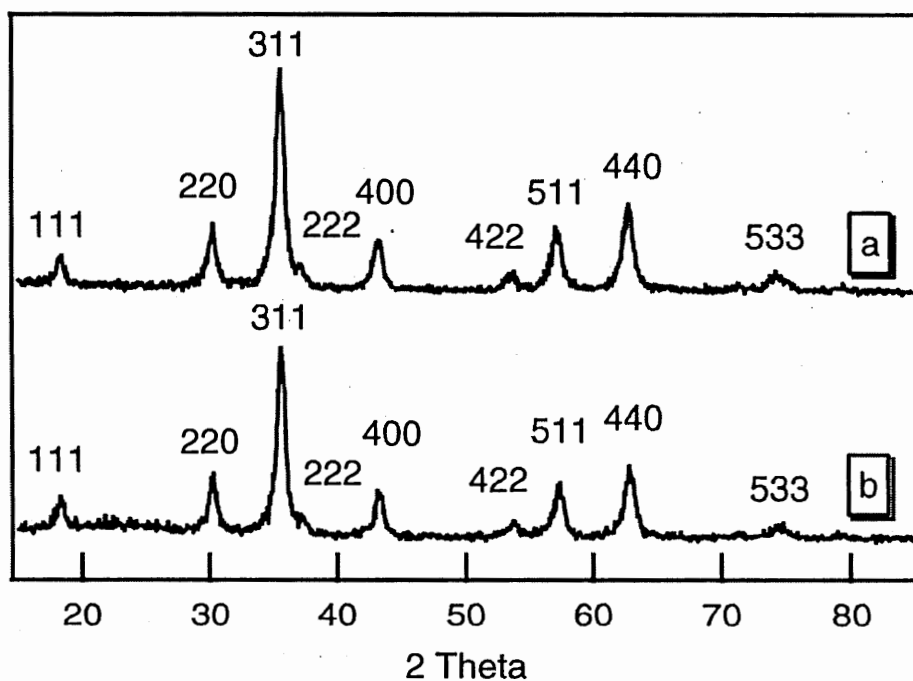


Figure 10.1 Powder x-ray diffraction pattern for (a) native 13 nm CoFe₂O₄ nanoparticles and (b) 13 nm CoFe₂O₄ nanoparticles coated with silica

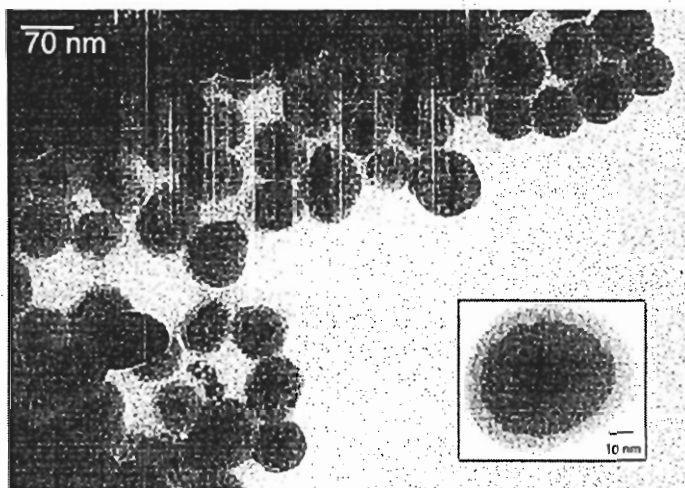


Figure 10.2 TEM micrograph of silica-MnFe₂O₄ particles. Inset shows a higher magnification of a silica-ferrite nanoparticle with diameter 79 nm.

Pure SiO₂ nanoparticles, prepared following the same procedure of silica shell formation but without the addition of the magnetic nanoparticles, have shown spherical shapes with a size of ~59 nm. As Figure 10.2 shows, inclusion of the magnetic nanoparticles increases the size of the final nanoparticulate composite and the contour of the silica composite exhibits distortions reflecting the shape of the ferrite nanoparticles. Although the size of SiO₂ spheres can be tuned by varying the water to surfactant ratio,²⁰ small deviations from the water to surfactant ratio in these reaction conditions causes a lack of inclusion of magnetic nanoparticles into the silica shell. When the Igepal CO-520 concentration is increased or the concentration of water varied, a mixture of pure SiO₂ nanoparticles and uncoated magnetic nanoparticles are observed under TEM. Instead, the control over the size of the silica thickness can be achieved by varying the reaction time.

Dried nanoparticles were characterized with a Quantum Design MPMS-5S SQUID magnetometer. Temperature dependent zero field cooled (ZFC) and field cooled (FC) susceptibility measurements reveal that the blocking temperature for both the CoFe_2O_4 and MnFe_2O_4 samples did not change upon coating with silica shell. Figure 10.3 shows the field dependent magnetization at 5 K of ~ 13 nm CoFe_2O_4 nanoparticles before and after silica coating. The saturation magnetization (M_S) and remanent magnetization (M_R) clearly decrease upon coating while the coercivity (H_C) remains nearly constant. Figure 10.4 shows the field dependent magnetization results for ~ 12 nm MnFe_2O_4 particles. The saturation and remanent magnetization also decrease upon coating with silica. The coercivity for silica coated MnFe_2O_4 is 715 G, which is a 10% decrease in the coercivity with respect to the bare MnFe_2O_4 nanoparticles (798 G). This certainly is much higher than a 1% change in coercivity upon coating CoFe_2O_4 with silica.

The energy barrier (E_A) for rotation of magnetization orientation in a single domain particle has been described by the Stoner-Wohlfarth theory and is given by

$$E_A = KV \sin^2\theta \quad (10.1)$$

where K is the anisotropy of the material, V is the volume of the nanoparticle, and θ is the angle between an applied magnetic field and the easy axis of a nanoparticle.²¹ The blocking temperature of a material is defined as the temperature for a given measurement time at which the moments are no longer blocked and are able to overcome the energy barrier E_A . The coercivity can be considered as a measure of the magnetic field strength

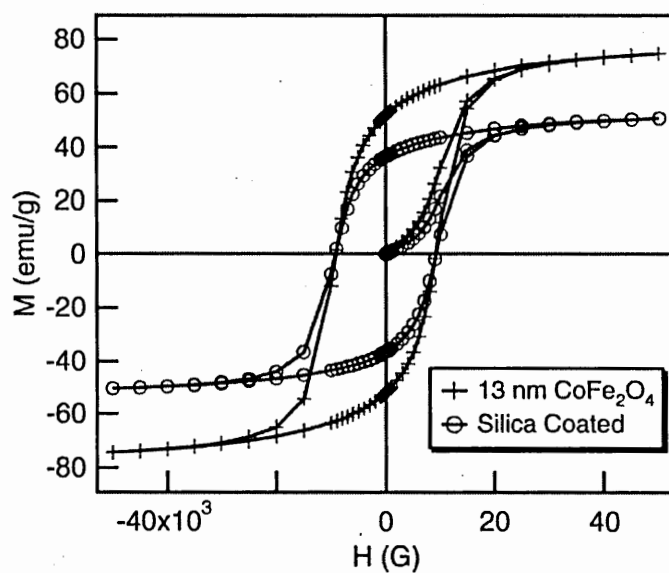


Figure 10.3 Field dependent magnetization at 5 K for 13 nm CoFe_2O_4 nanoparticles before and after silica coating

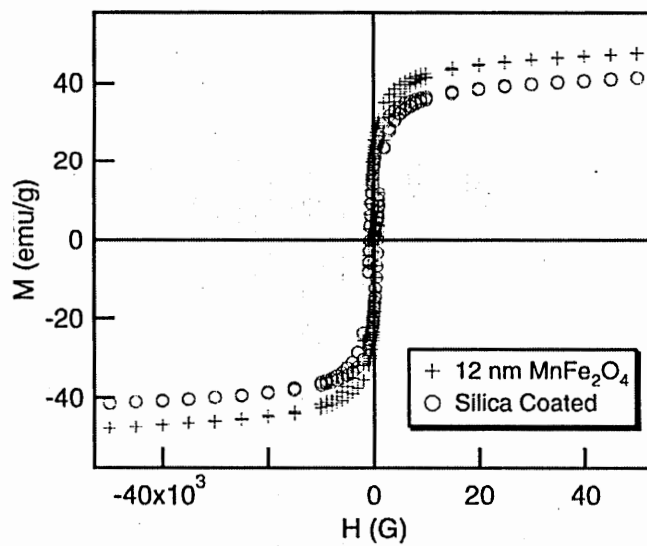


Figure 10.4 Field dependent magnetization at 5K for 12 nm MnFe_2O_4 nanoparticles before and after silica coating

that is required to achieve changes of magnetization direction in a material.²² Lowering the anisotropy of a material will lower the activation energy barrier following Equation 10.1 and results in a lower blocking temperature and a lower applied field required for spin reversal, i.e. a lower coercivity. As the observed magnetic properties of nanoparticles are a combination of many anisotropy mechanisms such as magnetocrystalline anisotropy, surface anisotropy and interparticle interactions, coating ferrite nanoparticles with silica will likely affect the contributions of the surface anisotropy and interparticle interactions to the net anisotropy K .

Many authors have reported lower blocking temperatures and smaller coercivities for ferrofluid samples when interparticle interactions are decreased via dilution.^{23,24} However, the effects are typically seen when the volume fraction of nanoparticles is < 10-20%. At larger packing fractions, the magnitude of the particle-particle separations as a function of particle volume concentration is likely not significantly reduced to resolve changes in properties. In this study, the blocking temperature of the ferrite-silica particles did not change with respect to the native ferrite and the coercivity of the CoFe_2O_4 -silica particles also did not change within experimental error. In Chapter 7, the effect of dilution upon the magnetic properties of CoFe_2O_4 was discussed. The blocking temperature of ~ 8.5 nm CoFe_2O_4 remained constant at 236 ± 1 K down to 5% mass percentage dilutions. At 0.005%, the blocking temperature was diminished to only 230 K from the “bulk” undiluted sample. At the volume fraction of the CoFe_2O_4 nanoparticle dispersed in the silica in this study, such dilution is likely not great enough to result in a change in the blocking temperature or coercivity.

The magnetic properties observed for the ferrite-silica particles are more consistent with changes to the surface anisotropy. Néel first proposed the presence of surface anisotropy to account for the effects of symmetry reduction at nanoparticle surfaces upon spin-orbit couplings.²⁵ The surface anisotropy (K_s) of a nanoparticle contributes to the total magnetic anisotropy as

$$K = K_{\text{xtal}} + (6/d) K_s \quad (10.2)$$

where K_{xtal} is the “bulk” magnetocrystalline anisotropy and d is the particle diameter.²⁶ Because the surface anisotropy is known to decrease upon coating,²⁷ K will become smaller and hence a smaller coercivity is expected. Recently Vestal and Zhang have reported that ligands, such as benzoic acid, bound onto the surface of MnFe_2O_4 nanoparticles will reduce the coercivity with respect to the native MnFe_2O_4 nanoparticle and can be explained as a reduction of the surface anisotropy.²⁸ Despite the decrease in coercivity, the blocking temperature of the modified particles remained constant. A similar result is found here; the coercivity of MnFe_2O_4 -silica particles decreases by ~10% with respect to the native MnFe_2O_4 nanoparticle, but the blocking temperature does not vary. This consistency suggests that the changes in the surface anisotropy lead to the observed magnetic behavior of the ferrite-silica particles.

The fact that the MnFe_2O_4 -silica particles display a coercivity decrease, while CoFe_2O_4 -silica particles show no coercivity change is likely due to the different contribution of the magnetocrystalline anisotropy to the net anisotropy of the sample. The MnFe_2O_4 nanoparticles have a weaker magnetocrystalline anisotropy ($K = 0.056$

J/cm^3),²⁹ while the magnetic anisotropy in CoFe_2O_4 nanoparticles is high ($K = 0.22 \text{ J}/\text{cm}^3$).¹⁸ After the formation of ferrite-silica nanoparticles, the surface anisotropy of the magnetic core is expected to change as discussed above. Similar changes in surface anisotropy (ΔK_s) as a result of coating with silica will display a more pronounced effect on K for ferrite-silica composite samples with a smaller magnitude of original magnetocrystalline anisotropy such as MnFe_2O_4 and hence a larger effect on H_C is observed. A similar result is observed for the effects of ligand modification upon the magnetic properties of MnFe_2O_4 and CoFe_2O_4 nanoparticles. For example, $\sim 4 \text{ nm}$ MnFe_2O_4 nanoparticles show a $\sim 50\%$ decrease in the coercivity after modification with benzenethiol.²⁸ However, the coercivity of $\sim 4 \text{ nm}$ CoFe_2O_4 after modification with benzenethiol decreases by only $\sim 7\%$.

The observed decrease in the magnetization values reflects the standard practice of normalizing the magnetization by sample mass. In the silica-coated samples, there is less magnetic material per gram and the magnetization readings are divided by substantial mass of silica. Consequently, both the saturation and remnant magnetization values decrease upon silica coating. Attempts to quantify the percentage of magnetic material in order to normalize by mass of magnetic material have been unsuccessful as methods to dissolve the silica coating also destroy or alter the ferrite particles. Other reports follow a similar methodology and report the magnetic properties per silica + magnetic nanoparticle net mass.^{9,16,17,30} The reduced remanence value (M_R/M_S) does not significantly change from the native CoFe_2O_4 nanoparticles (0.64) and the silica coated core-shell nanoparticles (0.67). Similarly, the reduced remanence remains comparable for the uncoated MnFe_2O_4 nanoparticles (0.43) and the silica-coated sample (0.41). This

consistency in the shape of the hysteresis curves further confirms that the observed decreases in magnetization are primarily due to a lower amount of magnetic material per mass rather than any potential magnetic couplings of spins at the interface between the magnetic nanoparticulate core and the silica shell matrix.

10.4 Conclusion

In summary, two spinel ferrite MFe_2O_4 ($M = Co, Mn$) nanoparticles have been coated with silica using a reverse micelle microemulsion method. Both spinel ferrite core materials were prepared prior to encapsulating with silica and therefore, versatility in the selection of the magnetic core is possible without the need to develop a new set of synthesis conditions when a new magnetic core is desired. Magnetic measurements show a reduction in saturation and remanent magnetization that is attributed to the reduced portion of magnetic material per gram of ferrite-silica composite nanoparticles. The coercivity of $MnFe_2O_4$ -silica nanoparticles decreases a small amount from the value in native magnetic nanoparticles, which was not observed for the $CoFe_2O_4$ -silica system. This decrease is likely due to the larger contribution of the surface anisotropy to the total anisotropy of $MnFe_2O_4$ nanoparticles due to its weaker magnetocrystalline anisotropy. Using the reverse micelle microemulsion method, a wide range of spinel ferrite nanoparticle cores can easily be coated with a silica shell. Such a method increases the potential for development of tunable magnetic silica for magneto-electronic and biomedical applications.

10.5 References

- (1) Sun, S.; Murray, C. B.; Weller, D.; Folks, L.; Moser, A. *Science* **2000**, 287.
- (2) Häfeli, U.; Schütt, W.; Teller, J.; Zborowski, M., Eds. *Scientific and Clinical Applications of Magnetic Carriers*; Plenum: New York, 1997.
- (3) Caruso, F. *Adv. Mater.* **2001**, 13, 11.
- (4) Krauss, P. R.; Chou, S. Y. *Appl. Phys. Lett.* **1997**, 71, 3174.
- (5) Qhobosheane, M.; Santra, S.; Zhang, P.; Tan, W. *Analyst* **2001**, 126, 1274.
- (6) Gerion, D.; Pinaud, F.; Williams, S. C.; Parak, W. J.; Zanchet, D.; Weiss, S.; Alivisatos, A. P. *J. Phys. Chem. B* **2001**, 105, 8861.
- (7) Levy, L.; Sahoo, Y.; Kim, K. S.; Bergey, E. J.; Prasard, P. N. *Chem. Mater.* **2002**, 14, 3715.
- (8) Atarashi, T.; Kim, Y. S.; Fujita, T.; Makatsuka, K. *J. Magn. Magn. Mater.* **1999**, 201, 7.
- (9) Santra, S.; Tapeç, R.; Theodoropoulou, N.; Dobson, J.; Hebrad, A.; Tan, W. *Langmuir* **2001**, 17, 2900.
- (10) Wang, H.; Nakamura, H.; Yao, K.; Maeda, H.; Abe, E. *Chem. Lett.* **2001**, 7, 1168.
- (11) Correa-Duarte, M. A.; Giersig, M.; Kotov, N. A.; Liz-Marzan, L. M. *Langmuir* **1998**, 14, 6430.
- (12) Liu, Q.; Xu, Z.; Finch, J. A.; Egerton, R. *Chem. Mater.* **1998**, 10, 3936.
- (13) Kltoz, M.; Ayrat, A.; Guizard, C.; Ménager, C.; Cabuil, V. *J. Colloid Interf. Sci.* **1999**, 220, 357.

- (14) Tartaj, P.; González-Carreño, T.; Serna, C. J. *J. Phys. Chem. B* **2003**, *107*, 20.
- (15) Phillipse, A. P.; Bruggen, M. P. B. v.; Pathmamanoharan, C. *Langmuir* **1994**, *10*, 92.
- (16) Grasset, F.; Labhsetwar, N.; Li, D.; Park, D. C.; Saito, N.; Haneda, H.; Cador, O.; Roisnel, T.; Mornet, S.; Duguet, E.; Portier, J.; Etourneau, J. *Langmuir* **2002**, *18*, 8209.
- (17) Tago, T.; Hatsuta, T.; Miyajima, K.; Kishida, M.; Tashiro, S.; Wakabayashi, K. *J. Am. Ceram. Soc.* **2002**, *85*, 2188.
- (18) Rondinone, A. J.; Samia, A. C. S.; Zhang, Z. J. *J. Phys. Chem. B* **1999**, *103*, 6876.
- (19) Liu, C.; Zou, B.; Rondinone, A. J.; Zhang, Z. J. *J. Phys. Chem. B* **2000**, *104*, 1141.
- (20) Arriagada, F. J.; Osseo-Asare, K. *J. Colloid Interf. Sci.* **1999**, *211*, 210.
- (21) Stoner, E. C.; Wohlfarth, E. P. *Phil. Trans. Roy. Soc. A* **1948**, *240*, 599.
- (22) Bertotti, G.; Academic Press: San Diego, 1998, p 10.
- (23) El-Hilo, M.; O'Grady, K.; Chantrell, R. W. *J. Magn. Magn. Mater.* **1992**, *114*, 295.
- (24) Dormann, J. L.; Fiorani, D.; Tronc, E. *J. Magn. Magn. Mater.* **1999**, *202*, 251.
- (25) Néel, L. *J. Phys. Radium* **1954**, *15*, 225.
- (26) Dimitrov, D. A.; Wysin, G. M. *Phys. Rev. B* **1994**, *50*, 3077.
- (27) Gradmann, U. *J. Magn. Magn. Mater.* **1991**, *100*, 481.
- (28) Vestal, C. R.; Zhang, Z. J. *J. Am. Chem. Soc.* **2003**, *125*, 9828.

- (29) Rondinone, A. J.; Liu, C.; Zhang, Z. J. *J. Phys. Chem. B* **2001**, *105*, 7967.
- (30) Aliev, F. G.; Correa-Duarte, M. A.; Mamedov, A.; Ostrander, J. W.; Giersig, M.; Liz-Marzan, L. M.; Kotov, N. A. *Adv. Mater.* **1999**, *11*, 1006.

APPENDIX A

SYNTHESIS OF MAGNESIUM ALUMINUM OXIDE/COBALT FERRITE CORE/SHELL NANOPARTICLES AND THEIR MAGNETIC CHARACTERIZATION

Abstract

Magnesium aluminum oxide, MgAl_2O_4 spinel nanoparticles have been synthesized using normal micelle microemulsion methods. A mixed magnesium-aluminum hydroxide is initially formed which after annealing at 600 °C forms nanocrystalline MgAl_2O_4 spinel. By controlling reactant concentration in the micelle solution, the particle size has been tuned over the range 4 – 20 nm. The reaction pathways have been determined by using the characterization methods such as X-ray diffraction, thermogravimetric analysis (TGA) and differential scanning calorimetry (DSC). Core/shell $\text{MgAl}_2\text{O}_4/\text{CoFe}_2\text{O}_4$ nanoparticles were prepared using seed-mediated methods. The magnetic properties showed unusual behavior – coercivity increased with shell thickness, while the blocking temperature decreased then increased with shell thickness.

A.1 Introduction

Spinel proper, MgAl_2O_4 is used in a wide range of applications such as catalysis and sensors.¹⁻³ For many of its applications, a high surface area is greatly desired. Nanometer-sized spinel particles certainly offer great advantages for the fulfillment of this requirement.⁴ Nanosize spinel particles have been previously prepared by methods such as sol-gel, spray-drying, complexation, co-precipitation, and decomposition of metal alkoxides.⁵⁻⁸ Although these synthesis routes produce nanosized particles, ease of tuning particle size is difficult. Furthermore, most of the above-described methods require employing costly equipment. The expensive and moisture-sensitive precursors in these methods also drive up the cost greatly for producing large quantities of high surface area MgAl_2O_4 powders.

Over the past decade, microemulsion synthesis methods utilizing normal micelles have emerged as a versatile route to form a wide range of nanoparticle materials. Metal (e.g. Cu), semiconductor (e.g. CdS), and spinel ferrite (e.g. CoFe_2O_4) nanoparticles with low size dispersity have been prepared using this method.⁹⁻¹² One advantage of this versatile method is that the nanoparticle size can be easily adjusted by small condition changes in the synthesis procedure. For example, chemometric modeling has shown that adjusting the metal cation concentration and the reaction temperature allow control over the size of spinel ferrite nanoparticle.¹³ The feasibility of using these simple synthesis adjustments to control nanoparticle size was demonstrated for a range of spinel ferrite nanoparticles - CoFe_2O_4 , ZnFe_2O_4 , and MgFe_2O_4 , which possess unique and important magnetic properties. MgAl_2O_4 spinel nanoparticles are non-magnetic. However, they have the same features in terms of crystallographic structures, chemical coordinations and

bonding. Moreover, the surface structure of the nanoparticles is the same. The successful synthesis of MgAl_2O_4 spinel nanoparticles using similar microemulsion methods will help us in understanding of magnetic properties of spinel ferrite nanoparticles at the atomic level.

Here the use of normal micelle microemulsion methods for the synthesis of MgAl_2O_4 nanoparticles is reported. This aqueous method uses readily available, inexpensive, and easily handled precursors of $\text{Mg}(\text{NO}_3)_2$ and $\text{Al}(\text{NO}_3)_3$, and eliminates the extra handling requirements that usually associate with moisture sensitive precursors. Using the chemometric model developed in normal micelle microemulsion methods for size control synthesis of spinel ferrite MFe_2O_4 nanoparticles, the size of the MgAl_2O_4 nanoparticles can be tuned by minor adjustments to the synthesis conditions. Furthermore, the synthesis and magnetic properties of core/shell magnetic nanoparticles with MgAl_2O_4 nanoparticles used as a non-magnetic core and CoFe_2O_4 serving as a shell material are discussed. As the core is non-magnetic this system provides a unique opportunity to isolate the contributions of a magnetic surface to the magnetic properties.

A.2 Experimental

A.2.1 MgAl_2O_4 Nanoparticle Synthesis

A normal micelle microemulsion method was used to prepare MgAl_2O_4 spinel nanoparticles. Aqueous solutions of $\text{Mg}(\text{NO}_3)_2$ (Fisher, 0.008M) and $\text{Al}(\text{NO}_3)_3$ (Fisher, 0.016M) were added to an aqueous solution sodium dodecyl sulfate (Aldrich, 0.090M) to

form the normal micelles. NH_4OH (Fisher, 30% wt) was added dropwise until the pH reached ~ 10.3 , and then the solution was stirred overnight. Ethanol was added to flocculate the particles and the precipitate was collected by centrifugation. The samples were dried in a 100°C oven for one hour, then ground and annealed in a tube furnace at 800°C for 20 hours. Following the chemometric model developed by Rondinone, et.al.¹³ the particle size was varied by adjusting the metal cation concentration in solution while keeping a 1:2 ratio between Mg and Al cations respectively.

A.2.2 Synthesis of $\text{MgAl}_2\text{O}_4/\text{CoFe}_2\text{O}_4$ Core/Shell Nanoparticles

$\text{MgAl}_2\text{O}_4/\text{CoFe}_2\text{O}_4$ core/shell nanoparticles were prepared using a seed-mediated method. MgAl_2O_4 nanoparticles with mean size 7.7 nm were prepared as described above. The nanoparticle were then stirred in concentrated NaOH overnight and subsequently collected by centrifugation. The particles were rinsed with water and recollected by centrifugation. The MgAl_2O_4 nanoparticles were then sonicated in 100mL 0.045 M aqueous sodium dodecyl sulfate solution. To this solution 0.0742g CoCl_2 and 0.12g FeCl_2 dissolved in 60 mL water was added and the mixture stirred overnight. The solution was then heated to 70°C . Methylamine (23mL) was diluted up to 120mL with water and added to the heated nanoparticle/metal cation solution and stirred at 70°C for 1 hour. After cooling, the samples were centrifuged and washed with EtOH/water. The sample color was reddish-brown. The shell thickness was varied by adjusting the amount of MgAl_2O_4 seed nanoparticles used in the reaction.

A.2.3 Instrumentation

X-ray diffraction patterns were collected on a Bruker D8 Advance x-ray diffractometer using Cu K- α radiation. Particle sizes were determined from the average broadening of the five strongest diffraction peaks using the Scherrer equation.

Transmission electron microscopy (TEM) experiments were performed on a JEOL 100C operating at 100 kV. High-resolution TEM studies were performed on a Hitachi HF-2000 field emission gun TEM operating at 200kV equipped with an EDS spectrometer.

SQUID measurements were performed on a Quantum Design MPMS-5S magnetometer.

Thermogravimetric analysis (TGA) and differential scanning calorimetry (DSC) were collected at a heating rate of 17°C /min to 1000°C using a Netzsch Luxx STA 409 PG.

The specific surface area was measured using a Micromeritics ASAP 2000 with the BET method using nitrogen gas.

A.3 Results and Discussion

A.3.1 Synthesis and Characterization of MgAl_2O_4

Normal micelle microemulsion methods are able to produce MgAl_2O_4 nanoparticles having mean diameters from 4 – 20 nm. In order to obtain a stable microemulsion with a clear solution of the metal cations and surfactant as compared to a turbid cloudy solution, an excess of the sodium dodecyl sulfate surfactant was required. When low concentrations of the metal cations were used smaller sized MgAl_2O_4 nanoparticles were obtained. This is consistent with the chemometric model established by Rondinone, et. al. for size control of spinel ferrite nanoparticles using this normal micelle method.¹³ Although the chemometric model indicated increasing the reaction

temperature results in larger sized nanoparticles for the spinel ferrite systems, this was not observed in the MgAl_2O_4 synthesis. By testing a variety of bases such as KOH, NaOH, NH_4OH , and TPAOH, it was clear that the choice of base also did not affect the nanoparticle size. However, it is critical to maintain a pH below 11, otherwise MgO impurities are formed. This results from the formation of a soluble aluminum species, $\text{Al}(\text{OH})_4^-$ at $\text{pH} > 12$, thereby creating an excess of Mg species in the precipitate.

The x-ray diffraction pattern of the dried precipitate is shown in Figure A.1a. The peaks do not match with peak positions for MgAl_2O_4 , $\text{Al}(\text{OH})_3$, or $\text{Mg}(\text{OH})_2$, but agree

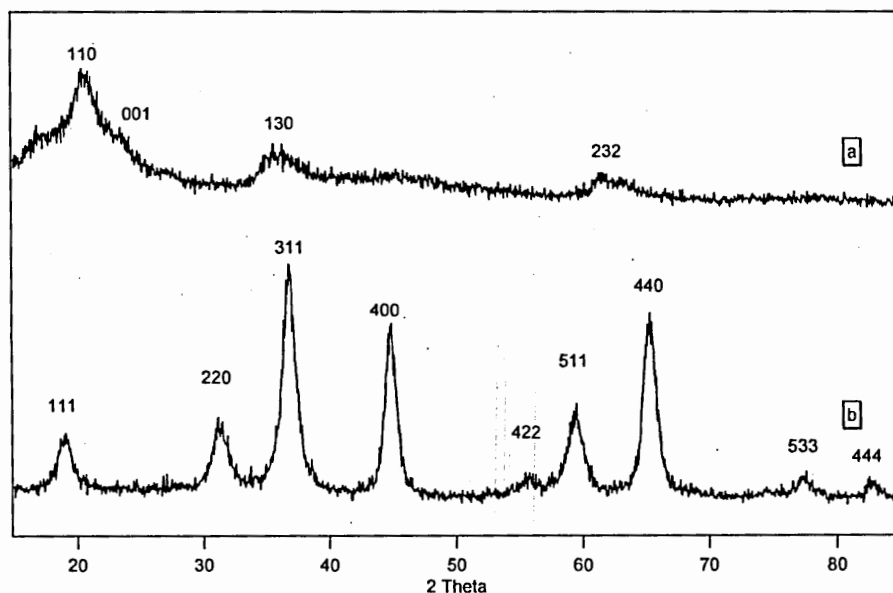


Figure A.1. X-ray diffraction patterns for (a) the initial precipitated white powder and (b) 8 nm MgAl_2O_4 nanoparticles formed after annealing the powder sample shown in (a).

closely with a mixed magnesium-aluminum hydroxide phase of $\text{MgAl}_2(\text{OH})_8$ (Table A.1). It is worthwhile to notice that the quality of standard X-ray diffraction pattern of $\text{MgAl}_2(\text{OH})_8$ is not fully satisfactory. After heating the sample to just 300 °C, these peaks disappear and the x-ray diffraction studies show only an amorphous phase. Bragg diffraction peaks of MgAl_2O_4 are observed when the samples are annealed at 800 °C for 20 hours (Figure A.1b). Table A.2 shows clearly that the peaks match very well with the standard X-ray diffraction pattern of MgAl_2O_4 . A typical TEM micrograph for the annealed sample shown in Figure A.2 indicates the formation of spherical particles. The size determined from the Scherrer fitting of the broadened x-ray diffraction peaks agreed well with the direct TEM observations. BET analysis of the 20 nm spinel nanoparticles yielded a surface area of 79.0 m²/g. After the annealing temperature is raised to 1100 °C, bulk phase spinel is formed (Table A.2).

Table A.1. d-spacing Comparison for Initial Precipitate and $\text{MgAl}_2(\text{OH})_8$

d - dried precipitate (Å)	d- $\text{MgAl}_2(\text{OH})_8$ (Å) ^a	hkl
5.035	4.790	110
4.320	4.370	001
2.447	2.428	130
1.976	1.953	112
Not observed	1.508	-331
1.464	1.455	232

^a Reference ICDD-PDF Card # 35-1274. Quality (i)

Table A.2. *d*-space Comparison for Spinel Samples

<i>d</i> - nanoparticle (Å)	<i>d</i> - annealed at 1100°C (Å)	<i>d</i> - MgAl ₂ O ₄ (Å) ^b	<i>hkl</i>
4.673	4.684	4.660	111
2.862	2.865	2.858	220
2.439	2.441	2.437	311
Not observed	2.339	2.335	222
2.021	2.025	2.020	400
1.649	1.651	1.650	422
1.555	1.557	1.555	511
1.428	1.430	1.429	440
Not observed	1.366	1.366	531
Not observed	1.271	1.278	620
1.233	1.233	1.233	533
Not observed	1.217	1.219	622
1.166	1.168	1.167	444

^b Reference ICDD-PDF Card #21-1152. Quality (*)

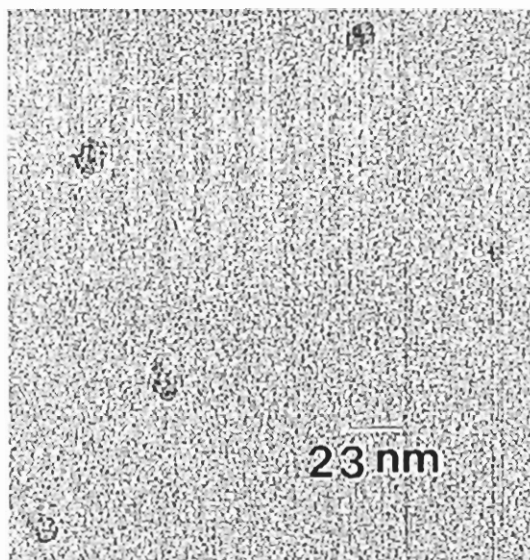


Figure A.2. TEM micrograph of 13 nm MgAl_2O_4 nanoparticles.

The TGA/DSC curves for MgAl_2O_4 nanoparticulate samples showed a 6% mass loss from 30-150 °C associated with an endothermic peak that is characteristic of the loss of adsorbed water. No other features were observed with the rising temperature, indicating once formed, this nanostructure of spinel is very stable.

The reaction pathways in the formation of MgAl_2O_4 nanoparticles are determined with the thermal analysis in combination with x-ray diffraction studies. The TGA/DSC curves for the initial dried precipitate are shown in Figure A.3. In the TGA curve, three clear mass losses occurred. The first was a broad 10% weight loss over the temperature range 30-200 °C. The next mass loss of 25% occurred at 220-280 °C and followed by a sharp 7% decrease at 310 °C. At higher temperatures, the sample still slowly loses weight until ~ 525 °C when the weight loss levels. The DSC study shows corresponding

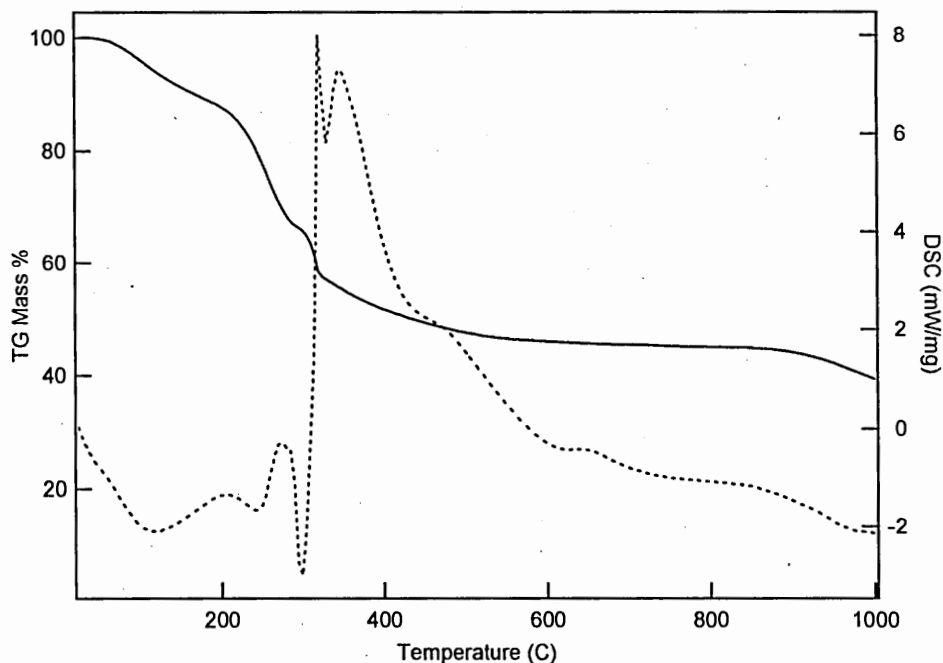


Figure A.3. TGA (solid line) and DSC (dashed line) curves for precipitated product.

endothermic peaks over the temperature range of the first two mass losses. Around the third mass loss, a complicated overlap of endothermic and exothermic peaks was observed. A weak exotherm was also observed at $\sim 625^{\circ}\text{C}$.

In order to determine what is occurring between 200-450 $^{\circ}\text{C}$ in the DSC curve for the initial precipitate, TGA/DSC studies were performed on $\text{Al}(\text{OH})_3$ and $\text{Mg}(\text{OH})_2$ samples. The results are presented in Figures A.4 and A.5, respectively. Three mass loss regions are observed in the $\text{Al}(\text{OH})_3$ sample. The first two mass loss regions of 30-180 $^{\circ}\text{C}$ and 220-380 $^{\circ}\text{C}$ exhibit sharp endothermic peaks in the DSC curve. The third region of 380-500 $^{\circ}\text{C}$ shows a weaker endotherm (Figure A.4). After the initial adsorbed water loss, the $\text{Mg}(\text{OH})_2$ sample displayed two regions of mass loss with one in 330-370 $^{\circ}\text{C}$ and a shoulder at 370-420 $^{\circ}\text{C}$ with corresponding endothermic peaks in the DSC curve.

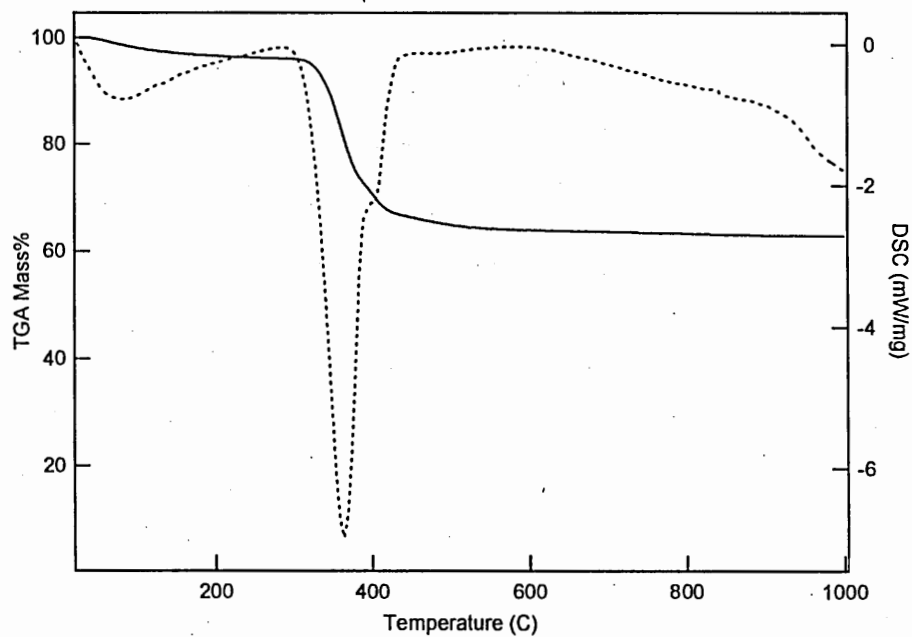


Figure A.4. TGA (solid line) and DSC (dashed line) curves for $\text{Al}(\text{OH})_3$ standard.

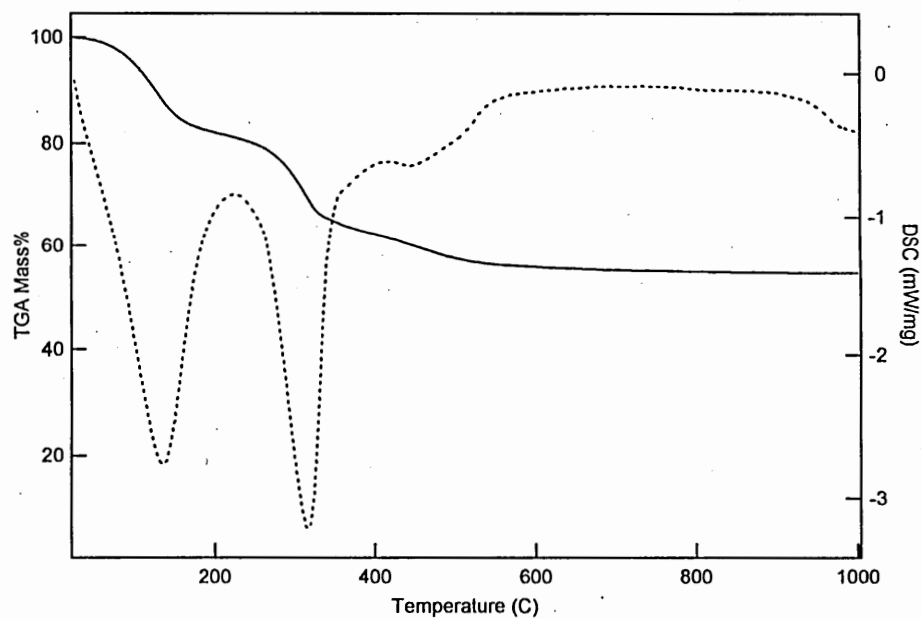


Figure A.5. TGA (solid line) and DSC (dashed line) curves for $\text{Mg}(\text{OH})_2$ standard.

The transitions for the aluminum and magnesium hydroxide standards do not match exactly with the weight loss regions and DSC curves for the initial precipitated sample in the synthesis of MgAl_2O_4 nanoparticles shown in Figure A.3. However, as the x-ray diffraction studies suggest that the precipitated sample is a magnesium-aluminum mixed hydroxide, they may still provide some insights for interpreting the transitions in the precipitated products. The first region of mass loss in 30-200 °C with an associated endothermic peak is likely due to the loss of adsorbed water than has been seen in all of the samples. The next two endothermic peaks with maxima at 240 °C and 300 °C may be associated with the loss of hydroxide from aluminum in the mixed magnesium-aluminum hydroxide sample. During the third mass loss at 310 °C, a large exothermic peak begins, which is immediately followed by an endothermic transition likely resulting from the loss of hydroxide from magnesium in the mixed hydroxide. After the interruption of this loss transition, the rest of the exothermic peak continues. This large exothermic peak is likely the result of a phase transition from the $\text{MgAl}_2(\text{OH})_8$ phase to the oxide phase. This transition is likely initiated by the loss of hydroxide associated with the endothermic peaks. Such a phase transition is consistent with the x-ray diffraction results that indicate the disappearance of hydroxide phase after annealing at 300 °C. The weak exothermic peak at 650 °C with no corresponding mass loss is likely the crystallization transition in which the amorphous oxide powder becomes nanocrystallites and the lattice energy is released. This is also in a very good agreement with the results from x-ray diffraction studies. At 700 °C, very weak Bragg reflections are finally observed.

A.3.2 Preliminary Characterization of Core/Shell Nanoparticles

An x-ray diffraction pattern for the core/shell nanoparticle is shown in Figure A.6. Although very weak, peaks of CoFe_2O_4 appear as shoulders in the x-ray patterns. The EDS spectrum taken of the nanoparticles with the electron beam focused at the edge of the particle and at the center are shown in Figure A.7 and A.8. It is clear that the EDS spectrum shows strong Co and Fe peaks (and weak Mg and Al peaks due to slight beam drift) when the beam is focused on the edge of the nanoparticle and strong Mg, and Al peaks with weak Co and Fe peaks when the beam is focused at the center of the particle. Such findings confirm a core/shell structure. Core/shell samples were not formed when the amount of MgAl_2O_4 nanoparticle seed was less than 0.03g.

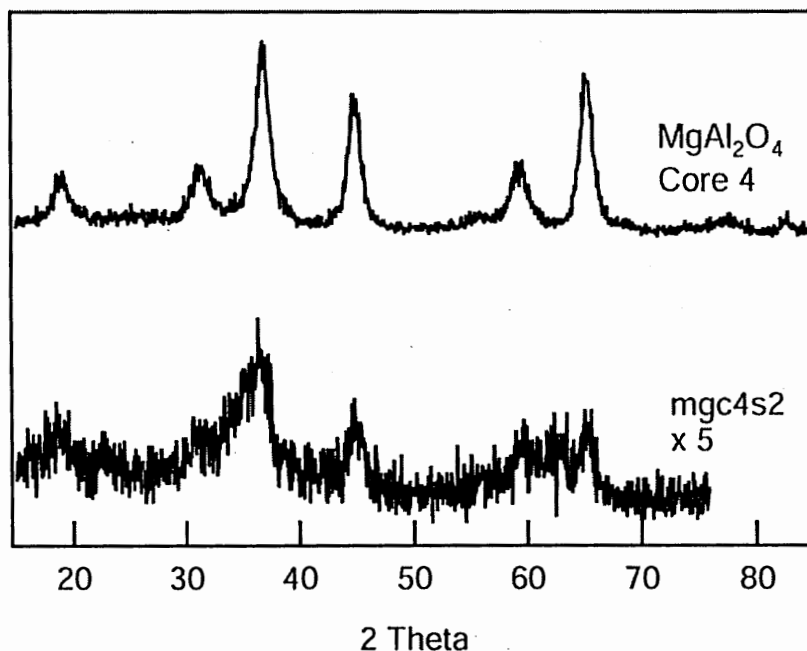


Figure A.6. X-ray diffraction patterns for (top) MgAl_2O_4 core and (bottom) same core after seed-mediated synthesis.

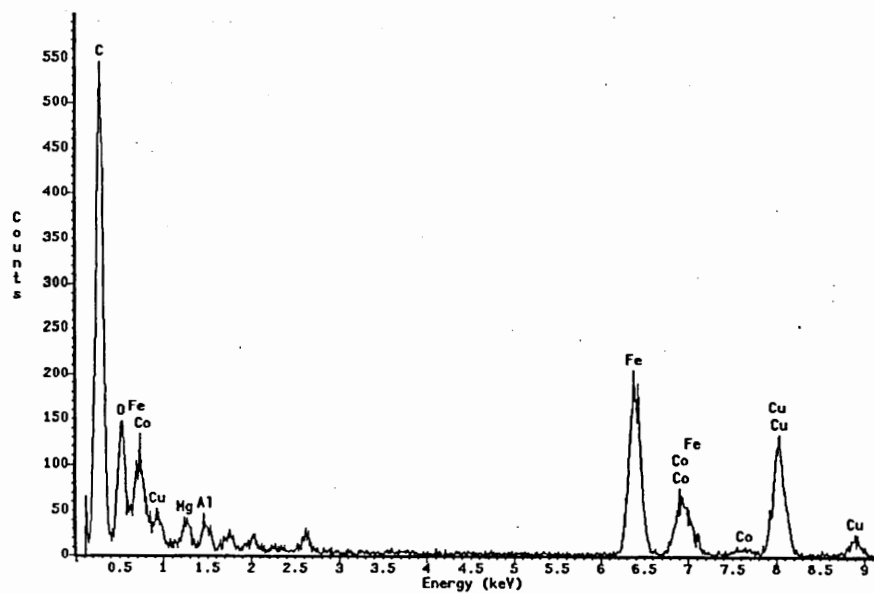


Figure A.7. TEM-EDS spectrum taken near edge of nanoparticle.

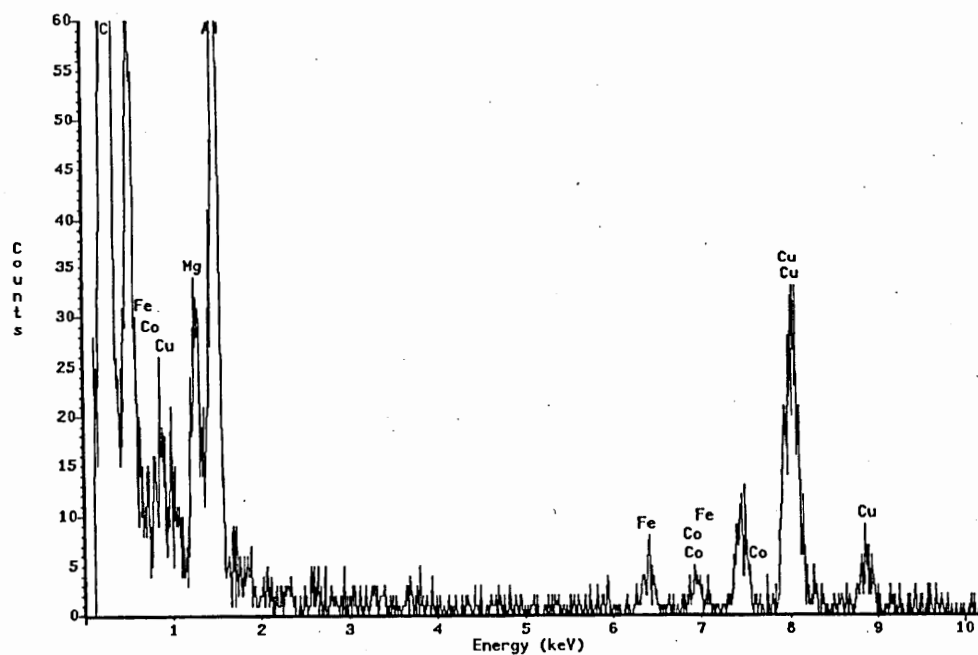


Figure A.8. TEM-EDS spectrum taken at center of nanoparticle.

The effect of increasing the CoFe_2O_4 shell thickness upon the blocking temperature is shown in Figure A.9 as a function of saturation magnetization. The saturation magnetization was used instead of shell thickness due to the error in estimating the shell thickness from x-ray studies, as increases in magnetization will occur with increasing volume of CoFe_2O_4 . The blocking temperature shows a decrease with increasing shell thickness, followed by an increase at larger volumes of CoFe_2O_4 . The effect of the shell thickness upon the coercivity is shown in Figure A.10. The coercivity increases with shell thickness over the entire range.

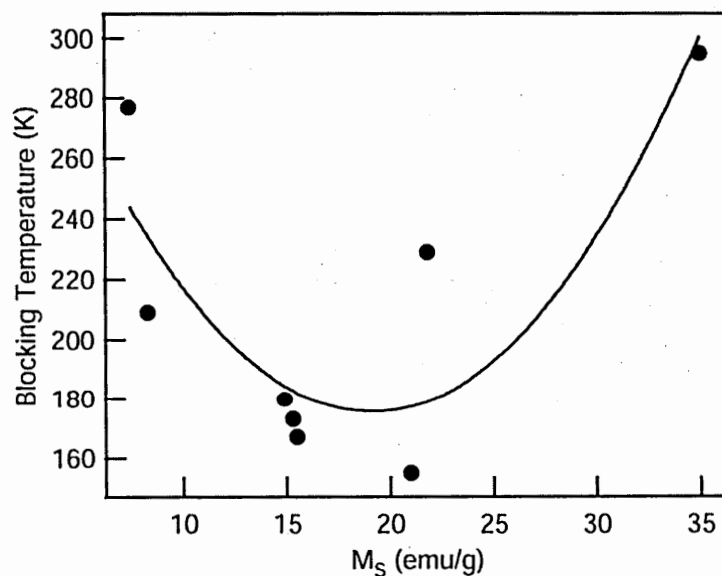


Figure A.9. Blocking temperature of $\text{MgAl}_2\text{O}_4/\text{CoFe}_2\text{O}_4$ core/shell nanoparticles as a function of saturation magnetization (M_S).

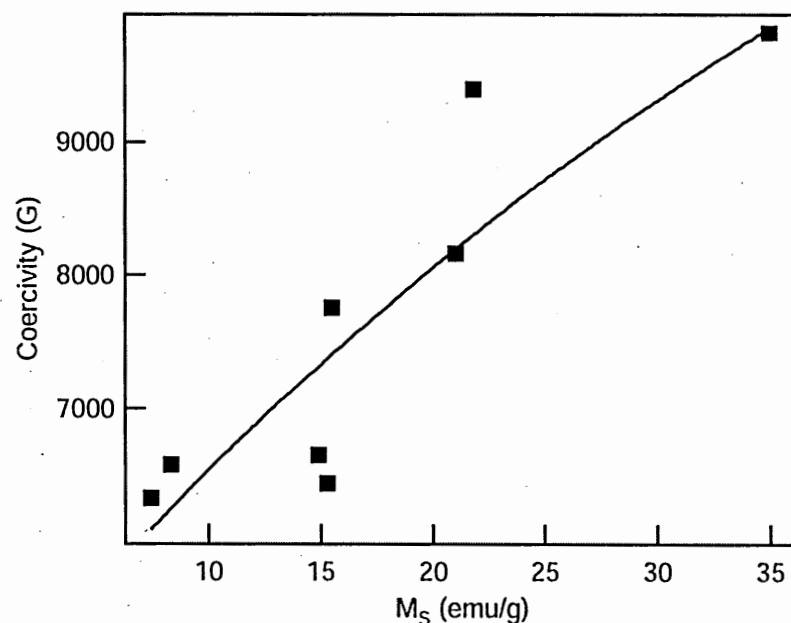


Figure A.10. Coercivity as a function of saturation magnetization (M_S) for $\text{MgAl}_2\text{O}_4/\text{CoFe}_2\text{O}_4$ core/shell nanoparticles.

The diverging behavior of the coercivity and blocking temperature is quite interesting. The coercivity represents the field strength required to move the magnetization from one direction to another, while the blocking temperature represents the temperature at which the magnetization vector can rotate from one direction to another. Traditionally, the two factors show the same trend as a function of particle size. As the core of the nanoparticle is non-magnetic, coherent rotation of the magnetization as described by Stoner-Wohlfarth theory certainly cannot occur and may be the root of the apparent discrepant data. The large blocking temperature at low shell thickness suggests that the surface moments experience difficulty in rotating the magnetization. This is likely the result of the lack of cooperative behavior between the moments due to the missing magnetically ordered core. The magnetization likely reverses by a curling-type

mechanism instead. As the shell thickness increases (from ~ 0.5 to 2 nm), the increase in magnetic volume appears to lead to coherency between the spins and it becomes easier to reverse the magnetization. At larger shell volumes, the blocking temperature increases again following a more classical Stoner-Wohlfarth approach. Changes in the reversal mechanism (for example from coherent rotation to curling) should be reflected in the coercivity. However, the increase in coercivity with shell thickness follows the commonly observed behavior of increased coercivity with magnetic nanoparticle diameter. This trend suggests that the magnetization reversal for thin shell materials is easy to overcome by an external magnetic field even though thermal activation of moment reversal is difficult. More studies are certainly needed to determine the origin of this unusual magnetic behavior.

A.4 Conclusions

MgAl_2O_4 spinel nanoparticles with mean size of $4\text{--}20\text{ nm}$ can be synthesized by using normal micelle microemulsion methods. Size control is achieved simply through adjusting the metal cation concentration in the synthesis process. X-ray diffraction combined with TGA/DSC studies suggests that the initial dried white precipitate is likely a mixed magnesium-aluminum hydroxide phase which loses water to form an amorphous oxide phase at $\sim 300\text{ }^\circ\text{C}$. The sample crystallizes at $\sim 650\text{ }^\circ\text{C}$ and forms nanocrystalline MgAl_2O_4 spinel. $\text{MgAl}_2\text{O}_4/\text{CoFe}_2\text{O}_4$ core/shell nanoparticles have been prepared using seed-mediated methods. The preliminary results show that the magnetic properties display interesting diverging behavior. The blocking temperature decreased, then increased with shell thickness. The coercivity, on the other hand, increased with

shell thickness over the entire range. The reasons for such behavior are currently not understood, but suggest differences in thermally activated versus field driven reversal of the magnetization vector.

A.5 References

- (1) Muraki, H.; Fujitani, Y. *Appl. Catalyst* **1989**, *47*, 75.
- (2) Sehested, J.; Carlsson, A.; Janssens, T. V. W.; Hansen, P. L.; Datye, A. K. *J. Catal.* **2001**, *197*, 200.
- (3) Seiyama, N.; Yamazoe, N.; Arai, H. *Sensor Actuator* **1983**, *4*, 85.
- (4) Kang, Y. C.; Choi, J. S.; Park, S. B. *Eur. Ceram. Soc.* **1998**, *18*, 641.
- (5) Varnier, O.; Hovnanian, N.; Larbot, A.; Bergez, P.; Cot, L.; Charpin, J. *Mater. Res. Bull.* **1994**, *29*, 479.
- (6) Montouillout, V.; Massiot, D.; Duoy, A.; Coutres, J. P. *J. Am. Ceram. Soc.* **1999**, *82*, 3299.
- (7) Wang, M.; Muhammed, M. *Mater. Sci. Forum* **1997**, *235-238*, 241.
- (8) Pati, R. K.; Pramanik, P. *J. Am. Ceram. Soc.* **2000**, *83*, 1822.
- (9) Pileni, M. P. In *Nanoparticles and Nanostructured Films*; Fendler, J. H., Ed.; Wiley - VCH: Weinheim, 1997, p 71.
- (10) Petit, C.; Jain, T. K.; Billoudet, F.; Pileni, M. P. *Langmuir* **1994**, *10*, 4446.
- (11) Moumen, N.; Pileni, M. P. *Chem. Mater.* **1996**, *8*, 1128.
- (12) Liu, C.; Rondinone, A. J.; Zhang, Z. J. *Pure Appl. Chem.* **2000**, *72*, 37.
- (13) Rondinone, A. J.; Samia, A. C. S.; Zhang, Z. J. *J. Phys. Chem. B* **2000**, *104*, 7919.

APPENDIX B

CHARACTERIZATION OF COBALT-ZINC FERRITE/ZINC FERRITE CORE/SHELL NANOPARTICLES USING SMALL ANGLE NEUTRON SCATTERING

Abstract

$\text{Zn}_{0.05}\text{Co}_{0.95}\text{Fe}_2\text{O}_4/\text{ZnFe}_2\text{O}_4$ core/shell nanoparticles were characterized using small angle neutron scattering (SANS). The scattering was measured for three samples - 12 nm $\text{Zn}_{0.05}\text{Co}_{0.95}\text{Fe}_2\text{O}_4$ core sample, the 12 nm $\text{Zn}_{0.05}\text{Co}_{0.95}\text{Fe}_2\text{O}_4$ with a 2.5 nm shell, and with a 4.5 nm shell. Crossovers in scattering intensity occurred with temperature. The R_g determined from the Guinier region was found to decrease with increasing shell thickness.

B.1. Introduction

Interest in nanosized magnetic particles has increased in the past few years due to their wide range of applications such as high density information storage, ferrofluid technology, magnetically guided drug delivery, and magnetic resonance imaging (MRI) contrast agents.¹⁻³ Two important magnetic parameters that are important for use of magnetic nanoparticles in biomedical applications are that they be superparamagnetic below room temperature and that they have a high magnetization. Magnetic nanoparticles need to be superparamagnetic at room temperature to keep them from agglomerating and particles with a large magnetization would allow for enhanced MRI contrast, a lower applied field gradient to be applied to the patient during magnetically guided drug delivery, and a reduced concentration of magnetic particles needed for delivery.

Recently, Samia and Zhang synthesized new magnetic nanoparticle materials with a core-shell architecture that show improved promise for meeting these demands.⁴ Specifically a series of ~12 nm $\text{Zn}_{0.05}\text{Co}_{0.95}\text{Fe}_2\text{O}_4$ nanoparticles with varying thickness ZnFe_2O_4 shells were prepared. The magnetic behavior of the samples changes rather dramatically upon the addition of the ZnFe_2O_4 shell. For example, $\text{Zn}_{0.05}\text{Co}_{0.95}\text{Fe}_2\text{O}_4$ samples coated with a 1 nm ZnFe_2O_4 shell displays blocking temperatures over 300K lower than the $\text{Zn}_{0.05}\text{Co}_{0.95}\text{Fe}_2\text{O}_4$ core material and a large decrease in coercivity is observed after the addition of the ZnFe_2O_4 shell. However, despite the large drop in blocking temperature and coercivity, the magnetization remained high. The reasons for such changes in magnetic behavior are not clear. It is important to understand what

contributions affect the magnetization in these core-shell materials in order to further rationally develop these materials as tailorable magnetic materials.

Small angle neutron scattering (SANS) is an ideal technique for investigating the influence of the core-shell structure upon compositional and magnetic components and can provide useful information as to the influence of the shell thickness upon the magnetic correlation length and interparticle couplings. It is anticipated that the highly anisotropic $\text{Zn}_{0.05}\text{Co}_{0.95}\text{Fe}_2\text{O}_4$ core has a strong influence in aligning magnetic moments in the ZnFe_2O_4 shell and such interactions may lead to the observed changes in magnetic properties. Furthermore, the presence of a shell material may reduce interparticle exchange interactions and thereby also be affecting the measured magnetic response. Here preliminary temperature dependent small angle neutron scattering studies are reported for the 12 nm $\text{Zn}_{0.05}\text{Co}_{0.95}\text{Fe}_2\text{O}_4$ core sample, the 12 nm $\text{Zn}_{0.05}\text{Co}_{0.95}\text{Fe}_2\text{O}_4$ with a 2.5 nm shell, and with a 4.5 nm shell.

B.2. Experimental

Small angle neutron scattering studies were performed in collaboration with Dr. Julie Borchers from the National Institute of Standards and Technology (NIST). Experiments were performed using the 30m NG-3 SANS at the NIST Center for Neutron Research (NCNR). The powder samples were loaded into aluminum foil “pockets” and placed into a sample holder designed by Yumi. The samples were sealed inside a dry He-filled glovebox. A closed-cycle He refrigerator was used for temperature control. Data were collected with the detector position at 3m, 9m, and 13m and a wavelength of 8Å. Experiments were performed from 12K to 320K in 5 K increments for the sample with

shell thickness 4.5nm. Scattering at temperatures from 40K to 425K were measured for the sample with shell thickness 2.5nm, and 40K to 450K for the core sample. Background, empty cell, and transmission patterns were also collected at each temperature. Data reduction was performed using an IGOR Pro program written by Steven Kline.

B.3. Results and Discussion

Figures B.1 and B.2 summarized the effects of variable shell thickness upon the magnetic properties of $\text{Zn}_{0.05}\text{Co}_{0.95}\text{Fe}_2\text{O}_4/\text{ZnFe}_2\text{O}_4$ core/shell nanoparticles. From Figure B.1. it is clear that the blocking temperature drops dramatically upon coating with a thin shell layer, then continues to decrease with increasing shell thickness. Figure B.2 shows that the saturation magnetization remains high (nearly constant) even after coating, but at higher shell thickness, it begins to decrease.

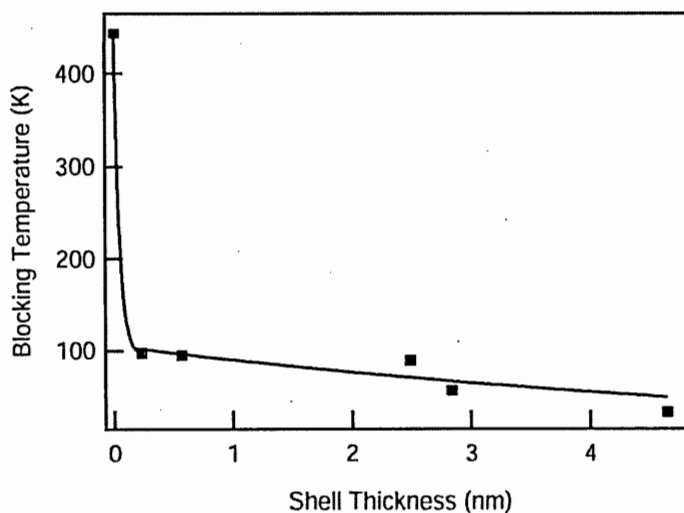


Figure B.1. Effect of ZnFe_2O_4 shell thickness upon the blocking temperature.

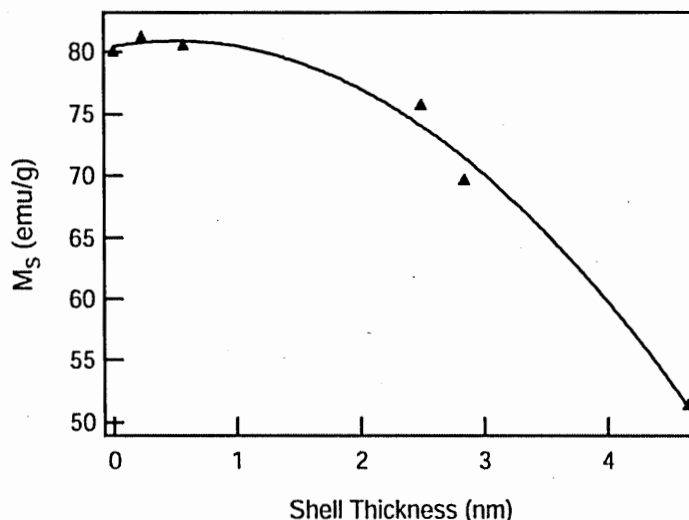


Figure B.2. Effect of ZnFe_2O_4 shell thickness upon saturation magnetization (M_s)

Figure B.3 shows typical raw SANS data. To determine the scattering intensity as a function of q this raw data is reduced using a NIST in-house designed program. The data reduction program incorporates the empty cell scans, other background scans, and instrumental configurations. Figure B.4 shows the reduced scattering results for a number of temperature measurements for the core nanoparticle. Interestingly, there are two temperature crossover points in which the scattering intensity changes. At $q < 0.01 \text{ \AA}^{-1}$ the 40K data is highest in intensity and the 450K data the weakest in intensity with the other temperatures scaling in between respectively. However around 0.01 \AA^{-1} a crossover in intensity occurs and the scattering at 450K is now the highest intensity and the 40 K data is the lowest in intensity. At $q = 0.79 \text{ \AA}^{-1}$ another crossover occurs and reverts back to 450K data being the least intense and the 40K data having the highest intensity. This crossover phenomenon was quite unexpected. The scattering intensity is a combination of the nuclear scattering and magnetic scattering. At low temperatures, the

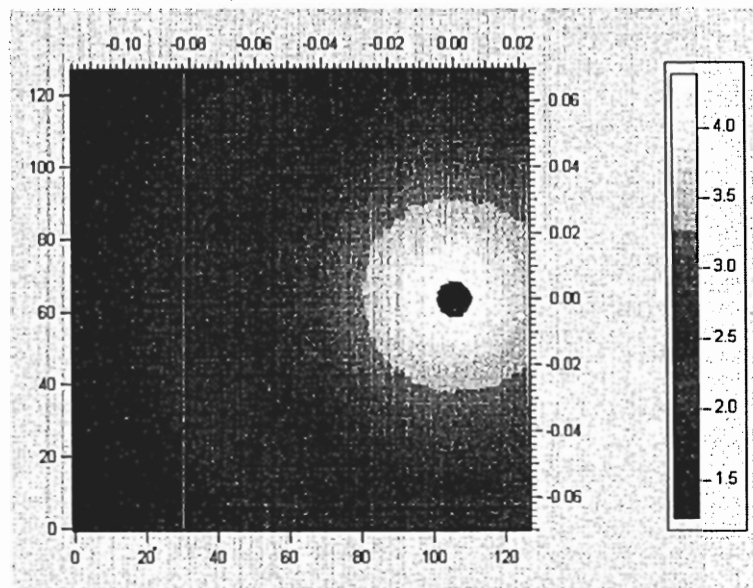


Figure B.3. Example of raw SANS data for core nanoparticle sample.

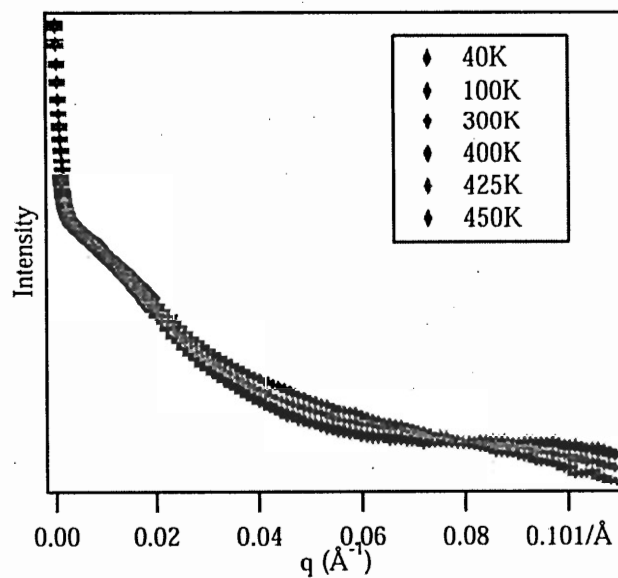


Figure B.4. Scattering intensity as a function of temperature for core nanoparticle.

magnetic scattering is enhanced and the intensity at low temperatures is expected to be larger than scattering intensities measured at higher temperatures. The low q and high q data fit this explanation. However, the physical meaning of these temperature dependent intensity crossovers is not yet clear. Similar crossovers were also observed in the two core/shell samples.

Figure B.5 shows the scattering results for 12 nm $\text{Zn}_{0.05}\text{Co}_{0.95}\text{Fe}_2\text{O}_4$ core sample, the 12 nm $\text{Zn}_{0.05}\text{Co}_{0.95}\text{Fe}_2\text{O}_4$ with a 2.5 nm shell, and with a 4.5 nm shell at 300K. Qualitatively, the scattering data show differences in the degree of curvature in the q range 0.01-0.02 \AA^{-1} and changes in the degree of inflection at low q ($<0.005 \text{ \AA}^{-1}$). The

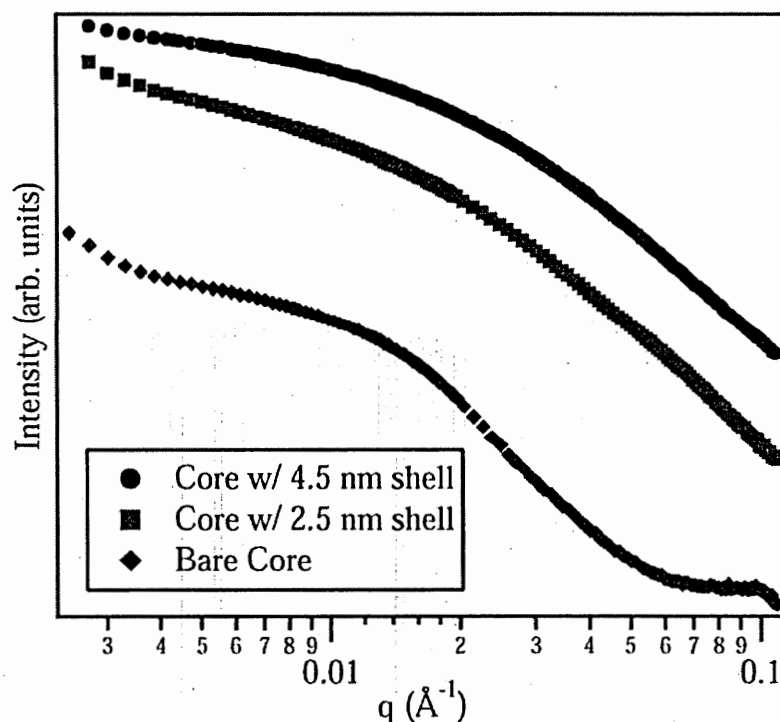


Figure B.5. SANS measurements at 300K for the $\text{Zn}_{0.05}\text{Co}_{0.95}\text{Fe}_2\text{O}_4$ core (\blacklozenge), the core with a 2.5 nm shell (\blacksquare) and the core with a 4.5 nm shell (\bullet).

low- q data is consistent with the lengthscale expected for interparticle coupling, and the changing degree of inflection may suggest changes in the interparticle interactions. Quantitative results can be obtained from analysis of different regions of the scattering data. Figure B.6 identifies a number of regions in which useful information may be extracted. Figure B.7 shows an example of a Porod plot. From this fit, the surface roughness can be determined. A slope of -3 represents a fractal surface, while a slope of -4 represents a completely smooth surface.⁶ The Porod plots indicate a slope of -3.4 for these samples, suggesting some surface roughness.

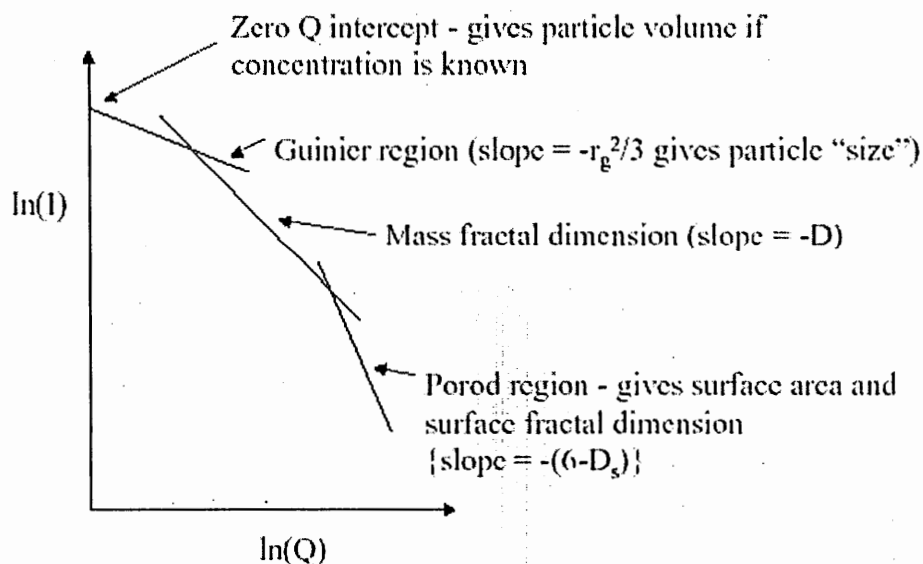


Figure B.6. Identification of regions in which data analysis can be performed.⁵

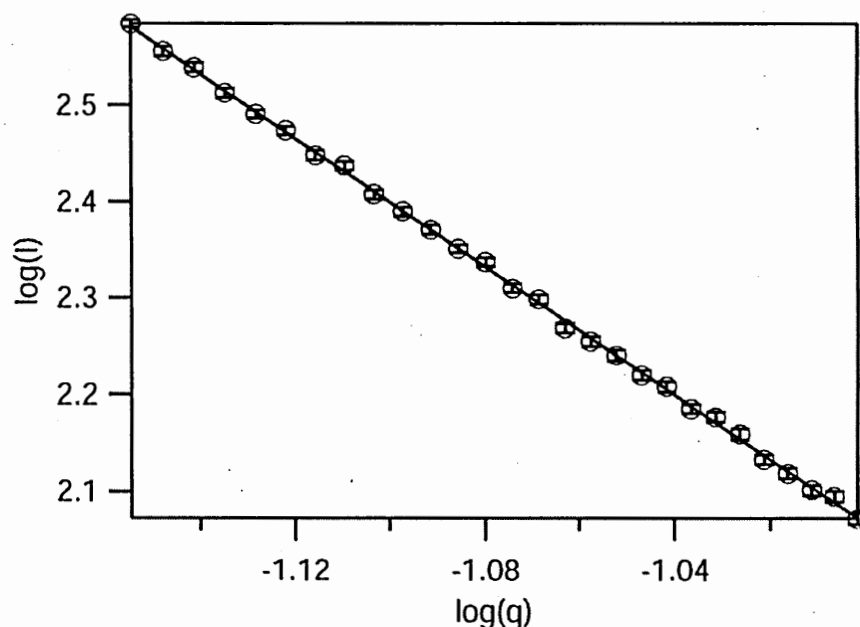


Figure B.7. Example of a Porod plot for the core sample.

The most interesting results were found in the Guinier region analysis. Figure B.8 shows an example of a Guinier fit to the scattering data for the core sample. From the Guinier fit, the radius of gyration (R_g), which is a measure of “particle” size, can be determined. The results from the Guinier fit for the three samples are compared in Table B.1. The R_g of the core sample (12.8 nm) agrees well the particle size determined from x-ray diffraction measurements (12.5 nm). Interestingly, the R_g *decreases* when the ZnFe_2O_4 shell is added! Furthermore, the R_g decreases even more for the sample with the largest shell, i.e. the largest net size!!! It is not entirely clear why the particle size appears to decrease with shell addition, although a diminishing magnetic correlation

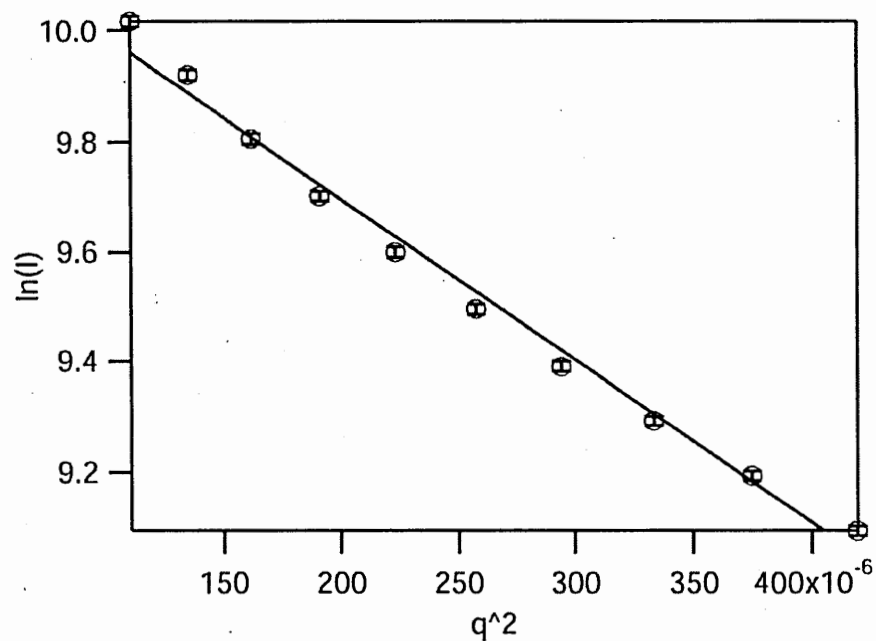


Figure B.8. Example of a Guinier plot for the core sample.

Table B.1. Summary of the R_g Determined from the Guinier Region of the SANS Data with X-ray (and TEM) Determined Particle Size.

Sample	SANS - R_g (nm)	X-ray Size (nm)
Core	12.8	12.5
+ 2.5 nm shell	10.5	17.5
+ 4.5 nm shell	9.6	21.5

length could contribute to this observation. Further studies under applied magnetic field are needed to isolate the magnetic contributions.

B.4 Conclusions

Control over the superparamagnetic state is critically important in further development of magnets for biomedical applications. Reducing the coercivity and blocking temperature while maintaining a high magnetization are the key factors in designing materials for biological applications. New magnetic nanoparticle materials with core-shell architecture show promise for the development of materials with these desired properties. However, the reasons for the dramatic changes in magnetic properties observed for $\text{Zn}_{0.05}\text{Co}_{0.95}\text{Fe}_2\text{O}_4/\text{ZnFe}_2\text{O}_4$ core/shell nanoparticles are not yet clear. To address these issues, temperature dependent SANS measurements have been performed on $\text{Zn}_{0.05}\text{Co}_{0.95}\text{Fe}_2\text{O}_4$ nanoparticles and $\text{Zn}_{0.05}\text{Co}_{0.95}\text{Fe}_2\text{O}_4$ nanoparticles with a 2.5 nm ZnFe_2O_4 shell and a 4.5 nm ZnFe_2O_4 shell. Interesting results such as a decrease in the R_g with increasing particles size were found. The decrease is suggested to originate from a decreasing magnetic size induced by the exchange interactions from the ZnFe_2O_4 shell. Wagner, et.al. have utilized SANS experiments performed under various applied fields to assist in resolving the relationship between the structural and magnetic contributions to the SANS signal for Fe nanoparticles.⁷ Future work includes measuring the SANS response of these core-shell nanoparticles in varying applied field (0 - 5T). From these experiments the contribution of magnetic interparticle interactions can be determined. Furthermore, the magnetic size of the nanoparticles (in contrast to structural nanoparticle size) can be measured.

B.5 References

- (1) Sun, S.; Murray, C. B.; Weller, D.; Folks, L.; Moser, A. *Science* **2000**, 287, 1989.
- (2) Raj, K.; Moskowitz, B.; Casciari, R. *J. Magn. Magn. Mater.* **1995**, 149, 174.
- (3) Häfeli, U.; Schütt, W.; Teller, J.; Zborowski, M., Eds. *Scientific and Clinical Applications of Magnetic Carriers*; Plenum: New York, 1997.
- (4) Samia, A. C. S. PhD. Thesis. Georgia Institute of Technology: Atlanta, 2002.
- (5) <http://www.ncnr.nist.gov/summerschool/ss02/index.html>.
- (6) Hammouda, B. *personal discussion* **2002**.
- (7) Löffler, J. F.; Braun, H.-B.; Wagner, W. *Phys. Rev. Lett.* **2000**, 85, 1990.

VITA

Christy Riann Vestal was born on July 5, 1977 in Lynchburg, Virginia to Michael and Janet Vestal. She graduated from Nelson County High School in Lovingston, Virginia in 1995 and was valedictorian. Her undergraduate studies were performed at James Madison University in Harrisonburg, Virginia. She graduated magna cum laude in 1999 with a B.S. in Chemistry. Her honors thesis entitled "Reactions of Various First Row Transition Metal 2,4-Pentanedionato Complexes Under CVD Conditions" was directed by Dr. Thomas C. DeVore and was awarded the Phi Kappa Phi Award for the best honors thesis at James Madison University in 1999. Her graduate work was conducted at the Georgia Institute of Technology in Atlanta, Georgia under the direction of Dr. Z. John Zhang. She graduated with a Ph.D. in chemistry in 2004.